
\mathbb{Z}_2 LATTICE GAUGE THEORIES COUPLED TO DYNAMICAL MATTER

IN THE AGE OF QUANTUM SIMULATION

MATJAŽ KEBRIČ



München 2024

\mathbb{Z}_2 LATTICE GAUGE THEORIES COUPLED TO DYNAMICAL MATTER

IN THE AGE OF QUANTUM SIMULATION

MATJAŽ KEBRIČ

Dissertation
der Fakultät für Physik
der Ludwig-Maximilians-Universität
München

vorgelegt von
Matjaž Kebrič
aus Maribor, Slowenien

München, den 13. Juni 2024

Erstgutachter: Prof. Dr. Fabian Grusdt
Zweitgutachter: Prof. Dr. Luca Barbiero
Tag der mündlichen Prüfung: 25. Juli 2024

Zusammenfassung

Gittereichtheorien spielen eine wichtige Rolle zum Verständnis von stark korrelierten Systemen, besonders bei confinement (Einschluss) von Teilchen. Mit neuesten Quantumsimulatoren kann man Bausteine von solchen Systemen bereits untersuchen. Ein besseres theoretisches Verständnis von Gittereichtheorien und die Entwicklung von Methoden zur Untersuchung von solchen Systemen mit Quantumsimulatoren ist also notwendig.

In dieser Arbeit untersuchen wir die paradigmatische eindimensionale \mathbb{Z}_2 Gittereichtheorie, in welcher dynamische Materie an ein Eichfeld gekoppelt ist. Die Besonderheit dieser \mathbb{Z}_2 Gittereichtheorien ist der confinement von Teilchen (Partonen) in Dimere (Mesonen), welcher durch eine nicht lokale Eichwechselwirkung vermittelt wird. Wir benutzen numerische Berechnungen und komplementieren diese mit analytischen Argumenten.

Wir entwickeln eine vollständige Erklärung von confinement, und untersuchen mithilfe verschiedener numerischer Methoden den confinement von Teilchen. Bei endlichen Temperaturen beobachten wir einen glatten crossover zwischen confinement und freien Teilchen. Die Mesonen formen sich schon bei höheren Temperaturen, allerdings ist Kohärenz durch thermische Fluktuationen zerstört und die Teilchen erscheinen als frei. Diese \mathbb{Z}_2 Gittereichtheorie könnte man im Quantumsimulator mit ultrakalten Atomen simulieren. Wir untersuchen deswegen verschiedene geometrische Observablen die in solchen Systemen einfach zugänglich sind.

Motiviert durch die Entwicklung von Quantumsimulatoren, untersuchen wir zudem auch verschiedene Phasendiagramme von \mathbb{Z}_2 Gittereichtheorien und entdecken dabei interessante Physik, die durch das Zusammenspiel von Eichfeld und lokalen Wechselwirkungen entsteht. Wir entdecken eine Mott-Isolator-Phase von Partonen bei halber Füllung, und eine Mott-Isolator-Phase von Mesonen bei zwei drittel Füllung, wenn die Materie eine globale $U(1)$ Symmetrie hat. Wenn wir zusätzlich supraleitende Terme berücksichtigen, welche die globale $U(1)$ Symmetrie zerstören, erhalten wir ein System, was der Kitaev-Kette ähnelt. In diesem Regime, enthält die fast volle oder fast leere Kette ähnliche confinement-Eigenschaften, weil die Teilchenfluktuationen, welche die Physik dominieren, von Partonpaaren ausgeht. Wir zeigen daher, dass man den topologischen Übergang in Kitaev Ketten als confinement-deconfinement Übergang in diesen \mathbb{Z}_2 Gittereichtheorien verstehen kann.

Wir entwickeln zusätzlich eine mean-field Theorie für die \mathbb{Z}_2 Gittereichtheorien, in welchen wir einen Produktansatz wählen und damit die Materieteilchen von dem Eichfeld entkoppeln. Das Gauss Gesetz wird durch Lagrange-Multiplikatoren eingesetzt. Die mean-field Theorie kann wichtige Eigenschaften von exakten \mathbb{Z}_2 Gittereichtheorie erfassen, einschließlich von confinement.

Schließlich erforschen wir auch das mixed-dimensional XXZ Model, welches zu einer \mathbb{Z}_2 Gittereichtheorie transformiert werden kann. Wir zeigen nun, dass sich in diesem System auch Mesonen bei niedrigen Temperaturen formen, die einen Übergang zu freien Partonen bei höheren Temperatur haben. Ein solches System kann man mit kalten Atomen mit magnetischem Dipol simulieren.

Unsere theoretischen Ergebnisse ebnen den Weg für ein besseres Verständnis über die \mathbb{Z}_2 Gittereichtheorien, insbesondere confinement. Damit sind unsere Ergebnisse auch relevant für zukünftige Quantensimulationen, weil wir auch neue Methoden entwickeln um die \mathbb{Z}_2 Gittereichtheorien in Experimenten zu untersuchen.

Abstract

Lattice gauge theories have an important role in understanding strongly correlated systems in particular the problem of confinement. The recent progress in quantum simulation already allows us to study simple building blocks of such systems. A better theoretical understanding of lattice gauge theories and how they could be studied in quantum simulation platforms is thus needed.

In this thesis we study a paradigmatic one-dimensional \mathbb{Z}_2 lattice gauge theory (LGT), where dynamical matter is coupled to a gauge field. The hallmark of this \mathbb{Z}_2 LGT is confinement of particles (partons) into bound dimers (mesons), which is mediated through a non-local gauge interaction. We employ numerical calculations using matrix-product states, complemented by analytical arguments in certain limits.

We provide a general explanation of confinement, and study different probes of confinement numerically. At finite temperature we uncover a smooth crossover from a confined to a thermally deconfined regime. There we discover that mesons are in fact already preformed at high temperature, where thermal fluctuations make them incoherent. The \mathbb{Z}_2 LGT could be implemented in state-of-the-art quantum simulators with cold atoms. For that reason, we likewise study simple geometric probes of confinement, which are readily accessible in quantum simulation experiments.

Motivated by the prospect of quantum simulation, we also study different phase diagrams of the \mathbb{Z}_2 LGT and uncover rich physics driven by the interplay of non-local gauge mediated interaction and local repulsion between partons. We show that when matter has a global $U(1)$ symmetry, a parton Mott state can be stabilized at half filling and a meson Mott state can be realized at two-thirds filling. By including superconducting terms, which explicitly break the global $U(1)$ symmetry of the matter, we obtain a system resembling a gauged Kitaev chain. There, a nearly empty or fully filled lattices show similar confined features, since matter fluctuations that dominate the physics in that regime are constituted by parton pairs. We thus demonstrate that the topological transition in Kitaev chains can be understood as a confinement transition.

In addition, we develop a mean-field theory for the \mathbb{Z}_2 LGT by employing a product ansatz where we decouple matter and gauge fields, but the Gauss law is enforced on the mean-field level via Lagrange multipliers. The mean-field theory qualitatively captures the main features of the exact \mathbb{Z}_2 LGT, including confinement.

Finally, we study a mixed-dimensional XXZ model, which can be mapped to a \mathbb{Z}_2 LGT. We show that such systems can exhibit confined mesons at finite temperature, which transition to a deconfined parton gas. Such systems can be simulated with cold atoms with magnetic dipoles.

Our theoretical results pave the way towards a better understanding of \mathbb{Z}_2 LGTs, in particular confinement. All of this is relevant for future quantum simulations, as we develop new probes suitable for experimental platforms.

Publications

This thesis is based on the following list of publications and preprints, with partial text overlap. These papers are a result of fruitful collaborations with many co-authors, which all contributed to the final versions of the manuscripts. A short description of contributions of different authors is specified below for each manuscript.

Publications and preprints:

1. **Matjaž Kebrič**, Luca Barbiero, Christian Reinmoser, Ulrich Schollwöck, and Fabian Grusdt. *Confinement and Mott transitions of dynamical charges in one-dimensional lattice gauge theories*. Physical Review Letters **127**, 167203, October 2021. [1]

MK performed DMRG calculations of the exact \mathbb{Z}_2 LGT, and performed the analytical calculations for the Luttinger liquid parameter in the confined phase, particle-hole mapping, and infinite NN repulsion limit. LB performed DMRG calculations in the string length basis. CR performed the Monte Carlo calculations. FG proposed the mapping to the string-length basis, performed analytical calculations of the compressibility, and supervised the project. MK and FG wrote the manuscript. All authors contributed to the analysis and the final manuscript.

We note that this project started already during the author's master thesis studies [2]. As a result some important results, necessary for writing a comprehensive physical description presented in this thesis related to Ref. [1], already appeared in [2].

2. **Matjaž Kebrič**, Umberto Borla, Ulrich Schollwöck, Sergej Moroz, Luca Barbiero, and Fabian Grusdt. *Confinement induced frustration in a one-dimensional \mathbb{Z}_2 lattice gauge theory*. New Journal of Physics **25**, 013035, January 2023. [3]

MK performed the DMRG calculations and wrote most of the manuscript. UB performed iDMRG calculations of the pair-pair correlations. LB and FG proposed the initial idea. FG supervised the project. All authors contributed to the analysis and writing of the final manuscript.

3. **Matjaž Kebrič**, Jad C. Halimeh, Ulrich Schollwöck, and Fabian Grusdt. *Confinement in (1+1)-dimensional \mathbb{Z}_2 lattice gauge theories at finite temperature*. Phys. Rev. B **109** 245110, June 2024. [4]

MK performed the MPS calculations and wrote most of the manuscript. JCH performed the exact diagonalization quenches, and wrote the Quench dynamics section.

FG supervised the project. All authors contributed to the analysis and writing of the final manuscript.

4. **Matjaž Kebrič**, Ulrich Schollwöck, and Fabian Grusdt. *Mean-field theory of $1 + 1D \mathbb{Z}_2$ lattice gauge theory with matter*. Preprint on arXiv, April 2024. [5]

FG proposed the parton mean-field ansatz. MK performed all of the calculations and wrote the manuscript. FG supervised the project. All authors contributed to the analysis and writing of the final manuscript.

In preparation

In addition, the following manuscript was in preparation, which is also part of this thesis:

1. **Matjaž Kebrič**, Lin Su, Alexander Douglas, Michal Szurek, Ognjen Marković, Ulrich Schollwöck, Annabelle Bohrdt, Markus Greiner, and Fabian Grusdt. *Mixed-dimensional XXZ model*. *In preparation*, June 2024. [6]

MK performed the DMRG and analytical calculations. AD and LS performed Monte Carlo and exact-diagonalization calculations. LS, AD, MS, and OM performed the experiment. FG, AB, and MG supervised the project. All authors contributed to the analysis and writing of the final manuscript. The title and author order was preliminary at the time of writing this thesis.

Other publications

Furthermore, the author of this thesis was involved in the following publication, which is not included in this thesis:

- Hannah Lange, **Matjaž Kebrič**, Maximilian Buser, Ulrich Schollwöck, Fabian Grusdt, and Annabelle Bohrdt. *Adaptive quantum state tomography with active learning*. *Quantum* 7, 1129, October 2023. [7]

Contents

Zusammenfassung	iii
Abstract	v
Publications	vii
Introduction	1
1 Theoretical background and introduction	5
1.1 Quantum simulation	6
1.1.1 Quantum simulation of LGTs	8
1.2 Introduction to lattice gauge theory	9
1.2.1 Minimal coupling of the gauge field to matter	10
1.2.2 Gauss law in lattice gauge theory	11
1.2.3 A $U(1)$ lattice gauge theory with matter	13
1.2.4 \mathbb{Z}_N lattice gauge theory	17
1.2.5 \mathbb{Z}_2 lattice gauge theory	20
1.3 Numerical simulation of the \mathbb{Z}_2 lattice gauge theory	23
1.3.1 Numerical calculations using DMRG	23
1.3.2 Mapping to the spin model	25
1.3.3 Finite temperature calculations	31
2 Confinement in \mathbb{Z}_2 lattice gauge theories with matter	35
2.1 One-dimensional \mathbb{Z}_2 lattice gauge theory with matter	36
2.2 Confinement in simple limits	38
2.3 Probing confinement in a one-dimensional \mathbb{Z}_2 LGT coupled to matter	41
2.3.1 Green's function	41
2.3.2 Friedel oscillations	42
2.3.3 String-length distributions from snapshots	44
2.4 Solution of the confinement problem	46
2.4.1 Naive bosonization	46
2.4.2 The string-length basis	48
2.4.3 Confinement in the string-length basis	50
2.4.4 Field-theory analysis of the string-length basis	53

2.5	Summary of the confinement problem	54
3	Phase diagrams of 1+1D \mathbb{Z}_2 lattice gauge theories with dynamical U(1) matter	55
3.1	Introduction	55
3.2	Confined and deconfined Luttinger liquid	56
3.2.1	Free partons	57
3.2.2	Confined mesons	57
3.3	Phase diagram at two-thirds filling	59
3.3.1	Analytical limits at two-thirds filling	59
3.3.2	Charge gap at two-thirds filling	61
3.4	Phase diagram at half-filling	65
3.4.1	Analytical limits at half-filling	65
3.4.2	Fluctuating dimers	67
3.4.3	Phase diagram	71
3.4.4	Pre-formed parton plasma	76
3.5	Summary and conclusion	81
4	Confinement in a lattice gauge theory at finite temperature	83
4.1	Introduction	83
4.2	Green's function at finite temperature	86
4.3	Friedel oscillations at finite temperature	90
4.4	String length distributions at finite temperature	92
4.5	Summary and conclusion	95
5	Phase diagram of the \mathbb{Z}_2 LGT with superconducting terms	97
5.1	Introduction	98
5.2	Hamiltonian of the \mathbb{Z}_2 LGT coupled to matter with superconducting terms	98
5.2.1	Mapping to the one-dimensional superconducting model	100
5.3	Phase diagram in the absence of particle conservation	102
5.3.1	Entanglement entropy	102
5.3.2	Confinement	109
5.4	Summary and conclusion	114
6	Mean-field theory of the \mathbb{Z}_2 lattice gauge theory	117
6.1	Introduction	118
6.2	Derivation of the mean-field theory	118
6.3	Phase diagram of the mean-field theory	121
6.3.1	Ising model with transverse and longitudinal fields	121
6.3.2	Numerical simulation of the mean-field theory	122
6.3.3	Entanglement entropy calculations in the mean-field theory	123
6.4	Confinement in the mean-field theory	126
6.4.1	Green's function in the mean-field theory	126
6.4.2	String-length histograms in the mean field theory	129

6.4.3	Summary of the Mean-field theory phase diagram	129
6.5	Comparison between the mean-field theory and the exact LGT	132
6.5.1	Ground state energy comparison	132
6.5.2	Electric field polarization comparison	133
6.6	Summary and conclusion of the mean-field theory for the LGT	135
7	Beyond one-dimension: mixed dimensional XXZ model	137
7.1	Introduction	137
7.2	Model	138
7.2.1	Mapping to the \mathbb{Z}_2 lattice gauge theory	140
7.3	Ground state phase diagram	143
7.3.1	Numerical simulation of the mixed-dimensional XXZ model with MPS	143
7.3.2	Spin-spin correlations	144
7.3.3	Super-stripe order at finite magnetization	146
7.3.4	Summary of the ground state results	148
7.4	Meson gas at finite temperature	148
7.4.1	Melting the stripe order	149
7.4.2	Confinement in the context of LGT	150
7.5	Conclusion and outlook	152
	Conclusion and Outlook	155
	A Mapping between the hard core bosons and the XXZ model	159
	B Details on the structure factor calculations	161
B.1	Peaks at the origin	161
B.2	Details on peak heights	162
B.3	Finite size effects in the static structure factor	162
	C Solution of the mean-field theory for the matter sector	165
	List of Figures	169
	Bibliography	173
	Acknowledgements	191

Introduction

Understanding matter has been one of the primary goals of modern physics. As with any physical concept, there are different levels of understanding of how matter is formed and why it exhibits certain properties [8]. The standard model is believed to explain the smallest fundamental particles and forces between them, which bind them into known matter [9]. Understanding these elementary building blocks of matter is generally in the domain of particle or high energy physics. On a different level, condensed matter physics deals with the interplay of many atoms that are made of such subatomic particles. There, quantum mechanics gives rise to completely new phenomena compared to those seen in elementary particle physics, and one does not care about quarks and gluons that bind the atoms together [8, 9]. This interplay gives rise to exciting phenomena like high-temperature superconductivity [10]. The observation that seemingly simple, or well known fundamental laws of nature can give rise to different and new phenomena was nicely summarized in the well known paper by P. W. Anderson [8].

An important concept to understand matter and its properties is confinement, which appears in many different branches of physics. It is well known that quarks confine into baryons and mesons [10, 11]. However, understanding how exactly and why does this even happen is still not completely clear, despite tremendous progress over the past decades [9]. In condensed matter physics, pairing of particles arises in superconductivity, where in conventional superconductors Cooper pairs [12] are bound states that form the conventional BCS theory [13, 14]. The exact mechanism of high-temperature superconductors, where the BCS theory fails, is still unknown [15]. However, there are indications that pairing of electrons is an important ingredient [15]. Although in such context, one usually does not talk about confinement, but merely about bound states, phenomena related to cuprates can be discussed in terms of lattice gauge theories [16, 17]. In particular, topological transitions in condensed matter physics are often discussed in the context of confinement-deconfinement transitions [17, 18]. Although Anderson would perhaps argue that these phenomena emerge on different scales and while they certainly explain different physics, it is remarkable that seemingly similar models emerge for different underlying mechanisms.

A better fundamental understanding of "simple" lattice gauge theories, which can be derived from big open questions is thus desirable, and perhaps one of the steps towards solving some of them. Here, quantum simulations, where ultracold atoms are trapped in an optical lattice, could help us in the future by simulating these theoretical models [19, 20]. A natural way towards simulating the most complicated models is thus to start with

simpler ones. Remarkably, building blocks of a \mathbb{Z}_2 LGT have already been experimentally implemented in a cold atom setup [21, 22], which could be extended to larger systems [23]. One important aspect in the context of quantum simulations, is thus to study the physics of such models, map out their phase diagrams, and develop physical probes to investigate interesting phenomena like confinement. This is the goal of this thesis: To explore \mathbb{Z}_2 LGTs by investigating their phase diagrams, the mechanism of confinement, and develop physical probes suitable for quantum simulation platforms where these phenomena could be studied.

More precisely, in this thesis we study a \mathbb{Z}_2 lattice gauge theory (LGT) in one spatial dimension, where dynamical matter is coupled to a \mathbb{Z}_2 gauge field. The hallmark of this theory is that it exhibits confinement of individual particles into bound states that remain dynamical. In analogy to confinement of two quarks in particle physics, we dub these confined states mesons. The confinement of individual particles, which we accordingly dub as partons, is mediated by the \mathbb{Z}_2 gauge field. More precisely, the confinement emerges from a set of local constraints, the so called Gauss law constraint, as a linear confining potential in \mathbb{Z}_2 electric strings that connect parton pairs.

LGTs were developed to study confinement in particle physics and are in particular useful as lattice formulations enable numerical simulations [9, 24, 25]. For example in the standard model the non-Abelian $SU(3)$ LGT describes the strong interaction [9, 26]. However, numerical simulations of LGTs are generally complicated as the Monte Carlo simulations [9] are hindered by the sign problem at finite doping when matter is coupled to gauge fields [26–28]. By considering a one-dimensional system in this thesis, we employ the density-matrix renormalization group method, which is free of the sign problem. This allows us to study the \mathbb{Z}_2 LGT for arbitrary doping and for arbitrary parameter values. We complement our large scale numerical calculations with analytical calculations in certain limits.

In a way, the Abelian \mathbb{Z}_2 LGT can be regarded as a simplification of LGTs encountered in the standard model, and one could thus view it as a simple toy model of confinement. Generalizations to more complicated gauge structures, or the continuum limit are in fact rather complicated, although some connections can be made [26]. This is different in condensed matter physics, where \mathbb{Z}_2 LGTs emerge as effective low energy theories in strongly correlated systems [17, 29, 30]. In particular, they appear in the study of the fractionalization of charges, which may be related to high-temperature superconductivity [16, 29] and in the study of topological phases [17]. Hence, the \mathbb{Z}_2 LGTs are a powerful tool in strongly correlated systems.

All of this motivated us to study the one-dimensional (1 + 1D) \mathbb{Z}_2 LGT coupled to dynamical matter in this thesis. One of our main goals was to understand the mechanism of confinement in such \mathbb{Z}_2 LGT and how it could be probed in quantum simulation experiments. For that we study various probes of confinement ranging from the behaviour of the gauge invariant Green's function, to geometric probes like the electric string lengths. Matrix-product states calculations allow us to study these probes in the ground state as well as at finite temperature. With numerical calculations at finite temperature we show

that confinement persists also at low temperature with a smooth crossover to a deconfined regime at high temperature. In addition, we demonstrate how it can be detected from snapshots that can be obtained from quantum simulation experiments.

In addition to confinement, we map out phase diagrams at different fillings, where the interplay of confinement and other interactions, which can be implemented with cold atoms, results in rich and interesting physics. These phase diagrams are thus directly relevant for quantum simulations. Furthermore, we study new phenomena arising from the interplay of confinement and local matter interactions. For example, we uncover a regime where the interplay of confinement and local repulsion among partons results in quantum frustration, which gives rise to plasma-like fluctuations. There, partons appear deconfined on short length scales.

We also study generalized \mathbb{Z}_2 LGTs where matter is not conserved, due to particle number fluctuations. There the system exhibits confinement already in the absence of the dynamic gauge field in addition to the regime where the confinement is mediated via the \mathbb{Z}_2 gauge field. We relate the phase diagram found for the extended \mathbb{Z}_2 LGT to the phase diagram of the two-dimensional \mathbb{Z}_2 LGT. To gain even better insights into the \mathbb{Z}_2 LGTs we also develop a mean-field theory description, which successfully captures all relevant phases, including confinement. This furthermore helps with the interpretation of our previous results.

Finally, we uncover confinement-deconfinement transition in a mixed-dimensional XXZ model, by using the \mathbb{Z}_2 LGT interpretation, developed earlier in this thesis. Such systems can be directly implemented in cold atom experiments with Erbium [6, 31]. There, the stripe-order that we predict theoretically has been recently realized, which can be interpreted in terms of partons being bound to stripes [6].

We thus believe that our work provides new and interesting results on \mathbb{Z}_2 LGT coupled to matter. We give a thorough physical description of one-dimensional \mathbb{Z}_2 LGTs. In particular we provide a detailed explanation of confinement in the ground state as well as its crossover to deconfinement at finite temperature, and map out the relevant phase diagrams at different fillings. Moreover, we develop probes that could be used in cold atom experiments to study these phenomena and thus pave the way for future quantum simulations. Finally, the simulation of the paradigmatic \mathbb{Z}_2 LGT could be used as a benchmark for future quantum simulation of more complicated systems.

Outline

This general introduction is followed by a slightly more technical introduction in Chapter 1, where we set the stage in a more concrete way. We shortly introduce quantum simulation with cold atoms, and how they could be used to simulate LGTs. We then introduce the \mathbb{Z}_2 LGT by coupling gauge field to matter. We start by discussing the infinite $U(1)$ gauge group, which we truncate to a finite, cyclic \mathbb{Z}_N , and finally to the \mathbb{Z}_2 group. The derivation is not mathematically rigorous. However, along the way we introduce many important concepts, like the Gauss law. In the last section of Chapter 1, we also introduce the numerical methods used throughout this thesis and explain how we obtain the numerical results for

the \mathbb{Z}_2 LGT.

In Chapter 2, we focus on confinement in the \mathbb{Z}_2 LGT with matter. Due to extensive introductions in the previous chapter we immediately start discussing some simple arguments for the confinement mechanism. We consider different probes of confinement, and demonstrate how confinement can be studied in our numerical calculations. We also discuss confinement probes suited for quantum simulation experiments, and demonstrate their efficiency. Finally, we provide a formal explanation of the confinement problem in \mathbb{Z}_2 LGTs by mapping the system to a non-local string length basis. Chapter 2 is based on Ref. [1], with numerical results also from Refs. [4, 5].

In Chapter 3 we explore different phase diagrams when the matter coupled to \mathbb{Z}_2 LGT has a global $U(1)$ symmetry. We discuss the parton and meson Luttinger liquid found for generic fillings and parameter regimes. We focus on the filling of two-thirds and half filling, where confinement and nearest-neighbor repulsion among matter results in rich phase diagrams. The discussion of the phase diagram at two-thirds filling is based on Ref. [1], and the discussion of the phase diagram at half filling is based on Ref. [3].

In the following Chapter 4 we again study confinement, however this time at finite temperature. We uncover a smooth confinement-deconfinement crossover as a function of temperature. In addition, we find evidence that mesons are already pre-formed at high temperature relative to the crossover temperature. This in a way breaks the conventional wisdom where we could expect deconfinement at finite temperature, due to the well known deconfined limit when $T \rightarrow \infty$. Chapter 4 is based on Ref. [4].

In Chapter 5 we study confinement in a generalized \mathbb{Z}_2 LGT, by including terms that break the global $U(1)$ symmetry of the matter. We establish a phase diagram in terms of confinement as a function of lattice filling. We uncover that in the almost completely empty or filled lattice, superconducting terms induce fluctuations of confined partons, even without the presence of any dynamics of the \mathbb{Z}_2 gauge fields. We draw some important connections to the \mathbb{Z}_2 LGT in two dimensions, in particular to the phase diagram established by Fradkin and Shenker [32]. Chapter 5 is based on the first part of Ref. [5].

In the subsequent Chapter 6, we develop a mean-field theory of the generalized \mathbb{Z}_2 LGT coupled to matter. By using a product ansatz we decouple matter from the gauge field, and enforce the Gauss law on the mean-field level. We directly compare the mean-field theory to the exact \mathbb{Z}_2 LGT and find good qualitative agreement. In particular, the mean-field theory for the gauge field qualitatively captures the main features of the exact \mathbb{Z}_2 LGT, including confinement. The biggest shortcoming is that it does not capture the regime where matter has a global $U(1)$ symmetry, which the mean-field theory for the gauge field always explicitly breaks. Chapter 6 is based on the remaining part of Ref. [5].

In Chapter 7 we study a mixed-dimensional XXZ model on a cylinder, where interactions in the shorter direction are simplified to simple ferromagnetic Ising coupling. The main motivation is the realization of such system in cold atoms with magnetic dipoles. We find a connection of such system to a \mathbb{Z}_2 LGT with matter, and uncover a confinement-deconfinement transition. Chapter 7 is based on the upcoming Ref. [6].

In the last chapter we conclude and give an outlook for future research directions.

Chapter 1

Theoretical background and introduction

In this chapter, we start with a broader theoretical introduction into the topic of this thesis. This chapter sets the \mathbb{Z}_2 lattice gauge theory (LGT) and other related theoretical concepts in a broader physical perspective. We introduce and define the main properties of the \mathbb{Z}_2 LGT and thus provide a formal footing of the concepts used throughout this thesis.

We start by briefly introducing quantum simulation with ultracold atoms and shed light on how platforms based on ultracold atoms can be used as a new toolbox to study complicated strongly correlated systems. We concisely discuss how quantum simulation platforms are used to simulate basic building blocks of LGTs, and how large scale simulations could be possible in the future. This is in fact one of the main motivations why we study the one-dimensional \mathbb{Z}_2 LGT in such detail in this thesis.

We then proceed to define the \mathbb{Z}_2 lattice gauge theory, by demonstrating the origin of minimal coupling of matter to gauge fields, and the concept of Gauss law. We briefly discuss the $U(1)$ LGT, related quantum link models, define \mathbb{Z}_N LGT, and finally arrive at the paradigmatic \mathbb{Z}_2 LGT coupled to dynamical matter. We also briefly discuss one of our ultimate goals of this thesis: understanding of confinement in this class of LGTs.

Our motivation to study confinement in \mathbb{Z}_2 LGT has its origins in condensed-matter physics and connections to strongly correlated systems like spin liquids and high-temperature superconductivity [17, 29, 33]. We thus approach the topic from a condensed matter and quantum simulation perspective. However, we also briefly discuss how LGTs are used to study the long standing problem of confinement in high energy physics, for which they were originally developed [24, 25].

In the final section, we briefly discuss the numerical methods used throughout this thesis. Focusing mainly on one-dimensional systems, we employ the formalism of matrix-product states and the density-matrix renormalization group (DMRG) method [34, 35].

This chapter thus serves as a motivational section for the chapters that follow. At the same time, the second and the last part of this chapter become more and more technical as we define some important concepts and methods.

1.1 Quantum simulation

Quantum simulation with ultracold atoms is a new tool to study strongly correlated many body systems [19, 20, 36, 37]. In such systems, atoms are cooled down to energy scales where thermal fluctuations give way to quantum effects [19, 38, 39]. The atoms are then trapped in an optical potential generated by standing waves of interfering lasers [19, 40–42].

Such construction of optical lattices means that dimension and geometry of the lattice can be tuned [19, 40, 41]. For example, one can realize a two-dimensional square lattice [43, 44], a lattice with triangular geometry [45], or a hexagonal lattice [46]. In addition, by using lasers with different frequencies, double well structures can be implemented as well [21]. In these cases neutral atoms can be trapped due to alternating electric potential coming from the laser light, which makes them polarized [19, 40]. The laser light is detuned away from the resonance of the internal structure of the atom in order to avoid heating [40]. When the frequency of the laser is lower than the resonance $\Delta_f \equiv \omega - \omega_0 < 0$, the beam is said to be red-detuned and atoms will be generally trapped in the potential intensity maximum [40]. In the blue-detuned case, $\Delta_f > 0$, the atoms are generally trapped in the potential minima [40]. The strength of the dipole trapping is proportional to the laser intensity, and is inversely proportional to the detuning $V_{\text{trap}} \propto I/\Delta_f$ [40]. The scattering rate (heating), however, scales as I/Δ_f^2 [40]. Experimentalists thus typically prefer high detuning and high laser intensity, when implementing the lattice potentials.

Atoms trapped in the optical lattice can tunnel to the neighbouring sites, provided the trapping potential is not too high, and can interact with other atoms [19]. The interactions are typically highly tunable and can range from simple on-site repulsion to various long-range interactions [19]. An important concept to control some of these interactions are Feshbach resonances [47]. One can also tune interactions, which span over longer distances. For example, long-range interactions can be obtained by considering magnetic atoms, which interact via dipole-dipole interactions [31]. Polar ultracold molecules, which consist of different atomic species, also interact via dipole-dipole interactions that can be even stronger [48]. Another example are atoms in highly excited Rydberg states, which possess very strong interactions [38]. Due to such strong interaction, weak coupling to the excited regime, the so called Rydberg dressing, is already enough to implement strong and highly tunable interactions [49].

On-site interactions of a system of ultracold bosons trapped in an optical potential can be used to emulate a Bose-Hubbard Hamiltonian [50, 51]

$$\hat{\mathcal{H}}_{\text{BH}} = -t \sum_{\langle i,j \rangle} (\hat{a}_i^\dagger \hat{a}_j + \text{H.c.}) + \sum_i \epsilon_j \hat{n}_j + \frac{1}{2} U \sum_j \hat{n}_j (\hat{n}_j - 1). \quad (1.1)$$

Here we defined the hopping amplitude t between nearest-neighbor (NN) sites, the boson creation (annihilation) operator as \hat{a}^\dagger (\hat{a}), and the on-site density operator \hat{n}_j . The on-site repulsion strength equals to U , and ϵ_j determines the local chemical potential. A realization of a transition between the superfluid to a Mott insulator phase with ultracold atoms, governed by the Bose-Hubbard model, demonstrated by Greiner et al. [51], was a

break-through, which demonstrated quantum simulation with cold atoms. Many more experimental realizations and extended systems with ultracold bosons followed [52–54], to list just a few.

In addition to bosons, quantum simulation with ultracold fermions is also possible, where one can realize a two component spin system to study the Fermi-Hubbard model [19, 55], which can be expressed as [55]

$$\hat{\mathcal{H}}_{\text{FH}} = -t \sum_{\langle i,j \rangle, \sigma} \left(\hat{c}_{i,\sigma}^\dagger \hat{c}_{j,\sigma} + \text{H.c.} \right) + \sum_i \epsilon_j \hat{n}_j + U \sum_j \hat{n}_{j,\uparrow} \hat{n}_{j,\downarrow}. \quad (1.2)$$

Here $\hat{c}_{j,\sigma}^\dagger$ ($\hat{c}_{j,\sigma}$) are fermion creation (annihilation) operators, which carry spin $\sigma = \uparrow, \downarrow$. The Fermi-Hubbard model has been studied extensively already before the advent of quantum simulation, as it is believed to be the minimal model that could explain high-temperature superconductivity [19, 33, 56–58]. Recent numerical calculations show evidence that the simple Hamiltonian Eq. (1.2), might not be enough to reach the superconducting phase and additional terms like the next-neighbor hopping might be important [59, 60]. Despite how simple the Fermi-Hubbard model appears in Eq. (1.2) it has proved to be very hard to study numerically or analytically [61]. Hence, cold atom implementation of a Fermi-Hubbard model has been a major achievement as it might some day help us to understand this seemingly simple model better. Early successful experiments with fermions, e.g. in Ref. [62], were quickly followed by realizing the Fermi-Hubbard model at half-filling and achieving a Mott state [63, 64].

The last important component that we want to mention in the context of quantum simulation in this introductory section is the detection of trapped atoms and the measurement of their correlations. This became possible with the development of quantum gas microscopy, which enables site resolved imaging [65, 66].

In other words, by having a powerful microscope one can take a snapshot of the quantum system and detect exactly where the particles reside in the optical lattice, which opens the possibility to measure complicated correlations [19]. In addition, new development of more elaborate experimental schemes, in particular reducing the entropy by coupling the system to a dilute reservoir on the edge of the sample allowed for simulations to be performed at lower temperatures [19, 44]. This was achieved by using digital micro-mirror device (DMD) [67], which was used to divide the system into two subsystems, where the entropy from the center was transferred to the outer system [44, 68].

Combination of these developments lead to a remarkable realization of a long-range antiferromagnet by Mazurneko et al. in Ref. [44], by simulating the Hubbard model with cold atoms. Another remarkable achievement by Hilker et al. in Ref. [69] was the successful extraction of multi-point correlations from experimental data, which enabled the detection of hidden anti-ferromagnetic order in a one-dimensional doped Hubbard system.

We also briefly mention Rydberg tweezer arrays, where atoms are trapped in extremely focused laser beams, which can be rearranged to form various geometries, and ultimately make the atoms interact by exciting them to Rydberg states [19, 70–75]. This platform can be used to realize various spin systems [71, 72, 74, 75]. It is also a promising platform to be

used for digital quantum computation [73, 76]. Recently, successful implementation of 280 physical qubits has been demonstrated in Ref. [77].

With this we conclude the general introduction on the ultracold atom experiments. Above we presented some of the key results of quantum simulation with cold atoms. For recent reviews on this topic we refer the interested reader to Refs. [19, 55], which were also the main source for the above discussion. For more technical descriptions it is also useful to consider Refs. [41, 78, 79].

1.1.1 Quantum simulation of LGTs

Quantum simulations with cold atoms are also a promising platform to simulate lattice gauge theories [26, 80, 81]. The building block of the \mathbb{Z}_2 LGT, where matter is coupled to a gauge field, has been already successfully implemented by Schweizer et al. in Ref. [21], where a double well potential scheme with a mixture of two bosonic species was implemented to encode the matter and gauge degrees of freedom [21, 23]. Such building blocks can be scaled up to implement a one or two-dimensional \mathbb{Z}_2 LGT [23]. In this scheme matter and gauge degrees of freedom are encoded with two different species [21, 23]. To induce the matter–gauge coupling the density-dependent hopping scheme was used [21, 82–85]. A similar approach to implement a \mathbb{Z}_2 LGT building block was used by Görg et al. in Ref. [22], where the density-dependent Peirls phase was obtained via Floquet driving. In addition, there has been an experimental realization of a four-body ring-exchange interaction with ultracold atoms [86], that constitutes to the Kitaev’s toric code [87]. Kitaev’s toric code can be then considered as the $(2 + 1)\text{D}$ \mathbb{Z}_2 LGT without matter [81, 88–90].

There have been also a lot of new proposals for the experimental realization of \mathbb{Z}_2 LGTs coupled to matter [90, 91]. For example, a proposal by Homeier et al. in Ref. [91] is based on the Rydberg tweezers platform, where both link and matter sites are encoded by the atomic ground state and the excited Rydberg state.

Immense progress has also been made in simulating the $U(1)$ lattice gauge theory, formulated as quantum link models, where the infinite-dimensional Hilbert space of the $U(1)$ symmetry is discretized and represented by spin- S operators [81, 92–94]. As we will see in the next Section 1.2, quantum link models reproduce the lattice quantum electrodynamics (QED) only in the limit when $S \rightarrow \infty$ [81]. In cold atoms one typically has to truncate the link representation all the way down to $S = 1/2$ [81]. The first experimental realization was achieved by Mil et al. in Ref. [95], where a building block of a $U(1)$ LGT was realized. More experiments followed, where the implementations went above simple building blocks [81]. One of the most remarkable was the realization of a PXP model with Rydberg tweezer arrays by Bernien et al. in Ref. [96], which can be mapped to a $U(1)$ LGT, formulated as a spin- $1/2$ quantum link model (QLM) [81, 97]. Another experimental realization of a $U(1)$ QLM with full tunability has been demonstrated by Yang et al. in Ref. [98].

As argued by Halimeh et al. in Ref. [81], every quantum simulation experiment where both the matter and gauge degrees of freedom have to be implemented will encounter some level of gauge symmetry violation. This is simply due to the sheer complexity of implementing all of the local constraints, or as there will be some weak effective terms

which break it. No such errors arise when one integrates out the matter or gauge degrees of freedom by taking into account the Gauss law in the physical sector [81, 97, 99]. However, for systems where both degrees of freedom are present, gauge violations can be mitigated by imposing energetic constraints to other gauge sectors, by adding terms proportional to the Gauss law, $\propto V_G \sum_j (\hat{G}_j - g^{\text{tar}})^2$ [81, 100, 101]. Here \hat{G}_j is the local gauge symmetry generator with eigenvalues g_j , which we will formally introduce and explain its role in LGTs in the next Section 1.2. Such gauge protection terms contain multiple-body interaction terms, which are hard to implement experimentally [81]. This problem was mitigated by developing linear protection terms for $U(1)$ LGTs [102] and local-pseudogenerators for \mathbb{Z}_2 LGTs [91, 103], which reduce the complexity of the protection term.

As we have seen, quantum simulation of lattice gauge theories is an extremely active field of research, with a lot of new proposals and experimental realizations in the last few years. This is also one of the main motivations to explore the topics presented in this thesis. In addition to mostly Abelian theories discussed above, there have been many proposals for non-Abelian gauge theories as well [104–106]. We also note that in this section we have focused on analog quantum platforms. However, there are a lot of proposals and implementations using digital quantum platforms [107–114].

Furthermore, we did not go into any technical details of quantum simulations of LGTs, as we do not focus on development of new experimental schemes in this thesis. In contrast, we are mainly interested in exploring the physics of \mathbb{Z}_2 LGTs, which can already be realized in existing quantum simulation experiments, or what will at least be possible in the near future. For more details on quantum simulation of lattice gauge theories we refer the reader to recent reviews found in Refs. [80, 81], which were also the main source for the above section.

1.2 Introduction to lattice gauge theory

Before we start our analysis of the \mathbb{Z}_2 LGTs, we give a brief introduction and motivation on how lattice gauge theories are defined, and put the simplest \mathbb{Z}_2 LGT in a broader context of general LGTs. This will be in no way a rigorous derivation of the lattice gauge theories. For a more broad and general introduction we refer the interested reader to Refs. [24, 25, 115, 116]. Our introduction of LGTs follows a brief review in Ref. [26], which is based on the Kogut-Susskind Hamiltonian formulation of the LGTs found in Ref. [117]. This differs from the usual approach in high-energy physics (HEP), where one starts by writing an appropriate action of a given problem. We prefer the Hamiltonian formulation, since our interests in LGTs come from the condensed matter perspective, where one generally deals with Hamiltonians. In addition, the language of quantum simulation and the effective models that can be simulated are always given in the Hamiltonian formulation [19, 26, 81].

We note that we could have also taken a different, more historical approach, and start with the \mathbb{Z}_2 LGT as formulated by Wegner in Ref. [88], to study Ising transitions by using duality transformations [118]. Or we could start with the LGT developed by Wilson in Ref. [25], to understand the confinement of quarks in high energy physics. This was in fact

the starting point of Kogut and Susskind when developing the Hamiltonian formulation [117]. Finally, we note that a similar derivation has been performed also in Ref. [79], which we in part also used as a reference in the following sections.

1.2.1 Minimal coupling of the gauge field to matter

We start by considering a Hamiltonian which describes hopping of free fermions [26]

$$\hat{\mathcal{H}} = -t \sum_{\mathbf{n}, \mathbf{a}} \left(\psi_{\mathbf{n}+\mathbf{a}}^\dagger \psi_{\mathbf{n}} + \text{H.c.} \right) + \sum_{\mathbf{n}} \mu_{\mathbf{n}} \psi_{\mathbf{n}}^\dagger \psi_{\mathbf{n}}, \quad (1.3)$$

where $\psi_{\mathbf{n}}^\dagger$ can be generally considered to be a spinor. With \mathbf{n} we define a lattice site in a D -dimensional hypercube lattice. Furthermore, we define \mathbf{a} as the unit vector pointing along one of the D directions.

We will start with a simple Abelian case, where the global symmetry is $U(1)$, i.e. the gauge group G is the unitary group $U(1)$. We choose such a case since we believe it is the most instructive and will allow us to quickly make a connection to the \mathbb{Z}_2 lattice gauge theory. In the end of this introduction, we will briefly comment on the more complicated $SU(2)$ case.

If we consider the $U(1)$ case, the spinor $\psi_{\mathbf{n}}^\dagger$ ($\psi_{\mathbf{n}}$) in Eq. (1.3) can simply be a spinless fermion creation (annihilation) operator on site \mathbf{n} [26, 79]. The first term in Eq. (1.3) can be thus understood as the hopping term with some amplitude t , and the second term can be understood as a chemical potential term, $\mu_{\mathbf{n}}$, which for now has a site-dependence and could also be considered to be the site-dependent mass term [26].

Since the Hamiltonian in Eq. (1.3) contains only a hopping term and a chemical potential terms, it is clear that the Hamiltonian has a global $U(1)$ symmetry, where the particle number, $N = \sum_{\mathbf{n}} \psi_{\mathbf{n}}^\dagger \psi_{\mathbf{n}}$, is conserved. We can thus write a global gauge transformation of the operators as [26]

$$\psi_{\mathbf{n}} \rightarrow V \psi_{\mathbf{n}}, \quad \psi_{\mathbf{n}}^\dagger \rightarrow \psi_{\mathbf{n}}^\dagger V^\dagger, \quad (1.4)$$

which does not change the Hamiltonian in Eq. (1.3) since V has to be an element of the gauge group $G = U(1)$ and is thus unitary, $VV^\dagger = V^\dagger V = I$.

The essence of the lattice gauge theories is that global symmetries are promoted to local symmetries [119, 120], which we can formally write as making the gauge transformation in Eq. (1.4) local [26]

$$\psi_{\mathbf{n}} \rightarrow V_{\mathbf{n}} \psi_{\mathbf{n}}, \quad \psi_{\mathbf{n}}^\dagger \rightarrow \psi_{\mathbf{n}}^\dagger V_{\mathbf{n}}^\dagger. \quad (1.5)$$

Due to the local nature of the above transformation, the hopping term does not remain invariant and as a result transforms to [26]

$$\psi_{\mathbf{n}+\mathbf{a}}^\dagger \psi_{\mathbf{n}} \rightarrow \psi_{\mathbf{n}+\mathbf{a}}^\dagger V_{\mathbf{n}+\mathbf{a}}^\dagger V_{\mathbf{n}} \psi_{\mathbf{n}}. \quad (1.6)$$

In order to reinstate the symmetry, we can modify the hopping term of the Hamiltonian in a way that will make it invariant under the local transformation in Eq. (1.5). This is done by adding the so called "connection" $U_{\mathbf{n}, \mathbf{n}+\mathbf{a}}$ on the link between site \mathbf{n} and its neighboring

site $\mathbf{n} + \mathbf{a}$, which transforms as [26]

$$U_{\mathbf{n},\mathbf{n}+\mathbf{a}} \rightarrow V_{\mathbf{n}} U_{\mathbf{n},\mathbf{n}+\mathbf{a}} V_{\mathbf{n}+\mathbf{a}}^\dagger. \quad (1.7)$$

Here we use the notation where the link variable U is directed from \mathbf{n} towards $\mathbf{n} + \mathbf{a}$. The modified, gauge invariant Hamiltonian, thus becomes

$$\hat{\mathcal{H}} = -t \sum_{\mathbf{n},\mathbf{a}} \left(\psi_{\mathbf{n}+\mathbf{a}}^\dagger U_{\mathbf{n},\mathbf{n}+\mathbf{a}} \psi_{\mathbf{n}} + \text{H.c.} \right) + \sum_{\mathbf{n}} \mu_{\mathbf{n}} \psi_{\mathbf{n}}^\dagger \psi_{\mathbf{n}}, \quad (1.8)$$

where we note that no modification was needed for the chemical potential term since the operators act on the same site. With the operations performed above we obtained a Hamiltonian where the gauge degrees of freedom, represented by $U_{\mathbf{n},\mathbf{n}+\mathbf{a}}$, are minimally coupled to matter, ψ [79].

We note that all operators V , $V_{\mathbf{n}}$ and $U_{\mathbf{n},\mathbf{n}+\mathbf{a}}$ are elements of the gauge group G [26]. In the $U(1)$ case one can parameterize the connection as [26]

$$U_{\mathbf{n},\mathbf{n}+\mathbf{a}} = e^{i\theta_{\mathbf{n},\mathbf{n}+\mathbf{a}}}, \quad (1.9)$$

where $\theta_{\mathbf{n},\mathbf{n}+\mathbf{a}}$ are the so called group parameters residing on the lattice links [26, 79].

1.2.2 Gauss law in lattice gauge theory

Next we introduce the Gauss law, which is one of the fundamental aspects in LGTs and, as we will see in the following sections, imposes certain local constraints on the system. This generally complicates the calculations, but in some instances it can also be used to simplify the numerical effort, by using the constraints to integrate out matter or gauge degrees of freedom.

In the following, we will illustrate how a set of generators, $\hat{G}_{\mathbf{n}}$, of the local gauge transformation [26] correspond to a Gauss law in the LGT. These operators $\hat{G}_{\mathbf{n}}$ commute with the Hamiltonian by definition [1, 3–5, 26, 121],

$$[\hat{\mathcal{H}}, \hat{G}_{\mathbf{n}}] = 0, \quad (1.10)$$

and since we are considering an Abelian group also with each other [121],

$$[\hat{G}_{\mathbf{m}}, \hat{G}_{\mathbf{n}}] = 0. \quad (1.11)$$

This means that the Hamiltonian can be block diagonalized for different Hilbert space sectors, which are denoted by the set of eigenvalues $\{g_{\mathbf{n}}\}$, and are defined as

$$\hat{G}_{\mathbf{n}} |\psi\rangle = g_{\mathbf{n}} |\psi\rangle, \quad (1.12)$$

for every lattice site \mathbf{n} .

In the next step we would like to find the generators of the $U(1)$ gauge symmetry. For

that we consider the connection in Eq. (1.9), where we defined the group parameters $\hat{\theta}_{\mathbf{n},\mathbf{a}}$. From its structure, the group elements can be literally understood as the angular variables [26], for which one can define the canonical momentum [26, 79]

$$\hat{L}_{\mathbf{n},\mathbf{n}+\mathbf{a}} = -i \frac{\partial}{\partial \hat{\theta}_{\mathbf{n},\mathbf{n}+\mathbf{a}}}. \quad (1.13)$$

Such construction results in the correct commutator of the two quantities [26]

$$[\hat{\theta}_{\mathbf{n},\mathbf{n}+\mathbf{a}}, \hat{L}_{\mathbf{n},\mathbf{n}+\mathbf{a}}] = i. \quad (1.14)$$

Taking the analogy further, this is nothing else but the angular momentum and thus the generator of rotations [122]. This becomes apparent as the following commutation holds [26]

$$[\hat{L}_{\mathbf{n},\mathbf{n}+\mathbf{a}}, \hat{U}_{\mathbf{n},\mathbf{n}+\mathbf{a}}] = \hat{U}_{\mathbf{n},\mathbf{n}+\mathbf{a}}, \quad (1.15)$$

which means that the operator $\hat{U}_{\mathbf{n},\mathbf{n}+\mathbf{a}}$ acts as a raising operator for eigenstate $|\psi\rangle$ of the operator $\hat{L}_{\mathbf{n},\mathbf{n}+\mathbf{a}}$ [26, 79, 123]. This can be easily shown since

$$\hat{L}\hat{U}|\psi\rangle - \hat{U}\hat{L}|\psi\rangle = \hat{L}|\tilde{\psi}\rangle - l|\tilde{\psi}\rangle = |\tilde{\psi}\rangle \Rightarrow \hat{L}|\tilde{\psi}\rangle = (l+1)|\tilde{\psi}\rangle, \quad (1.16)$$

where we omit the lattice indices and define $|\tilde{\psi}\rangle = U|\psi\rangle$. We have thus shown that U raises the eigenvalue of the angular momentum by one, $l \rightarrow l+1$. This makes the eigenbasis of \hat{L} , a convenient basis to work in [26]. We will use it in the next section in order to obtain a better understanding in a more concrete setting.

We note that the analogy to the angular momentum is used to write a kinetic energy of the fields $\hat{\theta}_{\mathbf{n},\mathbf{n}+\mathbf{a}}$ by writing the Hamiltonian of the rotator [117, 124]

$$\hat{H}_r = \sum_{\mathbf{n},\mathbf{a}} \frac{\hat{L}_{\mathbf{n},\mathbf{n}+\mathbf{a}}^2}{2J_l}, \quad (1.17)$$

where J_l is the moment of inertia. Furthermore, Kogut and Susskind in Ref. [117] connected the angular momentum with the electric field, $L = E$, and the angular variables with the magnetic vector potential, $A = \theta$ [79]. Thus the Eq. (1.17) can be considered as the electric field energy [26, 79]. We will use this analogy to justify why the set of generators resemble the Gauss law.

Finally, we express the generators on a lattice site as a difference of angular momenta between links connected to these lattice sites, which reads as [24, 26, 117]

$$\hat{G}_{\mathbf{n}} = \sum_{\mathbf{a}} (\hat{L}_{\mathbf{n},\mathbf{a}} - \hat{L}_{\mathbf{n}-\mathbf{a},\mathbf{a}}). \quad (1.18)$$

Since we are interested in the lattice gauge theories coupled to matter one also has to take into account the so called dynamical charges, $Q_{\mathbf{n}}$, and the full Gauss law of the $U(1)$ lattice

gauge theory becomes [24, 26]

$$\hat{G}_{\mathbf{n}} = \sum_{\mathbf{a}} (\hat{L}_{\mathbf{n},\mathbf{n}+\mathbf{a}} - \hat{L}_{\mathbf{n}-\mathbf{a},\mathbf{n}}) - \hat{Q}_{\mathbf{n}}. \quad (1.19)$$

By relabeling the angular momentum operators to the electric field operators on the links

$$\hat{L}_{\mathbf{n},\mathbf{n}+\mathbf{a}} \rightarrow \hat{E}_{\mathbf{n},\mathbf{n}+\mathbf{a}}, \quad (1.20)$$

it becomes clear why this is called the Gauss law

$$\hat{G}_{\mathbf{n}} = \sum_{\mathbf{a}} (\hat{E}_{\mathbf{n},\mathbf{n}+\mathbf{a}} - \hat{E}_{\mathbf{n}-\mathbf{a},\mathbf{n}}) - Q_{\mathbf{n}}, \quad (1.21)$$

as the sum of all the links related to site \mathbf{n} is a lattice counterpart of the divergence of the electric field, $\nabla \cdot \vec{E}$ [79, 117]. Up to constants we thus obtain the full analogy to the "usual" Gauss law [125]

$$\nabla \cdot \vec{E} = 4\pi\rho, \quad (1.22)$$

where with the total charge ρ , we mean the combined contribution of the background (static) charges, $Q_{\mathbf{n}}^s$, and the dynamical gauge charges, $\rho = Q_{\mathbf{n}}^s + Q_{\mathbf{n}}$.

We note that for a non-Abelian $SU(2)$ case, the situation is more complicated. One has to define two sets of link operators: the so called left, $L_{\mathbf{n},\mathbf{n}+\mathbf{a}}$, and right set, $R_{\mathbf{n},\mathbf{n}+\mathbf{a}}$ [26]. As a consequence we also obtain two sets of generators of the group and the Gauss law becomes [26]

$$\hat{G}_{\mathbf{n}}^u = \sum_{\mathbf{a}} (\hat{L}_{\mathbf{n},\mathbf{n}+\mathbf{a}}^u - \hat{R}_{\mathbf{n}-\mathbf{a},\mathbf{n}}^u) - Q_{\mathbf{n}}^u, \quad (1.23)$$

where u are the group indices.

1.2.3 A $U(1)$ lattice gauge theory with matter

At this point we can, as an example, construct a $U(1)$ LGT Hamiltonian. For simplicity, we will consider a case with a two-dimensional square lattice. The matter fields are minimally coupled to fermionic matter [26],

$$\hat{\mathcal{H}}_{QED} = -t \sum_{\mathbf{n},\mathbf{a}} \left(\hat{c}_{\mathbf{n}}^\dagger \hat{U}_{\mathbf{n},\mathbf{n}+\mathbf{a}} \hat{c}_{\mathbf{n}+\mathbf{a}} + \text{H.c.} \right) + \mu \sum_{\mathbf{n}} (-1)^n \hat{c}_{\mathbf{n}}^\dagger \hat{c}_{\mathbf{n}}, \quad (1.24)$$

where $\mathbf{n} = (x, y)$ is a two-dimensional vector on a 2D square lattice and we define $n = x + y$ [26]. In addition, \mathbf{a} represents one of the two primitive vectors, pointing to the neighbouring lattice site $\mathbf{a} \in \{\mathbf{a}_1, \mathbf{a}_2\}$. Here $\mathbf{a}_1 = (1, 0)$, $\mathbf{a}_2 = (0, 1)$, and we set the lattice constant to $a = 1$. The Hamiltonian in Eq. (1.24) is just Eq. (1.8), where we relabeled the spinless fermion operators as $\psi \rightarrow \hat{c}$, and we adopted the staggered fermion formulation, which is one of the favored formulations to avoid the fermion doubling problem [26, 126].

In addition to the matter Hamiltonian coupled to the gauge field, we should also include a pure gauge Hamiltonian in order to induce dynamics in the gauge fields. By following

the angular momentum/electric field analogy, we can add a kinetic energy of the fields, Eq. (1.17), which is proportional to $\propto \hat{L}_{\mathbf{n},\mathbf{n}+\mathbf{a}}^2$ [26, 79].

Similarly, one could add a term proportional to the energy of the magnetic field $\propto \hat{B}_{\mathbf{n}}^2$ [24, 79]. However, so far we have not clearly defined what constitutes the magnetic field in our LGT. We can thus consider this question a bit broader and ask ourselves how can one obtain additional terms in the Hamiltonian, by combining different operators, which are gauge invariant [26]. Kogut and Susskind in Ref. [117] realized that gauge invariant operators can be constructed by using a product of \hat{U} 's. In other words this means that additional terms can be constructed by applying a set of \hat{U} operators on a closed loop Γ , which correspond to the continuity of the electric flux lines [117]. In addition, by including matter fields one can also consider a product of \hat{U} operators, which form paths that end with matter operators [26, 117]. Adding terms that contain \hat{U} terms, which couple different links, is also necessary in order to make the LGT non-trivial as they induce dynamics in gauge fields [117].

Kugut and Susskind thus added the "simplest" of such terms by considering the magnetic term in Wilson's action [25]. In the Hamiltonian representation this are the plaquette terms, which can be written as a trace of a product of operators over the smallest possible loop [24, 26, 79, 117],

$$\begin{aligned}\hat{\mathcal{H}}_A &= -J \sum_{\square} (\text{tr} (\hat{U}_{\mathbf{n},\mathbf{n}+\mathbf{a}_1} \hat{U}_{\mathbf{n}+\mathbf{a}_1,\mathbf{n}+\mathbf{a}_1+\mathbf{a}_2} \hat{U}_{\mathbf{n}+\mathbf{a}_1+\mathbf{a}_2,\mathbf{n}+\mathbf{a}_2} \hat{U}_{\mathbf{n}+\mathbf{a}_2,\mathbf{n}}) + \text{H.c.}) \\ &= -J \sum_{\square} \cos(\hat{\theta}_{\mathbf{n},\mathbf{n}+\mathbf{a}_1} + \hat{\theta}_{\mathbf{n}+\mathbf{a}_1,\mathbf{n}+\mathbf{a}_1+\mathbf{a}_2} + \hat{\theta}_{\mathbf{n}+\mathbf{a}_1+\mathbf{a}_2,\mathbf{n}+\mathbf{a}_2} + \hat{\theta}_{\mathbf{n}+\mathbf{a}_2,\mathbf{n}}),\end{aligned}\quad (1.25)$$

where the former is a general expression and the latter equality holds for the Abelian $U(1)$ LGTs [26]. The sum is to be understood to run over all plaquettes \square . In addition, the last equality in Eq. (1.25) can be understood as a discrete curl of the magnetic vector potential, $\nabla \times \hat{\theta}_{\mathbf{n},\mathbf{n}+\mathbf{a}} = \hat{\theta}_{\mathbf{n}+\mathbf{a}_1,\mathbf{n}+\mathbf{a}_1+\mathbf{a}_2} - \hat{\theta}_{\mathbf{n},\mathbf{n}+\mathbf{a}_2} - \hat{\theta}_{\mathbf{n}+\mathbf{a}_2,\mathbf{n}+\mathbf{a}_1+\mathbf{a}_2} + \hat{\theta}_{\mathbf{n},\mathbf{n}+\mathbf{a}_1}$ [117]. Thus, if we again take the analogy with electromagnetism where we identified θ as the magnetic vector potential, we see that $\nabla \times \theta = \nabla \times A = B$. Thus the term in Eq. (1.25) can be expanded in the low energy limit as [24]

$$\hat{\mathcal{H}}_A \approx -J \sum_{\mathbf{n} \in \square} \left(1 - \frac{(\hat{B}_{\mathbf{n}})^2}{2} + \dots \right), \quad (1.26)$$

and we indeed obtain terms proportional to $\propto B^2$. This is therefore the so called magnetic term, which can be also understood as the gauge field self-interaction [26].

Finally, by putting all of these terms together we can write a $U(1)$ lattice gauge theory Hamiltonian with fermionic matter [26, 79]

$$\begin{aligned}\hat{\mathcal{H}}_{U(1)} &= -t \sum_{\mathbf{n},\mathbf{a}} \left(\hat{c}_{\mathbf{n}}^\dagger e^{i\hat{\theta}_{\mathbf{n},\mathbf{n}+\mathbf{a}}} \hat{c}_{\mathbf{n}+\mathbf{a}} + \text{H.c.} \right) + m \sum_{\mathbf{n}} (-1)^n \hat{c}_{\mathbf{n}}^\dagger \hat{c}_{\mathbf{n}} \\ &\quad + \frac{g^2}{2} \sum_{\mathbf{n},\mathbf{a}} \hat{L}_{\mathbf{n},\mathbf{n}+\mathbf{a}}^2 + \frac{1}{2g^2} \sum_{\square} \cos \left(\sum_{\langle \mathbf{q},\mathbf{u} \rangle \in \square} \hat{\theta}_{\mathbf{q},\mathbf{u}} \right).\end{aligned}\quad (1.27)$$

Here t is the hopping amplitude of the fermions on the lattice sites, m is the mass of the fermions, and g is the coupling constant [26]. The Gauss law in Eq. (1.19) becomes [26]

$$\hat{G}_{\mathbf{n}} = \sum_{\mathbf{a}} (\hat{L}_{\mathbf{n},\mathbf{n}+\mathbf{a}} - \hat{L}_{\mathbf{n}-\mathbf{a},\mathbf{n}}) - \left[\hat{c}_{\mathbf{n}}^{\dagger} \hat{c}_{\mathbf{n}} - \frac{1}{2} (1 - (-1)^n) \right], \quad (1.28)$$

where the dynamical charge part is expressed as [26]

$$Q_{\mathbf{n}} = \hat{c}_{\mathbf{n}}^{\dagger} \hat{c}_{\mathbf{n}} - \frac{1}{2} (1 - (-1)^n). \quad (1.29)$$

This means that we have matter particles (electrons) in our system when even lattice sites are occupied, i.e., when the term $(-1)^n > 0$, and we consider to have anti-matter (positrons) when odd lattice sites ($(-1)^n < 0$) are empty. All other case are considered to be simply empty states. The physical Hilbert sector is the one without background (static) charges, i.e., when $\hat{G}_{\mathbf{n}} |\psi\rangle = 0$ [26].

This $U(1)$ LGT represents the compact QED, which is the lattice gauge theory describing electrodynamics [26]. It has been substantially studied as the Abelian version of a broader class of lattice gauge theories. Initial studies relied on analytical considerations in particular to the perturbation theory in strong coupling limits [24, 127–129]. Such $U(1)$ LGTs are always confining for $1 + 1D$ and $2 + 1D$ [24, 127, 128, 130]. The $1 + 1D$ case is special in a way that it was solved exactly by Schwinger [131]. However, in $3 + 1D$ there are two regimes: confined and deconfined [24]. In the confined phase, the energy between test charges grows linearly as function of their distance in the limit when $g \gg 1$ [24]. Contrarily, in the weak coupling limit $g \ll 1$, the energy is constant as a function of distance, which corresponds to the deconfined phase [24]. We furthermore note that most of the discussion in the early work on lattice gauge theories considered pure gauge theories without coupling to dynamical matter field.

With the advancement in numerical simulations, LGTs can be treated with quantum Monte Carlo calculations [26, 27, 132–134]. However, the fermionic sign problem can cause serious problems for arbitrary fillings (finite chemical potential) [26–28]. In $1 + 1$ dimension one can also employ a matrix-product states (MPS) approach and use DMRG, which does not have the sign problem and can be used to study the ground state properties as well as dynamics [34, 35, 135].

The usual way to tackle the $U(1)$ LGT numerically is to make the Hilbert space of the gauge (electric) field finite [81]. Such approach is also in particular useful for quantum simulation of LGTs with cold atoms [81, 95, 97, 98, 136–139]. Truncation of the Hilbert space is performed by representing the gauge and electric link variables with spin operators [81,

136, 140],

$$\begin{aligned}
\hat{U}_{\mathbf{n},\mathbf{n}+\mathbf{a}} &= \frac{1}{\sqrt{S(S+1)}} \hat{S}_{\mathbf{n},\mathbf{n}+\mathbf{a}}^+, \\
\hat{U}_{\mathbf{n},\mathbf{n}+\mathbf{a}}^\dagger &= \frac{1}{\sqrt{S(S+1)}} \hat{S}_{\mathbf{n},\mathbf{n}+\mathbf{a}}^-, \\
\hat{L}_{\mathbf{n},\mathbf{n}+\mathbf{a}} &= \hat{S}_{\mathbf{n},\mathbf{n}+\mathbf{a}}^z,
\end{aligned} \tag{1.30}$$

where S is the total spin quantum number, which sets the total Hilbert space dimension, \hat{S}^+/\hat{S}^- are the spin raising/lowering operators and \hat{S}^z is the operator of the spin in the z -direction. With the above definition the Hamiltonian in Eq. (1.27) becomes [26, 140, 141]

$$\begin{aligned}
\hat{H}_{QLM} &= -\frac{t}{\sqrt{S(S+1)}} \sum_{\mathbf{n},\mathbf{a}} \left(\hat{c}_{\mathbf{n}}^\dagger \hat{S}_{\mathbf{n},\mathbf{n}+\mathbf{a}}^+ \hat{c}_{\mathbf{n}+\mathbf{a}} + \text{H.c.} \right) + m \sum_{\mathbf{n}} \hat{c}_{\mathbf{n}}^\dagger \hat{c}_{\mathbf{n}} + \frac{g^2}{2} \sum_{\mathbf{n},\mathbf{a}} (\hat{S}_{\mathbf{n},\mathbf{n}+\mathbf{a}}^z)^2 \\
&\quad + \frac{1}{2g^2 S^2 (S+1)^2} \sum_{\square} (\hat{S}_{\mathbf{n},\mathbf{n}+\mathbf{a}_1}^+ \hat{S}_{\mathbf{n}+\mathbf{a}_1,\mathbf{n}+\mathbf{a}_1+\mathbf{a}_2}^+ \hat{S}_{\mathbf{n}+\mathbf{a}_2,\mathbf{n}+\mathbf{a}_1+\mathbf{a}_2}^- \hat{S}_{\mathbf{n},\mathbf{n}+\mathbf{a}_2}^- + \text{H.c.}).
\end{aligned} \tag{1.31}$$

This is the so called "spin-gauge Hamiltonian", also known as the quantum link model (QLM) [26, 136–140]. Here we effectively approximate the continuous $U(1)$ group elements with finite number of elements, more precisely with $2S+1$ possible values of $\hat{L} = \hat{S}^z$. In the limit when $S \rightarrow \infty$ we thus retrieve the original $U(1)$ LGT [140]. That is because the commutator [81]

$$\left[\hat{U}_{\mathbf{n},\mathbf{n}+\mathbf{a}}, \hat{U}_{\mathbf{m},\mathbf{m}+\mathbf{a}}^\dagger \right], \tag{1.32}$$

has to be zero in the $U(1)$ LGT. However, in the QLM formulation it takes the form [81]

$$\left[\hat{U}_{\mathbf{n},\mathbf{n}+\mathbf{a}}, \hat{U}_{\mathbf{m},\mathbf{m}+\mathbf{a}}^\dagger \right] = \delta_{\mathbf{n},\mathbf{m}} \frac{2\hat{S}_{\mathbf{n},\mathbf{n}+\mathbf{a}}^z}{S(S+1)}, \tag{1.33}$$

and vanishes only when $S \rightarrow \infty$ [81]. Nevertheless, the gauge symmetry is retained also for finite values of S [26].

The Gauss law can also be also rewritten in terms of spin operators [138, 141]:

$$\hat{G}_{\mathbf{n}} = \sum_{\mathbf{a}} (\hat{S}_{\mathbf{n},\mathbf{n}+\mathbf{a}}^z - \hat{S}_{\mathbf{n}-\mathbf{a},\mathbf{n}}^z) - \left[\hat{c}_{\mathbf{n}}^\dagger \hat{c}_{\mathbf{n}} - \frac{1}{2} (1 - (1)^n) \right]. \tag{1.34}$$

The physical sector is the sector without background (static) charges and its eigenvalues thus equal to $\hat{G}_{\mathbf{n}} |\psi\rangle = 0$ [26, 138, 140].

Such model can be studied by performing numerical calculations using exact diagonalization (ED), limited to low system sizes, or MPS based algorithms [139, 140]. MPS calculations can be even extended to $2+1$ D systems, where the system size in one of the directions is restricted only to few lattice sites. For example, if we define the dimension of the system in x and y -direction as L_x and L_y , respectively, then one typically considers $L_y \ll L_x$ [138].

Remarkably, it has been shown using MPS and ED results that in $1+1$ D the spin S

needed to approach the continuum limit, $S \rightarrow \infty$, can be very low [26, 81, 136, 140]. Generally spins of only $S \approx 5$ are enough to reproduce the exact QED results, and in some instances already $S \lesssim 3$ suffices [140]. Furthermore, it has been shown that in the pure gauge case $S \lesssim 3$ is sufficient for generic value of g , whereas for strong coupling $g \gg 0$ already $S \approx 1$ is enough [136].

These results show that a relative small local Hilbert space is sufficient to simulate the $U(1)$ LGT, which means that quantum simulations with cold atoms is a promising platform to simulate this class of LGTs [26].

1.2.4 \mathbb{Z}_N lattice gauge theory

We now turn to the \mathbb{Z}_N lattice gauge theory, which we will be able to directly connect to the \mathbb{Z}_2 case. We first note that in contrast to the $U(1)$ LGT, \mathbb{Z}_N is a discrete symmetry, which means that some relations will be slightly different [79]. However, a general \mathbb{Z}_N , where N is an integer $N \in \mathbb{Z}$, is a sub-group of the $U(1)$ group. The $U(1)$ LGT can be recovered for the case when the appropriate limit of a discrete \mathbb{Z}_N LGT is taken, to be more precise, by considering $N \rightarrow \infty$ [26].

Let us now depart from the angular momentum language and embrace the whole analogy to the electrodynamics introduced by Kogut [24], already mentioned in the previous section. For that we redefine the variables used in the previous section as

$$\hat{E}_{\langle i,j \rangle} = \hat{L}_{\mathbf{n},k}, \quad \hat{A}_{\langle i,j \rangle} = \hat{\theta}_{\mathbf{n},k} \quad (1.35)$$

where $\hat{E}_{\langle i,j \rangle}$ can be understood as the \mathbb{Z}_N lattice gauge analog of the electric field, and $\hat{A}_{\langle i,j \rangle}$ is the \mathbb{Z}_N lattice gauge analog of the magnetic vector potential. We note that we also switched to the link notation where $\langle i,j \rangle$ denotes the link between neighboring lattice sites i and j [1, 3–6, 79]. We will use this notation throughout this thesis when describing link variables. Generally the direction of the link, i.e., whether we consider a link with direction from site i to j , which we denote as $\langle i,j \rangle$, or the opposite direction from j to i , $\langle j,i \rangle$, is important in case the field can take complex values, as is generally the case [26, 121]. As we will see in the \mathbb{Z}_2 case, the direction is not important as the field takes only real values [121].

The canonical commutation relation in Eq. (1.14) is thus also fulfilled as the commutation relation between the magnetic vector potential and the electric field takes the exactly same form [142]:

$$[\hat{A}_{\langle i,j \rangle}, \hat{E}_{\langle k,l \rangle}] = \delta_{\langle i,j \rangle, \langle k,l \rangle} i \quad (1.36)$$

As already mentioned before, the link operator $\hat{U}_{\langle i,j \rangle} = e^{i\hat{A}_{\langle i,j \rangle}}$ is thus a raising operator for the electric field. Hence, if we consider the electric field basis where [26]

$$\hat{E}_{\langle i,j \rangle} |e\rangle = e_{\langle i,j \rangle} |e\rangle, \quad (1.37)$$

the raising operator $\hat{U}_{\langle i,j \rangle}$ then results in

$$e^{i\hat{A}_{\langle i,j \rangle}} |e\rangle = |e+1\rangle, \quad (1.38)$$

as shown in Eq. (1.16). We note that the values of $e_{\langle i,j \rangle}$ for the $U(1)$ LGT can have any positive or negative integer value, $e \in \mathbb{Z}$ [26, 123].

The most straight forward way of turning the $U(1)$ LGT to a \mathbb{Z}_N LGT and then finally to a \mathbb{Z}_2 LGT, is to discretize the continuous gauge parameters $\hat{A}_{\langle i,j \rangle} = \hat{\theta}_{\mathbf{n},k}$ and its conjugated momenta $\hat{E}_{\langle i,j \rangle}$ restricting them to N discrete elements [119]. In other words we make the gauge group finite. To do that we can define the operator [26]

$$\hat{P}_{\langle i,j \rangle} = e^{i\delta\hat{E}_{\langle i,j \rangle}}. \quad (1.39)$$

In order to make the group finite we require that [26]

$$\left(\hat{P}_{\langle i,j \rangle}\right)^N = I, \quad (1.40)$$

which also has to hold for the link element,

$$\left(\hat{U}_{\langle i,j \rangle}\right)^N = I, \quad (1.41)$$

where I is the "identity" element. In addition, the elements have to remain unitary [26]:

$$\hat{U}_{\langle i,j \rangle}\hat{U}_{\langle i,j \rangle}^{-1} = \hat{P}_{\langle i,j \rangle}\hat{P}_{\langle i,j \rangle}^{-1} = I. \quad (1.42)$$

Furthermore, since $U_{\langle i,j \rangle}$ is the raising operator it also holds that [26, 142, 143]

$$\hat{P}_{\langle i,j \rangle}\hat{U}_{\langle i,j \rangle} = e^{i\delta}\hat{U}_{\langle i,j \rangle}\hat{P}_{\langle i,j \rangle}. \quad (1.43)$$

Rearranging the above expression as $\hat{U}_{\langle i,j \rangle} = e^{i\delta}\hat{P}_{\langle i,j \rangle}^\dagger\hat{U}_{\langle i,j \rangle}\hat{P}_{\langle i,j \rangle}$ and applying the expressions on both sides N times, we find

$$\begin{aligned} \left(\hat{U}_{\langle i,j \rangle}\right)^N &= \left(e^{i\delta}\hat{P}_{\langle i,j \rangle}^\dagger\hat{U}_{\langle i,j \rangle}\hat{P}_{\langle i,j \rangle}\right)^N \\ I &= e^{i\delta N}\hat{P}_{\langle i,j \rangle}^\dagger\hat{U}_{\langle i,j \rangle}\hat{P}_{\langle i,j \rangle}\hat{P}_{\langle i,j \rangle}^\dagger\hat{U}_{\langle i,j \rangle}\dots\hat{P}_{\langle i,j \rangle} \\ I &= e^{i\delta N}I, \end{aligned} \quad (1.44)$$

and thus $\delta = \frac{2\pi}{N}$. Relations in Eqs. (1.40)-(1.43) together with $\delta = \frac{2\pi}{N}$ therefore form the \mathbb{Z}_N algebra [143].

We already defined the representation of the $\hat{P}_{\langle i,j \rangle}$ in Eq. (1.40) so in the electric field basis the eigenvalues of the $\hat{P}_{\langle i,j \rangle}$ have the following structure [142]

$$\hat{P}_{\langle i,j \rangle} |e\rangle = e^{i\delta\hat{E}_{\langle i,j \rangle}} |e\rangle = e^{i\delta e_{\langle i,j \rangle}} |e\rangle, \quad (1.45)$$

where we can rewrite $\delta e(i, j) = 2\pi \frac{e}{N}$. From Eq. (1.16) we already know that the $\hat{U}_{\langle i, j \rangle}$ raises the eigenvalue of $\hat{E}_{\langle i, j \rangle}$ by an integer. Hence we have some freedom how we define e . The most straight forward way is to simply consider it to be an integer, which can take the values $0 \leq e(i, j) \leq N - 1$ [143]. However, one can also redefine it in a way that the electric field eigenvalues are "centered" around zero [142]. For example one can define it as [26, 142]

$$e = k - \frac{N-1}{2}, \quad 0 < k < N - 1. \quad (1.46)$$

We note the most important property of this group: This group is periodic, i.e., cyclic in a way that by applying the raising operator U multiple times on the link we will eventually obtain same eigenstates with a period of N operations [26, 143]. This can be demonstrated by considering the following operations

$$\begin{aligned} \hat{U}_{\langle i, j \rangle} |0\rangle &= |1\rangle \\ \hat{U}_{\langle i, j \rangle} |e\rangle &= |e+1\rangle \\ \hat{U}_{\langle i, j \rangle}^N |e\rangle &= I |e\rangle. \end{aligned} \quad (1.47)$$

The cyclic nature of the \mathbb{Z}_N group implies the property [143]

$$\hat{U}_{\langle i, j \rangle} |N-1\rangle = |0\rangle, \quad (1.48)$$

where we considered the initial definition where $0 \leq e \leq N - 1$. This property explicitly breaks the commutation relation between E and A in Eq. (1.36), which can be however recovered when $N \rightarrow \infty$ [143].

Finally, the Gauss law for the \mathbb{Z}_N case becomes [26, 143]

$$\hat{G}_j = e^{i\delta\hat{Q}_j} \prod_{\langle i, j \rangle \in +} \hat{P}_{\langle i, j \rangle}. \quad (1.49)$$

This is slightly different from the $U(1)$ case as now the \mathbb{Z}_N charge q_j is defined as [26]

$$\hat{G}_j |\psi\rangle = e^{-i\delta \sum_{\langle i, j \rangle \in +} \hat{E}_{\langle i, j \rangle} + i\delta\hat{Q}_j} |\psi\rangle = q_j |\psi\rangle, \quad (1.50)$$

where the sum in the exponent can be understood as the divergence of the electric field on site j , e.g. in 2 + 1D this is explicitly written as [143]

$$\nabla \cdot \mathbf{E} = \sum_{\langle i, j \rangle \in +} \hat{E}_{\langle i, j \rangle} = \hat{E}_{j, j+\mathbf{a}_1} + \hat{E}_{j, j+\mathbf{a}_2} + \hat{E}_{j, j-\mathbf{a}_1} + \hat{E}_{j, j-\mathbf{a}_2}. \quad (1.51)$$

This means that the Gauss law known from electrodynamics in the \mathbb{Z}_N case is actually in the exponent of the operators. With this we conclude the general discussion on the \mathbb{Z}_N lattice gauge theories.

1.2.5 \mathbb{Z}_2 lattice gauge theory

Here, we define the \mathbb{Z}_2 lattice gauge theory and connect it to the the general discussion in the previous sections. We first note that the \mathbb{Z}_2 group has only two elements [79] and we can explicitly express the operators \hat{P} and \hat{U} as

$$\hat{P} = e^{i\pi\hat{E}_{\langle i,j \rangle}}, \quad \hat{U} = e^{i\hat{A}_{\langle i,j \rangle}}, \quad (1.52)$$

since $\delta = \pi$ in Eq. (1.44). Accordingly, the electric-field basis has only two possible eigenvalues $e = 0, 1$ and thus

$$\hat{P}_{\langle i,j \rangle} |e\rangle = \pm |e\rangle. \quad (1.53)$$

Furthermore, the raising operator $\hat{U}_{\langle i,j \rangle}$ has a simple action

$$\hat{P}_{\langle i,j \rangle} |e\rangle = \pm |e\rangle \quad \Rightarrow \quad \hat{P}_{\langle i,j \rangle} \hat{U}_{\langle i,j \rangle} |e\rangle = \mp |e\rangle, \quad (1.54)$$

which is the consequence of the cyclic \mathbb{Z}_N algebra discussed in the previous section, more precisely the relation in Eq. (1.48).

The relation explained above thus motivates us to represent the link operators \hat{P} and \hat{U} in terms of Pauli matrices, i.e. with spin-1/2 operators [17, 18, 79, 87, 144]

$$\hat{P}_{\langle i,j \rangle} = \hat{\tau}_{\langle i,j \rangle}^x, \quad \hat{U}_{\langle i,j \rangle} = \hat{\tau}_{\langle i,j \rangle}^z. \quad (1.55)$$

The two Pauli matrices represent the the spin-1/2 operators as $\hat{S}^x = \frac{1}{2}\hat{\tau}^x$ and $\hat{S}^z = \frac{1}{2}\hat{\tau}^z$, where the x and z superscript denotes the spin component. In such representation, the electric field basis is therefore the spin-1/2 eigenvalue in the x basis. In the Pauli matrix representation it also becomes apparent that the application of a $\hat{\tau}^z$ operator simply flips the spin orientation in the x -basis.

With the above definition we can write a \mathbb{Z}_2 lattice gauge theory coupled to matter in a similar way as we did for the $U(1)$ case in Eq. (1.27). Most of the terms can be obtained by simply replacing the operators representing the $U(1)$ LGT with the \mathbb{Z}_2 representations, i.e., $\hat{U}_{\langle i,j \rangle} \rightarrow \hat{\tau}_{\langle i,j \rangle}^z$. However, more care has to be taken with the electric field term $\propto \hat{E}_{\langle i,j \rangle}^2$. That is because in our general \mathbb{Z}_N formulation we expressed only the exponent of such operator, $\hat{P}_{\langle i,j \rangle} = e^{i\delta\hat{E}_{\langle i,j \rangle}}$. This term can be approximated by writing a combination of the \hat{P} operators as [143, 144]

$$\frac{1}{2} \left(\hat{P}_{\langle i,j \rangle} + \hat{P}_{\langle i,j \rangle}^\dagger \right) = \frac{1}{2} \left(e^{i\delta\hat{E}_{\langle i,j \rangle}} + e^{-i\delta\hat{E}_{\langle i,j \rangle}} \right) = \cos\left(\delta\hat{E}_{\langle i,j \rangle}\right) \approx 1 - \frac{\hat{E}_{\langle i,j \rangle}^2}{2} + \dots, \quad (1.56)$$

which holds for low values of the electric field. We can express the $\hat{E}_{\langle i,j \rangle}^2$ term for the \mathbb{Z}_2 case, where $\hat{P}_{\langle i,j \rangle} = \hat{P}_{\langle i,j \rangle}^\dagger = \hat{\tau}_{\langle i,j \rangle}^x$ since Pauli matrices are Hermitian, as

$$\hat{E}_{\langle i,j \rangle}^2 \approx 2\hat{\tau}_{\langle i,j \rangle}^x. \quad (1.57)$$

With the above considerations we can thus write the \mathbb{Z}_2 lattice gauge theory as [79, 145]

$$\hat{\mathcal{H}}_{\mathbb{Z}_2} = -t \sum_{\langle i,j \rangle} \left(\hat{c}_i^\dagger \hat{\tau}_{\langle i,j \rangle}^z \hat{c}_j + \text{H.c.} \right) + m \sum_j (1)^n \hat{c}_j^\dagger \hat{c}_j - g^2 \sum_{\langle i,j \rangle} \hat{\tau}_{\langle i,j \rangle}^x + \frac{1}{2g^2} \sum_{\square} \prod_{\langle i,j \rangle \in \square} \hat{\tau}_{\langle i,j \rangle}^z, \quad (1.58)$$

where the magnetic term follows from Eq. (1.25) and Eq. (1.26). In addition, the Gauss law becomes [17, 26, 79, 121]

$$\hat{G}_j = e^{i\pi \hat{Q}_j} \prod_{\langle i,j \rangle \in +} \hat{\tau}_{\langle i,j \rangle}^x, \quad (1.59)$$

where $\hat{Q}_j = \hat{c}_j^\dagger \hat{c}_j - \frac{1}{2} [1 - (-1)^n]$ is the matter charge [114] similar as in the $U(1)$ case, which we defined in Eq. (1.29).

We note that this is greatly simplified in the case when we replace the staggered fermions with simple fermions and the mass term becomes a chemical potential term

$$m \sum_j (-1)^n \hat{c}_j^\dagger \hat{c}_j \rightarrow \mu \sum_j \hat{c}_j^\dagger \hat{c}_j. \quad (1.60)$$

There we simply write $\hat{Q}_j = \hat{n}_j = \hat{c}_j^\dagger \hat{c}_j$ [17]. Since this is a \mathbb{Z}_2 LGT, there are only two possible eigenvalues of the Gauss law, $\hat{G}_n |\psi\rangle = g_j |\psi\rangle$, $g_j = \pm 1$. We can again consider Eq. (1.50), and express the Gauss law as

$$\hat{G}_j |\psi\rangle = e^{i(\pi \hat{n}_j - \nabla \cdot \hat{\mathbf{E}})} |\psi\rangle = g_j |\psi\rangle. \quad (1.61)$$

The physical sector without background charges is the sector where $g_j = 1, \forall j$. In the case when fermions are not staggered this can be easily seen as the condition $\pi \hat{n} - \nabla \cdot \hat{\mathbf{E}} = 0$ that results in $\hat{G}_n |\psi\rangle = + |\psi\rangle$. This can be interpreted as matter particles being the sources or sinks of the \mathbb{Z}_2 electric field [79]. Contrarily, if $g_j = -1$, this means that there are static charges Q_j^s present on lattice sites, i.e., $\pi \hat{n} - \nabla \cdot \hat{\mathbf{E}} = \hat{Q}_j^s$.

With Eq. (1.58) we have thus obtained a Hamiltonian where matter \hat{c}_j , defined on the lattice sites, is coupled to the gauge field defined on the links, which is represented by spin-1/2 operators $\hat{\tau}_{\langle i,j \rangle}^{x,z}$. We note that the \mathbb{Z}_2 LGT Hamiltonian in Eq. (1.58) has some similarities with the quantum link models (truncated $U(1)$ LGT), which we defined in Eq. (1.31). In both cases particles (matter fields) on lattice sites are coupled to spins on the links between the sites. However, a major difference between both LGTs is that the QLM formulation does not have the \mathbb{Z}_N cyclic property, which we defined in Eq. (1.48), and thus the commutation relations in Eq. (1.36) remain valid. This is only approximately true for a general \mathbb{Z}_N , and is recovered once $N \rightarrow \infty$ [143].

In 1 + 1D \mathbb{Z}_2 LGT the magnetic plaquette term cannot be realized. The \mathbb{Z}_2 LGT without fermionic staggering in one dimension thus becomes

$$\hat{\mathcal{H}}_{\mathbb{Z}_2} = -t \sum_{\langle i,j \rangle} \left(\hat{c}_i^\dagger \hat{\tau}_{\langle i,j \rangle}^z \hat{c}_j + \text{H.c.} \right) - h \sum_{\langle i,j \rangle} \hat{\tau}_{\langle i,j \rangle}^x + \mu \sum_j \hat{c}_j^\dagger \hat{c}_j, \quad (1.62)$$

where we defined the chemical potential term with prefactor μ , which can be used to

control the filling of the chain. The 1 + 1D version of the Gauss law in Eq. (1.59) for the above Hamiltonian simplifies to [121]

$$\hat{G}_j = e^{i\pi\hat{n}_j} \hat{t}_{(j-1,j)}^x \hat{t}_{(j,j+1)}^x, \quad (1.63)$$

where we defined the on-site particle number $\hat{n}_j = \hat{c}_j^\dagger \hat{c}_j$. The \mathbb{Z}_2 LGT defined in Eq. (1.62) together with the corresponding Gauss law in Eq. (1.63) will be the main topic of this thesis.

Coming from the quantum electrodynamics (QED) or quantum chromodynamics (QCD) standpoint, one could argue that the \mathbb{Z}_2 LGT is a great simplification of the original LGTs. Thus the connection to more complicated LGTs, which are closer to describing QED or QCD might be rather weak. However, it was shown that in some instances \mathbb{Z}_N LGTs correctly describe phenomena seen in QCD, especially confinement [26, 146]. The motivation to study a simple \mathbb{Z}_2 LGT thus has some concrete connection to the study of confinement of quarks, besides the connection to high-temperature superconductivity and topological phase transitions [17, 18, 29]. Of course the main motivation to study the \mathbb{Z}_2 LGT in this thesis comes from the perspective of quantum simulation and connections to strongly correlated system, in particular high-temperature superconductivity [29]. However, we would like to stress that there are concrete connections also to HEP problems.

We also note that the \mathbb{Z}_2 LGT defined above couples to matter, which has a global $U(1)$ symmetry. A common HEP approach is to gauge the global symmetry, and thus from that perspective one could argue that here we gauged a sub-symmetry. This can lead to some inconsistencies if one wants to take the continuum limits [119]. However, we argue that the LGT formulated above has the correct gauge structure, Gauss law, and commutation relations. It therefore warrants the name *lattice gauge theory*. Furthermore, our main motivation of studying this system comes from condensed matter systems and quantum simulations with ultracold atoms, where such formulation can in fact be even more natural.

We conclude this section by briefly discussing the role of \mathbb{Z}_2 LGTs in condensed matter systems. As already mentioned before, \mathbb{Z}_2 gauge theories can arise as effective theories at low-energies in strongly correlated systems [29, 30]. The \mathbb{Z}_2 gauge theory formalism can be used to describe fractionalized phases of matter in models describing superconductivity [16, 17, 29, 30, 58, 147–149]. There, fractional phases can be related to the deconfined phase of the \mathbb{Z}_2 LGT [149]. For example, a \mathbb{Z}_2 gauge theory can be used to describe many interesting phases in a model describing p-wave superconductivity [30]. Furthermore, a gauge theory was developed, which interpolates between AFM order and d-wave superconductivity [29]. In addition, confinement-deconfinement transitions [24] of emergent gauge fields can be related to topological order [17, 150]. Gauge theories also generated a lot of interest in the study of Fermi surface reconstruction [16, 17, 151]. Finally, we mention algebraic charge liquids, proposed to explain the development of Fermi arcs in the region between the AFM and the superconducting regime [152].

1.3 Numerical simulation of the \mathbb{Z}_2 lattice gauge theory

Here we present details on numerical calculations of the 1 + 1D \mathbb{Z}_2 LGT where matter is coupled to the \mathbb{Z}_2 gauge field. In order to obtain the ground state results we employ the DMRG method [34, 35]. Throughout this thesis we use a MPS toolkit SYTEN [153, 154]. This toolkit contains, among many other features, DMRG implementations of spin system, which we use in order to find the ground state of the \mathbb{Z}_2 LGTs after integrating out the matter degrees of freedom. When employing DMRG calculations we therefore do not simulate the whole system that consists of matter fields (partons) and a \mathbb{Z}_2 gauge field (link variables). Instead, we take into account the Gauss law and its set of local constraints. This is because we are always interested in the physical gauge sector, which allows us to describe the system fully in terms of charge or link degrees of freedom. We use the later description by using the Gauss law constraint to the physically sector and integrate out the matter degrees of freedom. With that we express the \mathbb{Z}_2 LGT in the physical sector purely with the \mathbb{Z}_2 link variables, which becomes a spin-1/2 Hamiltonian. This mapping is exact, and we describe it in detail below.

1.3.1 Numerical calculations using DMRG

Density-matrix renormalization group (DMRG) can be understood as a variational method to find the ground state of a physical system [35, 155]. It was originally developed by White [34, 156], and can be used to study ground state properties of quantum systems, as well as to compute finite temperature states [35, 155]. It works best for one-dimensional systems, which can be understood in terms of the area laws [35, 155, 157]. These tell us that for gapped systems, for Hamiltonians, which contain local interactions, entanglement entropy scales as $S \propto L^{D-1}$, where L^D the system size and D is the spatial dimension [35, 155]. This is good news in one dimension where it scales as a constant. However, already in two dimensions entanglement scales linearly [155]. Up to some extent, the entanglement can be connected to the eigenvalue spectra, which is important as in the DMRG we truncate the system by taking only a certain number of the most important weights in the system [35, 155]. This is done via the singular value decomposition (SVD) where we truncate the number of singular values retained [35].

DMRG as a numerical method is well established. In this thesis we have not developed new methods or new variations of it. We merely used the already developed implementation in a powerful toolkit SYTEN [153, 154], where it is implemented within matrix-product states formalism. In this short section on DMRG we will thus not review the method in detail, as our focus in this thesis was to study the physical properties of the lattice gauge theories and strongly correlated systems. For an extensive review we refer the reader to Ref. [35]. A slightly shorter review, which contains all of the important details is available in Ref. [155]. Both of these references were followed in this short section, where we outline the very basic idea.

In the finite system DMRG we search for the ground state $|\psi\rangle$ for a given Hamiltonian

$\hat{\mathcal{H}}$ [35, 155]. The problem thus reduces to finding the minimal value of [35, 155]

$$E[|\psi\rangle] = \frac{\langle \psi | \hat{\mathcal{H}} | \psi \rangle}{\langle \psi | \psi \rangle}, \quad (1.64)$$

which can be formulated in terms of a Lagrange multiplier, $\lambda_{\mathcal{L}}$, where we have to minimize [35, 155]

$$\langle \psi | \hat{\mathcal{H}} | \psi \rangle - \lambda_{\mathcal{L}} \langle \psi | \psi \rangle. \quad (1.65)$$

By using the matrix-product state formulation we can efficiently calculate the extremum of the above equation, which boils down to solving an eigenvalue problem [35, 155].

Matrix-product states

Matrix-product states (MPS) are obtained by reshaping a generic pure quantum state [35, 155],

$$|\psi\rangle = \sum_{\sigma} c_{\sigma} |\sigma\rangle, \quad (1.66)$$

where $\{\sigma\}$ is the local state space, with local dimension d , and $|\sigma\rangle = |\sigma_1, \sigma_2, \dots, \sigma_{L-1}, \sigma_L\rangle$ [155]. Any such state can be reshaped into a matrix-product state expressed as [35, 155]

$$|\psi\rangle = \sum_{\sigma} M^{\sigma_1} M^{\sigma_2} \dots M^{\sigma_{L-1}} M^{\sigma_L} |\sigma\rangle, \quad (1.67)$$

by using a SVD decomposition [35, 155, 158]. Here, M^{σ_i} are matrices the dimension of which can grow the further away the lattice site that they represent resides from the start of the lattice [35]. The maximal dimension can be $d^{L/2} \times d^{L/2-1}$ [35, 155]. Such representation is in fact exact, and would thus grow with system size. However, we can truncate the above state as it can be reshaped by using the Schmidt decomposition [35, 155]

$$|\psi\rangle = \sum_{a_{\ell}=1}^r s_{a_{\ell}} |a_{\ell}\rangle_A |a_{\ell}\rangle_B. \quad (1.68)$$

Here $|a_{\ell}\rangle_{A,B}$ are different blocks to which the MPS can be reshaped, and r is the number of non-zero singular values s [155]. The truncation then takes place by retaining only the largest χ singular values s , while discarding all others. For more details we refer the reader to Ref. [35]

Finding the ground state

The ground state value is found by minimizing Eq. (1.65), which in the MPS language is expressed as [35, 155]

$$\sum_{\sigma'_{\ell}} \sum_{a'_{\ell-1} a'_{\ell}} H_{(\sigma_{\ell} a_{\ell-1} a_{\ell}), (\sigma'_{\ell} a'_{\ell-1} a'_{\ell})} - \lambda_{\mathcal{L}} M_{a_{\ell-1}, a_{\ell}}^{\sigma_{\ell}} = 0, \quad (1.69)$$

where the Hamiltonian $\hat{\mathcal{H}}$ is expressed in terms of a matrix-product operator (MPO), H . The above equation is thus reduced to solving an eigenvalue problem $Hv - \lambda_{\mathcal{L}}v$, for matrices up to the dimension of $d\chi^2 \times d\chi^2$, where χ is the bond dimension [35]. These matrices can be still very big, however, we only need to calculate the lowest eigenvalue which can be obtained by an iterative eigensolver [35, 155]. For example one can use the Lanczos method [35, 155, 158, 159]. The standard procedure is then to sweep through the chain and solve the eigenvalue problem on each site, reshape the matrices, and move on to the next site [35, 155]. After reaching the end of the chain we sweep in the opposite direction. We perform multiple sweeps until the energy stops to decrease.

In DMRG calculations performed to obtain numerical data in this thesis, we typically start with a random initial state. A slightly better method would be to already guess a state, which is close to the ground state and with that optimize the calculations. We mitigate the fact that we start with a random state by staging multiple rounds of our sweeps with different bond dimension χ . We thus have one or two rounds of sweeps at low bond dimension $\chi \sim 128$, which gives us a good guess for more costly sweeps at higher bond dimensions. We typically stop the calculations once the ground state energy after two consecutive sweeps does not decrease more than $\Delta E \sim 10^{-12}$, which is typically in units of hopping $[t]$ in the \mathbb{Z}_2 LGT. This is, practically speaking, already a good measure of convergence, which can be more formally checked by calculating the variance of the energy $\langle \hat{\mathcal{H}}^2 \rangle - (\langle \hat{\mathcal{H}} \rangle)^2$, that should be sufficiently low, e.g., $\sim 10^{-9}$ [35]. This of course only tells us whether or not the obtained state really is an eigenstate of $\hat{\mathcal{H}}$ and we still risk that our calculations got stuck in some local minima. For that we need to do more concrete checks of physical observable and determine whether or not the results make sense. A good method, when in doubt, is to check how a physical observable changes with increasing bond dimension χ [35].

1.3.2 Mapping to the spin model

In this section we apply the Gauss law constraint to the physical sector and derive the spin representation of the \mathbb{Z}_2 LGT, where \mathbb{Z}_2 gauge field is coupled to $U(1)$ hard-core bosons, [1, 3–5]

$$\hat{\mathcal{H}} = -t \sum_j \left(\hat{a}_j^\dagger \hat{\tau}_{\langle j, j+1 \rangle}^z \hat{a}_{j+1} + \text{H.c.} \right) - h \sum_j \hat{\tau}_{j, j+1}^x. \quad (1.70)$$

Here we defined the hard-core boson creation and annihilation operator as \hat{a}^\dagger and \hat{a} , respectively. We note that due to the Jordan-Wigner transformation the above formulation can be mapped to coupling gauge field to spinless fermions [1, 5]. This following derivation is based on Ref. [5].

The Gauss law in the \mathbb{Z}_2 LGT theory with dynamical matter is defined through a set of local operators [1, 3, 5, 121, 160]

$$\hat{G}_j = \hat{\tau}_{\langle j-1, j \rangle}^x (-1)^{\hat{n}_j} \hat{\tau}_{\langle j, j+1 \rangle}^x. \quad (1.71)$$

We remind the reader that $\hat{\tau}^x$ is a x -component Pauli matrix, and $\hat{n}_j = \hat{a}_j^\dagger \hat{a}_j$ is an on-site

hard-core boson (parton) number operator. As discussed in Section 1.2, \hat{G}_j commutes with the Hamiltonian, and its eigenvalues can have two possible values: $\hat{G}_j |\psi\rangle = g_j |\psi\rangle$, where $g_j = \pm 1$. The physical sector is the sector where all eigenvalues are positive $g_j = +1, \forall j$. Thus the Gauss law for the physical sector has the following action on any state in the physical gauge sector [5]

$$\hat{G}_j = \hat{\tau}_{(j-1,j)}^x (-1)^{\hat{n}_j} \hat{\tau}_{(j,j+1)}^x = I. \quad (1.72)$$

Rearranging the above expression allows us to express the on-site parton number operator exclusively in terms of the \mathbb{Z}_2 electric field variables connected to that lattice site as [5]

$$\hat{n}_j = \frac{1}{2} \left(1 - \hat{\tau}_{(j-1,j)}^x \hat{\tau}_{(j,j+1)}^x \right). \quad (1.73)$$

This expression simply tells us that the \mathbb{Z}_2 electric link variables are anti-aligned across an occupied lattice site and are aligned across a vacant matter site. We will use this connection also in the next Chapter 2 to define the \mathbb{Z}_2 electric strings. By using the above expression, Eq. (1.73), we can fully determine the orientation of the link variables, provided we have the knowledge of the position of each individual particle on the lattice. The opposite is of course also true.

We can therefore see that combined simulation of the matter sites and link sites in DMRG is redundant in the \mathbb{Z}_2 LGT when one wants to study the physical sector exactly. Integrating out the matter degrees of freedom thus provides an exact mapping to a purely spin system, and reduces the numerical complexity. As will become apparent soon, this comes with a cost of a reduced number of symmetries that can be used in the spin lattice, which is slightly offset by the fact that spin systems, even without symmetries, are well suited for DMRG calculations.

With the above definition of the on-site parton occupation operator, Eq (1.73), we can define the hard-core boson creation and annihilation operators, expressed fully in terms of the \mathbb{Z}_2 link variables as [5]

$$\begin{aligned} \left(\prod_{l<j} \hat{\tau}_{l,l+1}^z \right) \hat{a}_j^\dagger &:= \left(\prod_{l<j} \hat{\tau}_{l,l+1}^z \right) \frac{1}{2} \left(1 + \hat{\tau}_{j-1,j}^x \hat{\tau}_{j,j+1}^x \right), \\ \left(\prod_{l<j} \hat{\tau}_{l,l+1}^z \right) \hat{a}_j &:= \left(\prod_{l<j} \hat{\tau}_{l,l+1}^z \right) \frac{1}{2} \left(1 - \hat{\tau}_{j-1,j}^x \hat{\tau}_{j,j+1}^x \right). \end{aligned} \quad (1.74)$$

In order for the Gauss law to be conserved, each parton creation and annihilation operator has to be accompanied with the appropriate change of the electric field orientation. Hence, we add the string of $\hat{\tau}^z$ operators to \hat{a}^\dagger and \hat{a} . The operators on the left side thus act on the combined Hilbert space of matter sites and links, whereas the right hand side acts in the Hilbert space, which consists solely of the link variables. With this we eliminate the redundant matter lattice sites.

When defining the above operators in the link notation space only, we first have to project to the states, which are not annihilated after application of the creation or annihilation

lation operator. For example in order for the parton creation operator to add a parton at site j , site j has to be empty to begin with. In our case this is assured by first applying the operator $1 - \hat{n}_j = \frac{1}{2} \left(1 + \hat{\tau}_{\langle j-1, j \rangle}^x \hat{\tau}_{\langle j, j+1 \rangle}^x \right)$, which vanishes for the case when there already is a parton on site j , as is the case for the "matter" creation operator. In order to add a parton we then have to ensure that the electric variables are anti-aligned across site j . For that we flip all of the \mathbb{Z}_2 electric links from the beginning of the chain up to site j , which is done with a string of Pauli z matrices $\prod_{l < j} \hat{\tau}_{l, l+1}^z$. This is because applying a Pauli z matrix to an eigenstate in the x basis flips its orientation as discussed in Section 1.2.5. By applying the whole string starting from the beginning of the lattice we ensure that we do not introduce any other partons anywhere else in the chain. We could also start this sort of string at the end of the lattice.

The above mapping is similar to the string attachment defined by Borla et al. in Ref. [160] and somewhat resembles the Jordan-Wigner mapping used by Kitaev and Laumann when mapping the Kitaev chain to a spin system in Ref. [161]. However, we note that we did not use any Majorana operators in this mapping in contrast to the case in Ref. [160], which means that the mapping proposed here is not as complicated.

By using the mapping defined above in Eq. (1.73) and Eq. (1.74) we can express the full $1 + 1D$ \mathbb{Z}_2 LGT, Eq. (1.70), where gauge fields are coupled to dynamical hard-core bosons fully in terms of \mathbb{Z}_2 fields [1, 3–5, 160]

$$\hat{\mathcal{H}}_{LGT}^s = t \sum_{j=2}^L \left(4\hat{S}_{j-1}^x \hat{S}_{j+1}^x \hat{S}_j^z - \hat{S}_j^z \right) - h \sum_{j=1}^{L+1} 2\hat{S}_j^x. \quad (1.75)$$

Above we already implied that we consider open boundary conditions (OBC), and that our system starts and ends with a link variable. This means that the total number of spins equals to $L + 1$, where L is the number of matter lattice sites. In addition, we translated the link indices to the spin sites as $\langle j - 1, j \rangle \rightarrow j$. The Hamiltonian above does not contain the chemical potential, which we add in the next steps below. Furthermore, we replaced the Pauli matrices with their corresponding spin-1/2 operators: $\hat{\tau}_{\langle i, i+1 \rangle}^{x,z} = 2\hat{S}_j^{x,z}$ [6]. The above spin formulation was first used by Borla et al. in Ref. [160] where the mapping contained Majorana operators. However, the spin formulation could also be derived by simply relating the allowed matrix elements in terms of the \mathbb{Z}_2 variable configurations as was done for example in Ref. [2]. Finally we note that this spin model is also known as the kinetically constrained spin model [7, 162].

The Hamiltonian in Eq. (1.75) does not have any simple symmetries such as the global $U(1)$ symmetry, which would fix the total magnetization of the chain. As already stated before, this means that no symmetries for the spin lattices can be used in the MPS calculations. However, the spin model Eq. (1.75) does have a total conservation of the number of domain walls, which is simply the $U(1)$ symmetry for the hard-core bosons, since the Hamiltonian, Eq. (1.70), conserves the total particle number N .

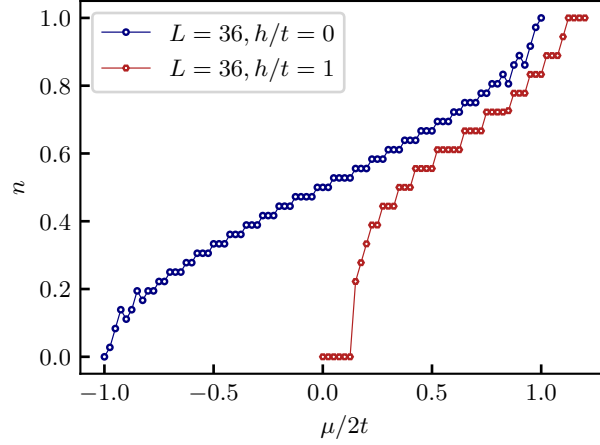


Figure 1.1: Filling of the chain, n , as a function of the chemical potential μ in the 1 + 1D \mathbb{Z}_2 LGT after integrating out the charges, Eq. (1.77). The blue circles correspond to the case where $h = 0$, and the red hexagons correspond to $h/t = 1$. This figure was obtained from Fig. S1 in the Supplemental material of Ref. [4].

In order to control the filling of the chain, we thus add a chemical potential term [5]

$$\hat{\mathcal{H}}_\mu^s = -\mu \sum_{j=1}^L \left(\hat{n}_j - \frac{1}{2} \right) = \mu \sum_{j=1}^L 2\hat{S}_j^x \hat{S}_{j+1}^x. \quad (1.76)$$

The whole spin-1/2 model, which we simulate with the DMRG is thus equal to

$$\hat{\mathcal{H}}^s = t \sum_{j=2}^L \left(4\hat{S}_{j-1}^x \hat{S}_{j+1}^x \hat{S}_j^z - \hat{S}_j^z \right) - h \sum_{j=1}^{L+1} 2\hat{S}_j^x + \mu \sum_{j=1}^L 2\hat{S}_j^x \hat{S}_{j+1}^x. \quad (1.77)$$

With such implementation we can simulate quite long chains: in this thesis we go up to lengths $L = 120$ [3]. We note that for the results in Chapter 4, the factor in the chemical potential was 4 and not 2 [4].

Controlling the filling with the chemical potential

Finding the right filling, which we define as $n = N/L$, by tuning the chemical potential term μ , can in some cases be an inconvenient task. In the free parton regime $h = 0$, we can simply use free fermion calculations in order to find the correct filling n , even in the case when we consider OBC [163]. However, at finite electric field term $h \neq 0$, this is not possible anymore. For this reason we generally perform calculations at smaller system sizes for different values of h , and sweep through a range of chemical potential values μ . In Fig. 1.1 we present a typical sweep through different values of μ for $L = 36$ lattice sites. We observe small plateaus of constant filling for short intervals of μ . These plateaus are related to the finite system size, i.e., the finite system size charge gap [4]. In the case presented

above, the system consists of free partons for $h = 0$, and of confined mesons for $h/t = 1$, the regimes which we study in the next Chapter 2. In both cases the system forms a gapless Luttinger liquid consisting of partons in the former, and mesons in the later case [1, 160]. Thus in the thermodynamic limit, $L \rightarrow \infty$, the plateaus will disappear [4] as the system is in fact gapless in the thermodynamic limit. We note that with such implementation the condition that the chain always starts and ends with an anti-string, and thus that we obtain even number of particles, is fulfilled only for $h > 0$; see Section 2.1 for the definition of strings and anti-strings. When $h = 0$, we also often obtain odd particle number, but since there is no dynamics in the gauge field this does not play a major role, and we often include such results in our analysis.

We note that the filling in the spin-1/2 model after integrating out the charges is simply calculated via the Gauss law constraint, Eq. (1.73), as [5]

$$n = \frac{1}{L} \sum_{j=1}^L \langle \hat{n}_j \rangle = \frac{1}{L} \sum_{j=1}^L \frac{1}{2} \left(1 - 4 \langle \hat{S}_{\langle j-1,j \rangle}^x \hat{S}_{\langle j,j+1 \rangle}^x \rangle \right), \quad (1.78)$$

where we again use the link notation for the spins in order to highlight the fact that partons reside on the matter sites.

Important operators in the spin formulation

In addition to the on-site density operator \hat{n}_j , we also have to express other important operators in terms of spins. Below we present some other important operators expressed in the spin formulation, which we will encounter in the next chapters.

We start with the density-density operator where we simply multiply Eq. (1.73) on different lattice sites:

$$\hat{n}_j \hat{n}_i = \frac{1}{2} \left(1 - 4 \hat{S}_{j-1,j}^x \hat{S}_{j,j+1}^x \right) \frac{1}{2} \left(1 - 4 \hat{S}_{i-1,i}^x \hat{S}_{i,i+1}^x \right). \quad (1.79)$$

The above expression can be simplified when $|i - j| = 1$, as $(\hat{\tau}_j^x)^2 = I$. Such terms are added to Eq. (1.77), when simulating the \mathbb{Z}_2 LGT with nearest-neighbor repulsion $\propto V \sum_j \hat{n}_j \hat{n}_{j+1}$.

Next we present the \mathbb{Z}_2 gauge invariant Green's function, which we study to probe confinement [1, 160]:

$$\mathcal{G}(i - j) = \left\langle \hat{a}_i^\dagger \left(\prod_{i \leq \ell < j} \hat{\tau}_{\ell, \ell+1}^z \right) \hat{a}_j \right\rangle. \quad (1.80)$$

We will describe how this function can be used to probe confinement and all of its properties in confined/deconfined regimes in the next Chapter 2. Here, we express it in terms of link variables by simply using the definition in Eq. (1.74), and write it in terms of the link

variables only [1, 3–5]:

$$\mathcal{G}(x) = \left\langle \frac{1}{4} \left(\prod_{x_0 \leq \ell < x} 2\hat{S}_{\langle \ell, \ell+1 \rangle}^z \right) \left(1 - 4\hat{S}_{\langle x-1, x \rangle}^x \hat{S}_{\langle x, x+1 \rangle}^x \right) \left(1 + 4\hat{S}_{\langle x_0-1, x_0 \rangle}^x \hat{S}_{\langle x_0, x_0+1 \rangle}^x \right) \right\rangle. \quad (1.81)$$

Some care has to be taken here with the order of the \mathbb{Z}_2 fields applied to the state. It is thus always good to consider matrix elements to which the operator, expressed purely in terms of links, maps to when applied to different physical states [1–5].

Superconducting terms

In Chapter 5 we will consider additional \mathbb{Z}_2 gauge invariant superconducting (SC) terms, which can be easily expressed in terms of link variables as [5]

$$\hat{\mathcal{H}}_\lambda^s = \lambda \sum_{\langle i, j \rangle} \left(\hat{a}_i^\dagger \hat{\tau}_{\langle i, j \rangle}^z \hat{a}_j^\dagger + \text{H.c.} \right) = \lambda \sum_{j=2}^{L-1} \left(4\hat{S}_{j-1}^x \hat{S}_{j+1}^x \hat{S}_j^z + \hat{S}_j^z \right). \quad (1.82)$$

Hence, in Chapter 5 we simulate the spin Hamiltonian, which contains the above terms in addition to all of the terms in Eq. (1.77). The Hamiltonian can then be expressed as [5]

$$\hat{\mathcal{H}}_{\text{SC}}^s = t \sum_{j=2}^L \left(4\hat{S}_{j-1}^x \hat{S}_{j+1}^x \hat{S}_j^z - \hat{S}_j^z \right) - h \sum_{j=1}^{L+1} 2\hat{S}_j^x + \lambda \sum_{j=2}^{L-1} \left(4\hat{S}_{j-1}^x \hat{S}_{j+1}^x \hat{S}_j^z + \hat{S}_j^z \right) + \mu \sum_{j=1}^L 2\hat{S}_j^x \hat{S}_{j+1}^x. \quad (1.83)$$

We note that for $\lambda \neq 0$, this Hamiltonian does not conserve the number of spin domain walls. This is because the SC terms explicitly break the $U(1)$ symmetry in the partons.

In the regime when $\lambda = -t$, the extended 1 + 1D \mathbb{Z}_2 LGT expressed in terms of link variables reduces to an Ising model with transverse and longitudinal fields and can be expressed as [5]

$$\hat{\mathcal{H}}^s = -t \sum_{j=2}^{L-1} 2\hat{S}_j^z - h \sum_{j=1}^L 2\hat{S}_j^x + \mu \sum_{j=1}^{L-1} 2\hat{S}_j^x \hat{S}_{j+1}^x. \quad (1.84)$$

In the opposite case, when $\lambda = t$, the Hamiltonian merely reduces to [5]

$$\hat{\mathcal{H}}^s = t \sum_{j=2}^{L-1} 8\hat{S}_{j-1}^x \hat{S}_{j+1}^x \hat{S}_j^z - h \sum_{j=1}^L 2\hat{S}_j^x + \mu \sum_{j=1}^{L-1} 2\hat{S}_j^x \hat{S}_{j+1}^x. \quad (1.85)$$

Throughout this thesis we will usually refer to Hamiltonians and correlation functions written in terms of matter and gauge field operators. However, we note that all of the numerical calculations come from MPS calculations where the matter fields were integrated out as described above. That is because we will always be interested in the exact physical Gauss sector without background charges. Hence, all of the DMRG calculations and observable were calculated via Hamiltonians and correlation functions expressed in terms of link variables, i.e., spins. We state once again that the mapping to the spin (link) formulation is exact, as we explicitly take into account the Gauss law constraint to the physical

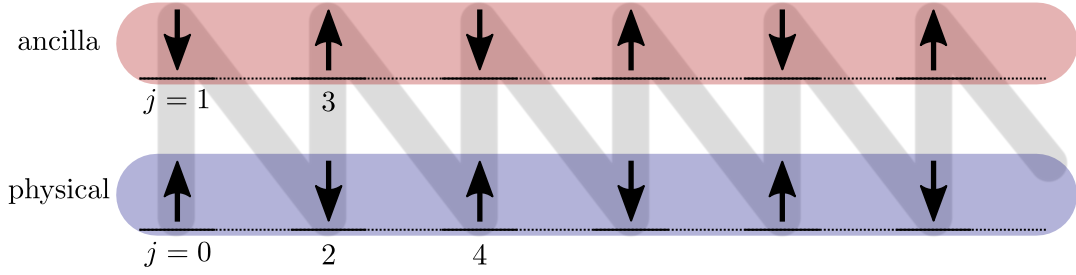


Figure 1.2: A sketch of the physical and auxiliary (ancilla) lattice sites, implemented with an extended MPS lattice. Every physical site residing on an even MPS lattice site labeled as $j = 2k, k \in \mathbb{Z}$, is maximally entangled to its corresponding auxiliary lattice site $j = 2k + 1$, in the initial, infinite temperature state $|\psi(\beta = 0)\rangle$. This figure was obtained from Fig. S2 in the Supplemental material of Ref. [4].

Gauss sector.

If one is interested in the effects of Gauss law violations, which become important in schemes to implement LGTs in quantum simulation platforms, the full \mathbb{Z}_2 LGT Hamiltonian has to be used [81, 91, 103]

1.3.3 Finite temperature calculations

Next, we explain how we perform finite temperature calculations for the $1 + 1\text{D}$ \mathbb{Z}_2 LGT using MPS. We employ the quantum purification scheme where we add an auxiliary lattice site to every physical lattice site, which acts as a thermal bath [164–168]. We use a trick where we encode the thermal mixed states by taking a trace over enlarged pure state [35].

Our finite temperature calculations are based on the spin formulation of the \mathbb{Z}_2 LGT after integrating out the matter degrees of freedom, introduced in the previous Section 1.3.2. In the finite temperature calculations, the total system size doubles. The MPS chain length thus increases as $L + 1 \rightarrow 2(L + 1)$, where L is the number of matter lattice sites, and $L + 1$ is the number of the links. The physical lattice sites in the MPS chain reside on even sites $j = 2k$, where $k \in \mathbb{Z}$, and auxiliary (ancilla) lattice sites correspond to the odd lattice site, $2k + 1$, as proposed in [164]. We sketch the MPS chain that corresponds to such configuration in Fig. 1.2. Note that there we started counting from 0 instead of 1, as was mentioned above.

In the quantum purification scheme a generic thermal state is represented with a pure state of the extended system, which is defined as [4, 164, 167]

$$|\psi(\beta)\rangle = e^{-\beta\hat{\mathcal{H}}/2} |\psi(\beta = 0)\rangle. \quad (1.86)$$

Here $|\beta = 0\rangle$, represents the state where auxiliary lattice sites and physical lattice sites are maximally entangled, and $\beta = 1/T$ is the inverse temperature, T [4]. Furthermore, $\hat{\mathcal{H}}$ is the Hamiltonian for which we want to calculate the thermal states and acts only on the physical lattice sites [164]. Thermodynamic averages of any physical operator $\hat{\mathcal{O}}$, acting on

the physical sites, can be calculated by computing [164, 167]

$$\langle \hat{\mathcal{O}} \rangle = \frac{\langle \psi(\beta) | \hat{\mathcal{O}} | \psi(\beta) \rangle}{\langle \psi(\beta) | \psi(\beta) \rangle}. \quad (1.87)$$

The starting point of the finite temperature calculations is to obtain the maximally entangled state $|\psi(\beta = 0)\rangle$. More precisely this is the state where every physical lattice site $j = 2k$ is maximally entangled to their corresponding ancilla site $j = 2k + 1$. In a generic spin-1/2 chain this would be the state where physical and their corresponding ancilla sites are in singlet states [35, 167]. In order to implement such state $|\psi(\beta = 0)\rangle$, we compute the ground state of the *entangler* Hamiltonian [4, 167]

$$\hat{\mathcal{H}}_e = - \sum_{j=0}^L \left(\hat{S}_{2j}^+ \hat{S}_{2j+1}^- + \text{H.c.} \right). \quad (1.88)$$

This Hamiltonian is chosen because its ground state is exactly $|\psi(\beta = 0)\rangle$ and we can simply use DMRG to find its ground state [4].

In the next step, we perform imaginary time evolution on the maximally entangled state [4, 164, 167]

$$|\psi(\beta)\rangle = e^{-\beta \hat{\mathcal{H}}/2} |\psi(\beta = 0)\rangle. \quad (1.89)$$

The time evolution is performed by employing Krylov algorithm [135] for the first few states in order to sufficiently grow the bond dimension of the MPS [4, 169]. The initial state has very low bond dimension of only $\chi = 2$, hence Krylov algorithm is employed for the first 10 steps, where we typically use a time step $\Delta\beta_K t/2 = 0.01$ [4]. For the rest of the time evolution we employ time-dependent variational principle [135]. There we typically use a slightly longer time step of $\Delta\beta_T t/2 = 0.05$ [4].

Since the Hamiltonian in Eq. (1.89) acts only on physical lattice sites, it is rewritten as [4]

$$\hat{\mathcal{H}}_s^T = t \sum_{j=1}^{L-1} \left(4\hat{S}_{2j-2}^x \hat{S}_{2j+2}^x - 1 \right) \hat{S}_{2j}^z - 2h \sum_{j=0}^L \hat{S}_{2j}^x + 2\mu \sum_{j=0}^{L-1} \hat{S}_{2j}^x \hat{S}_{2j+2}^x. \quad (1.90)$$

The energies of the system converge to the ground state energy as a function of β . Since the chemical potential μ is constant throughout the imaginary time evolution, chain fillings also slowly converge to the ground state results. We note that for technical reasons, we normalize the state already in every time-evolution step, and not after we reach very long β , as stated in Eq. (1.87).

A similar procedure as outlined here can be also employed for other spin systems [167]. In fact, the same procedure as stated above was used for the mixed-dimensional XXZ model in Chapter 7.4.

Time evolution methods for MPS

Before concluding this section we provide some basic ideas of the time evolution methods used to perform finite temperature calculations. To perform imaginary time evolution, we

use the MPS toolkit SYTEN [153, 154] throughout this thesis. We use the Krylov method and TDVP, which are already implemented in the toolkit. For a thorough review of these methods we refer the reader to Ref. [135], on which we base the following discussion, where we summarize the main points.

The Krylov method relies on the Krylov sub-space expansion in order to estimate the action of the time evolution operator on the physical state [135]

$$\hat{U}(\delta t) |\psi(t)\rangle = e^{-i\delta t \hat{H}} |\psi(t)\rangle = |\psi(t + \delta t)\rangle. \quad (1.91)$$

It relies on the Krylov sub-space \mathcal{K}_N , where the state $|\psi\rangle$ and Hamiltonian \hat{H} , define the sub-space containing the vectors $\{|\psi\rangle, \hat{H}|\psi\rangle, \hat{H}^2|\psi\rangle, \dots, \hat{H}^{N-1}|\psi\rangle\}$ [135]. More precisely, \mathcal{K}_N is spanned by vectors $|v_0\rangle, |v_1\rangle, \dots, |v_{N-1}\rangle$, which are all orthogonalized to each other and where any vector $|v_i\rangle$ is generated by applying \hat{H} to the previous vector $|v_{i-1}\rangle$ as suggested in the definition above [135]. The new time-evolved state is then calculated by solving the equation [135]

$$\hat{U}(\delta t) |\psi(t)\rangle \approx \arg_{|v\rangle \in \mathcal{K}_N} \min || |v\rangle - \hat{U}(\delta t) |\psi(t)\rangle || \equiv |\psi_N(t + \delta t)\rangle. \quad (1.92)$$

There are two main source of errors, the first one comes from the size of the Krylov sub-space expansion, which scales as $O(\delta^N)$ [135]. The second one comes from the MPS truncation error, which can be seen in the so called discarded weight [135]. Both errors can be reduced, however the numerical effort increases [135]. Therefore, for longer time evolution we switch to TDVP.

The time-dependent variational principle (TDVP), is a local method to perform time evolution, where the numerical calculations are constrained to a certain MPS manifold [135, 170, 171]. There we can thus specify the exact bond dimension, and the method is restricted to calculating the time-dependent Schrödinger equation only in that specific manifold [135]. The TDVP method is somewhat complex and we will not go into further details. We just mention that the main advantage of using TDVP is that it is numerically cheaper than the global Krylov method. In the global Krylov method, the entanglement can grow artificially fast as the states pick up more entanglement than the exact state would actually acquire under time-evolution [135]. For this reason, a TDVP method or a local Krylov method were developed in order to circumvent this [135].

There are four sources of error in the TDVP method [135]. The projection error is encountered when the bond dimension is too small, the time step error occurs when the times step δt is too big and scales as $O((\delta t)^3)$ per time step, and the third error arises when the local number of Krylov vectors is too small [135]. The fourth error arises in a two-site TDVP (2TDVP), where additional truncation takes place [135]. The bond dimension thus has to be sufficiently large before starting the TDVP, which is why it is useful to first use a global Krylov method for first few time steps, and then switch to TDVP, in the case the initial state has very low bond dimension [135, 169]. This is, for example, the case in our finite temperature calculations. One also needs to find a good time interval for each time step as the truncation error and the projection error increase with more time steps [135].

In contrast, the time step error and the error related the number of local Krylov vectors, decreases with shorter time steps [135].

With this we conclude the theoretical introduction. In the next chapter we start our discussion on \mathbb{Z}_2 LGT coupled to dynamical matter. In the chapters that follow we will often relate to the concepts and methods discussed in this chapter.

Chapter 2

Confinement in \mathbb{Z}_2 lattice gauge theories with matter

In this chapter we discuss the confinement problem in the one-dimensional (1 + 1D) \mathbb{Z}_2 LGT coupled to matter in the ground state. The confinement of partons into mesons is mediated via the \mathbb{Z}_2 gauge field. We first introduce the Hamiltonian of the paradigmatic 1 + 1D \mathbb{Z}_2 LGT, and the string-length picture, by considering the Gauss law constraint to the physical Hilbert space sector without background charges. We discuss confinement in a simple limit where matter dynamics is frozen. We continue by discussing different probes of confinement at generic fillings and Hamiltonian parameter values. We first discuss the Green's function behaviour, which decays exponentially in the confined phase, and as a power-law in the deconfined regime [1, 160]. We also discuss the abrupt change of the Friedel oscillations, the frequency of which halves in the confined phase, relative to the frequency observed in the deconfined phase at the same chain fillings [160]. To obtain the numerical result we employ DMRG calculations, where we eliminate the matter degrees of freedom by using the Gauss law constraint. We also develop an experimentally feasible probe of confinement by considering the string and anti-string length distributions, where a bimodal distribution is a robust signature of confinement. Such distributions are sampled from snapshots, obtained from our numerical calculations.

Finally, we provide an explanation of the confinement problem by mapping the system to a nonlocal string-length basis. We first show how a naive bosonization argument, where one integrates out the gauge degrees of freedom, does not capture confinement, and argue why a different approach is needed. By mapping the \mathbb{Z}_2 LGT to the string-length basis, we show that the confined phase relates to breaking of the translational symmetry in the new basis [1]. This explains why the matter in a 1 + 1D \mathbb{Z}_2 LGT confines into mesons as soon as the gauge field becomes dynamical.

This chapter is mainly based on Ref. [1], from which the content, including figures, has been adapted and extended. In addition, we also refer to some of the results from Refs. [3–5], from which we adapt some of the figures and results.

2.1 One-dimensional \mathbb{Z}_2 lattice gauge theory with matter

We start by introducing the 1 + 1D \mathbb{Z}_2 lattice gauge theory coupled to $U(1)$ matter, which we define as [1, 121, 160]

$$\hat{\mathcal{H}} = -t \sum_j \left(\hat{a}_j^\dagger \hat{\tau}_{\langle j, j+1 \rangle}^z \hat{a}_{j+1} + \text{H.c.} \right) - h \sum_j \hat{\tau}_{\langle j, j+1 \rangle}^x. \quad (2.1)$$

Here \hat{a}_j^\dagger (\hat{a}_j) are the hard-core boson creation (annihilation) operators. The term $U(1)$ matter, used above comes from the fact that the Hamiltonian conserves the total number of hard-core bosons. The \mathbb{Z}_2 fields are represented by Pauli matrices on the links, $\langle j, j+1 \rangle$, between lattice sites. The Pauli matrix $\hat{\tau}_{\langle j, j+1 \rangle}^x$ represents the \mathbb{Z}_2 electric field and $\hat{\tau}_{\langle j, j+1 \rangle}^z$ represents the \mathbb{Z}_2 gauge field. The motivation for such names can be found in the general introduction to lattice gauge theories in Chapter 1.2. Without loss of generality we consider $t, h \geq 0$, throughout this thesis. In addition, we note that in one-dimension we can map hard-core bosons to spinless fermions via Jordan-Wigner transformations [172, 173]. The physics thus remains the same if we replace the hard-core bosons with spinless fermions [1].

The first term in the Hamiltonian Eq. (2.1) is the nearest-neighbor (NN) hopping term for the hard-core bosons (partons) proportional to hopping amplitude t . Partons are minimally coupled to the \mathbb{Z}_2 gauge fields and the hopping term thus includes the $\hat{\tau}_{\langle j, j+1 \rangle}^z$ operator, which resides on the link between the two lattice sites where the parton hops; see Fig. 2.1. The second term in the Hamiltonian Eq. (2.1) is the \mathbb{Z}_2 electric field term, the strength of which is parameterized by h , and induces dynamics in the \mathbb{Z}_2 gauge field.

In addition to the Hamiltonian Eq. (2.1), one also has to consider a set of local operators [1, 121, 160],

$$\hat{G}_j = \hat{\tau}_{\langle j-1, j \rangle}^x e^{i\pi \hat{n}_j} \hat{\tau}_{\langle j, j+1 \rangle}^x, \quad (2.2)$$

which generate the gauge symmetry. Here we defined the hard-core boson on-site number operator $\hat{n}_j = \hat{a}_j^\dagger \hat{a}_j$. As already mentioned above, operators \hat{G}_j correspond to the generators of the \mathbb{Z}_2 symmetry group, and constitute the LGT counterpart of the Gauss law [1, 3–5, 121, 160], as discussed in Section 1.2.5. The operators in Eq. (2.2) thus commute with the Hamiltonian, $[\hat{\mathcal{H}}, \hat{G}_j] = 0, \forall j$, and since the gauge group is Abelian, also with each other $[\hat{G}_j, \hat{G}_i] = 0$. This means that the \mathbb{Z}_2 LGT Hamiltonian in Eq. (2.2), can be diagonalized in the basis of the \hat{G}_j operators. The eigenvalues of Eq. (2.2),

$$\hat{G}_j |\psi\rangle = g_j |\psi\rangle, \quad (2.3)$$

can take two different values, $g_j = \pm 1$. This means that the eigenvalues of \hat{G}_j on every matter lattice site can be considered to divide the Hilbert space \mathcal{H} into different sectors: $\mathcal{H} = \bigoplus_m \mathcal{H}(G^m)$, where $G^m = \{g_1^m, \dots, g_j^m, \dots\}$ [26]. The set of eigenvalues for every site thus labels the corresponding Hilbert space sector. We consider the physical sector where the eigenvalues are always positive on every lattice site, i.e., $g_j = +1, \forall j$. This corresponds to the Hilbert space sector without any background charges [1, 121, 160].

The direct consequence of considering only the physical Hilbert sector is obtaining a

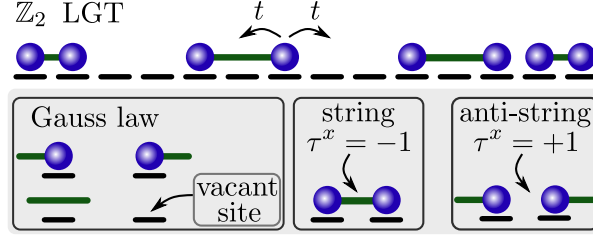


Figure 2.1: A sketch of a one-dimensional \mathbb{Z}_2 LGT, where a \mathbb{Z}_2 gauge field is coupled to $U(1)$ matter. The Gauss law constraint determines the orientation of the \mathbb{Z}_2 electric field in respect to the position of the matter on the lattice. Figure was modified from Fig. 1 in Ref. [1].

one-to-one relation between the electric field configuration $\hat{\tau}_{\langle i,j \rangle}^x$ and position of matter (hard-core bosons) in the lattice. From Gauss law, Eq. (2.2), we see that in order for the operator to always have a positive eigenvalue $g_j = +1$, the electric field configuration across an occupied lattice site, $\langle \hat{n}_j \rangle = 1$, has to be anti-aligned $\langle \hat{\tau}_{\langle j-1,j \rangle}^x \hat{\tau}_{\langle j,j+1 \rangle}^x \rangle = -1$. Contrarily, for vacant lattice site $\langle \hat{n}_j \rangle = 0$, the electric fields have to be aligned, $\langle \hat{\tau}_{\langle j-1,j \rangle}^x \hat{\tau}_{\langle j,j+1 \rangle}^x \rangle = +1$. In other words, in the physical gauge sector the Gauss law operator is equivalent to $\hat{G}_j = \hat{\tau}_{\langle j-1,j \rangle}^x e^{i\pi \hat{n}_j} \hat{\tau}_{\langle j,j+1 \rangle}^x = I$, where I is the identity element. We can thus write the direct connecting between the $\hat{\tau}^x$ orientations and the on-site particle occupation \hat{n}_j as [1]

$$\hat{n}_j = \frac{1}{2} \left(1 - \hat{\tau}_{\langle j-1,j \rangle}^x \hat{\tau}_{\langle j,j+1 \rangle}^x \right). \quad (2.4)$$

This has another important consequence, namely, we can define *strings* and *anti-strings*, which denote the orientation of the electric field $\hat{\tau}_{\langle i,j \rangle}^x$. Strings are defined as connected neighboring links where the orientation of the \mathbb{Z}_2 electric field is negative, $\langle \hat{\tau}_{\langle i,j \rangle}^x \rangle = -1$, and anti-strings are defined as connected links where $\langle \hat{\tau}_{\langle i,j \rangle}^x \rangle = +1$; see Fig. 2.1. Such definition together with the Gauss law constraint in Eq. (2.4), results in strings either starting or ending with partons (hard-core bosons). By following the analogy with the Gauss law, this makes partons sources and drains of the \mathbb{Z}_2 electric field. In other words, partons are connected in pairs by strings, i.e., electric fields of the same configuration; see Fig. 2.1. Every pair, two partons connected by a string, is thus preceded and followed by an anti-string (a set of $\langle \hat{\tau}_{\langle i,j \rangle}^x \rangle = +1$).

We generally consider finite chains with L matter lattice sites. We also consider that lattice starts and ends with a link variable, which results in $L + 1$ links. In addition, without loss of generality we typically assume that the chain starts and ends with an anti-string, i.e., positive electric field orientation, $\langle \hat{\tau}_{\langle 0,1 \rangle}^x \rangle = \langle \hat{\tau}_{\langle L,L+1 \rangle}^x \rangle = +1$. Hence, a first string in the lattice starts with the first particle. If we furthermore consider that we have an even number of partons in the system, this results in no partons being connected to the lattice edge by a string.

The above definition is in a way arbitrary and can be reversed in the case when $h \rightarrow -h$, which will become apparent in the next section. The above conditions, in particular of even parton number becomes important only for $h \neq 0$. In the numerical calculations in this

thesis, the above definitions are also fully considered only when $h > 0$.

2.2 Confinement in simple limits

We will now consider different terms in the Hamiltonian defined in Eq. (2.1) separately, and offer an intuitive explanation of confinement that arises in such a system.

The first term is the hopping term with amplitude t . Hard-core bosons, which we also denote as *partons*, for reasons that will become apparent soon, are allowed to hop to a neighboring lattice site; see also Fig. 2.1. The standard hopping term in Eq. (2.1) also contains the gauge field operator, represented with the Pauli matrix $\hat{\tau}_{\langle i,j \rangle}^z$ on the link across which the parton hops. This makes the partons minimally coupled to the \mathbb{Z}_2 gauge field. The Gauss law, Eq. (2.4), is thus fulfilled also after the parton hops, since the action of a $\hat{\tau}^z$ operator on the link variable flips the orientation of the spin in the x -basis. In the string picture, introduced in the previous section, this means that the string remains attached to the parton as it hops. Hence, although the matter is dynamical, the system always remains in the physical Hilbert sector, $g_j = +1, \forall j$.

The second term is the electric field term proportional to strength h , which induces dynamics in the gauge field [1, 4]. This analogy was discussed in the previous Section 1.2, where we saw that the electric field term can also be understood as the momentum operator. Electric field terms can thus be understood as the kinetic energy terms of the gauge field [26, 117, 121]. With the string-length picture described above, the electric field term in Eq. (2.1) energetically penalizes links where the electric field term has a negative eigenvalue, $\hat{\tau}_{\langle i,j \rangle}^x |\psi\rangle = -|\psi\rangle$. As a result, the finite electric field term, $h > 0$, favours anti-strings. In a system with finite number of partons, this results in linear confining potential for the strings. Hence, the strings tend to become as short as possible and individual partons confine into dimers (mesons).

The limit of static matter

Confinement of partons into mesons is most easily seen by considering the case where hopping is frozen, i.e., when we set $t = 0$. A single meson energy can be thus expressed as

$$E(\ell) = h\ell, \quad (2.5)$$

where ℓ is the length of the string, i.e., the number of links between two partons with $\langle \hat{\tau}_{\langle i,j \rangle}^x \rangle = -1$. By construction, it holds that $\ell \geq 1$. Similarly, anti-string energy would be equal to $E(\ell^a) = -h\ell^a$, where ℓ^a is the length of the anti-string (it also holds that $\ell^a \geq 1$). This means that strings tend to be as short as possible when $h > 0$ in order to minimize its energy and as a result partons connected with the same string effectively bind in a dimer, which we dub as *meson* in analogy to HEP. Contrarily, one can also claim that anti-string lengths tend to be as long as possible. A tightly confined meson is thus a state where two partons reside on neighbouring sites and thus the string length between them has the minimal possible value: $\ell = 1$.

Let us now consider N particles in a chain of length L , the chain filling is thus defined as $n = N/L$. As already discussed above, we consider even number of particles N , and we consider the chain, which starts and ends with a link (anti-string, $\langle \hat{\tau}_{(i,j)}^x \rangle = +1$). This means that we have $N/2$ strings and $N/2 + 1$ anti-strings. We now denote the lengths of strings connecting meson m (counting, for example, from the left) as ℓ_m , where $m \in \{1, 2, \dots, \frac{N}{2}\}$. The total energy of the system is thus equal to

$$E = h \sum_{m=1}^{N/2} \ell_m - h \left((L+1) - \sum_{m=1}^{N/2} \ell_m \right) = 2h \sum_{m=1}^{N/2} \ell_m - h(L+1). \quad (2.6)$$

We remind the reader that we consider $L+1$ links.

The upper boundary for the string length can be found by considering one string, ℓ^{\max} , to be of maximal possible length and all other remaining $N/2 - 1$ strings and $N/2 + 1$ anti-strings to be of minimal possible length $\ell, \ell^a = 1$, which yields:

$$\ell^{\max} = (L+1) - (N/2+1) - (N/2-1) = L+1-N. \quad (2.7)$$

The string-lengths are thus bounded as:

$$1 \leq \ell \leq L - N + 1. \quad (2.8)$$

We now see that the expression in Eq. (2.6), will be minimized when $\ell_m = 1, \forall m$ and thus the energy of the system where $t = 0$, will equal to

$$E_0 = hN - h(L+1). \quad (2.9)$$

We can rewrite this by normalizing the expression per lattice site, which results in

$$e_0 = E_0/L = h(n-1) + h/L. \quad (2.10)$$

In the thermodynamic limit, $L \rightarrow \infty$, the energy per lattice site is thus equal to $e_0 = h(n-1)$, where n is the chain filling as before.

We have thus shown that in the limit when the parton dynamics is frozen, $t = 0$, the energetically favored states in our system are tightly confined meson states, where the distances of strings connecting partons is minimal.

The limit of a strong electric field term

When the partons become dynamical, that is when $t > 0$, the general picture becomes more complicated. However, one can gain some intuition by considering hopping as a small perturbation in the limit when $h \gg t$, the calculation which was first performed by Borla et al. in Ref. [160].

The starting point is to consider a single tightly confined meson where $\ell = 1$, with energy $E_0 = h$. The partons in such a case are thus NN. If one of the partons hops away from their partner, the energy gain associated with that is $\Delta E = 2h$. This is because the

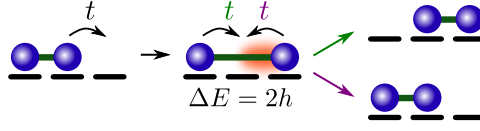


Figure 2.2: Second order hopping of mesons in the limit when $h \gg t$ [160]. After the first parton hops, the energy of the meson increases by $\Delta E = 2h$. In order to decrease the energy, the same parton can hop back to its original lattice site (lower state on the right). The other option is that the left parton hops towards its meson partner on the lattice site previously occupied by the parton that hopped first. This results in the overall hopping of the meson by one lattice site to the right (upper state on the right).

link orientation across which the parton hops has to change $\langle \hat{\tau}_{(i,j)}^x \rangle = 1 \rightarrow \langle \hat{\tau}_{(i,j)}^x \rangle = -1$; see Fig. 2.2. Such a state is energetically highly unfavorable, which means that one of the partons will hop towards the parton to which it is connected by a string in order to reduce its length. There are two options: the same parton that hopped first can either hop back to its meson partner, or the other parton will hop towards the parton, which was the first one to hop; see Fig. 2.2.

The effective second order perturbation theory yields an effective Hamiltonian for the mesons (dimers) [3, 160],

$$\hat{\mathcal{H}}_d = -t_d \sum_{j^*} \left(\hat{d}_{j^*}^\dagger \hat{d}_{j^*+1} + \text{H.c.} \right) + V_d \sum_{j^*} \hat{n}_{j^*}^d \hat{n}_{j^*+1}^d, \quad (2.11)$$

where we define the tightly confined meson creation operator as $\hat{d}_{j^*}^\dagger = \hat{a}_j^\dagger \hat{a}_{j+1}^\dagger$, and the meson on-site density operator as $\hat{n}_{j^*}^d = \hat{d}_{j^*}^\dagger \hat{d}_{j^*}$. In addition, the second order hopping parameter can be expressed as $t_d = t^2/2h$ [3, 160]. Furthermore, the lattice sites have to be redefined, as the meson which resides on two lattice sites, e.g., j and $j+1$, are squeezed into a single hard-core boson on site j^* . In a chain with finite doping, the perturbative hopping explained above is restricted if two mesons are nearest-neighbors, which results in the NN repulsion $V_d = 2t_d$ [3, 160]. More details on this effective model is given in Section 3.2.2.

Above we have also demonstrated that in the limit when $h \gg t$, confined mesons are mobile with the hopping amplitude given by t_d . Hence, confined mesons remain dynamic, and are not pinned to specific lattice sites.

The confinement problem becomes hard to tackle once the hopping amplitude t and electric field term h become of comparable strength, $t \sim h$. The other limit where $t \gg h$ is also hard to tackle perturbatively, as the \mathbb{Z}_2 electric field has highly non-local effects, which we comment in the next sections. However, in the limit when $h = 0$ the gauge field can be eliminated using Jordan-Wigner like string attachment and we obtain a free parton Hamiltonian [1, 5, 119, 121, 160]. More about such mapping will be presented in Section 2.4.1.

To answer the question whether the partons confine also in more complicated regimes ($t \sim h$ and $t \gg h$), one has to resort to numerical calculations and come up with physical observables that probe confinement. We discuss this in the next section.

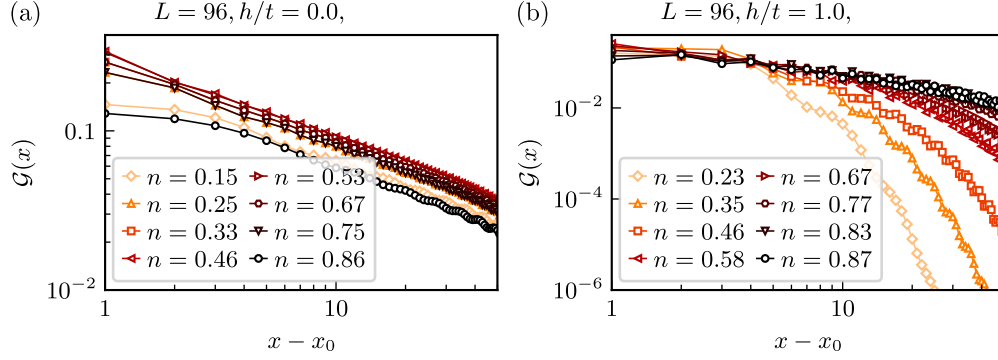


Figure 2.3: Gauge invariant \mathbb{Z}_2 Green's function Eq. (2.12) in a $1 + 1D$ \mathbb{Z}_2 LGT coupled to matter, Eq. (2.1), after integrating out the matter. (a) The Green's function decays with a power law for $h = 0$, indicating the deconfined regime. (b) The Green's function exhibits an exponential decay when $h/t = 1$. The decay decreases with higher filling n , however the decay remains exponential. Both axes are in a logarithmic scale. Figure was modified from Fig. 2 in Ref. [5].

2.3 Probing confinement in a one-dimensional \mathbb{Z}_2 LGT coupled to matter

2.3.1 Green's function

The first probe of confinement that we consider is the behavior of the \mathbb{Z}_2 gauge invariant Green's function defined as [1, 3–5, 160]

$$\mathcal{G}(i-j) = \left\langle \hat{a}_i^\dagger \left(\prod_{i \leq \ell < j} \hat{\tau}_{(\ell, \ell+1)}^z \right) \hat{a}_j \right\rangle. \quad (2.12)$$

Green's function can be understood as a non-local correlation function, which probes how "easy" it is to remove a particle at site j and add it to site i . We define the distance between these two sites as $x = |i - j|$. It thus directly probes whether a parton is free to roam the chain. For free partons the Green's function, Eq. (2.12), decays with a power law as a function of distance, $\mathcal{G}(x) \propto x^{-\gamma}$ [1, 160]. Contrarily, if a parton is part of a bound meson, i.e. if it is bound to another parton via a confining string, then the decay is exponential, $\mathcal{G}(x) \propto e^{-x/\xi}$ [1, 160].

The behaviour of the gauge invariant Green's function for the \mathbb{Z}_2 LGT in Eq. (2.1) was first considered by Borla et al. in [160], by performing DMRG calculations. It was revealed that the Green's function decays with a power law for $h = 0$ and exponentially for $h > 0$ [160]. Our calculations, where we integrate out the matter as discussed in Ref. 1.3.2, reveal the power law decay for $h = 0$ is robust for any chain filling n , whereas the strength of the exponential decay for $h/t = 1$, has a slight dependence on the filling; see Fig. 2.3 [5]. The above Fig. 2.3 was obtained by performing DMRG for a finite system size L using the MPS toolkit SyTEN [153, 154]. Furthermore, we chose $x_0 = i = 30$ which is at a finite value away

from the boundary and $x = j > 30$ [5]. This is to avoid boundary effects in a system with size $L = 96$, and open boundary conditions (OBC) [5]. As can be seen in Fig. 2.3(b), the exponential decay decreases with increasing chain filling n , which we associate with the overall reduced mobility of mesons in a more filled chain, which decreases the number of available sites.

The gauge invariant Green's function is thus an excellent probe of confinement as its behaviour clearly differentiates between deconfined and confined regime. However, we note that this is not a typical order parameter with a simple numerical value, for example, a number ranging between zero for confined and some finite number in the deconfined regime. Since one has to extract long-distance behaviour of the Green's function, we require fairly large system size, above what can typically be reached with exact diagonalization calculations. This means that one has to consider more advanced numerical techniques in order to obtain the long-distance behaviour of the Green's function like the DMRG based on MPS [4, 5, 160]. One could also consider Monte Carlo calculations where the Green's function Eq. (2.12), defined here for 1 + 1D, resembles a one-dimensional version of the Fredenhagen-Marcu order parameter [5, 174].

Furthermore, extracting the Green's function in a cold-atom experiment would be a rather difficult task. Therefore, although the Green's function is a good theoretical probe of confinement, simpler and perhaps more robust probes are desired, which we discuss in the following sections.

2.3.2 Friedel oscillations

The next probe of confinement that we consider are the Friedel oscillations, which emerge as boundary effects in calculations with OBC. This is the case for most of our numerical calculations in this thesis. More precisely, Friedel oscillations are density oscillations in a one-dimensional system, due to the presence of a boundary or impurity [175, 176]. The Friedel oscillations for non-interacting fermions can be calculated using the Bethe ansatz, or in some cases by considering simple plain waves [176, 177]

$$\delta n(x) = A \frac{\cos(2\pi n x + \varphi)}{x}, \quad (2.13)$$

where one assumes that the boundary is at $x = 0$ and we included a phase shift φ [176–179]. In the interacting case, the decay of Friedel oscillations generally takes the form [176, 177]

$$\delta n(x) = A \frac{\cos(2\pi n x + \varphi)}{x^\alpha}, \quad (2.14)$$

where α parameterizes the interaction between the particles in a chain [176–178]. In a chain with OBC we thus obtain a symmetric standing wave [176]

$$n_F(x) = A_1 + A_2 \left(\frac{\cos(2\pi n x + \varphi)}{x^\alpha} + \frac{\cos(2\pi n(L + 1 - x) + \varphi)}{(L + 1 - x)^\alpha} \right). \quad (2.15)$$

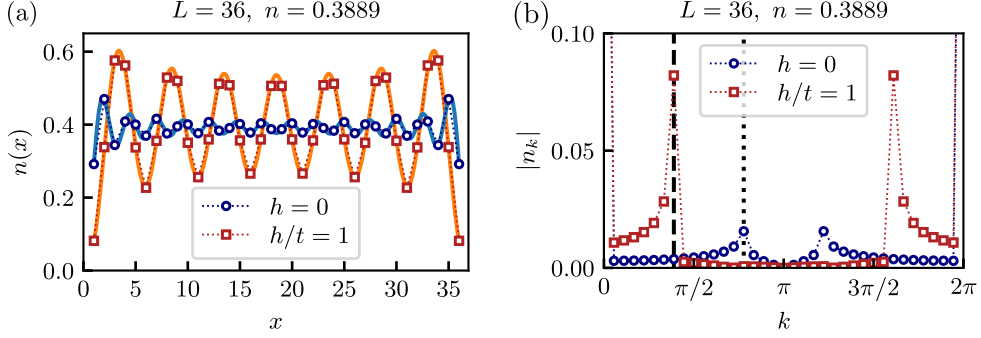


Figure 2.4: Friedel oscillations in a 1 + 1D \mathbb{Z}_2 lattice gauge theory Eq. (2.1), after integrating out the matter fields. (a) Density profile $n(x)$ for filling $n = 14/36$ in the free parton regime $h = 0$ (blue circles) and in the confined regime $h/t = 1$ (red squares). The light blue and orange solid lines correspond to fits of the data points with simple function Eq. (2.15). (b) Fourier transformation of the Friedel oscillations in the same parameter regimes. The vertical dotted line corresponds to the deconfined momentum $k = 2\pi n$, and the vertical dashed line to the confined momentum $k = \pi n$. The results presented in this figure are modified from Ref. [4], More precisely, these are modified Fig. 2 and Fig. S5. in Ref. [4].

Here we added model dependent fit parameters A_1 and A_2 to obtain a stable fit to the data.

Borla et al. in Ref. [160] first consider the density profiles $n(x)$ in the one-dimensional \mathbb{Z}_2 LGT chains and studied the effect of confinement on the Friedel oscillations. Numerical calculations showed that the frequency of the Friedel oscillations halve from $2\pi n$, for the deconfined case when $h = 0$, which is consistent with free partons, to πn in the confined regime when $h \neq 0$ [160]. Furthermore, it was shown that this abrupt change happens for very small electric field term, $h \ll t$, which indicates that mesons become confined for any non-zero value $h \neq 0$ [160]. This explanation follows from the fact that the density seemingly drops from n to $n/2$, indicating that confined mesons are the relevant emergent particles.

As an example we present the Friedel oscillations in Fig. 2.4 for a system of $N = 14$ partons in a chain of length $L = 36$, in the deconfined ($h = 0$) and the confined regime ($h/t = 1$) [4]. The results were again obtained by using the MPS toolkit SYTEN [153, 154], by simulating the spin model, Eq. (1.77), after integrating out the matter. By simply counting the number of peaks in the density profile $n(x)$ in Fig. 2.4(a), one can observe that the period of oscillation doubles in the confined regime. We fit the DMRG result also with Eq. (2.15), where in the confined regime we replace the argument of \cos , by $2\pi n \rightarrow \pi n$, and for $h = 0$, we fix $\alpha = 1$. The thick lines in Fig. 2.4(a) represent the fit results, and we highlight that fit results in the deconfined case, ($h = 0$), yield $\tilde{n} = 0.392$, $\tilde{L} = 35.94$, and in the confined case, ($h/t = 1$), yield $\tilde{n} = 0.399$, $\tilde{L} = 36.02$. In both cases the fits are within a few percent error (the worst is for $h/t = 1$, where $\delta n = \frac{n - \tilde{n}}{n} \approx 2.6\%$). For completeness we state that for $h = 0$: $\varphi = -1.618 \pm 0.014$, $A_1 = 0.392 \pm 0.0003$ and $A_2 = 0.145 \pm 0.002$, and for $h/t = 1$, $\alpha = 0.477 \pm 0.006$, $\varphi = -1.21 \pm 0.01$, $A_1 = 0.400 \pm 0.001$ and $A_2 = 0.273 \pm 0.004$.

Even more convincing are the result obtained by performing the Fourier transformation

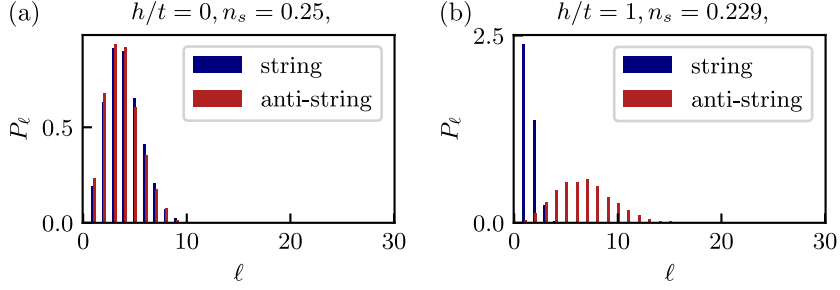


Figure 2.5: String and anti-string length distributions in a 1 + 1D \mathbb{Z}_2 lattice gauge theory Eq. (2.1) after integrating out matter. (a) In the deconfined regime $h = 0$ at filling $n_s = 0.25$, the string and anti-string length distributions are similar to each other as the partons are deconfined. (b) In the confined regime $h/t = 1$ at filling $n = 0.229$, the string length histogram peaks at length $\ell = 1$, whereas the anti-string length histogram develops a peak at a much larger length $\ell \approx 7$. The system size considered here is $L = 96$, and probabilities P_ℓ are normalized to unity. Number of snapshots taken was 400. This figure was modified from Fig. 3 in Ref. [5].

of the Friedel oscillations [4]

$$n_k = \frac{1}{L} \sum_{j=0}^{L-1} e^{-ikj} \langle \hat{n}_j \rangle. \quad (2.16)$$

Here we discretize the k -modes as $\Delta k = \frac{2\pi}{L}$ [4]. In Fig. 2.4(b) we show that the peaks at $2\pi n$ for $h = 0$, move to πn in the confined regime $h/t = 1$.

Friedel oscillations thus provide a good probe of confinement in systems with OBC. Since this probe simply involves obtaining the density profiles in the chains, it is well suited for cold atom experiments, providing one has access to density resolved snapshots. Furthermore OBC conditions can also be imposed for example with DMD devices [67] as mentioned in Section 1.1.

2.3.3 String-length distributions from snapshots

The last probe of confinement that we will discuss here are the string and anti-string length histograms, which are obtained from numerical snapshots [4, 5]. Snapshots can be obtained from our MPS results, by using the so-called perfect sampling algorithm [180, 181]. These algorithms are already implemented in SYTEN [153, 154], which we use to sample snapshots from our MPS.

The procedure to obtain the snapshots is as follows. We first find the ground state at a given parameter values, by using DMRG. The ground state is saved as MPS, from which we sample snapshots in the electric field basis. Each snapshot thus gives an orientation of the electric field $\langle \tau_{\langle i,j \rangle}^x \rangle$, e.g., an array $[-1, 1, 1, -1, -1, \dots]$. By sweeping through each snapshot we can thus determine the length of every string and anti-string, which we defined earlier as $\langle \hat{\tau}_{\langle i,j \rangle}^x \rangle = -1$ and $\langle \hat{\tau}_{\langle i,j \rangle}^x \rangle = +1$, respectively. By considering the orientation of the strings across each site we determine whether there is a parton or not. The string lengths are then defined as lengths between odd-even partons, and anti-strings as the distances between

even-odd partons. The partons are numbered starting from the beginning of the chain. Such definition is more robust as in the case when $h = 0$, the \mathbb{Z}_2 electric fields have a global \mathbb{Z}_2 symmetry. We gather these values, and by considering ~ 400 snapshots, we construct string and anti-string length histograms. In the confined regime strings are on average much shorter than the anti-strings since partons are confined into meson. As a result we obtain a bimodal distribution of strings and anti-strings [4, 5]. Contrarily, in the deconfined regime, string and anti-string length distributions are identical, i.e., have almost the same shape, width, and position of the peak. That is because partons are completely free, and there is no difference between strings and anti-strings.

An example of the string and anti-string length histograms in the deconfined and confined regime are presented in Fig. 2.5. We see that in the deconfined regime, where the partons are free and gauge fields can in fact be eliminated [1, 5, 160], the string and anti-string length distributions are identical. Both distributions peak between $\ell = 3$ and $\ell = 4$. This peak can be easily estimated as we know that the number of string and anti-strings in the whole chain of length L is $N + 1$, where N is the number of partons. The average string and anti-string lengths are the same in the deconfined regime and thus equal

$$\langle \ell \rangle = \frac{L + 1}{N + 1}. \quad (2.17)$$

In a thermodynamic limit this means $\langle \ell \rangle \approx \frac{1}{n}$. Thus the expected value for Fig. 2.5(a) where $n = 0.25$ is $\langle \ell \rangle = 3.88$, and thus consistent with the numerical results.

In the confined regime $h/t = 1$, presented in Fig. 2.5(b), strings peak at $\ell = 1$ and anti-strings at around $\ell_a \approx 6$. This is a clear signature of confinement as mesons are on average tightly bound, with no empty lattice sites between two partons which form a meson. If one assumes that the string-lengths peak at $\ell = 1$, then the anti-string length distribution peak can again be estimated as

$$\langle \ell_a \rangle = \frac{L + 1 - N/2}{N/2 + 1}. \quad (2.18)$$

In thermodynamic limit this yields $\langle \ell_a \rangle \approx \frac{1}{2n} - 1$. For the example in Fig. 2.5(b) where $n = 0.229$, the exact relation for finite L and N , gives us $\langle \ell_a \rangle \approx 7.2$. This estimate is slightly higher than the numerically obtained value in Fig. 2.5(b), which is closer to $\langle \ell_a \rangle \approx 6$. This is due to the naive assumption that all strings are of length $\ell = 1$. As can be seen in Fig. 2.5(b) there is a finite weight at string length $\ell = 2$, which reduces the average length of anti-strings. Finite number of these "extended" strings are in fact necessary as the mesons are mobile and hop via a second-order process [160], where the intermediate state is an extended string [4]; see the previous Section 2.2.

The string and anti-string length distributions are thus a robust measure of confinement, which can be readily obtained in experimental snapshots from cold atom experiments. The measurements can be performed either in the electric field basis or in the parton number basis. This method is however limited with the parton number as the peaks shift towards $\ell = 1$ for larger fillings as we have demonstrated in the simple results in Eq. (2.17) and Eq. (2.18). One could argue that the limiting filling can be set when the anti-string peak ℓ_a^p

and the string peak ℓ_s^p differ by at least one site $\ell_a^p - \ell_s^p = 1$, which means that the anti-string distribution peak has to be at least $\ell_a^p \geq 2$. We can thus consider the limiting case

$$\begin{aligned} \frac{L+1 - N_{\max}/2}{N_{\max}/2 + 1} &\stackrel{!}{=} 2, \\ N_{\max} &= \frac{2}{3}L + 2, \end{aligned} \quad (2.19)$$

which in the thermodynamic limit yields $n_{\max} \approx 2/3$, and should hold for $h \gg t$, when $\langle \ell_s \rangle \approx 1$. As already mentioned previously, for generic value of the electric field term h , not all strings have unity length $\ell = 1$ due to fluctuations. Thus the filling $n_{\max} = 2/3$ can be considered as an upper bound.

2.4 Solution of the confinement problem

In the previous section we provided numerical evidence that the system is indeed confining for generic value of the electric field term h . The most striking result obtained by Borla et al. in Ref. [160], shows that partons confine for any non-zero value of the electric field term $h \neq 0$. In this section we provide a formal solution of the confinement problem by mapping the one-dimensional \mathbb{Z}_2 LGT coupled to matter to a non-local string length basis. This section is based on Ref. [1].

Before we discuss the mapping to the string length basis and confinement in the new basis we first consider why a naive bosonization as proposed by Borla et al. in Ref. [160] does not yield confinement of partons.

2.4.1 Naive bosonization

Due to the Gauss law constraint where the eigenvalues of Eq. (2.2) are restricted to positive values at every lattice site, $g_j = +1, \forall j$, the system can be fully described by considering either gauge fields or matter particles alone. From the field-theory perspective it is therefore desirable to integrate out one of the redundant degrees of freedom. Here we will briefly show how one can eliminate the gauge fields when restricting oneself to the physical sector, following the calculations in the Appendix of Ref. [5].

In analogy to the Jordan-Wigner transformation we define dressed partons, by attaching a string of \mathbb{Z}_2 gauge operators $\left(\prod_{l<j} \hat{\tau}_{\langle l, l+1 \rangle}^z\right)$ to the usual parton operators [5, 119, 121, 160]

$$\hat{b}_j^\dagger = \left(\prod_{l<j} \hat{\tau}_{\langle l, l+1 \rangle}^z\right) \hat{a}_j^\dagger, \quad \hat{b}_j = \left(\prod_{l<j} \hat{\tau}_{\langle l, l+1 \rangle}^z\right) \hat{a}_j. \quad (2.20)$$

where, $\hat{b}_j^\dagger, (\hat{b}_j)$ are dressed hard-core boson creation (annihilation) operators. This construction follows directly from the Gauss law constraint, since a parton on site j changes the orientation of the electric field across that lattice site. Thus, adding or removing a parton at site j , results in changing the orientation of all electric field variables, either from the

left or right of site j , i.e., $\tau_{l,l+1}^x \rightarrow -\tau_{l,l+1}^x, l \in \{0, \dots, j-1\}$, or $\tau_{l,l+1}^x \rightarrow -\tau_{l,l+1}^x, l \in \{j, \dots, L\}$, respectively. Both definitions are equivalent and we choose the former one. The change of electric field orientation is formally achieved by applying a string of $\hat{\tau}_{\langle i,j \rangle}^z$ operator as defined above.

We can apply the same product of $\hat{\tau}_{\langle i,j \rangle}^z$ operators on both sides of Eq. (2.20) and express the initial hard-core operators in terms of the dressed hard-core operators as [5]

$$\hat{a}_j^\dagger = \left(\prod_{l < j} \hat{\tau}_{\langle l,l+1 \rangle}^z \right) \hat{b}_j^\dagger, \quad \hat{a}_j = \left(\prod_{l < j} \hat{\tau}_{\langle l,l+1 \rangle}^z \right) \hat{b}_j. \quad (2.21)$$

The above expression can be used to eliminate the \mathbb{Z}_2 gauge field from the hopping term of the \mathbb{Z}_2 LGT [5]

$$\hat{\mathcal{H}}_t = -t \sum_j \left(\hat{b}_j^\dagger \hat{b}_{j+1} + \text{H.c.} \right), \quad (2.22)$$

which becomes a simple tight binding term.

The next task is to express the \mathbb{Z}_2 electric field in terms of the hard-core operators. We again use the Gauss law constraint. Since we are considering only the physical sector without background charges Gauss law eigenvalues equal to $g_j = +1$. Hence, Eq. (2.2) is simply an identity operator I in the physical sector without background charges

$$\hat{G}_j = \hat{\tau}_{\langle j-1,j \rangle}^x e^{i\pi \hat{n}_j} \hat{\tau}_{\langle j,j+1 \rangle}^x = I. \quad (2.23)$$

By multiplying a set of \hat{G}_j on both sides of the equation, we thus again obtain an identity operator

$$\prod_{l < j} \hat{G}_j = e^{i\pi \sum_{l < j} \hat{n}_l} \hat{\tau}_{\langle j,j+1 \rangle}^x = I, \quad (2.24)$$

where we assumed the usual condition that the lattice starts with an anti-string, $\langle \hat{\tau}_{\langle 0,1 \rangle}^x \rangle = 1$, and the well known property of Pauli matrices $(\hat{\tau}^{x,y,z})^2 = I$ [122]. By applying $\hat{\tau}_{\langle j,j+1 \rangle}^x$ on both sides of Eq. (2.24), we can express the \mathbb{Z}_2 electric field term as [5, 160]

$$\hat{\tau}_{\langle j,j+1 \rangle}^x = e^{i\pi \sum_{l < j} \hat{n}_l}. \quad (2.25)$$

This is a highly non-local operator. The non-local nature of the electric field term is explicitly expressed in a way that it depends on the number of partons in the chain to the left of the link $\langle j, j+1 \rangle$. Since we consider hard-core bosons, a lattice site can be either occupied or empty. Thus the $\hat{\tau}_{\langle j,j+1 \rangle}^x$ operator remains real, and we can write $\hat{\tau}_{\langle j,j+1 \rangle}^x = \cos\left(\pi \sum_{l < j} n_l\right)$ [1], as the on-site number operator \hat{n}_j can only take two possible values $n_j = 0, 1$.

The \mathbb{Z}_2 LGT Hamiltonian Eq. (2.1) can thus be written in terms of dressed matter fields (hard-core boson operators) as [1, 5, 160]

$$\hat{\mathcal{H}}_b = -t \sum_j \left(\hat{b}_j^\dagger \hat{b}_{j+1} + \text{H.c.} \right) - h \sum_j \cos\left(\pi \sum_{l < j} n_l\right). \quad (2.26)$$

We note that the form of the on-site number operator remains the same as it did not contain any gauge fields

$$\hat{n}_j = \hat{a}_j^\dagger \hat{a}_j = \left(\prod_{l < j} \hat{\tau}_{(l,l+1)}^z \right) \hat{b}_j^\dagger \left(\prod_{l < j} \hat{\tau}_{(l,l+1)}^z \right) \hat{b}_j = \hat{b}_j^\dagger \hat{b}_j = \hat{n}_j^b. \quad (2.27)$$

The Hamiltonian in Eq. (2.26) is thus a result of integrating out the gauge fields, within the physical Gauss sector. It can now be bosonized by expressing the on-site density with a continuous function $\hat{n}_j \rightarrow n(x) = n^a - \partial_x \phi(x) / \pi$, where n^a is the average parton density [1]. The \mathbb{Z}_2 electric field term becomes [1]

$$-h \int \cos(\pi n^a - \phi(x)), \quad (2.28)$$

where we utilized the result $\sum_{l < j} \hat{n}_j = \int_0^x n(x) = \int_0^x dx (n^a - \partial_x \phi(x) / \pi) = n^a x - \phi / \pi$. The integral in Eq. (2.28) contains an oscillatory function with spatial dependence and is thus RG irrelevant [1, 160, 182]. Hence, the integral and thus the electric field term should vanish and the partons should remain free [1]. In other words, the non-local Green's function, which in the dressed picture is simply $\mathcal{G}(i-j) = \langle \hat{b}_i^\dagger \hat{b}_j \rangle$, should decay as a power law $\mathcal{G}(i-j) \sim |i-j|^{-\gamma}$ also for non-zero value of the electric field term, $h \neq 0$ [1, 182]. However, as it was shown with numerical calculations, the system is confining for any $h \neq 0$ [160]. We have therefore shown that the *naive* bosonization explained above does not explain confinement of partons into mesons, which calls for a better explanation. For that we turn to the string-length basis discussed in the next section. The failure of such a naive bosonization in this case, stems from the highly non-local nature of the electric field term, which challenges the standard bosonization procedure [1].

2.4.2 The string-length basis

The main problem encountered in the previous section, when we applied the standard bosonization procedure, was the highly nonlocal nature of the Hamiltonian, Eq. (2.26). This motivates us to find a new non-local basis in which the transformed Hamiltonian is local, and standard bosonization approach can be safely applied [1]. We thus consider the string-length basis where the length of strings and anti-strings become new bosonic occupation numbers. We define a new lattice with $\tilde{L} = N + 1$ lattice sites (equal to the combined number of strings and anti-strings), where $N = \sum_j n_j$ is the total number of partons. We define the new bosonic occupation numbers as $\tilde{\ell}_1 \dots \tilde{\ell}_{N+1} \geq 1$ [1], which are simply derived from string and anti-string lengths. More formally, we define the above bosonic occupation numbers by considering the position of partons at $x_1, \dots, x_l, \dots, x_N$, where the position of the l -th parton from the left is denoted by x_l . It thus holds that $x_l \in \{1, L\}$ [1]. The new bosonic occupation numbers are defined as [1]

$$\tilde{\ell}_1 = x_1 - 1, \quad \tilde{\ell}_l = x_l - x_{l-1} - 1, \quad \tilde{\ell}_{N+1} = L - x_N, \quad (2.29)$$

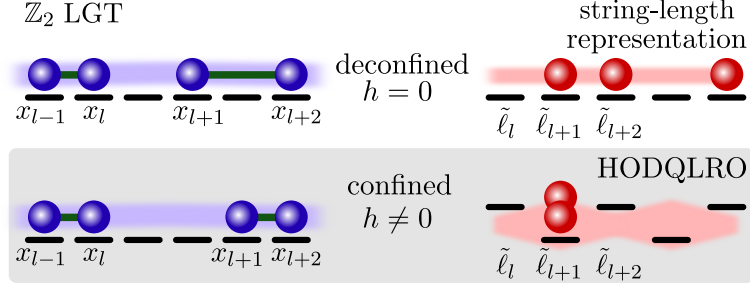


Figure 2.6: Mapping between the original and the string-length basis of the one-dimensional \mathbb{Z}_2 LGT. With x we denote the position of partons (blue) in the original \mathbb{Z}_2 LGT basis (left side of the figure). The on-site boson occupation in the string-length basis $\tilde{\ell}$ is illustrated with the appropriate number of bosons on that lattice site (red spheres). This figure was modified from Fig. 1 in Ref. [1].

which are similar to the string and anti-string lengths introduced in Section 2.2. However, in this definition lengths are reduced by one site, in order for the shortest possible string or anti-string to correspond to a vacuum bosonic state in the new basis; see Fig. 2.6. To be more precise, in Section 2.2 we defined string and anti-string lengths as $\ell_l = x_{l-1} - x_l$, where even l corresponds to strings and an odd l corresponds to anti-strings. In the definition of the bosonic occupation numbers in Eq. (2.29), we redefine string and anti-string lengths as $\tilde{\ell} = \ell - 1$. Thus any "extended string" ($\ell > 1$) can be consider as an excitation where the length of string or anti-string extended above the minimal possible length $\ell_0 = 1$, correspond to an excitation with $n = \ell - 1$ bosons; see also Fig. 2.6. In Fig. 2.6 we also denote the position of the partons with x in the original \mathbb{Z}_2 LGT basis, and the corresponding boson occupation number in the string-length representation with $\tilde{\ell}$.

With this we have found a one-to-one mapping from the original \mathbb{Z}_2 LGT basis, to the string-length basis. The original Fock configuration $|n_1, \dots, n_L\rangle$ can thus be directly connected to a new bosonic Fock configuration $|n_1, \dots, n_{N+1}\rangle$ as [1]

$$|n_1, \dots, n_L\rangle = |n_1, \dots, n_{N+1}\rangle \equiv \prod_{l=1}^{N+1} \frac{(\hat{\Psi}_l^\dagger)^{\tilde{\ell}_l}}{\sqrt{\tilde{\ell}_l!}} |0\rangle, \quad (2.30)$$

where we defined a new bosonic creation operator $\hat{\Psi}_l^\dagger$, which acts on the string-length vacuum state $|0\rangle$. The total number of bosons in the new basis, or string-length excitations equals to $\tilde{N} = \sum_l \tilde{\ell}_l = L - N$ [1].

The \mathbb{Z}_2 LGT Hamiltonian Eq. (2.1) in the new basis can be written as [1]

$$\hat{\mathcal{H}} = -t \sum_{\langle m,l \rangle} \left(\hat{\rho}_m^{-1/2} \hat{\Psi}_m^\dagger \hat{\Psi}_l \hat{\rho}_l^{-1/2} + \text{H.c.} \right) - h \sum_l (-1)^l \hat{\rho}_l, \quad (2.31)$$

where we defined the bosonic string-length density operator as $\hat{\rho}_l = \hat{\Psi}_l^\dagger \hat{\Psi}_l$. We can also

define the average bosom density [1]

$$\rho^\Psi = \frac{\tilde{N}}{\tilde{L}} = \frac{L - N}{N + 1} = \frac{1}{n^a} - 1 + \mathcal{O}(1/N). \quad (2.32)$$

Since the mapping to the new basis is exact, there exists a unitary transformation between the two bases [1]. This means that the spectrum of the Hamiltonian expressed in the original basis Eq. (2.1) and the spectrum of the Hamiltonian expressed in the new basis, Eq. (2.31), are identical [1]. By considering the construction of strings and anti-strings one can quickly map the original Hamiltonian into the new basis. In the following we consider the mapping of individual terms between the original and the new string-length basis.

Let us first consider the hopping term. The parton at position x_l can be connected to a string either from the left or from the right site, and the position of the anti-string follows accordingly; see Fig. 2.1. As the parton hops, the string length attached to that parton can either increase or decrease, which depends on the direction of hopping and from which side the parton connects to a string. The anti-string corresponding to that particular parton changes accordingly: it decreases in case the string length on the other side of the parton increases, or the anti-string length increases in cases the string length decreases. In the string length basis this means that when a parton l residing on x_l hops to the right, $x_l \rightarrow x_l + 1$, the two bosonic string occupations change as $\tilde{\ell}_l \rightarrow \tilde{\ell}_l + 1$ and $\tilde{\ell}_{l+1} \rightarrow \tilde{\ell}_{l+1} - 1$ as the neighboring partons remain on their same respective sites that is: x_{l-1} and x_{l+1} . Similar thing happens when the parton hops in a different direction. The hopping term in the new basis is simply a change of neighbouring bosonic number occupations by one, and as a result there are no Bose-enhancement terms as only one single Boson is allowed to hop [1]. The hopping term thus reads as $(\hat{\rho}_m^{-1/2} \hat{\Psi}_m^\dagger \hat{\Psi}_l \hat{\rho}_l^{-1/2} + \text{H.c.})$ [1].

The \mathbb{Z}_2 electric field term has to introduce the energy associated with the strings and anti-strings, which represent the orientation of the electric fields. From our construction we see that $\tilde{\ell}_l$, where the index is odd, $l \in 2k + 1, k \in \mathbb{Z}$, represents anti-strings and $\tilde{\ell}_l$, where the index is even, $l \in 2k, k \in \mathbb{Z}$, represents strings. Thus, the \mathbb{Z}_2 electric field term is simply a term proportional to the staggered on-site number value $\propto h(-1)^l \hat{\rho}_l$.

The mapping to the string-length basis is non-local, however the \mathbb{Z}_2 LGT Hamiltonian in the new basis, Eq. (2.31), is completely local [1].

2.4.3 Confinement in the string-length basis

Finally, we can consider confinement in the new non-local basis. For that we return to the \mathbb{Z}_2 gauge invariant Green's function, Eq. (2.12). For practical reasons we again write the gauge invariant Green's function operator explicitly as [1, 160]

$$\hat{\mathcal{G}}(i - j) = \hat{a}_i^\dagger \left(\prod_{i \leq \ell < j} \hat{\tau}_{\ell, \ell+1}^z \right) \hat{a}_j. \quad (2.33)$$

In the string language such operator becomes highly non local [1]. Since a parton is removed at site j and added at site i this means, due to the Gauss law, that the identity of

all strings has to be changed to anti-strings between sites i and j , and vice-versa, the anti-strings need to be changed to strings. This is the action of the operator Eq. (2.33) in the usual basis.

By taking a closer look at what happens with the strings and anti-strings, we can first note that the added parton at site i will either break a string or anti-string running through site i as the aligned electric fields across i have to become anti-aligned due to the Gauss law constraint Eq. (2.4), i.e. $\langle \hat{\tau}_{i-1,i}^x \hat{\tau}_{i,i+1}^x \rangle = 1 \rightarrow \langle \hat{\tau}_{i-1,i}^x \hat{\tau}_{i,i+1}^x \rangle = -1$. Let us define the site where the closest parton to the left of j resides on with x_{l-1} . The closest site with a parton to the right of the site j (before applying the Green's function operator) is thus x_l . The single bosonic string-length number $\tilde{\ell}_l = x_l - x_{l-1} - 1$ is divided into two new string length sites after the application of the Green's function operator, Eq. (2.33), with the new states being $\tilde{\ell}_L = i - x_{l-1} - 1$ and $\tilde{\ell}_R = x_l - i - 1$. Opposite thing happens at site j where the particle gets removed: we can defined x_{u-1} as the lattice site with a closest parton to the left of site j , and x_{u+1} with the site with a closest parton on the right side of j . Since in the usual notation $j = x_u$ the two bosonic string-length numbers $\tilde{\ell}_u = j - x_{u-1} - 1$ and $\tilde{\ell}_{u+1} = x_{u+1} - x_u - 1$ "merge" into one single site $\tilde{\ell}_{\tilde{u}} = x_{u+1} - x_{u-1} - 1$, after the application of the Green's function operator, Eq. (2.33).

We thus see that by adding a particle we divide the bosonic site $\tilde{\ell}_l$ into $\tilde{\ell}_L$ and $\tilde{\ell}_R$, whereas $\tilde{\ell}_u$ and $\tilde{\ell}_{u+1}$ merges into $\tilde{\ell}_{\tilde{u}}$. To be more precise, by keeping the correct labeling of partons as defined in Eq. (2.29) from the left to the right, we have to change the label of some partons accordingly. We have to relabel $x_l = i$, as the added parton at i in fact becomes the closest parton following the one at x_{l-1} . In addition, every following label becomes $x_m \rightarrow x_{m+1}$ until we reach u where the last relabeling happens only for $x_{u-1} \rightarrow x_u$, whereas the label of the next $(u+1)$ -th parton remains the same $x_{u+1} = x_{u+1}$. To summarize, the following relabeling takes place after applying operator in Eq. (2.33)

$$\begin{aligned}
 x_{l-1} &= x_{l-1}, \\
 i &\rightarrow x_l, \\
 x_m &\rightarrow x_{m+1}, \quad l \leq m < u \\
 x_{u+1} &= x_{u+1}.
 \end{aligned} \tag{2.34}$$

As a consequence of this relabeling we also have to relabel the new string-length bosonic numbers according to the definition in Eq. (2.29). On the one hand, we first note that we have to relabel $\tilde{\ell}_l = \tilde{\ell}_L$, $\tilde{\ell}_{l+1} = \tilde{\ell}_R$, and $\tilde{\ell}_{u+1} = \tilde{\ell}_{\tilde{u}}$, which are also the string-length occupation numbers that actually changed. On the other hand, all other bosonic string-length numbers m between $l+1$ and u are simply relabeled as $\tilde{\ell}_m \rightarrow \tilde{\ell}_{m+1}$. This can be again summarized

as [1]

$$\begin{aligned}
\tilde{\ell}_{l-1} &= \tilde{\ell}_{l-1}, \\
\tilde{\ell}_L &\rightarrow \tilde{\ell}_l, \\
\tilde{\ell}_R &\rightarrow \tilde{\ell}_{l+1}, \\
\tilde{\ell}_m &\rightarrow \tilde{\ell}_{m+1} \quad l+1 \leq m < u \\
\tilde{\ell}_{\bar{u}} &\rightarrow \tilde{\ell}_{u+1} \\
\tilde{\ell}_{u+2} &= \tilde{\ell}_{u+2}.
\end{aligned} \tag{2.35}$$

The most significant effect of the Green's function is that it shifts the bosonic string-length occupation numbers by one, $\tilde{\ell}_m \rightarrow \tilde{\ell}_{m+1}$, where we can also parameterize the range of m as $\tilde{x}_1 < m < \tilde{x}_2$, if we define $\tilde{x}_2 - \tilde{x}_1 = \tilde{x}$ [1]. Furthermore, for long wavelengths the distance in the usual lattice x , is related to the distance in the string-length basis as $\tilde{x} = n^a x$ [1]. We can thus write the Green's function in the string-length basis as [1]

$$\langle \hat{\mathcal{G}}(x) \rangle \simeq \langle \hat{T}(0, \tilde{x}) \rangle \tag{2.36}$$

where \hat{T} is the partial translation operator, which cyclically shifts all strings occupation by one unit between \tilde{x}_1 and \tilde{x}_2 [1]

$$\hat{T}(\tilde{x}_1, \tilde{x}_2) \left| \dots \hat{\ell}_{\tilde{x}_1-1} \hat{\ell}_{\tilde{x}_1} \dots \hat{\ell}_{\tilde{x}_2-1} \hat{\ell}_{\tilde{x}_2} \hat{\ell}_{\tilde{x}_2+1} \dots \right\rangle = \left| \dots \hat{\ell}_{\tilde{x}_1-1} \hat{\ell}_{\tilde{x}_2} \hat{\ell}_{\tilde{x}_1} \dots \hat{\ell}_{\tilde{x}_2-1} \hat{\ell}_{\tilde{x}_2+1} \dots \right\rangle. \tag{2.37}$$

By ignoring the change of local strings around \tilde{x}_1 and \tilde{x}_2 , which we already discussed in detail above, we can directly relate the Green's function Eq. (2.33) to the operation of translations. In other words: by considering the Green's function in the original basis we in fact probe the translational invariance in the string-length basis [1]. If the translation symmetry $\tilde{x} \rightarrow \tilde{x} + 1$ is broken, explicitly or spontaneously, the operator \hat{T} will decay exponentially and the partons will confine in the original \mathbb{Z}_2 LGT basis [1]

$$\langle \hat{\mathcal{G}}(x) \rangle \simeq \langle \hat{T}(0, \tilde{x}) \rangle \simeq e^{\tilde{\kappa} \tilde{x}} \simeq e^{\tilde{\kappa} n^a x}. \tag{2.38}$$

Here we parameterize the exponential decay with an inverse correlation length $\tilde{\kappa}$ [1].

The above argument shows why the \mathbb{Z}_2 LGT Eq. (2.33) is confining for any non-zero value of the electric field term, $h \neq 0$. That is because in the string-length basis, the \mathbb{Z}_2 electric field term explicitly breaks the translational symmetry as it introduces a staggered on-site potential energy $-h \sum_l (-1)^l \hat{\rho}_l$ [1]. The connection of confinement in the \mathbb{Z}_2 LGT to the translational-symmetry breaking in the non-local string-length basis has far wider consequences, since any term that explicitly breaks the translational symmetry will result in confinement as already stated above. As an example we can mention that a random $h_{\langle i,j \rangle}$ would also induce confinement. Moreover, spontaneously symmetry breaking in the case when $h = 0$, which arises due to some other interactions in the Hamiltonian that can be added, can result in a Mott insulating state [1].

2.4.4 Field-theory analysis of the string-length basis

To clarify the nature of the explicitly broken translational symmetry in the string-length basis, we consider a simple field-theory analysis of the \mathbb{Z}_2 LGT Hamiltonian. As discussed in Section 2.4.1, due to the non-local nature of the original Hamiltonian after integrating out the gauge fields, Eq. (2.26), naive bosonization does not yield confinement as the electric field term turns out to be RG irrelevant [1]. Since the Hamiltonian in the string-length basis is completely local, we can apply standard field-theory arguments [1]. We can thus consider the density-density correlations and apply the Luttinger-liquid theory, which yields [1]

$$\langle \delta\hat{\rho}(\tilde{x})\delta\hat{\rho}(0) \rangle \simeq \frac{\tilde{K}}{2\pi^2} \frac{1}{\tilde{x}^2} + \frac{(\rho^\Psi)^2}{2} \left(\frac{\tilde{\alpha}}{\tilde{x}} \right)^{2\tilde{K}} \cos(2\pi\rho^\Psi\tilde{x}) + \dots, \quad (2.39)$$

where \tilde{K} is the Luttinger liquid parameter in the string-length basis. Here we consider "local density fluctuations", which we defined as $\delta\hat{\rho}(\tilde{x}) = \hat{\rho}(\tilde{x}) - \rho^\Psi$. Furthermore, we can relate the string-length basis and the original basis.

In the original basis we can define $\delta\hat{n}(x) = \hat{n}(x) - n^a$. For short wavelengths, we can approximate $\hat{n}(x) \approx \Delta\hat{N}_a/\Delta x$, where we $\Delta\hat{N}_a$ is the number of particles per coarse-grained distance Δx [1]. In the string-length basis coarse grained density can be written in terms of $\hat{\rho}(\tilde{x}) \approx \Delta\hat{\ell}/\delta\tilde{x}$, where $\Delta\hat{\ell}$ is the total number of bosonic string-length numbers on coarse grained distance $\Delta\tilde{x}$. By taking into account the definition Eq. (2.29), this can be expressed as [1]

$$\Delta\hat{\ell} = \sum_{l \in \Delta\tilde{x}} \tilde{\ell}_l = x_{l_0} - x_{l_0-1} - 1 + \dots + x_{l+1} - x_l - 1 \dots + x_{l_0+\tilde{x}} - x_{l_0+\tilde{x}-1} - 1 = \Delta\hat{x} - \Delta\tilde{x}, \quad (2.40)$$

and we can therefore express the density in the string-length basis as $\hat{\rho}(\tilde{x}) \approx (\Delta\hat{x} - \Delta\tilde{x})/\Delta\tilde{x}$ [1]. The relation between the coarse grained densities in both basis is thus [1]

$$\hat{n}(x) \approx \{1 + \hat{\rho}[\tilde{x}(x)]\}. \quad (2.41)$$

With the above connection we can directly use the result Eq. (2.39) and make prediction for the density-density correlations in the original basis [1].

By considering the Luttinger-liquid theory and comparing expressions for compressibilities, we can also derive a connection between the Luttinger liquid parameter in both basis [1]

$$K = (n^a)^2 \tilde{K}, \quad (2.42)$$

where K is the Luttinger liquid parameter in the original basis. That is because the original Hamiltonian Eq. (2.1) remains gapless for any value of h [160]. By considering the strong limit where $h \gg t$, the second order perturbation calculations show that the Luttinger liquid parameter approaches $K = 8/9$ [1]. This yield $\tilde{K} = 2 > 1$ [1]. Since the density-density correlations in the string-length basis take the form Eq. (2.39) for generic h , this means that in the confined regime the string-length basis exhibits hidden off-diagonal quasi-long range order (HODQLRO) [1]; see Fig. 2.6.

2.5 Summary of the confinement problem

In this chapter we studied the confinement problem in the $1 + 1\text{D } \mathbb{Z}_2$ LGT. We introduced confinement as a phenomena where individual partons bind into pairs, forming dimer states, which we denote as mesons. Mesons in turn remain dynamical. The partons forming these mesons are connected with a string of electric fields with the same orientation. To offer an intuitive understanding of confinement, we first considered a simple limit where matter dynamics is frozen $t = 0$ and confinement arises due to a linear confinement potential, proportion to the \mathbb{Z}_2 electric field term h .

Next, we discussed various probes of confinement. The gauge invariant Green's function exhibits exponential decay in the confined regime, in contrast to a simple algebraic decay in the deconfined regime. In addition, the period of Friedel oscillations doubles in the confined regime at the same lattice filling in comparison to the deconfined regime. By numerical calculations, this was shown for any non-zero electric-field term $h \neq 0$ [160]. We also studied string and anti-string length distributions, which can be obtained from multiple snapshots of the systems. In our case we acquire snapshots by sampling from MPS, obtained from ground state calculations using DMRG. However, similar snapshots could be easily measured in quantum simulation experiments with cold atoms. With our calculations we showed that a bimodal distribution of string and anti-string lengths is a robust measure of confinement, readily accessible in cold atom experiments.

We proceeded with a section dedicated to solving the confinement problem. We first discussed why the naive bosonization does not explain the confinement in the original basis after integrating out the gauge degrees of freedom by using the Gauss law. We then introduce the string-length basis where, via a non-local basis transformation, we obtain a purely local Hamiltonian. There the string lengths become the new bosonic Fock states. By relating the Green's function to the translation operator in the new basis, we demonstrate that symmetry breaking in the new string-length basis results in confinement in the original \mathbb{Z}_2 LGT. The \mathbb{Z}_2 electric field term breaks this symmetry explicitly. We thus provided a general solution of the confinement problem in a class of $1 + 1\text{D } \mathbb{Z}_2$ lattice gauge theories with dynamical matter [1].

Chapter 3

Phase diagrams of 1+1D \mathbb{Z}_2 lattice gauge theories with dynamical $U(1)$ matter

In this chapter we study phase diagrams of the 1 + 1D \mathbb{Z}_2 lattice gauge theory with dynamical $U(1)$ matter in the ground state at different chain fillings. The motivation to study the phase diagrams comes from the potential realization of the 1 + 1D \mathbb{Z}_2 LGT in cold atom experiments. We are thus interested in what kind of rich physics can the paradigmatic \mathbb{Z}_2 LGT exhibit when the gauge fields are coupled to $U(1)$ conserving matter. Moreover, we study how this physics could be realistically probed in quantum simulation setups, by considering probes that could be used in experiments.

We first discuss the Luttinger liquids, which are formed in the confined and deconfined regime when the global parton number is conserved. Next, we include a nearest-neighbor (NN) repulsion between individual partons in addition to the hopping term, where matter is minimally coupled to the gauge field, and the \mathbb{Z}_2 electric field term. With this additional term, we obtain rich phase diagrams at two thirds filling $n = 2/3$ and at half-filling $n = 1/2$, which we discuss in two separate sections.

The section on the two-thirds filling is based on Ref. [1], and the section on the phase diagram at half-filling is based on Ref. [3]. In both cases the content, including figures, has been adapted and extended. We note that some of the numerical results related to Ref. [1] have already been obtained in the author's master thesis Ref. [2], which we label appropriately.

3.1 Introduction

In the previous chapter we studied confinement, which arises in the one-dimensional \mathbb{Z}_2 LGT coupled to dynamical matter. We saw how individual partons become confined into mesons, which remain dynamical. Since we consider a one-dimensional system, where the global particle number is conserved, a standard way of describing it is to consider the

Luttinger liquid (LL) theory [182].

In the regime where the \mathbb{Z}_2 electric field term is absent, the system is non-interacting and partons are essentially free. When partons become confined, that is when the \mathbb{Z}_2 electric field term is non zero, mesons become the relevant constituents of the system as seen from the Friedel oscillations, and a LL description becomes more complicated [1, 160]. However, in the regime when the confining \mathbb{Z}_2 electric field term is very strong, mesons can be considered as new hard-core bosons, which form their own meson Luttinger liquid.

By including a simple NN repulsion among partons, the aforementioned Luttinger liquids at half-filling and at two-thirds filling can undergo a transition to symmetry broken Mott states. To study these regimes at different fillings we employ DMRG [35, 153–155]. We also study different limits of our system analytically and use the LL theory where applicable.

When partons are confined into mesons, a NN repulsion term can stabilize a meson Mott state when the lattice filling equals to two-thirds. There, every single meson is followed by one empty lattice site. To achieve such Mott state, both interactions have to work together: the \mathbb{Z}_2 electric field has to confine the partons into mesons, and the NN repulsion has to ensure that mesons keep one lattice site distance between each other. We reveal this state by considering the meson charge gap.

At half-filling the case is different. A strong enough NN repulsion among partons stabilizes a parton Mott state, where every parton is followed by one empty lattice site. However, when the \mathbb{Z}_2 electric field term is included, this state is destroyed as partons tend to confine into mesons. On the interface, when the two interactions are of similar strength, the state becomes frustrated. This results in strong fluctuations of the meson size, and partons appear as if they were deconfined on short length scales. On longer length scales they remain confined. This behaviour is revealed in the Green's function behaviour. To study the Mott state we calculate the charge gap and consider a static structure factor, which is an experimentally feasible probe of confinement.

By mapping out these phase diagrams we pave the way for future quantum simulation experiments. There, the global particle number conservation is usually directly encoded in the setup, and thus a \mathbb{Z}_2 LGT with U(1) matter could be studied.

3.2 Confined and deconfined Luttinger liquid

We first discuss the phases of matter for generic fillings formed by the 1 + 1D \mathbb{Z}_2 lattice gauge theory with the U(1) conserving matter. Here we define the \mathbb{Z}_2 LGT again for convenience as [1, 3, 5, 160]

$$\hat{\mathcal{H}} = -t \sum_j \left(\hat{a}_j^\dagger \hat{\tau}_{(j,j+1)}^z \hat{a}_{j+1} + \text{H.c.} \right) - h \sum_j \hat{\tau}_{(j,j+1)}^x. \quad (3.1)$$

This \mathbb{Z}_2 LGT forms two distinct Luttinger liquids in the deconfined and confined regimes due to the global parton (meson) number conservation [1, 160].

We will first show that in the deconfined regime where $h = 0$, the system reduces to

free partons, which we denote as the deconfined parton Luttinger liquid (LL). In the second limit, we will consider the strong electric field limit $h \gg t$, and show that in the limit when the partons are tightly confined, mesons form a confined Luttinger liquid [160].

3.2.1 Free partons

As we have already shown in Section 2.4.1, by using the dressed parton formulation Eq. (2.20), we can eliminate the gauge field and obtain a simple free parton Hamiltonian for the case when $h = 0$, which we once again write as

$$\hat{\mathcal{H}}_t = -t \sum_j \left(\hat{b}_j^\dagger \hat{b}_{j+1} + \text{H.c.} \right). \quad (3.2)$$

Free partons in a one-dimensional chain form a gapless Luttinger liquid where the long-distance density-density correlations decay with a power law, and the Luttinger liquid parameter is simply $K = 1$ [182]. For generic fillings the system remains a LL even by including nearest-neighbor interactions of the form [182]

$$\hat{\mathcal{H}}_{\text{NN}} = V \sum_j \hat{n}_j^b \hat{n}_{j+1}^b, \quad (3.3)$$

where $\hat{n}_j^b = \hat{b}_j^\dagger \hat{b}_j = \hat{a}_j^\dagger \hat{a}_j = \hat{n}_j$, since $(\hat{\tau}^z)^2 = I$; see Section 2.4.1 for details. However, with the inclusion of NN interactions the Luttinger liquid parameter K is modified [182]. The value of K decreases for repulsive interaction $V > 0$ and is thus $K < 1$. For attractive NN interactions $V < 0$, however, the value of K increases $K > 1$.

The only exception to this Luttinger liquid behaviour is at half-filling $n^b = 0.5$, where for $V > 2t$ the system forms a simple Mott insulating state, with non-zero charge gap [182]. In such a state, partons are arranged in a lattice in a way that every occupied lattice site is followed by one vacant lattice site ([...1, 0, 1, 0, ...]).

The free parton model with NN interactions can in fact be mapped to a XXZ spin-1/2 chain and solved via the Bethe ansatz [182], see also Appendix A. There, the Mott state at $n = 1/2$ corresponds to the symmetry breaking AFM phase [182].

3.2.2 Confined mesons

We can now consider the limit where $h \gg t$, which results in tightly confined mesons. In Borla et al. in Ref. [160] they first studied this regime by considering hopping as small perturbation and developed an effective Hamiltonian for the mesons from second order perturbation calculations. We also note that this regime was already mentioned in Section 2.2. For convenience we repeat some of the main points and expand the discussion in terms of a transition from a LL to a Mott state.

To understand this mapping, we can start again in the classical limit where $t = 0$, and thus for $h > 0$, the ground state is formed of partons tightly confined into dimers of length $\ell = 1$. Since mesons are tightly confined when $t = 0$ and $h > 0$, we define hard-core bosonic

operators as [3, 160]

$$\hat{d}_j^\dagger = \hat{a}_j^\dagger \hat{\tau}_{\langle j, j+1 \rangle}^z \hat{a}_j^\dagger, \quad \hat{d}_j = \hat{a}_j \hat{\tau}_{\langle j, j+1 \rangle}^z \hat{a}_j. \quad (3.4)$$

By including the hopping term as a perturbation $t \ll h$, we obtain a hard-core bosonic model with NN interactions, where the new hard-core bosons are in fact mesons [3, 160]

$$\hat{\mathcal{H}}_d = -t^d \sum_{\langle i, j \rangle} \left(\hat{d}_i^\dagger \hat{d}_j + \text{H.c.} \right) + \tilde{V} \sum_{\langle i, j \rangle} \hat{n}_i^d \hat{n}_j^d, \quad (3.5)$$

where we defined $\hat{n}_j^d = \hat{d}_j^\dagger \hat{d}_j$. The lattice sites are also redefined as one meson is defined on a single site j , and therefore the number of total lattice sites is reduced by the number of partons $N^d = N/2$ to $L^d = L - N/2$. The meson density is thus defined as $n^d = \frac{N/2}{L - N/2}$ and is connected to the parton density as [3, 160]

$$n^d = \frac{1}{\frac{2}{n} - 1}. \quad (3.6)$$

All of the terms in the effective mesonic model in Eq. (3.5) come from second order perturbation theory [160]. We can first consider a tightly confined dimer where the partons sit next to each other, e.g., on site $j - 1$ and j . They are connected by a single string on the link $\langle j - 1, j \rangle$. By including $t \ll h$, one of the partons can hop to a lattice site away from their partner, as an example we can consider the parton on site j hopping to site $j + 1$. The energy of such an "extended" dimer increases by $\Delta E = 2h$, as the anti-string on link $\langle j, j + 1 \rangle$ becomes a string due to the Gauss law constraint, $\langle \hat{\tau}_{\langle j, j+1 \rangle}^x \rangle = +1 \rightarrow \langle \hat{\tau}_{\langle j, j+1 \rangle}^x \rangle = -1$. Since this process involves an energetically highly unfavorable state, the extended string has to be reduced in the next step. This can be achieved in two ways; see also Fig. 2.2.

In the first case, the other parton on site $j - 1$ hops to site j . In this case, the string-length is again reduced to $\ell = 1$, however the two partons now reside on sites j and $j + 1$ and have thus moved together by one lattice site to the right. This process thus explains the second-order mechanism, which results in the hopping of mesons in Eq. (3.5), and the corresponding amplitude is $t^d = t^2 / (2h)$ [160].

In the second case, the same parton that has hopped first from site j to $j + 1$, hops back to site j , in which case the final state is exactly the same as in the beginning with the two confined partons residing on sites $j - 1$ and j . Such processes are not possible when two mesons are NN, which results in the NN repulsion in Eq. (3.5), where $V^d = 2t^d = t^2/h$ [160]. The factor "2" in $V^d = 2t^d$ comes from both NN mesons being unable to undergo such fluctuation.

In the limit of tightly confined mesons $h \gg t$, we thus obtain an effective hard-core boson model with NN repulsion, where we consider mesons as the new hard-core bosons. As already mentioned before, such models can be mapped to a XXZ chain and form a Luttinger liquid for generic parameter values [1, 160, 182]. The only exception is at half-filling, where a NN repulsion $V > 2t$ results in a gapped Mott insulating state [182]. However, in the effective model, Eq. (3.5), the parameter ratios are fixed at $V^d = 2t^d$ when $h \gg t$. The perturbative calculations therefore suggest that the system is exactly at the transition point

to the Mott state when $n^d = 0.5$, i.e., when the parton filling is at two-thirds, $n = 2/3$.

We thus see that the confined mesons at $h \neq 0$ form a special *meson* Luttinger liquid in the 1 + 1D \mathbb{Z}_2 LGT Hamiltonian, Eq. (3.1), when the parton number is conserved, i.e., there is a global $U(1)$ symmetry in the matter [1, 3, 160]. Furthermore, for high value of the electric-field term $h \gg t$, mesons can be described by a simple hard-core meson model with a NN repulsion [160].

3.3 Phase diagram at two-thirds filling

We will now study the phase diagram of the 1 + 1D \mathbb{Z}_2 LGT coupled to $U(1)$ matter, at two-thirds filling $n = 2/3$ [1]. The section is based on Ref. [1]. As already discussed in Section 3.2.2 in the limit when $h \gg t$, the second order perturbation theory suggest that the mesons form a Luttinger liquid, which is right at the transition point to the Mott insulating state at $n = 2/3$ [160]. We thus consider a version of the paradigmatic 1 + 1D \mathbb{Z}_2 LGT with additional NN repulsive interactions between partons [1, 3]

$$\hat{\mathcal{H}} = -t \sum_j \left(\hat{a}_j^\dagger \hat{\tau}_{\langle j, j+1 \rangle}^z \hat{a}_{j+1} + \text{H.c.} \right) - h \sum_j \hat{\tau}_{\langle j, j+1 \rangle}^x + V \sum_j \hat{n}_j \hat{n}_{j+1}, \quad (3.7)$$

where $V \geq 0$.

3.3.1 Analytical limits at two-thirds filling

Tightly confined meson limit

By considering the limit $h \gg t, V$, discussed in Section 3.2.2, we can simply add the NN repulsion to the hard-core meson model [1, 3]

$$\hat{\mathcal{H}}_d = -t^d \sum_{\langle i, j \rangle} \left(\hat{a}_i^\dagger \hat{a}_j + \text{H.c.} \right) + (\tilde{V} + V) \sum_{\langle i, j \rangle} \hat{n}_i^d \hat{n}_j^d, \quad (3.8)$$

where we implicitly ignore the repulsion V between the NN partons within the meson, as we assume $h \gg V$. Considering the Luttinger liquid arguments from the mapping to the XXZ chain, which states that the transition to the Mott state occurs for $V^d > 2t^d$, we thus see that any non-zero NN repulsion, $V > 0$, will result in a meson Mott state [1, 182].

Infinite NN repulsion limit

The other limit, which we consider is the case when $V \gg t, h$. A detailed consideration of this limit can be found in the Supplemental materials of Ref. [1], here we just sketch the main considerations.

We can start by considering the particle-hole mapping of the original Hamiltonian

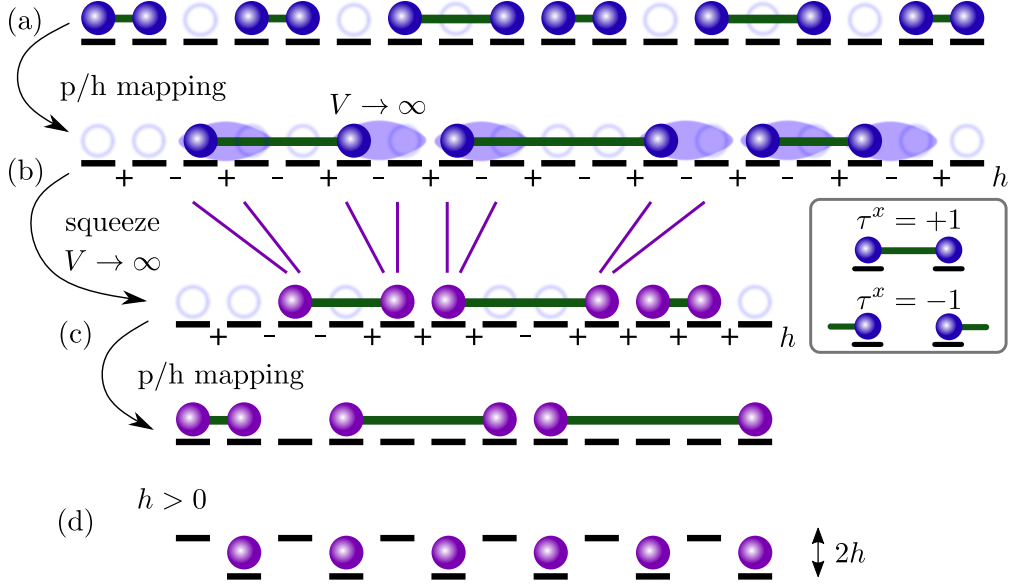


Figure 3.1: Steps in obtaining the $V \rightarrow \infty$ limit of the \mathbb{Z}_2 LGT coupled to matter at two-thirds filling $n = 2/3$. (a) Demonstration of the particle-hole transformation of the original \mathbb{Z}_2 LGT Hamiltonian. (b) Squeeze of a single hole and a consecutive lattice site that has to always remain empty when $V \rightarrow \infty$. (c) Second particle-hole mapping, which brings us back to the matter picture. (d) A translational symmetry breaking gap emerging as $h > 0$. This figure was modified from Fig. S8 in the Supplementary material of Ref. [1].

Eq. (3.1) that can be expressed as [1, 2]

$$\hat{\mathcal{H}}^h = -t \sum_j \left(\hat{h}_j^\dagger \hat{\tau}_{(j,j+1)}^z \hat{h}_{j+1} + \text{H.c.} \right) - h \sum_j (-1)^j \hat{\tau}_{(j,j+1)}^x + V \sum_j \hat{n}_j^h \hat{n}_{j+1}^h, \quad (3.9)$$

where \hat{h}_j^\dagger (\hat{h}_j) is a hole creation (annihilation) operator that arises from the particle-hole mapping $\hat{a}^\dagger \rightarrow \hat{h}, \hat{a} \rightarrow \hat{h}^\dagger$, and $\hat{n}_j^h = 1 - \hat{n}_j$ is the hole on-site number operator [1, 2, 121]. Furthermore, in order to obtain the correct form of the Gauss law, we have to perform a mapping on the links as well: $\hat{\tau}_{j,j+1}^x \rightarrow (-1)^j \hat{\tau}_{j,j+1}^x$ and $\hat{\tau}_{j,j+1}^y \rightarrow (-1)^j \hat{\tau}_{j,j+1}^y$ [1, 2].

By considering the limit $V \rightarrow \infty$ in the particle-hole transformed picture, we can effectively assume that no parton can have an additional empty lattice site to their right side [1]. We thus assume that every hole spans over two lattice sites, see Fig. 3.1. As a result, the effective lattice filling is rewritten as $n' = \frac{N^h}{L - N^h}$, and the chain length reduces by the number of holes N^h [1]. Due to this construction, we also have to shift the electric field staggering across lattice sites occupied by a hole [1]

$$-h \sum_{j=1}^N (-1)^j \hat{\tau}_{(j,j+1)}^x \rightarrow -h \sum_{j=1}^{L-N^h} (-1)^j \left(\prod_{i \leq j} (-1)^{\hat{n}_i^h} \right) \hat{\tau}_{(j,j+1)}^x. \quad (3.10)$$

Furthermore, every meson still carries an electric field energy that we have to take into

account. We thus have to add the following term [1]

$$-h \sum_{j=1}^{L-N} (-1)^j \left(\prod_{i<j} (-1)^{\hat{n}_i} \right) \hat{\tau}_{\langle j,j+1 \rangle}^x \hat{n}_j. \quad (3.11)$$

The resulting Hamiltonian in the limit when $V \rightarrow \infty$ can be expressed as [1]

$$\begin{aligned} \hat{\mathcal{H}}'_h = & -t \sum_j \left(\hat{h}_j^\dagger \hat{\tau}_{\langle j,j+1 \rangle}^z \hat{h}_{j+1} + \text{H.c.} \right) - h \sum_j (-1)^j \left(\prod_{i \leq j} (-1)^{\hat{n}_i^h} \right) \hat{\tau}_{\langle i,i+1 \rangle}^x \\ & - h \sum_j (-1)^j \left(\prod_{i < j} (-1)^{\hat{n}_i^h} \right) \hat{\tau}_{\langle i,i+1 \rangle}^x \hat{n}_j^h. \end{aligned} \quad (3.12)$$

By performing a second particle-hole transformation back to the particle picture, we express the \mathbb{Z}_2 LGT in the limit when $V \rightarrow \infty$ after some simple algebra as [1]

$$\begin{aligned} \hat{\mathcal{H}}' = & -t \sum_j \left(\hat{a}_j^\dagger \hat{\tau}_{\langle j,j+1 \rangle}^z \hat{a}_{j+1} + \text{H.c.} \right) - h \sum_j (-1)^j \left(\prod_{i \leq j} (-1)^{\hat{n}_i} \right) \hat{\tau}_{\langle j,j+1 \rangle}^x \\ & + h \sum_j (-1)^j \left(\prod_{i < j} (-1)^{\hat{n}_i} \right) \hat{\tau}_{\langle j,j+1 \rangle}^x (1 - \hat{n}_j). \end{aligned} \quad (3.13)$$

The field terms can be further simplified by taking into account the Gauss law constraint, Eq. (2.25), which gives us [1]

$$\hat{\mathcal{H}}' = -t \sum_j \left(\hat{a}_j^\dagger \hat{\tau}_{\langle j,j+1 \rangle}^z \hat{a}_j + \text{H.c.} \right) - h \sum_j (-1)^j \hat{n}_j. \quad (3.14)$$

Finally, we can simplify the expression by eliminating the gauge fields, and using the trick in Eq. (2.21) to obtain the final expression [1]

$$\hat{\mathcal{H}}' = -t \sum_j \left(\hat{b}_j^\dagger \hat{b}_j + \text{H.c.} \right) - h \sum_j (-1)^j \hat{n}_j^b, \quad (3.15)$$

where $\hat{n}_j^b = \hat{b}_j^\dagger \hat{b}_j$.

The main result of this mapping is that we obtain a band insulator with a gap $\Delta = 2h$, for $h > 0$, in the limit when $V \rightarrow \infty$ at parton filling $n = 2/3$, which translates to meson filling of $n' = 1/2$ [1]. We have therefore shown that the limit $V \gg t, h$ also results in a meson Mott state.

3.3.2 Charge gap at two-thirds filling

From the analytical limits, we see that the Mott state at two-thirds filling $n = 2/3$ appears when both parameters h and V are non-zero and one of them is very large relative to the hopping amplitude t . To study this Mott state for generic parameter values, we consider numerical calculations using DMRG [34, 35]. We note that the numerical results presented

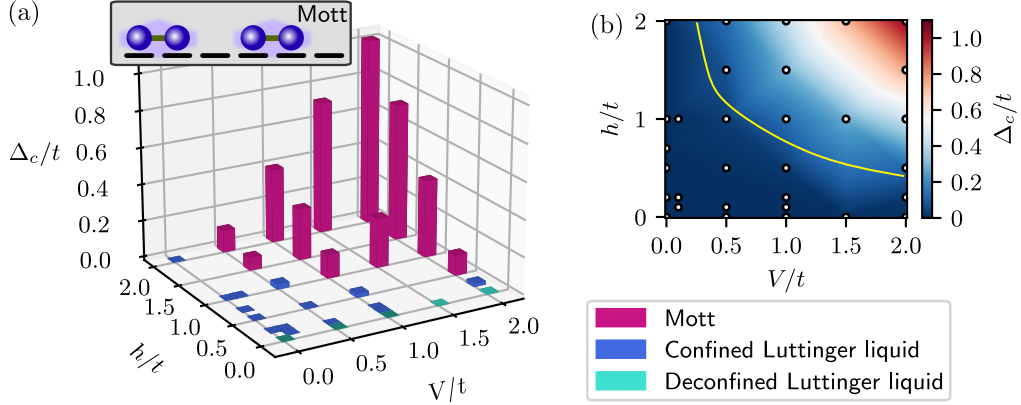


Figure 3.2: The charge gap, Eq. (3.16), extrapolated in the thermodynamic limit for the 1 + 1D \mathbb{Z}_2 LGT with NN interactions, Eq. (3.7), after eliminating matter via the Gauss law. (a) The values where the charge gap exceeds $\Delta_c/t > 0.05$ are labeled with violet and denote a meson Mott insulator regime, sketched in the inset. Blue color denotes vanishing charge gap $\Delta_c/t \leq 0.05$, where dark blue denotes the gapless, confined, meson Luttinger liquid, and the light blue denotes the deconfined, free parton Luttinger liquid. (b) The heat map of the same results as in (a) where we draw an approximate boundary (yellow line) between the Mott state and gapless regime by hand. The figure is modified from Fig. 2 in Ref. [1], and the inset sketch is modified from Fig. 1 in Ref. [1]. These numerical results have already been obtained and presented in Ref. [2]

here have already been obtained during the author's Master thesis, Ref. [2]. In order to connect them to the previous analytical results, and to provide a broad overview we present them here as well.

In order to probe the phase diagram, in particular the Mott phase, we consider the meson charge gap, which we define as [1–3]

$$\Delta_c(L, N) = \frac{1}{2} \left[\left(E_{N+2}^L - E_N^L \right) - \left(E_N^L - E_{N-2}^L \right) \right]. \quad (3.16)$$

Here, we denote the ground state energy E_N^L , for a system with total number of particles N , in a chain with length L . The charge gap in this case is specifically designed to probe the gap of adding/removing a meson, i.e. a pair of partons, hence $E_{N\pm 2}^L$ in Eq. 3.16 [1–3]. This is to ensure that we consider the case with even parton numbers and thus no partons become stuck to the boundaries of the lattice, when $h \neq 0$ [3].

In order to calculate the charge gap defined in Eq. (3.16) with DMRG, we calculate the ground state values E_N^L and $E_{N\pm 2}^L$, where $n = N/L = 2/3$, for multiple chain lengths L . We then extrapolate the value of the charge gap Δ_c in the thermodynamic limit, $L \rightarrow \infty$, by fitting the data Δ_c as a function of the inverse system length $1/L$ [1, 2]. We use a quadratic function, which gives us excellent fit results, and extract the value of the fitting function at $x = 1/L = 0$; see Fig. 3.3(a) [1, 2]. We note that since we integrate out matter degrees of freedom via Gauss law and simulate the pure spin model, we have to tune the

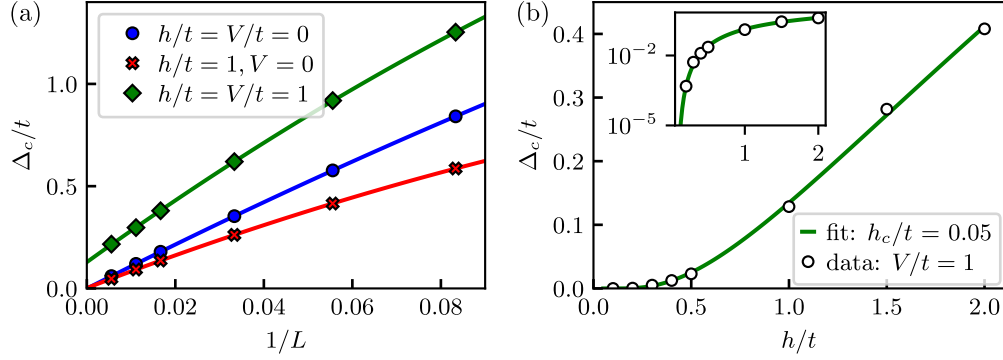


Figure 3.3: Details on the numerical calculations of the charge gap, Δ_c . (a) Example of extrapolations in the thermodynamic limit by plotting the charge gap $\Delta_c(N, L)$ as a function of the inverse chain length $1/L$, and fitting the data with a quadratic function to extrapolate the value at $L \rightarrow \infty$. In every case the ratio was fixed to $n = N/L = 2/3$. (b) Charge gap in the thermodynamic limit Δ_c , as a function of the electric field h , for constant NN repulsion $V/t = 1$. The green line represents the fit with Eq. (3.17), where the transition value was determined manually and fixed to $h_c/t = 0.05$. The figure is modified from Fig. S7 in the supplementary material of Ref. [1]. These numerical results have already been obtained and presented in Ref. [2]

correct chemical potential μ in order to control the filling n ; see Section 1.3.2. The chemical potential term contribution to the overall energy has to be subtracted when computing the ground state energy; see also details in Ref. [1, 2].

The charge gap results, extrapolated to the thermodynamic limit Δ_C , for generic parameter values h and V are presented in Fig. 3.2. We see that the value of the charge gap increases with increasing h and V , meaning that indeed both parameters have to be non-zero in order to achieve the Mott insulating state. We thus conclude that since $h \neq 0$, the confined mesons form a gapped Mott state, where every confined dimer is followed by a single empty site, and we thus coin the term meson Mott state [3].

Moreover, we observe signatures of a Berezinskii-Kosterlitz-Thouless (BKT) transition to the Mott state, by fitting the charge gap with an exponential function defined as [1, 2, 182, 183],

$$\Delta_c^{\text{BKT}} \propto e^{B/\sqrt{h-h_c}}. \quad (3.17)$$

In this case we consider constant NN repulsion V and the gap opening is a function of the electric field term h . The results for $V/t = 1$, together with the fit with Eq. (3.17) can be seen in Fig. 3.3(b) [1].

We thus conclude that at two-thirds filling, $n = 2/3$, the system forms a meson Mott state for finite values of h and V , with a substantial charge gap. In this case, the mesons are confined since $h \neq 0$, and due to the additional NN interactions $V > 0$, they form a symmetry broken state. In this state, they arrange themselves in a pattern where every meson (tightly confined dimer), is followed by exactly one empty lattice site; see the inset in Fig. 3.2(a). Thus, the system is in a simple doubly degenerate ground state.

To understand this, we can consider a tightly confined dimer in the case when hopping

is frozen, i.e., $t = 0$ and $h, V \neq 0$. Since we are at two thirds filling the next tightly confined dimer will be two lattice sites away, having a vacant site in between in order to avoid the NN repulsion V . Since we consider the regime where $h \neq 0$, this means that an extended dimer will acquire an extra energy $\Delta E = 2h$. Contrarily, since the dimer is not tightly confined anymore, the extended string spans over one vacant site and the energy decreases by $\Delta E = -V$. However, since we are at two thirds filling there is already a neighboring dimer next to the extended dimer so the parton immediately gains a new NN repulsion energy $\Delta E = +V$ from the neighboring site. The total energy gain for any extended dimer is therefore simply $\Delta E = +2h$, and the meson Mott state is as we described above: confined mesons arranged in a lattice, where every meson has a single vacant lattice site in between [1, 3].

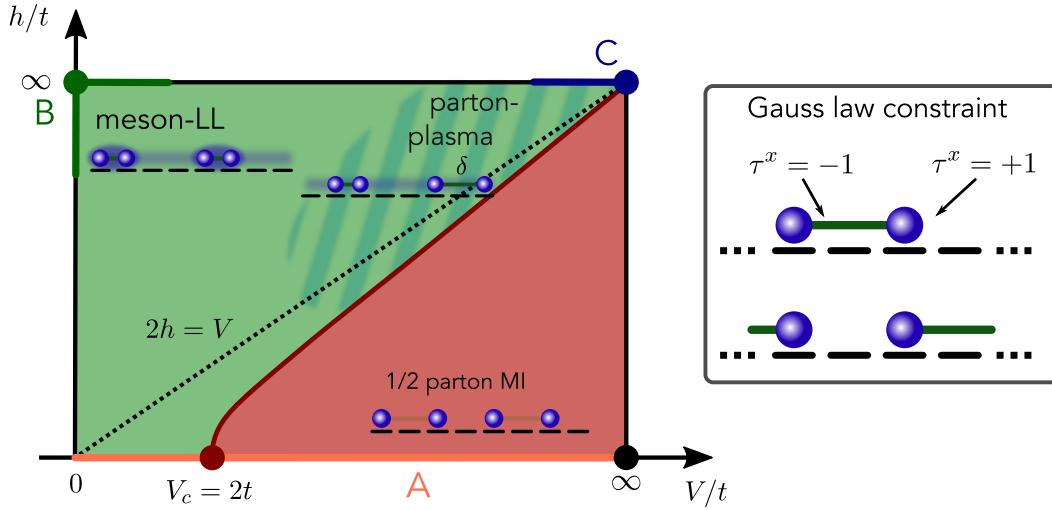


Figure 3.4: Sketch of a phase diagram of the 1 + 1D \mathbb{Z}_2 LGT, Eq. (3.7), coupled to dynamical $U(1)$ charges at half-filling $n = 1/2$. In the absence of the \mathbb{Z}_2 electric field term $h = 0$ (region denoted with A), the NN repulsion stabilizes a parton Mott state for $V \geq 2t$. This state remains stable upon introduction of a weak electric field term. In the other limit where the \mathbb{Z}_2 electric field term is non-zero, but the NN repulsion is absent (region B), the partons confine into mesons, which form a confined LL. On the line $2h = V$, but for vanishing hopping $t \rightarrow \infty$ (region C), partons are confined into two different meson states, which are energetically degenerate. Reintroducing hopping as perturbation gives rise to a pre-formed parton-plasma like regime. This figure is modified from Fig. 1 in Ref. [3].

3.4 Phase diagram at half-filling

Next we consider the 1 + 1D \mathbb{Z}_2 LGT with NN repulsion, Eq. (3.7), at one-half filling, $n = 1/2$, which is another special chain filling. In contrast to the two-thirds case, where the \mathbb{Z}_2 electric field term h and the NN repulsive interaction V together stabilize a meson Mott state, in the half-filling case the two interactions have opposite effects, which results in quantum frustration [3]. Similarly to before, we consider analytical calculations in tractable limits together with numerical DMRG calculations in order to construct the ground state phase diagram at half-filling, which is summarized in Fig. 3.4.

3.4.1 Analytical limits at half-filling

There are three tractable limits, or regimes in the phase diagram that we can consider at half-filling, $n = 1/2$, highlighted on the phase diagram and denoted with letters A, B, and C. Theoretically perhaps the easiest regime is the case where the \mathbb{Z}_2 electric field term is zero, $h = 0$, denoted with A, and the system is simply a hard-core parton model with repulsive NN interactions. The next limit B corresponds to tightly confined partons in the regime when $h \gg t, V$ which we already discussed in Section 3.2.2 and Section 3.3.1. The regime C is the highly interacting regime $h, V \gg t$, with interesting parton-plasma-like features. We will study each of these limits separately in detail.

Free partons and tightly confined dimers at half-filling

Before we dive into the first theoretical limit B for $h \gg V, t$, we quickly comment on the regime where $V = 0$, already well known from the previous discussion on parton and meson LL in Section 3.2. In the phase diagram, Fig. 3.4, this is the vertical line at $V = 0$.

As already mentioned in Section 3.2, at $h = 0$, the partons are completely free and form a simple LL, with $K = 1$ [1, 3, 160, 182]. When the \mathbb{Z}_2 electric field becomes non-zero, mesons confine and form a confined LL, with more complicated interactions and K , with HODQLRO in the string-length basis [1].

With increasing value of the \mathbb{Z}_2 electric field term, we enter the limit B, where mesons are tightly confined, and we can apply the second order perturbation theory, where hopping t , is considered to be a small perturbation, which yields an effective hard-core model with NN repulsion for the mesons, Eq. (3.5) [1, 3, 160].

We can once again add the NN repulsion V between bare partons, if we stay in the regime where dimers are tightly confined $h \gg t, V$, and thus obtain Eq. (3.8), which we write explicitly again here for convenience [1, 3]

$$\hat{\mathcal{H}}_d = -t^d \sum_{\langle i,j \rangle} \left(\hat{d}_i^\dagger \hat{d}_j + \text{H.c.} \right) + (\tilde{V} + V) \sum_{\langle i,j \rangle} \hat{n}_i^d \hat{n}_j^d. \quad (3.18)$$

We remind the reader that $\tilde{V} = 2t^d$ [160]. We note that the above expression does not depend on filling. This time we are not at $n = 2/3$, which equals to half-filling in the hard-core meson model, $n^d = 1/2$, and any $V > 0$ results in the Mott state of mesons, as discussed in Section 3.3.1. Contrarily, in the case at half-filling $n = 1/2$, which we consider here, the system remains a meson Luttinger liquid even for $V > 0$, as this equals to $n^d = 1/3$ in the hard-core meson model. That is because $(V^d + V) > 2t^d$ in the hard-core meson model Eq. (3.18), only results in the Mott state when $n^d = 1/2$ [1, 182]. The consequence of this is that the meson LL remains stable at $h \gg t$, even for weak NN repulsion V . This limit of course holds as long as the mesons are confined, i.e., $h \gg V$. Thus, the extended region around the limit denoted with B, where $h \gg V, t$ is a meson Luttinger liquid as sketched in Fig 3.4.

Zero electric field term

Next we consider the regime where the \mathbb{Z}_2 electric field term is zero, $h = 0$, and there are no fluctuations in the gauge field. We can once again consider the dressed parton formulation, Eq. (2.20), and eliminate the gauge fields to obtain a hard-core boson system with NN repulsion [1]

$$\hat{\mathcal{H}}_b = -t \sum_j \left(\hat{b}_j^\dagger \hat{b}_{j+1} + \text{H.c.} \right) + V \sum_j \hat{n}_j^b \hat{n}_{j+1}^b. \quad (3.19)$$

As already mentioned before, such a model can be mapped to a XXZ spin-1/2 chain; see Appendix A. The diagram of this model can be determined by using the Bethe ansatz [182, 184–186]. The system governed by Hamiltonian Eq. (3.19), forms a Luttinger liquid for generic fillings n , and parameter values t, V [182], as already mentioned in Section 3.2. The

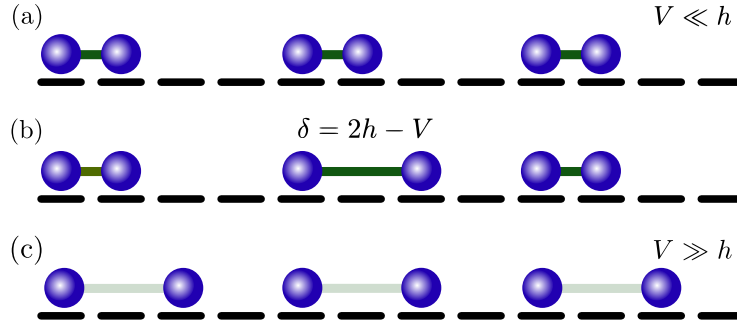


Figure 3.5: Different configurations of dimers in the limit of $t = 0$ and $h, V > 0$. (a) In the regime where $2h > V$, tightly confined dimers $\ell = 1$ are energetically the most favorable configurations. (b) An extended dimer with $\ell = 2$ has an energy difference of $\delta = 2h - V$ in comparison to the tightly confined dimer. (c) In regime $V > 2h$ extended dimers $\ell = 2$ are energetically more favorable than the tightly confined dimers. This figure is modified from Fig. 2 in Ref. [3].

only exception is half-filling where a Mott insulating (MI) state is stabilized for dominant NN repulsion, $V > 2t$ [182].

We can thus determine that the region A of the half-filling \mathbb{Z}_2 LGT phase diagram, highlighted in Fig. 3.4, exhibits a transition to a parton Mott state when $V > 2t$ and $h = 0$. This is a simple Mott state of partons at half-filling, where the partons arrange themselves as sketched in the inset of Fig. 3.4, denoted with $1/2$ parton MI. In the Mott insulating state at half-filling, every lattice site occupied by a parton is followed by a vacant lattice site.

3.4.2 Fluctuating dimers

The last regime that we consider analytically is the highly interacting limit where both NN repulsion and the \mathbb{Z}_2 electric field term are of comparable strength, $V \approx 2h \gg t$ [3]. This regime is denoted with C in the phase diagram in Fig. 3.4.

Absence of hopping

We start by first considering the limit where the parton hopping is frozen, $t = 0$. Depending on the relative strength of parameters $h, V > 0$, two kinds of dimers can be energetically most favorable [3].

We can first note that when the string is extended by one lattice site to $\ell = 2$, the energy gain associated by this extension corresponds to $\Delta E_{+1} = 2h$, as the anti-string had to be changed to string according to the Gauss law constraint [3]. Thus, dimers will not be extended over long strings as this is energetically costly, and we can expect that dimers will be as short as possible, as discussed in Section 2.2. This means that mesons will favor tightly confined dimer states, where partons are nearest neighbors and thus the string length is minimal, $\ell = 1$, as depicted in Fig. 3.5(a). However, since such meson states involve two partons on neighboring sites, such tightly confined dimers also exhibit NN

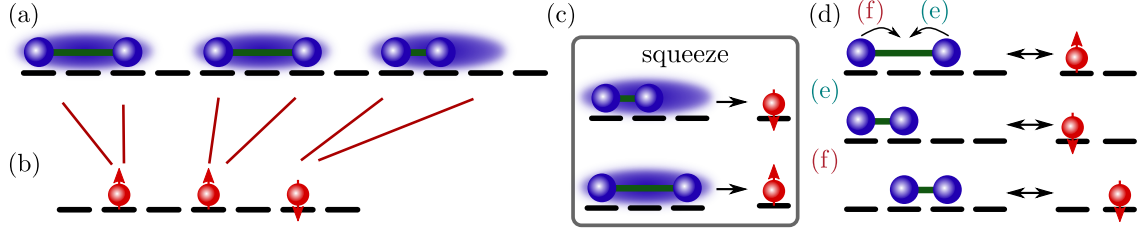


Figure 3.6: The pseudospin picture of squeezed mesons in the limit where $2h \approx V \gg t$. (a) The original basis with only two allowed meson states. (b) The pseudospin basis, where the mesons in (a) become squeezed into hard-core pseudospins, which we denote with red spheres with arrows indicating the pseudospin orientation. (c) Definition of the two pseudospins and their corresponding dimer configurations. (d) Allowed hoppings of partons, which result in on-site pseudospin flip (e) or pseudospin flip and additional hopping over one lattice site (f). The original basis picture is sketched on the left, and the pseudospin basis is sketched on the right. This figure is modified from Fig. 3 in Ref. [3].

repulsion $\Delta E_{\text{NN}} = +V$. Therefore we can express the energy of an isolated dimer in the regime where $h, V > 0$ as [3]

$$E_\ell = V\delta_{1,\ell} + 2h\ell, \quad (3.20)$$

where we defined the string length $\ell \geq 1$, and $\delta_{1,\ell}$ is the Kronecker delta function. Next we define the energy difference between the dimer of minimal possible length $\ell = 1$, and the energy of dimer with the string extended by one site $\ell = 2$ [3]

$$\delta = E_2 - E_1 = 2h - V. \quad (3.21)$$

We see that there are two possible dimer configurations, which can minimize energy for different finite values of h and V : the *tightly confined* dimer with minimum string length $\ell = 1$, is favored when $2h > V$, conversely, the *extended* dimer $\ell = 2$, will be favoured in the regime where $V > 2h$ [3]. The extended dimer is sketched in Fig. 3.5(b). Any longer dimers will always be energetically unfavorable for $h > 0$ as the difference is always positive $E_3 - E_2 = 2h > 0$, since there is no additional NN energy contribution.

We have thus demonstrated that for $2h = V$, the two states have the same energy and that this line represents the boundary between the two regimes of tightly confined dimers, $2h > V$, and extended dimers $2h < V$. In the former case, $2h > V$, the tightly confined mesons can be arranged in many possible ways in the lattice at half-filling, where at least one vacant site is left between two neighboring mesons. This results in an extensive degeneracy of the ground state, and in a meson Luttinger liquid, once hopping t is reintroduced [3]. Contrarily, there are only few options how to arrange extended dimers in the lattice for the case when $2h < V$; see Fig. 3.5(c). There, we obtain a simple Mott state of partons with a two-fold overall degeneracy [3], which is similar to the Mott state obtained in the limit when $h = 0$ and $V > 2t$. We thus see that $2h = V$ is indeed the boundary between a parton Mott state and tightly confined mesons when $t = 0$; see Fig. 3.4.

Hopping as small perturbation

We can now reintroduce hopping t as a small perturbation $h, V \gg t$. We restrict our Hilbert space in the perturbation to only two states: dimers of length $\ell = 1$ and $\ell = 2$, i.e., any meson with $\ell > 2$ is forbidden. With this constraint we can squeeze the two dimer states into two types of mesons, which we can consider to be of pseudospin-up (extended meson) or pseudospin-down (tightly confined meson), as sketched in Fig. 3.6. In this construction we always squeeze 3 lattice sites into a single one, as defined in Fig. 3.6(c). The newly defined pseudospin particles have a hard-core property as the original partons and mesons, i.e., two pseudospin on the same lattice site (up and down), do not represent any physical state [3].

By considering this construction we can write a new effective Hamiltonian for the squeezed particles [3]

$$\hat{\mathcal{H}}_s = \hat{P} \left[-t \sum_j \left(\hat{c}_{\uparrow,j}^\dagger \hat{c}_{\downarrow,j+1} + \hat{c}_{\uparrow,j}^\dagger \hat{c}_{\downarrow,j} + \text{H.c.} \right) + \frac{t^2}{2(\delta + V)} \sum_j \hat{n}_{\downarrow,j} \hat{n}_{\uparrow,j+1} \right. \\ \left. + \frac{t^2}{\delta + V} \sum_j \hat{n}_{\downarrow,j} \hat{n}_{\downarrow,j+1} + \delta \sum_j n_{\uparrow,j} \right] \hat{P}. \quad (3.22)$$

Here we define the pseudospin-up creation operator as $\hat{c}_{\uparrow,j}^\dagger$, and the pseudospin-down creation operator as $\hat{c}_{\downarrow,j}^\dagger$ [3]. In addition, we also define the corresponding on-site number operators $\hat{n}_{\downarrow,j} = \hat{c}_{\downarrow,j}^\dagger \hat{c}_{\downarrow,j}$, and $\hat{n}_{\uparrow,j} = \hat{c}_{\uparrow,j}^\dagger \hat{c}_{\uparrow,j}$ [3]. Finally, we also define the operator \hat{P} , which projects into a subspace with no double occupancy of pseudospins, and without states that are energetically penalized by the NN repulsion [3].

The first two terms in the Hamiltonian Eq. (3.22) are the remaining allowed hopping terms of partons, see Figs. 3.6(d)–3.6(f). In an extended dimer, sketched in Fig. 3.6(d), the partons can only hop towards each other, since any other hopping would extend the string beyond the allowed length $\ell > 2$, and would lead to configurations that we project out as energetically unfavorable. When the right parton hops towards its left meson counterpart, Fig. 3.6(d) to 3.6(e), the squeezed pseudospin remains on the same lattice site, however the orientation of the pseudospin changes from up to down. The opposite process can of course also occur where in the tightly confined state the right parton hops to the right, which is formalized as $\hat{c}_{\uparrow,j}^\dagger \hat{c}_{\downarrow,j}$, and is just the Hermitian conjugate of the described case leading to Fig. 3.6(e) from initial state in Fig. 3.6(d). The second possible case is that the left meson hops towards its right meson counterpart, Fig. 3.6(f), which in addition to the pseudospin flip also results in moving the parton one site to the right. Once again, the opposite process is also possible, which we can formalize as $\hat{c}_{\uparrow,j}^\dagger \hat{c}_{\downarrow,j+1}$, which is just the Hermitian conjugate of the described case leading to Fig. 3.6(d) from initial state in Fig. 3.6(f).

Next, we consider the NN repulsion term, where we simply consider the cases where the NN configurations of pseudospins are allowed, since the actual partons containing these pseudospins are not neighbors; see Fig. 3.7. We consider the second-order perturbation in the same way as in the second-order perturbation of tightly confined dimers where NN

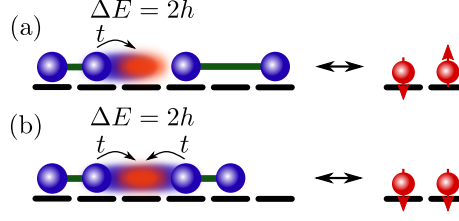


Figure 3.7: Second-order perturbation NN repulsion terms between pseudospin configurations. (a) Repulsion due to restricted hopping of the parton of the tightly confined dimer towards the neighboring dimer on the right. (b) Repulsion due to restricted hopping of partons in both tightly confined dimers. This figure is modified from Fig. 9 in the Appendix of Ref. [3].

repulsion comes from restriction of parton fluctuations [160]. The only two contributing configurations are when two pseudospin-down states are NN, and when a pseudospin-down is a NN to the left of a pseudospin-up, which we sketch in Fig. 3.7. In both cases the left dimer has to be tightly confined $\ell = 1$. The right dimer can be extended or tightly confined. In the former case, the repulsion equals to $t^2/4h$ and in the latter, where partons of the both dimers are not allowed to fluctuate, the repulsion is $t^2/2h$. The repulsion terms together thus yield [3]

$$\hat{\mathcal{H}}_s^{2nd} = \frac{t^2}{2V} \sum_j \hat{n}_{\downarrow,j} \hat{n}_{\uparrow,j+1} + \frac{t^2}{V} \sum_j \hat{n}_{\downarrow,j} \hat{n}_{\downarrow,j+1}. \quad (3.23)$$

Let us note that the NN configuration terms, which are highly energetically penalized and thus projected out by the operators \hat{P} , in addition to double occupancies, can be expressed as [3]

$$\hat{H}_s^V = \left[V \sum_j \hat{n}_{\uparrow,j} \hat{n}_{j+1} \right], \quad (3.24)$$

where $\hat{n}_{j+1} = \hat{n}_{\uparrow,j+1} + \hat{n}_{\downarrow,j+1}$. As already stated before, since we consider $V \gg t$, configurations contributing to the above terms involve NN partons that belong to different mesons.

The last term in the Hamiltonian Eq. (3.22) comes directly from the fact than when $\delta > 0$, tightly confined dimers will be favored and thus extended dimers, i.e., pseudospin-up states will cost energy relative to the tightly confined dimers as we expressed in Eq. (3.21). Of course the opposite holds for $\delta < 0$.

In order to explicitly express the perturbative NN repulsion in terms of δ , we rewrote the denominators in Eq. (3.22) of the perturbative NN repulsion explicitly as $2h = \delta + V$, since we defined $\delta = 2h - V$.

From the Hamiltonian, which we constructed in the limit, $h, V \gg t$ with an additional requirement $2h \approx V$, we can conclude that close to $\delta \approx 0$, strong partons fluctuations are allowed when hopping is reintroduced [3]. In highly doped regimes, which is the case at half-filling $n = 1/2$, we thus expect that strong fluctuations between tightly confined dimers $\ell = 1$ and extended dimers $\ell = 2$, will result in an apparent deconfined behaviour

on short to intermediate length scales, comparable to the average parton spacing in such a regime [3]. We coin this regime the parton-plasma regime in analogy to high-energy physics, as the short-ranged parton fluctuations are plasma-like [3].

Furthermore, considering the cases where $\delta \neq 0$ and one of the parameters become dominant, we can recover the behaviour, which leads to the Mott state on the one hand, and the confined meson LL on the other hand. In the case where $2h > V$, we regain the meson LL liquid as $\delta > 0$ favours tightly confined mesons [3]. In the opposite case where $\delta < 0$, we see that extended dimers are favoured and thus hopping is suppressed whereas the second-order perturbative NN repulsion increases, which eventually leads to a Mott state.

3.4.3 Phase diagram

From the analytical considerations, where we considered different limits, we can already conjecture the phase diagram sketched in Fig. 3.4. In the regime labeled with A, when $h = 0$, we obtained a simple 1/2-parton Mott state for $V > 2t$ as discussed in Section 3.4.1. On the other hand, when the NN repulsion is zero $V = 0$, we have established that partons confine into mesons with non-zero electric field term, $h \neq 0$, as discussed in Section 3.4.1. Mesons become tightly confined for stronger values of the electric field term h , where we can consider them to be new hard-core particles forming a meson LL, which remains stable also for small NN repulsion, $V \ll h$, since the filling $n = 1/2$ is far away from a possible formation of a meson Mott state at $n = 2/3$, which we discussed in Section 3.3.

Finally, in the regime where $2h \approx V$, we showed that dimers can become frustrated, which leads to parton-plasma like fluctuations as hopping is considered as a small perturbation $t \ll h, V$. This regime can also be considered as a crossover regime where the 1/2-parton Mott state is destroyed as partons confine into mesons that become dynamical and form a meson LL [3].

In order to complete the full phase diagram, which we already sketched from our analytical considerations, we in addition turn to numerical calculations. We explicitly probe the parton Mott insulating phase by considering the charge gap and the static structure factor. For that we employ finite DMRG calculations implemented within the MPS toolkit SYTEN [153, 154]. We consider chains with length up to $L = 120$, unless stated otherwise. In addition, we once again integrate out the matter via Gauss law and simulate the spin Hamiltonian; see Section 1.3.2.

Charge gap at half-filling

A parton Mott state will exhibit non-zero value of the charge gap, which we define as [1, 3]

$$\Delta_c(L, N) = \frac{1}{2} \left[\left(E_{N+2}^L - E_N^L \right) - \left(E_N^L - E_{N-2}^L \right) \right]. \quad (3.25)$$

We defined it in exactly the same way as in the two-thirds filling case, discussed in Section 3.3. Thus E_N^L is once again the ground state energy for a chain with length L , with

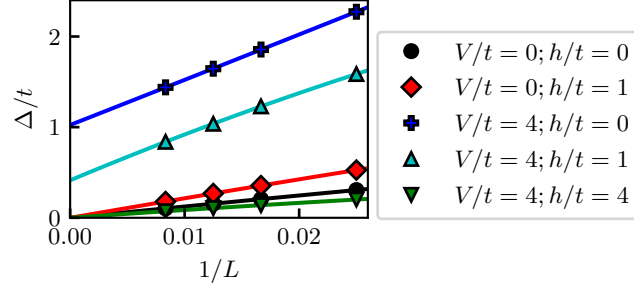


Figure 3.8: Details on the extrapolation of the charge gap in the thermodynamic limit for half-filling $n = 1/2$. This figure is modified from Fig. 10(a) in the Appendix of Ref. [3].

N partons, which constitutes to filling $n = N/L$. We once again consider E_N^L and $E_{N\pm 2}^L$, since we will consider the gap for generic values of h and V . In addition, we again consider only even numbers of partons, which have the potential to be paired with each other, thus avoiding to be stuck to one of the edges of the chain [3].

Similar as before, we calculate the charge gap for different chain lengths L at a fixed filling, $n = 1/2$, and extrapolate the values to the thermodynamic limit

$$\Delta_c(L, N) = \lim_{L \rightarrow \infty} \Delta(N, L). \quad (3.26)$$

The finite size scaling is performed in the same way as in the two-thirds filling case. We extrapolate the charge gap results by plotting the values of Eq. (3.25), which we obtain from DMRG calculations, as a function of $1/L$, and fit the quadratic function to the data. The value of the quadratic function at $x = 1/L = 0$ thus gives us the value of Eq. (3.25) in the thermodynamic limit. Typical fits can be seen in Fig. 3.8, where we consider system lengths of $L = 40, 60, 80, 120$. These lengths had to be adjusted for different parameter values in order to ensure convergence of the DMRG calculations [3]. Since we simulate the spin model where we tune the chemical potential in order to obtain the correct filling, we have to subtract the energy contribution of the chemical potential term [3].

The results for the charge gap as a function of the electric field term h and NN repulsion V are presented in Fig. 3.9(a) [3]. The obtained phase diagram shows that there is a significant charge gap in the regime where $V > 2t$ and $V > 2h$, which is in agreement with our analytical considerations. As an example we also show the details on the charge gap opening at $V = 5$ as a function of h in Fig. 3.9(b), which shows that the onset of non-zero gap value indeed appears around $h \approx V/2 = 2.5t$. In addition, we also present the details on the gap opening as a function of the NN repulsion V in the absence of the \mathbb{Z}_2 electric field term $h = 0$ in Fig. 3.9(c). In this regime the LL theory predicts a Berezinskii-Kosterlitz-Thouless (BKT) transition at $V = 2t$ [3, 182]. In order to study this transition further we again consider the BKT exponential function [1, 3, 182, 184]

$$\Delta_c^{\text{BKT}} \propto e^{B/\sqrt{V-V_c}}, \quad (3.27)$$

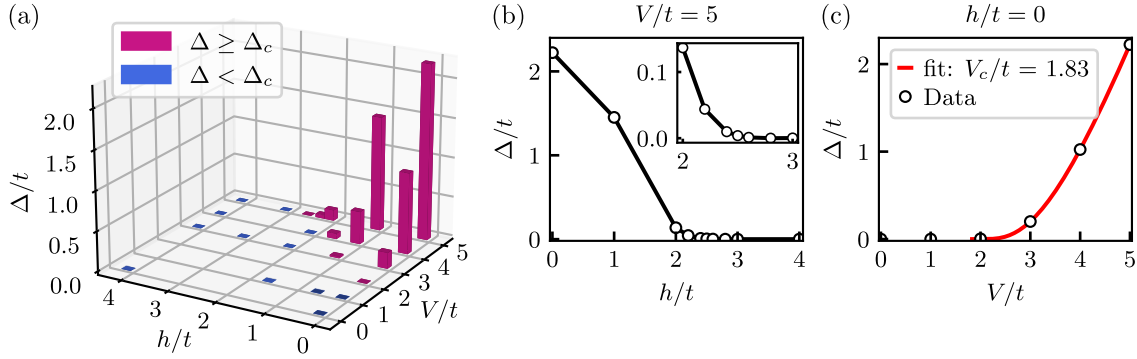


Figure 3.9: The charge gap, Eq. (3.25), in the \mathbb{Z}_2 LGT after eliminating matter via Gauss law, extrapolated in the thermodynamic limit for $n = 1/2$. (a) The charge gap in the thermodynamic limit as a function of h and V . The Purple bars denote the gap values where $\Delta \geq \Delta_0$, and the blue bars denote the gap values where $\Delta < \Delta_0$. We define the cutoff value as $\Delta_0 = \Delta(h/t = 0, V/t = 2)$. (b) Details on the charge opening as a function of the electric field term h at a constant value of the NN repulsion $V/t = 5$. (c) Details on the charge opening as a function of the NN repulsion V at zero value of the electric field term $h = 0$. This figure is modified from Fig. 4(a) in Ref. [3]; and Fig. 10(b) and Fig. 10(c) in the Appendix of Ref. [3].

which we again state here for convenience. The difference here is that the gap is a function of V and not h as was the case considered at two-thirds filling. The fit with this function can be seen in Fig. 3.9(c), where we fixed the transition value to $V_c = 1.83t$, which we found as the value with the lowest covariance matrix elements, after scanning through different values of V_c . This value is around 9% off from the expected value of $V_c = 2t$. We attribute this to the peculiar exponential BKT function that is hard to fit to the data, and to slight errors in the extrapolation of the gap to the thermodynamic limit. Even though, the exact transition is hard to establish, our results are very close to the expected value.

We conclude that there is a finite charge gap indicating the parton Mott state for parameter values $V \geq 2t$ and $V \gtrsim 2h$.

Static structure factor

Next we consider the static structure factor, which we define as [3, 187]

$$S(k) = \frac{1}{\mathcal{N}} \sum_{j,l} e^{-i(j-l)k} \langle \hat{n}_j \hat{n}_l \rangle, \quad (3.28)$$

where as usual we define $\hat{n}_j = \hat{a}_j^\dagger \hat{a}_j$, and we denote the normalization factor by \mathcal{N} . Technical details on the structure factor can be found in Appendix B. The static structure factor generally probes transitional symmetry broken phases and thus complements the charge gap calculations [3]. However, the static structure factor is much easier to measure in a quantum simulator, and could thus be used as an experimental probe of confinement. There,

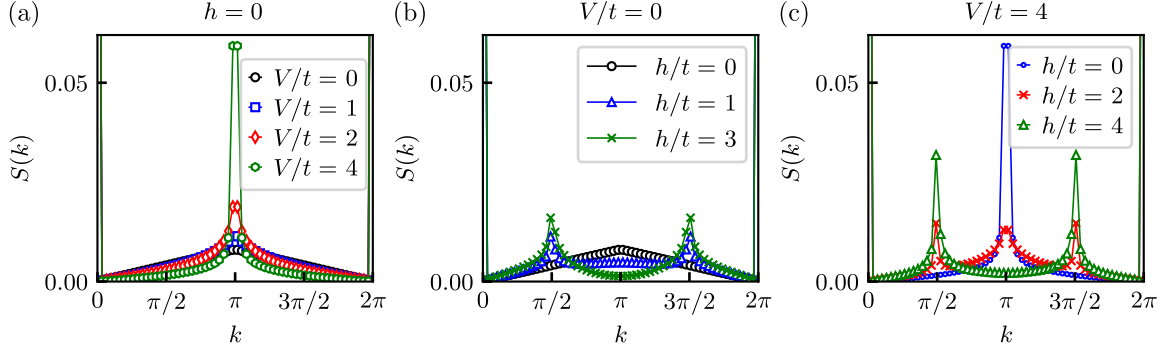


Figure 3.10: The structure factor Eq. (3.28) at half-filling. (a) The structure factor in the absence of the \mathbb{Z}_2 electric field term $h = 0$, for different values of the NN repulsion V , reveals a parton Mott peak at $k = \pi$. (b) Structure factor for different values of h and no NN repulsion $V = 0$. We observe low peaks at $k = \pi/2$ and $k = 3\pi/2$, when $h > 0$. (c) Structure factor as a function of h and V , where the peaks at $2h = V = 4t$ have the same heights. This figure was modified from Fig. 5 in Ref. [3].

one would have the measure the spatial configuration of the matter, or the configuration of the \mathbb{Z}_2 electric field.

We use DMRG to calculate the structure factor as a function of the electric field h and NN repulsion V . We observe two different types of peaks in our calculations: at half-integer and at integer multiples of π [3].

The peaks at $k = \pi$ directly probe the parton Mott state, and grow with increasing NN repulsion V as can be seen for $h = 0$ in Fig. 3.10(a). The peak at $k = \pi$ remains low for $V \leq 2t$, and rises significantly only when $V > 2t$, which is in agreement with the transition to the parton Mott insulating state where the partons arrange in a long-ranged staggered configuration [3].

In the regime with no NN repulsion $V = 0$, but with increasing electric field term h , we observe small peaks at half-integer multiples of π , that is at $k = \pi/2, 3\pi/2$, as can be seen in Fig. 3.10(b). These peaks rise only slightly with increasing h . Peaks at $k = \pi/2$, would generally mean that the system has a structure with period of four lattice sites [3]. However, since the charge gap is zero in this regime, we conclude that these peaks are related to short-range correlations. Peaks at $k = \pi/2$ are thus only algebraically localized instead of exponentially, which would suggest long-rang order [3].

Furthermore, we observe a low and broad peak at $k = \pi$ for free partons, $h = V = 0$; see Fig. 3.10(b). This peak disappears for $h/t = 1$, and is replaced with the half-integer π peaks. Since we are at a finite system size, in the case of these results $L = 120$, we can remember that the Friedel oscillation frequency halves in the confined regime where $h \neq 0$. We thus associate the small peak at $k = \pi$, in the free parton regime $h, V = 0$ to the Friedel oscillations at half-filling $n = 1/2$, which correspond to $k = 2\pi n = \pi$ [3, 160]. In the confined regime, the Friedel oscillations halve to $k = \pi n$, and for half-filling thus correspond to modest peaks at half-integer multiples of π . We thus associate the small peaks at $k = \pi/2, 3\pi/2$ to the confined meson Luttinger liquid, and to finite size effects

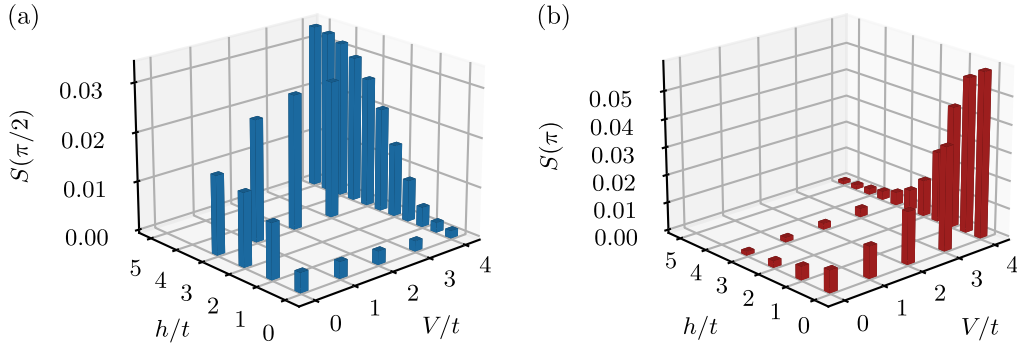


Figure 3.11: Height of the structure factor peaks at $k = \pi/2$ and $k = \pi$ in the \mathbb{Z}_2 LGT after eliminating matter via Gauss law, at half-filling $n = 1/2$. (a) Peak at $k = \pi/2$, acquires a small value for $h \neq 0$, which is enhanced by V close to the frustrated regime, $\delta = 0$, and $h, V \gg t$. (b) Peak height at $k = \pi$ directly probes the parton Mott state and resembles the charge gap results. This figure was modified from Fig. 4 in Ref. [3].

in our system with length $L = 120$. We expect these peaks to become less prominent in the thermodynamic limit $L \rightarrow \infty$, for $h \gg t$, since tightly confined mesons form a gapless meson LL [3]. More details on the size dependence of the structure factor can be found in Appendix B.

Next we consider the frustrated regime, $2h = V$, where analytical calculations showed that the tightly confined and extended dimers become degenerate in the limit when $t \rightarrow 0$ and we thus expect strong fluctuations between the two dimer states for small t . The structure factor results, Eq. (3.28), at high NN repulsion $V = 4t$ for different values of the \mathbb{Z}_2 electric field term h are presented in Fig. 3.10(c). The strong peak at $k = \pi$ at $h = 0$, decreases significantly for $h = 2t$, which is the special degenerate point where $\delta = 0$. It furthermore drops for $h = 4t$. This means that the parton Mott state is indeed melted by the non-local electric field term, which introduces the linear confinement in the strings. The half-integer peaks at $k = \pi/2, 3\pi/2$ appear for $h = 2t$ and further increase with increasing value of the field term. This shows that the partons indeed bind into mesons. However, due to the NN repulsion V , the meson LL has some short range correlations, which are associated with dimer fluctuations and the second-order NN repulsion in the effective model Eq. (3.22). The height of both peaks at $2h = V$ is approximately the same and thus shows that this is indeed a very interesting regime.

We summarize the peak height values at $k = \pi$, and $k = \pi/2$ as a function the electric field term h and NN repulsion V in Fig. 3.11 The behaviour of structure factor peaks at $k = \pi$ and at $k = \pi/2, 3\pi/2$ thus determines the behaviour of the system in a similar way as the charge gap. This is in particular true for the peak at $k = \pi$, which directly probes the order with period of two lattice sites. The partons arrange in a staggered fashion in the $1/2$ -parton Mott state, where every occupied lattice site is followed by a vacant site, this means that the structure factor peak at $k = \pi$ is a direct, experimentally feasible probe of the parton Mott state. Peaks at $k = \pi/2, 3\pi/2$, are a bit more subtle, since they are associated with the Friedel oscillations of the confined mesons in a finite chain of length L ,

and not with long-range correlations. We thus expect them to vanish in the thermodynamic limit $L \rightarrow \infty$. However, they would appear in quantum simulation experiments with OBC.

3.4.4 Pre-formed parton plasma

In this section, we take a closer look at the regime where we can obtain two energetically degenerate meson states in the absence of hopping. As already discussed in the previous Section 3.4.2, this is the regime where $2h = V$ in the absence of hopping $t = 0$. There, the two possible mesons with length $\ell = 1$ and $\ell = 2$, which we dubbed as the tightly confined and extended dimer, respectively, dominate the physics when weak hopping is reintroduced as small perturbation, $t \ll h, V$ [3]. As discussed in Section 3.4.2, the exact relation between the electric field term h and the NN repulsion V is important close to $2h = V$. That is because these are two competing interactions, which result in very different behaviour once one of them becomes dominant. At the commensurate filling $n = 1/2$, dominant NN repulsion $V \gg h, t$, results in a simple parton Mott state of lattice sites alternating between filled and vacant lattice sites [3]. This behaviour was confirmed by a substantial charge gap as well as the peak in the static structure factor at $k = \pi$. In the other limit, where the electric field term is dominant, $h \gg V, t$, partons become tightly confined into mesons with $\ell = 1$, which form a meson LL, where NN repulsion V plays only a minor role and can only modify the value of the LL parameter [3].

The two limits mentioned above and studied in Section 3.4.1 can be interpreted in terms of a LL of confined partons and a Mott state of individual partons, respectively [3]. However, the exact nature of the transition between these two regimes and the behaviour at the interface is not clear. That is because the interplay of the non-local \mathbb{Z}_2 electric field term and the local NN parton repulsion results in highly frustrated states at $2h = V$ and high doping [3]. Due to the energetic degeneracy of the two meson states in this regime, partons are allowed to fluctuate and thus their behaviour is hard to capture only in terms of the well known behaviour of the Mott state or the LL [3].

We can investigate this regime closer by starting in the parton Mott state. As discussed in Section 3.4.2, the Mott transition occurs close to $2h = V$ and $V \geq 2t$, which is also supported by the charge gap and static structure factor results presented in Fig. 3.9 and Fig. 3.11, obtained from DMRG calculations. Close to the transition line $2h = V$, the confined mesons are allowed to fluctuate between the tightly confined state $\ell = 1$ and the extended dimer state $\ell = 2$, as the two states are degenerate with energy difference $\delta = 2h - V$, in the limit $t \rightarrow 0$ [3]. At this point we emphasise the fact, that the parton pairs are overall confined, since the non-zero electric field term $h \neq 0$ imposes further energy gain for dimers, which are extended above the the string length $\ell > 2$. However, at the high filling $n = 1/2$, partons would not have a lot of space to propagate even in the deconfined phase. Thus, due to high filling at $n = 1/2$ and due to strong fluctuations of mesons between the tightly confined state $\ell = 1$ and the extended state $\ell = 2$, which are energetically almost the same, the partons effectively behave as deconfined on short length scales [3]. We dub the region around the $2h = V$ line as the *pre-formed parton-plasma* regime [3]. We formalize the deconfined, short length-scale behaviour in the next subsection, where we consider the

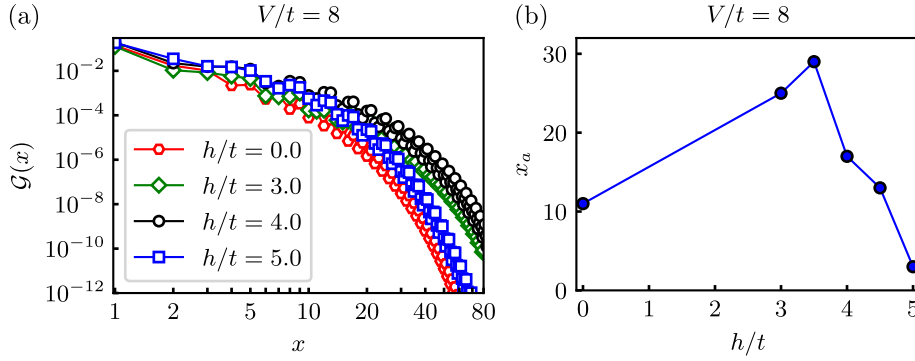


Figure 3.12: Green's function, Eq. (3.29), in the \mathbb{Z}_2 LGT after eliminating the matter via Gauss law, for different values of the electric field term h and a high value of the NN repulsion $V/t = 8$. (a) Green's function decay for different values of the electric field term h on a log – linear plot. (b) Estimated length x_a , on which the Green's function behaviour transitions from the initial power-law to an exponential decay. This figure was modified from Fig. 6 in Ref. [3].

already familiar probe of confinement: the gauge invariant Green's function.

Green's function

As already described earlier, the behaviour of the \mathbb{Z}_2 gauge invariant Green's function, can be studied in order to probe confinement of partons. Here we define the Green's function again for convenience [1, 3, 160]

$$\mathcal{G}(i-j) = \left\langle \hat{a}_i^\dagger \left(\prod_{i \leq \ell < j} \hat{\tau}_{(\ell, \ell+1)}^z \right) \hat{a}_j \right\rangle. \quad (3.29)$$

Furthermore, we reiterate that the Green's function at long distances decays with a power-law in the deconfined regime and exponentially in the confined regime [1, 3, 160]. For the $U(1)$ matter this means that it decays exponentially for any $h \neq 0$ [1, 160].

Following the discussion on the pre-formed parton-plasma regime, the Green's function can exhibit different, more complicated behavior on short length scales, before the long-distance behaviour is established [3]. In agreement with the apparent deconfined behaviour of partons on short length scales in the strongly frustrated regime $2h \approx h$, we find power-law scaling on short to intermediate length scales; see Fig. 3.12. The power-law scaling on short to intermediate length scales resembles the parton plasma phase on length scales, which are significantly above the inter-particle spacing at half-filling [3].

We analyse the behaviour in Fig. 3.12 in greater detail by fitting the Green's function results with a function containing power-law as well as exponential decay, which we define as [3]

$$f_f = A_f x^{-\alpha_f} e^{-\beta_f x}. \quad (3.30)$$

Here we define the distance in the Green's function as $x = |i - j|$, α_f is the strength of the

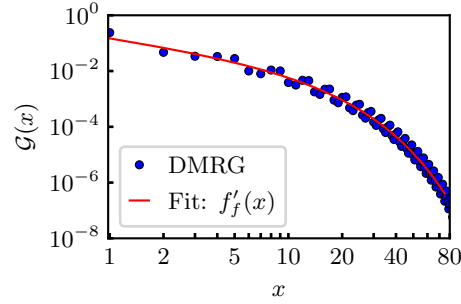


Figure 3.13: Green's function fitted with Eq.(3.31) for parameter values $2h = V = 4t$ in the \mathbb{Z}_2 LGT after eliminating matter via Gauss law. The length of the chain is $L = 120$. This figure was modified from Fig. 15 in Ref. [3].

power law decay, and β_f is a parameter quantifying the strength of the exponential decay [3]. The power-law decay, parameterized by α_f thus captures the (possible) deconfined behaviour of the Green's function, and the exponential decay arising from confinement on long length scales is captured by the parameter β_f [3]. The values of these two parameters can thus be used to distinguish the nature of the Green's function decay on different length scales.

For technical reasons, we generally consider the logarithm of the Green's function and distance x in order to extract the tricky nature of the exponential decay. The fitting function has to be modified accordingly [3]

$$f'_f = A'_f - \alpha_f x' - \beta_f e^{x'}, \quad (3.31)$$

where $x' = \log(x)$ and $f'_f = \log(f_f)$. More technical details on the fits can be found in the Appendix of Ref. [3]. A typical fit of the Green's function with Eq. (3.31) is shown in Fig. 3.13. We consider different values of h and V across the whole phase diagram of the 1 + 1D \mathbb{Z}_2 LGT at half-filling $n = 1/2$. The results for the fitting parameters α_f and β_f are presented in Fig. 3.14.

The value of the exponential decay parameter β_f is close to zero for low values of h , and starts increasing with increasing value of h , indicating an overall confined phase; see Fig. 3.14(b). The increase of β_f follows the line $2h = V$, which agrees with our previous analytical arguments and numerical data [3]. Contrarily, the value of the power-law decay parameter α_f is substantial for low values of the confining electric field h , and decreases with the increasing value of h ; see Fig. 3.14(a). The region where $\alpha_f \gtrsim 0.5$, has a similar lobe shape as the charge gap values in Fig. 3.9, indicating that the mesons become tightly confined outside the region bounded by $V < 2t$ and $h > V/2$. Green's function results thus agree with our previous analytical arguments and numerical results. The finite value of the parameters α_f and β_f , extracted at $2h \approx V$, show that we indeed observe two different types of behaviours at the same time on different length scales [3].

Such a behaviour can already be clearly observed in Fig. 3.12, where we see that the

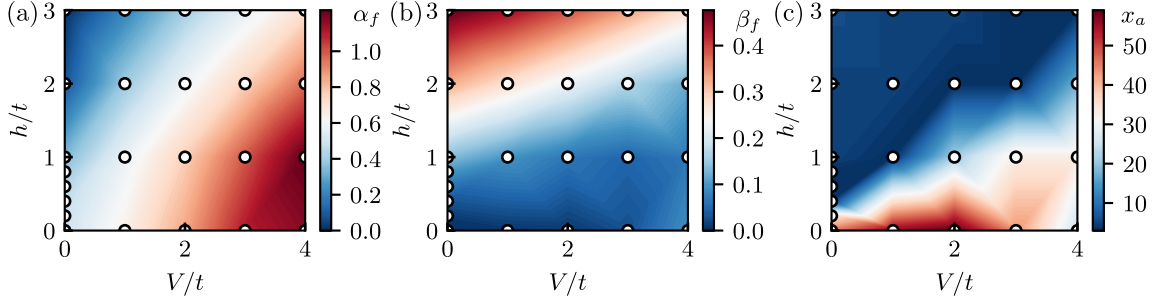


Figure 3.14: Green's function fit results at different parameter values h and V in the \mathbb{Z}_2 LGT after eliminating matter via Gauss law. (a) The power-law decay parameter α_f extracted by fitting Eq. (3.31) to the numerical data. (b) The exponential decay parameter β_f obtained by fitting Eq. (3.31) to the DMRG data. (c) Estimated crossover distance x_a from the power-law to the exponential decay of the Green's function, extracted by fitting the function Eq. (3.32) to different number of data points. This figure was modified from Fig. 7 in Ref. [3].

Green's function decay at $2h = V$ has the slowest initial decay, in comparison to other values of h . This decay appears to obey a power-law on short to intermediate length scales, which eventually turns into the expected exponential decay at longer distances [3].

In order to estimate the crossover distance where the algebraic decay turns into the exponential decay more precisely, we fit the data with a power-law function [3]. For technical reasons we again consider the logarithm of the Green's function obtained from the DMRG calculations, and thus the fitting function has to be adjusted appropriately as [3]

$$f_c = A_c - \alpha_c \log(x). \quad (3.32)$$

We estimate the crossover length by fitting different number of data point, i.e., by considering the Green's function up to different lengths $1 \leq x \leq x_c$, at different parameter values h and V . We start the fits already at $x_c = 3$ and consider the data points all the way up to $x_c = 80$ [3]. The fit result with data points up to $x_a = x_c$ with the lowest sum of the absolute value of the covariance matrix elements, is declared as the fit result where the decay of the Green's function is best described with a power-law function. The distance x_a is thus the estimated length where the nature of the Green's function starts to become exponential and the power-law function can not capture the decay correctly. The results at high NN repulsion $V = 8t$ are presented in Fig. 3.12(b) and the results for generic values of h and V in Fig. 3.14(c). We see that for high values of the electric field term $h \gg t$ and far away from the $2h = V$ line, where the partons are tightly confined into mesons, values drop close to the minimal possible value $x_a \approx 3$, which means that there is no power-law character, and partons are confined on all length scales [3]. The other regime at $h = 0$ where the cutoff values exceed $x_a \gtrsim 30$, signals a power-law behaviour and thus the deconfined regime. Such a behaviour is indeed observed for $h = 0$ and $V \lesssim 2t$ [3].

After establishing that the cutoff values x_a correctly capture the confined and deconfined nature of partons, we turn our attention to the behaviour close to $2h = V$ line. There we indeed observe that the obtained cutoff values lie in the range $15 \lesssim x_a \lesssim 25$. This means that

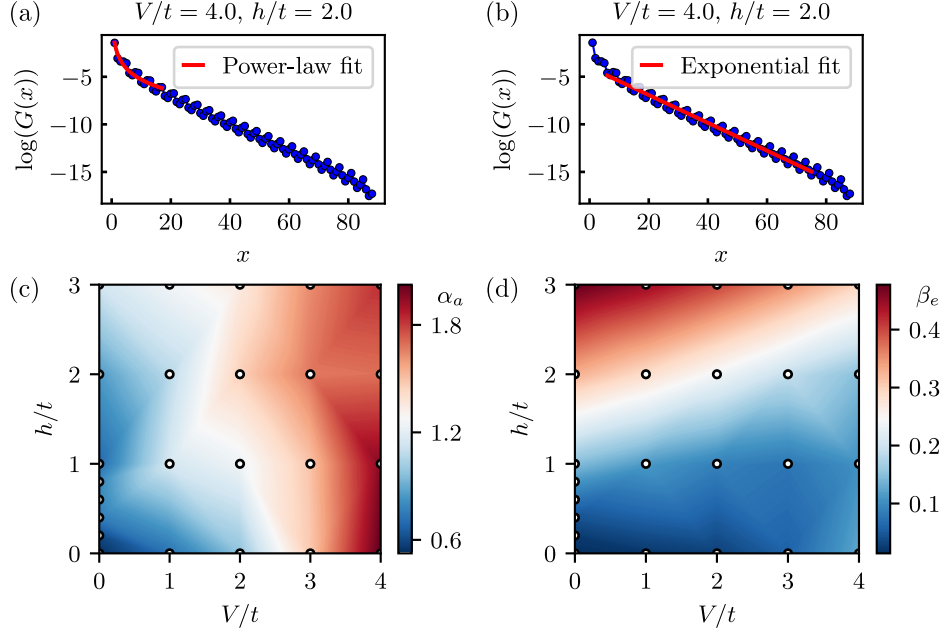


Figure 3.15: Green's function fits with a power-law and an exponential function in the frustrated regime $2h = V = 4t$ in the \mathbb{Z}_2 LGT after eliminating matter via Gauss law. (a) The power-law Eq. (3.33), matches the first few data points of the Green's function. (b) at longer length scales, the exponential function, Eq. (3.34), better captures the overall Green's function decay. (c) Extracted power-law exponent for different values of h and V from fitting the data points with Eq. (3.33). (d) Exponential decay parameter β_e from fitting the data points with Eq. (3.34), shows similar features as the full fit in Fig. 3.14. The data is shown on a log-lin scale. This figure was modified from Fig. 16 in Ref. [3].

the partons behave as if they were deconfined on short length scales $x \lesssim 10$, but on longer length scales $x \gtrsim 30$ the exponential behaviour prevails, meaning that partons are confined on long length scales [3]. The obtained cutoff values between $15 \lesssim x_a \lesssim 25$, close to the line $2h = V$ thus signal the pre-formed parton-plasma like behaviour on short to intermediate length scales, consistent with our analytical predictions, and numerical results [3].

We also fit the data with functions containing only the power-law decay, or only the exponential decay. A typical fit with a power-law function [3]

$$f_a = A_a x^{-\alpha_a} \quad (3.33)$$

is presented in Fig. 3.15(a). The results for the power-law decay exponent α_a for different parameter values h and V can be seen in Fig. 3.15(c). These results are similar to the fit results with the full fitting function in Fig. 3.14.

Similarly, we present a typical fit with a purely exponential function [3]

$$f_e = A_e e^{-\beta_e x} \quad (3.34)$$

in Fig. 3.15(b). The extracted parameter β_e for different values of h and V , matches very well

the values extracted from the full fit in Fig. 3.14. To perform the above fits with Eq. (3.33) and Eq. (3.34), respectively, we again consider the logarithm of the Green's function values [3]. The fitting functions have to be modified accordingly [3]. In addition, we vary the fit interval $x_{\min} < x < x_{\max}$ in order to find the best fit. This is again chosen to be the fit with the lowest sum of absolute values of the covariance matrix elements of the fit. Further details on the Green's function fits can be found in the Appendix of Ref. [3].

Pair-pair correlations

We briefly note that one can also consider the pair-pair correlations, which directly probe the correlations between different mesons in the system defined as [3]

$$\langle \hat{b}_i^\dagger \hat{b}_j \rangle = \langle \hat{a}_i^\dagger \hat{\tau}_{\langle i, i+1 \rangle}^z \hat{a}_{i+1}^\dagger \hat{a}_j \hat{\tau}_{\langle j, j+1 \rangle}^z \hat{a}_{j+1} \rangle. \quad (3.35)$$

When mesons are tightly confined, they form a gapless LL and the meson correlation function Eq. (3.35) should exhibit a power-law decay [3, 182]. This was indeed observed by performing iDMRG calculations showing that the pair-pair correlations exhibit a power law decay for $2h \geq V$. For $2h < V$, the pair-pair correlations exhibit an exponential decay, which signals the Mott insulating state, in agreement with our analytical arguments and numerical results [3].

3.5 Summary and conclusion

In this chapter we studied phase diagrams of the paradigmatic 1 + 1D \mathbb{Z}_2 lattice gauge theory, coupled to dynamical $U(1)$ charges. In addition to the hopping term, where the dynamical charges are minimally coupled to the gauge fields, and the \mathbb{Z}_2 electric field term, which induces dynamics in the gauge fields, we also consider the NN repulsion, $V \geq 0$, among bare partons as this can be realized in cold-atom simulation experiments of such systems. We considered hard-core bosons in our one-dimensional chains. However, due to the Jordan-Wigner mapping in one-dimension [1, 3, 172, 188], hard-core bosons can be mapped to spinless fermions, and thus the results generally hold also for fermions [1, 3].

In the first part of this chapter we studied the two possible Luttinger liquid realizations [1, 160]. The parton LL is formed in the absence of the confining \mathbb{Z}_2 electric field term. Upon introducing the NN repulsion V , the LL parameter changes for different fillings accordingly, which can be studied by mapping the system to a spin-1/2 XXZ chain, where one can utilize the Bethe ansatz [182]. In this regime, where $h = 0$, but $t, V > 0$ the system generally remains a LL for different chain fillings n . The only exception is the half-filling case where the partons can form a Mott insulating state, stabilized by $V \geq 2t$. There, the partons arrange themselves in a staggered way, where every other lattice site is filled with a parton [3]. When the electric field term is non-zero $h \neq 0$, partons confine into mesons as discussed previously in Chapter 2. There, mesons form a Luttinger liquid with rather complicated LL parameters. In the limit of strong electric field term $h \gg t$ and $V = 0$, the

mesons can be considered to be tightly confined, forming well defined hard-core particles, which can be described with a simple hard-core boson Hamiltonian with NN repulsion, derived from second order perturbation theory [160]. This mapping shows that confined mesons for $h \gg t$ at two-thirds filling, $n = 2/3$, are right at the edge of undergoing a transition to a meson Mott state.

This simple analysis of different LLs, which can be formed in the LGT, shows that half and two-thirds fillings can host interesting and very different phase diagrams with rich physics. This motivated us to study the phase diagrams of both regimes in detail in two separate sections of this chapter.

In Section 3.3 we focused on the two-thirds filling. By using analytical and numerical calculations we demonstrated that the combination of the non-local \mathbb{Z}_2 electric field term and local NN repulsion can stabilize a meson Mott state [1]. There, confined mesons arrange periodically in the lattice where every tightly confined meson (two partons on neighboring sites) is followed by a single empty lattice site. This gapped Mott state was directly probed by calculating the charge gap using the DMRG, where we uncovered a substantial charge gap for large values of h and V .

In the following Section 3.4 we studied the half-filling regime. We considered 3 tractable limits: absence of the electric field term $h = 0$, absence of the NN repulsion $V = 0$ and substantial confining field $h \gg t$, and the parton plasma regime $2h \approx V \gg t$. The analytical calculations were complemented with state-of-the-art numerical calculations, where we utilized the DMRG. More precisely, we used the MPS toolkit SYTEN [153, 154]. We uncovered a meson LL for non-zero value of h , which remains stable also for small values of the NN repulsion V . In the absence of the electric field term $h = 0$, the NN repulsion stabilizes a simple parton Mott state for $V \geq 2t$, as expected from the parton LL considerations [182]. This Mott state is destabilized by the electric field term once it approaches the line $2h = V$. There we uncovered that mesons, which are overall confined on long length scales due to the non-zero electric field term $h \neq 0$, are allowed to fluctuate between a tightly confined meson with string length $\ell = 1$ and extended meson with string length $\ell = 2$. In fact the two meson states are energetically equivalent in the limit $t \rightarrow 0$. This results in a highly frustrated regime, with strong parton fluctuations between the two meson states when hopping is reintroduced $t \ll h, V$, close to the line $2h \approx V$ [3]. In addition to the fact that at $n = 1/2$ we are at reasonably high doping, partons appear to be deconfined on short to intermediate length scales [3]. We dubbed this region as the pre-formed parton-plasma state. Signatures of such a behaviour are also revealed in numerical calculations of the Green's function that exhibits an initial power-law decay with a delayed exponential decay setting in on longer length scales. The destabilization of the Mott state is also revealed in the static structure factor calculations, which are more suitable for quantum simulation setups.

In conclusion, we revealed that at two-thirds filling both interactions work together to stabilize the meson Mott state, whereas at half-filling the two interactions compete with each other, which results in a highly frustrated regime. In both cases, the phase diagrams exhibit extremely rich physics, ready to be studied in quantum simulation setups with cold atoms.

Chapter 4

Confinement in a lattice gauge theory at finite temperature

So far, our study of the paradigmatic $1 + 1\text{D } \mathbb{Z}_2$ LGT in this thesis has been focused on its ground state properties. In this chapter, we study confinement in the $1 + 1\text{D } \mathbb{Z}_2$ LGT with matter at finite temperature. We consider the Green's function behavior and uncover a smooth confinement-deconfinement crossover as a function of temperature. In addition, we study Friedel oscillations, and sample string and anti-string length histograms obtained from snapshots, which offer a deeper understanding of confinement. Both of these observables are also motivated by quantum simulation experiments with cold atoms, where quantum many-body snapshots are naturally obtained. We show that these probes exhibit signatures of confinement already above the crossover temperature defined by the Green's function results. These results go beyond the conventional wisdom where a deconfined phase would be expected already for any finite temperature, since it is well known that the system has to be deconfined in the infinite temperature limit. We show that Friedel oscillations and string length histograms are a robust measure of confinement, which we propose as simple and reliable probes suitable for cold-atom experiments.

This chapter is based on Ref. [4], from which the content, including figures, has been adapted and extended.

4.1 Introduction

Studying LGTs at finite temperature is generally complicated and there are still many open problems: for example, understanding quark confinement in hadrons at finite temperature and their transition to a quark gluon plasma at very high temperatures [4, 25, 189]. The $1 + 1\text{D } \mathbb{Z}_2$ LGT coupled to $U(1)$ matter that we study here is a much simpler version of LGTs studied in HEP, and from such perspective can be understood as a simple toy model. However, it has direct connections to condensed matter physics, including spin liquids and high-temperature superconductivity [1, 16, 29, 30, 58, 147–149]. For these reasons, the study of finite-temperature properties of such \mathbb{Z}_2 LGT and the related nature of confinement is

extremely compelling.

Perhaps an even bigger motivation to study confinement at finite temperature in the 1 + 1D \mathbb{Z}_2 LGT comes from significant advancements in quantum simulations involving cold atoms, where LGTs generated significant interest in recent years [21–23, 26, 80, 81, 95]. In fact, significant progress in simulating LGTs with cold atoms has been made [80, 81], most notably is perhaps simulating the building blocks of the \mathbb{Z}_2 LGTs [21, 22] by utilizing the Floquet scheme [23]. Hence, quantum simulations with cold atoms could be used in the future to study confinement in LGTs for different geometries and gauge groups. Answering the question if the partons confine in a paradigmatic \mathbb{Z}_2 LGT also at finite temperature is thus an important question, which needs to be answered. Furthermore, developing realistic experimental probes capable of detecting confinement at finite temperature is also crucial for the experimental study of confinement.

In this chapter, we study the 1 + 1D \mathbb{Z}_2 LGT where dynamical $U(1)$ matter is coupled to gauge fields at finite temperature. We define the paradigmatic 1 + 1D \mathbb{Z}_2 LGT once again here for convenience [1, 3, 4, 160]

$$\hat{\mathcal{H}} = -t \sum_j \left(\hat{a}_j^\dagger \hat{\tau}_{(j,j+1)}^z \hat{a}_{j+1} + \text{H.c.} \right) - h \sum_j \hat{\tau}_{(j,j+1)}^x. \quad (4.1)$$

As before \hat{a}_j^\dagger (\hat{a}_j) are the hard-core boson creation (annihilation) operators. Furthermore, $\hat{\tau}_{(j,j+1)}^z$ and $\hat{\tau}_{(j,j+1)}^x$ are the Pauli matrices representing the \mathbb{Z}_2 gauge and electric field, respectively. In addition, for clarity we once again state the Gauss law, defined with a set of operators [1, 3–5, 121, 160]

$$\hat{G}_j = \hat{\tau}_{j-1,j}^x \hat{\tau}_{j,j+1}^x (-1)^{\hat{n}_j}, \quad (4.2)$$

which commute with the Hamiltonian $[\hat{\mathcal{H}}, \hat{G}_j] = 0$, and with each other on different lattice sites $[\hat{G}_i, \hat{G}_j] = 0$. It effectively divides the Hilbert space into different sectors, where eigenvalues $\hat{G}_j |\psi\rangle = g_j |\psi\rangle$ can take two possible values $g_j = \pm 1$. As usual we only consider the sector without any background charges, which is defined as the sector where $g_j = +1, \forall j$. Hence, when performing numerical simulations, we again eliminate the matter field via the Gauss law, and simulate the spin model; see Section 1.3 for details.

The Gauss law gives us the already well defined string anti-string picture, where the partons are connected in pairs with \mathbb{Z}_2 electric fields with equal signs. This allows us to define strings as electric field values with negative orientation (in the x -basis), and the anti-strings as electric field with positive orientation, sketched in Fig. 4.1(a) [4]. For a more in depth discussion on the string and anti-string length picture we refer the reader to Chapter 2.1.

We note that here we do not include the NN repulsion V as was the case in Chapter 3, where we studied phase diagrams in the ground state. That is because we focus solely on the study of confinement at finite temperature T . At this point we reiterate that in the ground state, the \mathbb{Z}_2 electric field term can be understood as the term, which induces a linear confining potential, by imposing an energy cost for every string. Hence, long strings become energetically unfavourable, which results in partons confining into mesons, where

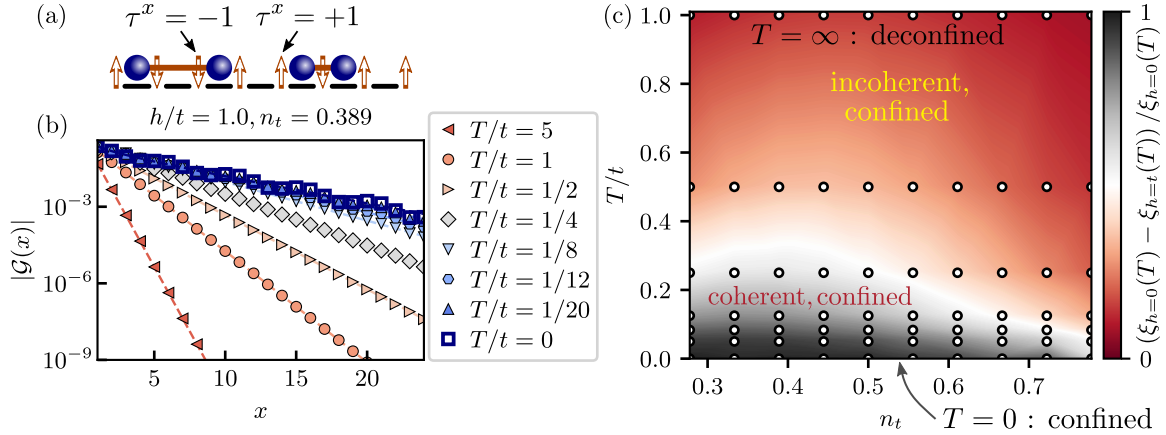


Figure 4.1: The 1 + 1D \mathbb{Z}_2 LGT coupled to dynamical matter. (a) A sketch of the system, where pairs of hard-core bosons (blue spheres) are connected by the \mathbb{Z}_2 electric strings, which denote the negative orientation of the \mathbb{Z}_2 electric field. (b) Green's function Eq. (4.5) results for different temperatures T , and constant chemical potential μ , which yields the filling $n_t = 14/36$ in the ground state. The dashed lines are the fit results with Eq. (4.6). (c) Heat map diagram of the difference between the correlation lengths for $h = 0$ and $h/t = 1$ presented as a function of the temperature T and the target filling n_t . The difference is normalized by the correlation length for $h = 0$ at the corresponding temperature T . The white dots represent the data points, from which the software triangulated the heat diagram. The white color in the heat diagram indicates the crossover regime. This figure was obtained from Fig. 1 in Ref. [4].

the string length ℓ is short. While a meson state in the limit $h \rightarrow \infty$ tends to be a state with two neighboring partons and thus $\ell = 1$, see Fig. 4.1(a), the partons bound in a meson are generally allowed to fluctuate for finite values of h and t , and thus average string lengths can be longer than $\ell = 1$. However, it is important to keep in mind that the average string length approaches the minimum possible length $\ell = 1$, already for relatively low values of h/t [160].

In order to study confinement we again consider the Green's function. In the ground state it decays exponentially in the confined phase, $h \neq 0$, and with a power-law decay in the deconfined regime, $h = 0$ [1, 3, 4, 160]. In addition, we also consider Friedel oscillations, the period of which doubles in the confined regime, and we directly consider the string and anti-string length histograms, which we obtain by sampling snapshots. To obtain our results we employ state-of-the-art MPS calculations [34, 35, 135], which we explain in the next section.

More precisely, we make use of the concept of quantum purification [164, 165, 167, 168], which we also outline in Section 1.3.3. The trick is to attach an additional or "ancillary" lattice site to every physical lattice site. The ancillary lattice sites are entangled to the physical lattice sites and act as a thermal bath in the system [4, 164]. The starting point of our calculations is to first implement the state $|\psi(\beta = 0)\rangle$ where the physical sites are maximally entangled with the ancillary lattice sites. At this point we define the inverse

temperature $\beta = 1/T$. To obtain the maximally entangled state we calculate the ground state of the so called *entangler* Hamiltonian [167]; see the Section 1.3.3 for more details. This state is obtained by using DMRG implemented with MPS [35]. After that we perform imaginary time evolution [135] of the maximally entangled state with the \mathbb{Z}_2 LGT Hamiltonian Eq (4.1), which gives us its state at finite temperature T [164, 165, 167]. This can be formally expressed as [135, 164, 165, 167]

$$|\psi(\beta)\rangle = e^{-\beta\hat{\mathcal{H}}/2} |\psi(\beta = 0)\rangle, \quad (4.3)$$

where $|\psi(\beta)\rangle$ is the pure state of the extended system representing the finite temperature state. We note that the Hamiltonian in the imaginary time evolution acts only on the physical lattice sites [135, 164]. Any thermodynamic average of a physical observable can be then calculated as [164, 167]

$$\langle \hat{\mathcal{O}} \rangle = \frac{\langle \psi(\beta) | \hat{\mathcal{O}} | \psi(\beta) \rangle}{\langle \psi(\beta) | \psi(\beta) \rangle}. \quad (4.4)$$

The thermodynamic average of the energy of the system, $\langle \hat{\mathcal{H}} \rangle$, and other physical observables like the chain filling, thus slowly converge to the ground state values with increasing β . This can be understood as the thermal state being cooled down to the ground state $T = 0$, when $\beta \rightarrow \infty$. A few examples of this are shown in Fig. 4.2. We note that all time evolutions are carried out at finite chemical potential μ . When presenting data we usually label the so called target filling n_t , which is the filling to which it converges in the ground state at $\beta \rightarrow \infty$. Hence, presented data at finite temperature T always deviate from the target filling as shown in Fig. 4.2. For relevant inverse temperature $\beta t > 1$, it typically does not deviate more than $\Delta N = \pm 2$, however for higher temperature $T/t > 1$, such deviations are more significant, which one has to keep in mind when analyzing the results. Nevertheless, we label the data below in terms of target fillings n_t , as it is more convenient, and we anyway study in detail only the regime where $\beta T > 1$, where the deviations become small as described above. In this chapter we typically consider $L = 36$ lattice sites, which results in $2L + 2 = 74$ spin sites in the finite temperature calculations [4].

More technical details on the quantum purification method, explicitly defined spin Hamiltonian to which we map the original \mathbb{Z}_2 LGT model, as well as for the details on how we define the ancillary lattice sites in the MPS chain are presented in Section 1.3.3 and in the Supplementary material of Ref. [4].

4.2 Green's function at finite temperature

In order to study confinement at finite temperature we consider the \mathbb{Z}_2 gauge invariant Green's function, defined as [1, 3, 4, 160]

$$\mathcal{G}(i-j) = \left\langle \hat{a}_i^\dagger \left(\prod_{i \leq \ell < j} \hat{\tau}_{\ell, \ell+1}^z \right) \hat{a}_j \right\rangle. \quad (4.5)$$

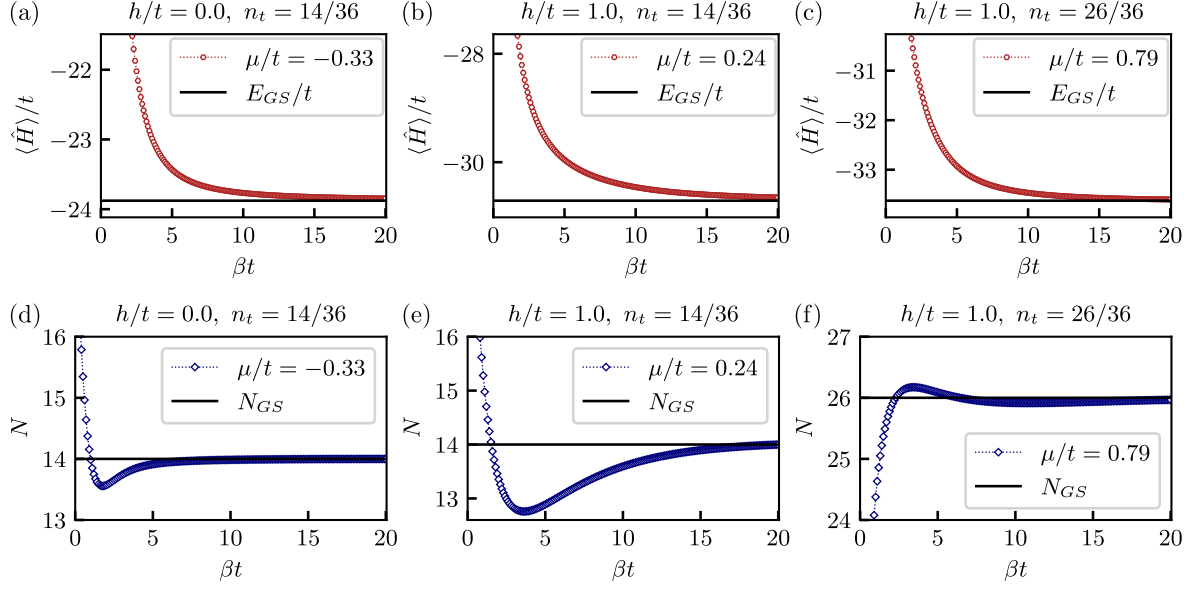


Figure 4.2: Finite temperature expectation values of observable in the 1 + 1D \mathbb{Z}_2 Hamiltonian, Eq. (1.85), after eliminating matter via Gauss law as a function of inverse temperature $\beta = 1/T$ at fixed chemical potential μ . The first row shows the expectation value of the Hamiltonian $\langle \hat{H} \rangle$, and the second row shows the parton number N . The parameter values for (a) and (d) are $h = 0$, $\mu/t = 0.33275$, which yields the filling $n_t = 14/36$ in the ground state, which we also refer to as the target filling. For (b) and (e) the parameter values are $h/t = 1$, $\mu/t = 0.242$, which yields $n_t = 14/36$ in the ground state. For (c) and (f) the parameters are $h/t = 1$, $\mu/t = 0.7875$, which yields $n_t = 26/36$. In all cases the finite temperature value of $\langle \hat{H} \rangle$ and n converges to the ground state results marked with horizontal lines labeled E_{GS} and N_{GS} , respectively. This figure was obtained from Fig. S3 in the Supplementary material of Ref. [4].

As already stated before, in the ground state $T = 0$, the Green's function decays exponentially in the confined regime, and with a power-law in the deconfined regime [1, 4, 160]. The Green's function, Eq. (4.5), is a non-local, gauge invariant, correlation function. As such it will decay exponentially in both regimes for any finite temperature, $T > 0$ [4]. However, the decay rates will be different as in the confined regime, as the exponential decay will have an additional contribution coming from confined mesons. Such complex nature of the Green's function complicates the clear distinction between the confined and deconfined regime at finite temperature $T > 0$ [4]. We overcome this complication by directly comparing the decay rates of the Green's function in both regimes, and thus establish a crossover region where the thermal fluctuations begin to dominate the behaviour of the system [4].

To be more precise, we fit the Green's function results with a function that contains algebraic as well as exponential decay profiles [4]

$$f_G \propto x^{-\alpha} e^{-x/\xi}. \quad (4.6)$$

The main goal of fitting the Green's function with the above function is to extract the cor-

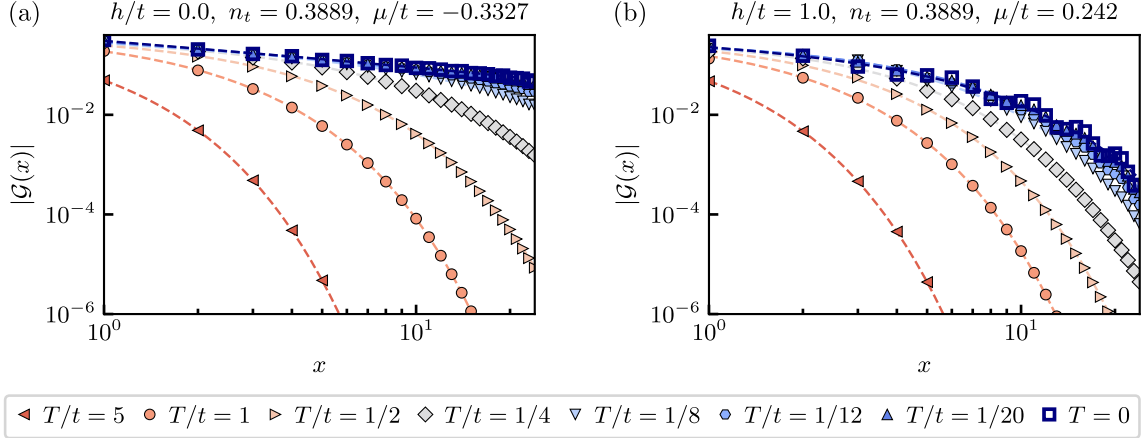


Figure 4.3: Green's function, Eq. (4.5), results shown on a log-log scale at a target filling of $n_t = 0.3889$, for different temperatures T in the regime with and without the \mathbb{Z}_2 electric field term. (a) Green's function at different temperatures T in the absence of the \mathbb{Z}_2 electric field term. The decay of the Green's function changes from a power-law in the ground state to exponential decay, which becomes stronger at higher temperature. (b) Green's function decays exponentially at any temperature when the electric field term is finite $h/t = 1$. The rate of the exponential decay increases with increasing temperature. This figure was modified from Fig. S4 in the Supplementary material of Ref. [4].

relation length, defined as ζ , which is used to parameterize the strength of the exponential decay [3]. In addition, we also define the power-law decay exponent α . For technical reasons, we in fact fit the logarithm of the data points in order to better capture the exponential nature of the Green's function behaviour. The fit function is thus modified to [4]

$$f_G = A - \alpha \log(x) - \frac{x}{\zeta}. \quad (4.7)$$

An example of the Green's function results for different temperatures T and for $h/t = 1$, together with the fit results using Eq. (4.6) can be seen in Fig. 4.1(b).

The difference between the regimes where the electric field term h is zero and non zero can be directly observed, by comparing finite temperature results of the Green's function at similar fillings n . As an example, we present the Green's function results on a log-log scale at target filling of $n_t = 14/36$ in Fig. 4.3. As can be seen in Fig. 4.3(a), the Green's function in the regime where the electric field is zero $h = 0$ decays with a power law in the ground state, $T = 0$, and exponentially at finite temperature $T > 0$. The curves at finite temperature converge towards the ground state power law decay results with decreasing temperature. The Green's function in the regime where the \mathbb{Z}_2 electric field term is non-zero $h/t = 1$, shown in Fig. 4.3(b), exhibits exponential decay already in the ground state $T = 0$, consistent with the previous results. At finite temperatures the exponential decay is stronger, with the Green's function curves again approaching the ground state results with decreasing value of temperature T . Comparing the curves at around $T/t = 0.25$ in both cases already shows that the exponential decay is much faster in the case when

$h/t = 1$. This difference is increased for temperatures below this temperature, $T/t < 0.25$, with $h = 0$, eventually converging to the power-law curve when $T \rightarrow 0$, as discussed above. Contrarily, the curves for $h = 0$ and $h/t = 1$, at $T/t = 1$, appear to have similarly strong exponential decay. This already shows that the Green's function behaviour is clearly different in both regimes ($h = 0$ and $h/t = 1$) and we thus see that mesons are confined at low temperature.

To study the Green's function behaviour more precisely, we directly compare the correlation length in the two parameter regimes: $h = 0$, for which we know that the partons in the ground state of Hamiltonian Eq (4.1) are deconfined, and $h/t \neq 0$, where we know the partons in the ground state confine into mesons. To be more precise, we consider the difference of the correlation lengths in both regimes [4]

$$\Delta\tilde{\zeta}(T) = (\tilde{\zeta}_{h=0}(T) - \tilde{\zeta}_{h=t}(T)), \quad (4.8)$$

at the same temperature T , and comparable target fillings n_t . We plot the results of the difference Eq. (4.8) normalized by the correlation length for free partons $\tilde{\zeta}_{h=0}(T)$ at the same temperature T in Fig. 4.1(c). We see that close to the ground state where $T = 0$, the correlation lengths between the regimes where $h = 0$ and $h/t = 1$ differ significantly, which indicates that partons are confined and as a result contribute significantly to the exponential decay of the Green's function. In contrast, for high temperatures $T \approx t$, the correlation lengths become comparable, meaning that exponential decay in both cases stems from thermal fluctuations. We define the crossover boundary as the region where [4]

$$\tilde{\zeta}_{h=0}(T) - \tilde{\zeta}_{h=t}(T) = \frac{1}{2}\tilde{\zeta}_{h=0}(T). \quad (4.9)$$

Our results summarized in Fig. 4.1(c) show that the crossover region is at approximately $T/t \approx 0.25$, and has a weak lattice filling dependency [4]. The filling dependency could be related to the weaker exponential decay of the Green's function at higher filling observed in the ground state due to reduced mobility of the mesons, see Section 2.3. We note that the results in Fig. 4.1(c) are plotted as a function of target filling n_t . This is the filling obtained in the ground state, $T = 0$, for a specific chemical potential μ . We once again note that imaginary time evolutions were performed for constant chemical potentials and not constant fillings n [4]. As a result, actual fillings $n(T)$, slightly deviate from the target fillings n_t for every run at $h = 0$ and $h/t = 1$, respectively [4]; see Fig. 4.2. However, we estimated that the deviations do not exceed $|n_{h=t}(T) - n_{h=0}(t)|/n(T) < 20\%$ for $T/t < 1$ [4]. We thus plot the data points in Fig. 4.1(c) as a function of n_t . Further details on the density dependence as a function of temperature, $n(T)$, for a constant chemical potential μ , can be found in the Supplement of Ref. [4].

In conclusion, the finite temperature value of the crossover temperature $T/t \approx 0.25$, obtained from the Green's function results thus show that partons remain confined for low but finite temperatures, before the thermal fluctuation begin to dominate [4].

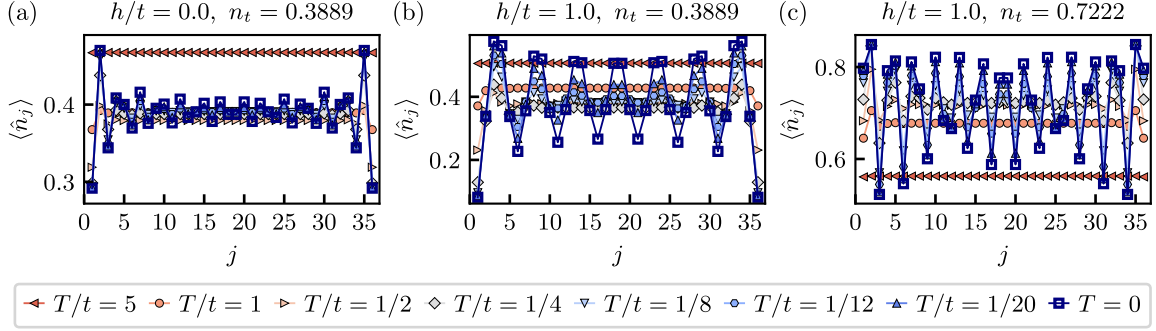


Figure 4.4: Density profile $\langle \hat{n}_j \rangle$ in the 1 + 1D \mathbb{Z}_2 LGT at different temperatures and electric field values. (a) Friedel oscillations in the density profile in the deconfined regime, $h = 0$, for target filling $n_t = 14/36 \approx 0.3889$. (b) The density profile in the confined regime $h/t = 1$, for the same target filling as in (a), $n_t = 14/36 \approx 0.3889$. (c) Friedel oscillations at higher filling $n_t = 26/36 \approx 0.7222$ in the confined regime, $h/t = 1$. The chain length in all cases is $L = 36$. This figure was obtained from Fig. S5 in the Supplementary material of Ref. [4].

4.3 Friedel oscillations at finite temperature

Next we consider the behaviour of Friedel oscillations at finite temperature. As already discussed in Section 2.3.2, the Friedel oscillations frequency halves in the confined regime in comparison to the deconfined regime [160]. In the confined regime the frequency of the oscillations equals to $k_F = \pi n$, and in the deconfined regime to $2k_F = 2\pi n$ [4, 160]. Such abrupt change of oscillation frequency is thus an indication of confinement where mesons, which remain mobile, are the well-defined constituents of the system. In the confined regime, mesons form the aforementioned LL, and scatter of the chain boundaries collectively instead of individual partons, as is the case in the deconfined case.

Density profiles at finite temperature

Similar confinement features in the Friedel oscillations should thus be visible also at finite but low temperature, as the Green's function results show that partons remain confined in this regime. For that reason we calculate the density profiles in the chain, in the regime with and without the \mathbb{Z}_2 electric field term, at different temperatures T and fillings n . The main goal is to investigate whether similar features can be seen at finite temperature as in the ground state. We present some of the typical density profiles $\langle \hat{n}_j \rangle$ for different values of filling and the electric field term h in Fig. 4.4.

We can directly compare the oscillations in Fig. 4.4(a) and Fig. 4.4(b), where we present the density profiles at different temperatures T for zero and finite electric field term h , at the same average target filling, $n_t = 14/36$. The frequency in the ground state in the deconfined state $h = 0$ is indeed double the frequency in the confined regime $h/t = 1$. This can be observed by simply counting the number of peaks in the density profiles in the both regimes, since the target filling is the same. For low temperatures, $T/t \leq 0.25$, the density

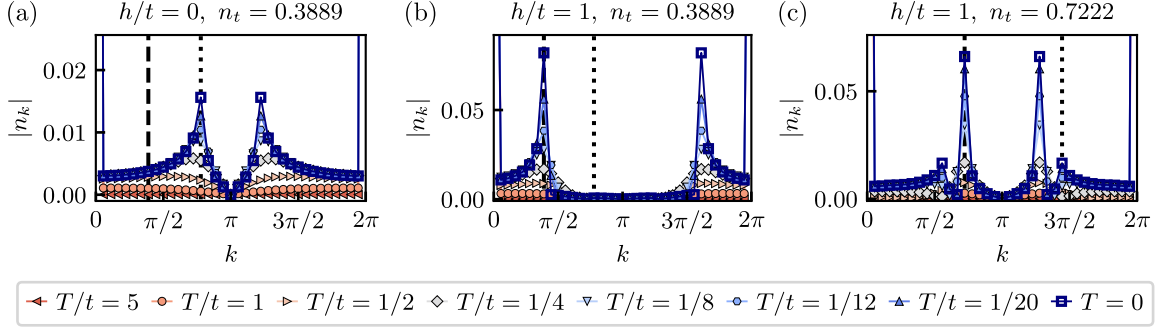


Figure 4.5: Fourier transformation Eq. (4.10), of the density profiles in 1 + 1D \mathbb{Z}_2 LGT. (a) Friedel oscillations of the deconfined partons for $h = 0$, exhibit well defined peaks at $k = 2\pi n$ (vertical dotted line), for temperatures below $T/t \leq 0.25$. At higher temperature such peaks are not observed as the amplitude of the oscillations decreases. (b) Friedel oscillations in the regime where $h/t = 1$, exhibit well defined peaks at $k = \pi n$ (vertical dashed line), for temperatures below $T/t \leq 0.25$, indicating a confined meson gas. (c) At higher filling $n = 26/36$ we observe a small peak at $k = 2\pi n$ as well as high peaks at $k = \pi n$, for low temperature $T/t \leq 0.25$. Both of these peaks rise together with decreasing temperature T . This figure was obtained from Fig. 2 in Ref. [4].

profiles are similar to the ground state profiles, however the amplitude of the oscillations decreases with increasing temperature, until the density profiles become almost completely flat. This is also in part due to the fact that our results were performed at finite chemical potential and not finite filling. Thus for very high temperatures $T/t > 1$, densities in fact start to deviate significantly from the target value and approach half filling, $n = 1/2$ [4]; see previous Section 4.1 for the details on the filling as a function of temperature, $n(T)$ at finite chemical potential μ .

At higher fillings for $h/t = 1$, the density profiles become less clear due to increased frequency; see Fig. 4.4(c). However, the number of peaks still corresponds to the number of mesons in the system, which means that the doubling of the Friedel frequency can still be observed.

Fourier transformation of density profiles at finite temperature

In order to study the frequency of the Friedel oscillations in greater detail, we perform a Fourier transformations of the density profile $\langle \hat{n}_j \rangle$, which we define as [4]

$$n_k = \frac{1}{L} \sum_{j=0}^{L-1} e^{-ikj} \langle \hat{n}_j \rangle. \quad (4.10)$$

Here, we discretize the momentum modes as $\Delta k = 2\pi/L$, where L is the system size per usual definition [4]. Typical results of the Fourier transformation of the density profiles are presented in Fig. 4.5. These are in fact the Fourier transformations of the density profiles presented in Fig. 4.4.

We immediately see a big difference between the $h = 0$ and $h/t = 1$ results at the same target filling $n_t = 14/36$ in Fig. 4.4(a) and 4.4(b). In the deconfined regime in the ground state, we observe a well pronounced peak at $k = 2\pi n$, consistent with previous results. At finite temperature these peaks become broader, and are hard to resolve above $T/t > 0.25$. On the other hand with decreasing temperature, the shapes and height of the peak converges towards the peak in the ground state.

In the regime where $h/t = 1$, we observe a well defined peak at $k = \pi n$, in the ground state $T = 0$ [4], which is consistent with the behaviour of the Friedel oscillations in the confined regime [160]. The peak at $k = \pi n$ becomes visible at around $T/t \approx 0.25$, and converges to the ground state peak shape with decreasing temperature T . In the regime $h/t = 1$, and at filling $n_t = 0.3889$ we do not observe any peaks at $k = 2\pi n$ at any temperature T [4]. This means that there is no transition from a meson to a parton gas at high temperature, which would be reflected in a shift of peaks from $k = \pi n$ to $k = 2\pi n$, with increasing temperature T [4]. This suggests that mesons are already pre-formed well above the crossover temperature, defined via the Green's function correlation lengths [4]. Calculations of Friedel oscillations therefore suggest that partons are in fact confined up to high temperatures, where the thermal fluctuations completely dominate the system and thus destroy any coherence in pre-formed mesons [4].

However, at higher fillings $n > 0.5$, we do observe additional, small peaks at $k = 2\pi n$, even in the regime where the electric field term is finite, $h/t = 1$. As an example we present the case at $n = 0.7222$ in Fig. 4.5(c). Further analysis shows that both peaks appear simultaneously at low temperature $T/t \lesssim 0.25$, and there is no shift between the two peaks with lowering the temperature [4]. We thus associate the peaks at $k = 2\pi n$, at higher fillings with fluctuation of holes. In fact holes at such fillings are significantly more mobile, i.e., can move more easily than mesons, which explains why they can contribute to the weak peaks at $k = 2\pi n$.

The analysis of the Friedel oscillations at finite temperature shows that partons are confined into mesons for low temperatures $T/t \lesssim 0.25$, as we showed that frequencies of the Friedel oscillations are half the expected frequency for the free partons. In addition, we show that there is no transition from the meson Friedel oscillation frequency $k = \pi n$ to the higher, free parton Friedel oscillation frequency $k = 2\pi n$ with increasing temperature in the regime with non-zero electric field term. The peaks found after the Fourier transformation at $k = \pi n$ in the confined regime at low temperature, merely decrease with increasing temperature until they can no longer be resolved. This means that mesons are pre-formed already at temperatures well above the crossover temperature defined by the Green's function [4]

4.4 String length distributions at finite temperature

In addition to the Green's function behaviour and the frequency of the Friedel oscillations, we also consider the string-length distributions in our system at finite temperature. As already discussed in Section 2.3.3, string and anti-string length distributions can be used

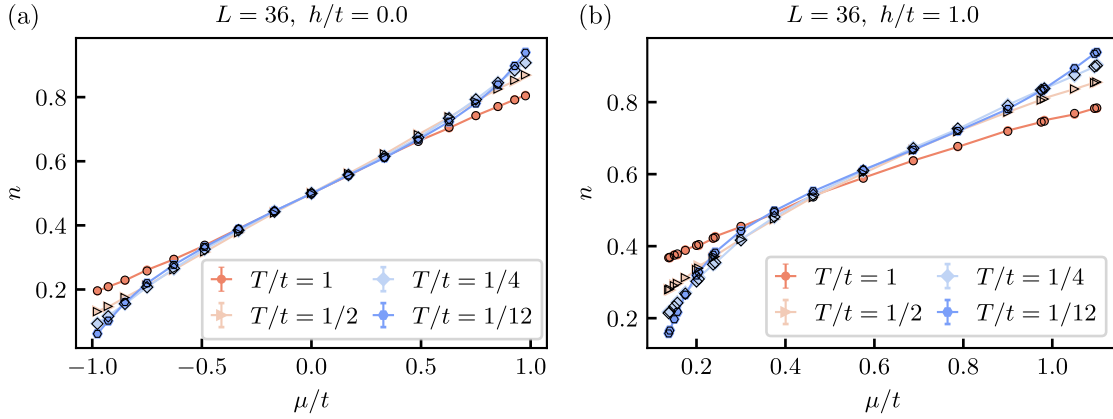


Figure 4.6: Chain filling n in the \mathbb{Z}_2 LGT after integrating out the matter degrees of freedom via Gauss law, as a function of the chemical potential μ , at different temperatures T , obtained via snapshots and directly from MPS. Filled markers without a margin represent the chain filling obtained from averaging the snapshot fillings, and open black markers represent the densities obtained directly from the MPS. Data derived from the snapshots also contains error bars. (a) In the deconfined regime, $h/t = 0$, the curves are symmetric around $\mu = 0$. (b) For non-zero electric field $h/t = 1$, the curves become asymmetric and are shifted to higher values of μ . Markers of the same shape represent the same temperature T . Notice also how the densities tend to $n = 1/2$, for higher temperature, as observed in Fig. 4.2. This figure was obtained from Fig. S6 in the Supplementary material of Ref. [4].

as a robust measure of confinement. Here we study the distribution of string lengths (distances between partons connected by the same string), and the distribution of the anti-string lengths (distances between consecutive mesons), which gives us a direct microscopic probe of confinement. That is because electric strings should be on average much shorter than the anti-strings when partons confine into mesons. Thus, differences in the string and anti-string length distributions are a robust measure of confinement.

The main motivation to study the string-length distributions, however, comes from the fact that this is an experimentally easily accessible quantity [4]. It can be obtained by considering on-site density-resolved snapshots in ultra-cold atomic setups. In such a snapshot one has to extract the lengths between odd-even and even-odd particles, respectively in order to obtain the string and anti-string lengths.

We study whether the string and anti-string length distributions are also an effective probe of confinement at finite temperature and thus be used in experiments. We sample snapshots from MPS states [180], where we use the so called perfect sampling [181], which is implemented in SYTEN [153, 154]. We sample in the electric field basis, i.e., the eigenbasis of the $\hat{\tau}^x$ operators. In order to determine the length of the strings we simply consider the Gauss law, where anti-aligned electric field on the neighbouring links indicates a parton residing on the lattice site connected by the two links. After the position of partons in the lattice is established, we record the lengths of strings residing between odd-even partons, and the lengths of anti-string, which connect the even-odd partons (as labeled from the start of the chain). We typically sample 2000 snapshots for every data set [4]. Such high

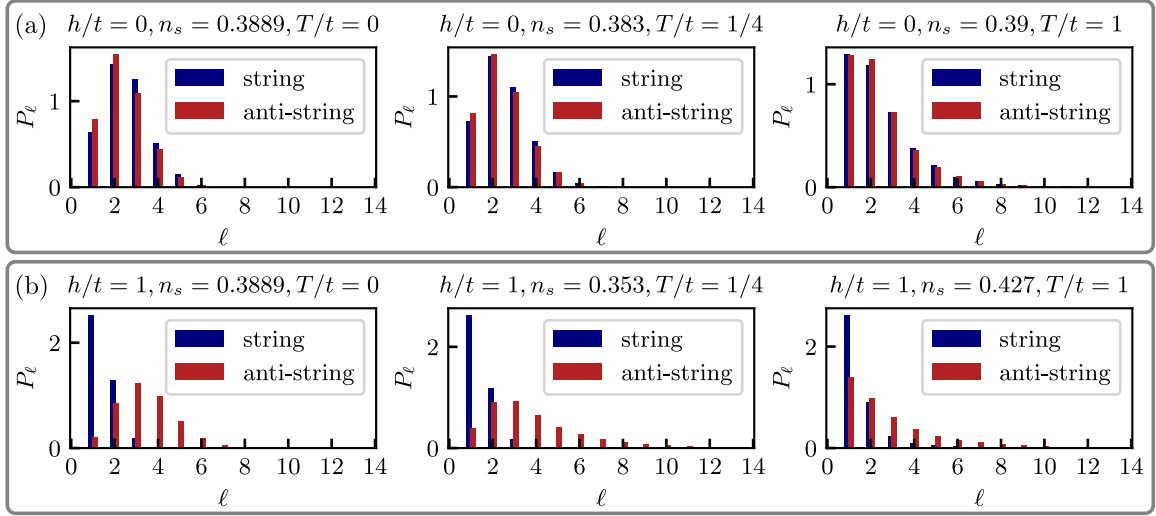


Figure 4.7: String and anti-string length distributions obtained from snapshots of the $1+1\text{D } \mathbb{Z}_2$ LGT after eliminating the matter. (a) The string-length and anti-string length distributions are qualitatively similar in the deconfined regime $h = 0$, across different temperature values T . (b) In the regime where the \mathbb{Z}_2 electric field is finite $h/t = 1$, we observe different (bimodal) distributions for strings and anti-strings in the ground state and at low temperatures $T/t \lesssim 0.25$. At high temperatures the distributions become similar to each other with both having a peak at $\ell = 1$, however these peaks are higher for string than anti-string lengths, indicating pre-formed mesons. This figure was obtained from Fig. 3 in Ref. [4].

number gives us expectation values for the average chain fillings very close to the results obtained directly from the MPS state; see Fig. 4.6. The error bars, which are typically smaller than the data points, are defined as $\sigma/\sqrt{N_s}$, where σ is the standard deviation and N_s is the total snapshot number [4]. In addition, such benchmark serves as a consistency check that snapshots in the \mathbb{Z}_2 electric basis correctly capture the correct physics. More details on snapshots can be found in the Supplement of Ref. [4].

The results at an approximate filling of $n = 14/36$, for different electric field values and temperatures are presented in Fig. 4.7. In the ground state, $T = 0$, we see a clear difference in the distributions in the confined and deconfined states. In the deconfined regime $h = 0$, string and anti-string distributions have the same shape and are almost exactly the same, see Fig. 4.7(a). This indicates that there is no difference between strings and anti-strings since there are no fluctuations in the gauge fields and partons are completely free. In the confined state, however, we see that string lengths are peaked at $\ell = 1$; see Fig. 4.7(a). This indicates that partons are confined into mesons, with most of them being tightly confined. There is also a finite weight at $\ell = 2$, which indicates that mesons are indeed mobile, as their hopping is governed by the second order hopping process of partons, where, the intermediate state is the extended meson $\ell = 2$ [160]. We discussed this process in Section 3.2.2.

For the ground state we thus show that the confined phase exhibits a clear bimodal distribution of string and anti-strings. We observe similar features as in the ground state at low temperatures up to the approximate crossover temperature defined by the Green's

function calculations, $T/t \lesssim 0.25$ [4]. For increasing temperatures $T \geq t$, we observe that the distributions at approximately same filling and different values of the electric field h , become similar to each other. In both regimes the distributions peak at $\ell = 1$, and exhibit long tails. Such change of behaviour across $T/t \approx 0.25$ is consistent with the smooth crossover between the confined and deconfined regime at $T \rightarrow \infty$, observed in the Green's function behaviour and the Friedel oscillations [4]. Furthermore, in Fig. 4.7 we see that at fairly large temperature $T = t$, which is above the crossover region $T/t \approx 0.25$, the height of the string peaks at ℓ is higher than the anti-string length peak. This is consistent with the Friedel oscillation results, and thus supports our claim that mesons are pre-formed at high temperatures relative to the crossover temperature [4].

Our results thus show that string-length distributions could be a good probe of confinement in quantum simulation experiments, which naturally operate at finite temperature. The observed crossover temperature $T/t \approx 0.25$, lies within the reach of current cold atom capabilities in terms of temperature [19, 55].

4.5 Summary and conclusion

In this chapter we studied confinement of partons into mesons in the paradigmatic $1 + 1D$ \mathbb{Z}_2 LGT with dynamical matter at finite temperature. We employed state-of-the-art MPS calculations in order to obtain results in the ground state and at finite temperature. As a first probe of confinement, we considered the gauge invariant Green's function, which directly probes confinement of partons into mesons. In the ground state the Green's function decays exponentially in the confined state and with a power-law in the deconfined state. At finite temperature, thermal fluctuations result in exponential decay in both regimes. In order to extract the confinement contribution to the overall exponential decay, we compared the correlation lengths in the regime with and without the confining electric field term. We uncover a smooth confinement-deconfinement crossover at around $T/t \approx 0.25$. In addition to the Green's function, we also considered Friedel oscillations whose frequency halves in the confined regime. The behaviour of these frequencies corresponding to the confined phase suggests that mesons are pre-formed at high temperatures well above the crossover region [4]. Furthermore, we consider string and anti-string length distributions, which we obtain from snapshots that we numerically sample from our MPS. We show that string-length distributions are a reliable and robust probe of confinement at finite temperature, which could be readily obtained in cold atom experiments.

In conclusion, our results demonstrate that partons confine into mesons also at low but finite temperature and thus pave the way towards understanding the confinement crossover in the paradigmatic $1 + 1D$ \mathbb{Z}_2 LGT coupled to dynamical matter [4]. On the one hand, confinement in the ground state limit $T = 0$ is clear from previous studies, where it was shown that partons confine for any non-zero value of the electric field term $h \neq 0$ [1, 160]. On the other hand, conventional reasoning tells us that in the infinite temperature limit $T \rightarrow \infty$, partons will always be deconfined [4]. From these limits one could speculate that any finite temperature could lead to deconfinement. By uncovering the smooth confinement-

deconfinement crossover, we thus showed that finite temperature behaviour is more intricate than expected. Furthermore, the confinement signatures at high temperatures, i.e., the signatures of pre-formed mesons at temperatures above the crossover temperature shows us that confinement is in fact far more resilient to temperature fluctuations than what one could naively expect. We thus showed that the study of confinement in a simple \mathbb{Z}_2 LGT is already within reach of the existing quantum simulators, both digital and analog [4]. Furthermore, we expect that our results could be extended to \mathbb{Z}_2 LGTs with more complicated interactions, and also to mixed dimensional settings, where multiple \mathbb{Z}_2 LGT chains could be coupled. All of these systems could be also implemented in quantum simulation platforms. Finally, our results could also help to understand confinement at finite temperature in LGTs with more complicated gauge groups [4].

Chapter 5

Phase diagram of the \mathbb{Z}_2 LGT with superconducting terms

In this chapter we discuss a phase diagram of the 1 + 1D \mathbb{Z}_2 LGT with dynamical charges, where we include pair creation and annihilation terms. As a result, the global parton number is not conserved since the \mathbb{Z}_2 LGT Hamiltonian breaks the global $U(1)$ symmetry [5]. Moreover, superconducting (SC) terms somewhat complicate the physical picture as the parton number fluctuations can give rise to new effects. A \mathbb{Z}_2 gauge field coupled to $U(1)$ matter, which we studied so far, can be thus considered as a special case of the \mathbb{Z}_2 LGT, and adding SC terms can be understood as a generalization of the problem studied so far. However, we note that in terms of quantum simulation experiments, $U(1)$ symmetry corresponding to the parton number conservation can be implemented more naturally.

The Hamiltonian studied in this chapter is also known as the gauged Kitaev chain, which was initially studied by Borla et al. in Ref [119]. In the first part of this chapter we reproduce the phase diagram from Ref [119], by considering entanglement entropy calculations.

We then proceed in a different direction, by focusing on the microscopic picture of confinement in this system, and reach slightly different conclusions about confinement of the partons in the limit of a static \mathbb{Z}_2 gauge field [5]. We employ DMRG calculations, which we combine with analytical calculations to further validate our numerical calculations and to distinguish different phases of the system. We consider the gauge invariant Green's function, and string length histograms obtained from snapshots, sampled from MPS. Besides the confinement at finite \mathbb{Z}_2 electric field term, we also find signatures of confinement in the limit of static gauge field, where the electric field term is zero $h = 0$. This regime can be related to the transition between the symmetry protected topological (SPT) state and the trivial state in the context of Kitaev chain [87, 161, 190–192], to which the system can be mapped in the limit when $h = 0$ [5, 119]. In addition, the results presented in this chapter show that due to the SC terms no Mott transitions or frustrated regimes are possible, on account of parton pair fluctuations. The SC terms thus significantly change the phase diagram of the \mathbb{Z}_2 LGT coupled to matter.

We note that in the next Chapter 6, we develop a mean field theory description for

the extended \mathbb{Z}_2 LGT studied here. The results from this chapter will be used to directly benchmark the mean-field theory for the \mathbb{Z}_2 LGT.

This chapter is based on Ref. [5], from which the content, including figures, has been adapted and extended.

5.1 Introduction

As already mentioned, in this chapter we study the 1 + 1D \mathbb{Z}_2 LGT where dynamical charges are coupled to gauge fields. The Hamiltonian contains pair creation and annihilation terms, i.e., the superconducting terms, which explicitly break the $U(1)$ symmetry in the charges and thus the global parton number is not conserved. In a way, such \mathbb{Z}_2 LGT formulation is closer to the formulations found in HEP as there is no global $U(1)$ symmetry related to the parton number conservation.

In certain limits, the \mathbb{Z}_2 LGT with SC terms can be mapped to known systems. In the absence of the \mathbb{Z}_2 electric field term, the system maps to the Kitaev chain [160, 190], which can be furthermore mapped to a spin-1/2 system [161, 191, 192]. To be more precise: it maps directly to the transverse field Ising model [160, 161, 191, 192]. The Kitaev chain was studied extensively as it exhibits a transition between topological and trivial states [190]. By considering the Green's function and string-length distributions, we uncover that the trivial state, which in terms of the transverse field Ising chain can also be considered as the spontaneously symmetry broken (SSB) phase [119], exhibits confining features [5]. This goes against the conventional understanding of confinement in the \mathbb{Z}_2 LGT with matter, since the gauge fields are static as the electric field term is zero $h = 0$. Hence, there is no linear confining potential related to the \mathbb{Z}_2 electric strings. Nevertheless, partons appear confined as they emerge directly from the SC terms that induce parton pair fluctuations. This means that the transition from the symmetry-protected topological (SPT) phase to the trivial state in the Kitaev chain can be understood as the confinement transition in the \mathbb{Z}_2 LGT picture [5]. As such it can be related to the topological confinement transition found in the 2 + 1D toric code [5, 32, 87, 193].

By including the \mathbb{Z}_2 electric field term, the system becomes more complicated and the direct mapping to the Kitaev chain is not possible. However, in a certain limit we show that the \mathbb{Z}_2 LGT can be mapped to a transverse field Ising model with additional longitudinal field. In the regime when the \mathbb{Z}_2 electric field term is finite, partons are always confined into mesons. The system corresponds to the confined Higgs phase, similar to the one found in the 2 + 1D \mathbb{Z}_2 LGT [5, 32, 119]. At high fillings the system again transitions to a SSB phase, where partons remain confined.

5.2 Hamiltonian of the \mathbb{Z}_2 LGT coupled to matter with superconducting terms

We again consider a one-dimensional system, where hard-core bosons are coupled to a \mathbb{Z}_2 gauge field. We define a generalized version of the 1 + 1D \mathbb{Z}_2 LGT by including the pair

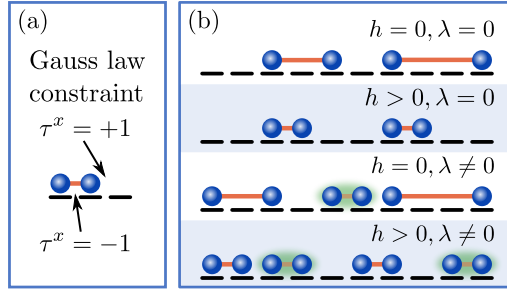


Figure 5.1: A sketch of a 1 + 1D \mathbb{Z}_2 LGT with SC terms, Eq. (5.1), where dynamical charges are coupled to a \mathbb{Z}_2 gauge field. (a) Sketch of the Gauss law constraint in the physical sector, which enforces anti-aligned \mathbb{Z}_2 electric field values across an occupied lattice site. The constraint allows us to define strings where the electric field value is negative $\tau^x = -1$ (orange line), and anti-string where $\tau^x = +1$ (no line). (b) Sketches of different regimes in the 1 + 1D \mathbb{Z}_2 LGT Eq. (5.1). The upper row representing the deconfined, free parton state, the second row (from top) represent the confined regime, where partons confine into mesons, the third row (from top) represents the regime with non-zero SC terms $\lambda \neq 0$, which explicitly breaks the parton number conservation, and the last row is a sketch of a confined regime with non-zero SC term. This figure was modified from Fig. 1 in Ref. [5].

creation and annihilation terms, which explicitly break the global $U(1)$ symmetry of the charges as [5, 119]

$$\hat{\mathcal{H}} = -t \sum_{\langle i,j \rangle} \left(\hat{a}_i^\dagger \hat{\tau}_{\langle i,j \rangle}^z \hat{a}_j + \text{H.c.} \right) - h \sum_{\langle i,j \rangle} \hat{\tau}_{\langle i,j \rangle}^x + \lambda \sum_{\langle i,j \rangle} \left(\hat{a}_i^\dagger \hat{\tau}_{\langle i,j \rangle}^z \hat{a}_j^\dagger + \text{H.c.} \right) + \mu \sum_j \hat{n}_j. \quad (5.1)$$

Here $\hat{a}_i^\dagger \hat{\tau}_{\langle i,j \rangle}^z \hat{a}_j^\dagger$ is a gauge invariant term that creates a pair of partons on neighbouring sites, and μ is the chemical potential term that is used to control the parton filling in the chain [5]. All other terms remain the same as in the previous chapters in this thesis: the hardcore bosons are defined on the lattice sites with creation (annihilation) operators defined as \hat{a}_j^\dagger (\hat{a}_j), and $\hat{\tau}_{\langle i,j \rangle}^z$ represents the \mathbb{Z}_2 gauge field defined on the links; see for example Eq. (2.1) in Chapter 2. We also note that in our numerical calculations we always consider $t > 0$. In addition to the Hamiltonian, we also consider the Gauss law, which we once again state here for convenience [1, 3–5, 121, 160]

$$\hat{G}_j = \hat{\tau}_{j-1,j}^x \hat{\tau}_{j,j+1}^x (-1)^{\hat{n}_j}. \quad (5.2)$$

We again choose the physical sector where the eigenvalues of Eq. (5.2) on every lattice site equal to $g_j = +1$. This results in \mathbb{Z}_2 electric field values being anti-aligned across an occupied lattice site, allowing us to define strings that connect parton pairs; see Fig. 5.1(a). The added superconducting term in the Hamiltonian proportional to $\propto \lambda$, explicitly breaks the $U(1)$ symmetry of the charges. It adds or removes a pair of partons that explicitly breaks the total parton conservation in the system [5]. Although the average parton number in the system is thus not conserved, we define the average parton number density in the usual

way as [5]

$$n = \frac{1}{L} \sum_{j=1}^L \langle \hat{n}_j \rangle. \quad (5.3)$$

5.2.1 Mapping to the one-dimensional superconducting model

As already mentioned before, the Hamiltonian Eq. (5.1) is also known as the *gauged Kitaev chain* studied by Borla et al. in Ref. [119]. In order to better understand the newly defined \mathbb{Z}_2 LGT Hamiltonian Eq. (5.1), we provide the explicit connection to the Kitaev chain. We consider the case where the \mathbb{Z}_2 electric term is zero $h = 0$ [5]. In this regime there is no induced dynamics in the gauge fields and we can eliminate the charges by using the definition of dressed partons \hat{b}_j , Eq. (2.20); see Section 2.4.1 for details. After eliminating the gauge field $\hat{\tau}^z$, the Hamiltonian Eq. (5.1) can be expressed as [5]

$$\hat{\mathcal{H}} = -t \sum_j \left(\hat{b}_j^\dagger \hat{b}_{j+1} + \text{H.c.} \right) + \lambda \sum_j \left(\hat{b}_{j+1}^\dagger \hat{b}_j^\dagger + \text{H.c.} \right) + \mu \sum_j \left(\hat{b}_j^\dagger \hat{b}_j - 1/2 \right), \quad (5.4)$$

where we added a constant offset in the chemical potential term. This energy offset does not change the physics, but brings our Hamiltonian in a well known form. Namely, the Hamiltonian in Eq. (5.4) resembles the *spin-polarized superconductor* model [161, 190]. However, the particles in Eq. (5.4) are hard-core bosons and not fermions, as is the case in the one-dimensional superconductor model [190]. In one-dimension we can map spinless fermions to hard-core bosons and vice-versa by employing the Jordan-Wigner transformation [172, 188]. This is done by attaching the so called Jordan-Wigner strings to the operators in order to obtain the correct commutation or anti-commutation relations [172, 173, 188]. The hard-core boson creation and annihilation operators can thus be expressed in terms of spinless fermions as [172, 173, 188]

$$\hat{b}_j^\dagger = \left(\prod_{l < j} e^{i\pi \hat{n}_l} \right) \hat{c}_j^\dagger, \quad \hat{b}_j = \left(\prod_{l < j} e^{-i\pi \hat{n}_l} \right) \hat{c}_j, \quad (5.5)$$

where \hat{c}_j^\dagger , (\hat{c}_j) is the spinless fermion creation (annihilation) operator [5]. Inserting the relation in Eq. (5.5) into Hamiltonian Eq. (5.4), we obtain the one-dimensional superconducting model studied by Kitaev [5, 161, 190]

$$\hat{\mathcal{H}}_K = -t \sum_j \left(\hat{c}_j^\dagger \hat{c}_{j+1} + \text{H.c.} \right) - \lambda \sum_j \left(\hat{c}_{j+1}^\dagger \hat{c}_j^\dagger + \text{H.c.} \right) + \mu \sum_j \left(\hat{c}_j^\dagger \hat{c}_j - 1/2 \right). \quad (5.6)$$

Due to the Jordan-Wigner transformation the sign of the SC interaction changed, $\lambda \rightarrow -\lambda$. We note that in literature the term is usually written with a positive sign in front of the SC term in Eq. (5.6) [5, 119, 161, 190]. Furthermore, the model Eq. (5.6) in the parameter regime when $\lambda = -t$ (in our notation) is often called the Kitaev chain [119, 191].

With the use of the dressed parton notation and the use of the Jordan-Wigner transformation we showed that the \mathbb{Z}_2 LGT where hard-core boson are coupled to gauge fields,

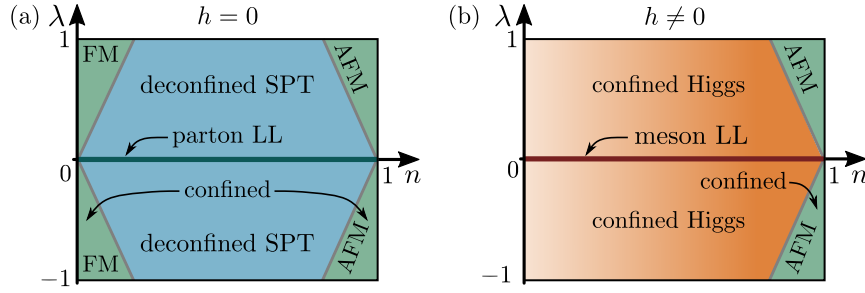


Figure 5.2: Qualitative sketch of the phase diagram of a 1 + 1D \mathbb{Z}_2 LGT with SC terms Eq. (5.1). (a) In the limit of static gauge fields, when $h = 0$, the system forms a parton LL on the line $\lambda = 0$. For non-zero SC term $\lambda \neq 0$, the system can be mapped to a Kitaev chain, and exhibits a symmetry protected topological (SPT) state for $t < 2|\mu|$, with a transition to a ferromagnetic (FM) symmetry broken state at low filling and a transition to an antiferromagnetic (AFM) symmetry broken state at high filling. (b) For non-zero electric field term, the system forms a confined meson LL on the special $\lambda = 0$ line. For non-zero value of the SC term $\lambda \neq 0$, the system forms a Higgs phase up to high chain filling, where the system transitions to an AFM symmetry broken phase. This figure was modified from Fig. 1 in Ref. [5].

maps to the Kitaev chain in the limit when the \mathbb{Z}_2 electric field is zero [5]. We will use this mapping throughout this chapter in order to help with the interpretation of numerical results. A similar mapping was already performed by Borla et al. in Ref. [119]. In that work, authors focused on the so called gentle gauging of the Kitaev chain, and mapped out the phase diagram as a function of the chemical potential μ [119]. We will focus more on the microscopic picture of confinement, and its dependence on the chain filling n , which we control with μ [5].

The Kitaev chain has been studied extensively in context of topology and Majorana edge modes [87, 161, 190–192]. It has been shown that the Kitaev chain exhibit a transition to a topological state for $t/|\mu| < 2$ [190]. We also note that the sign of the SC term in the \mathbb{Z}_2 LGT Eq. (5.1) can be changed via a unitary transformation [5]

$$\hat{a}_j^\dagger \rightarrow i\hat{a}_j^\dagger, \quad \hat{a}_j \rightarrow -i\hat{a}_j. \quad (5.7)$$

This means that the sign of λ is arbitrary, as in both cases $|\lambda| > 0$ opens a SC gap, and the system can form a non-trivial state [5, 119]. However, Borla et al. [119] argued that since the above mapping does not preserve the time reversal symmetry, phases at $\lambda > 0$ and $\lambda < 0$ are distinct.

Finally, we note that the Kitaev chain, Eq. (5.6), for $\lambda = -t$, maps to a transverse field Ising model [5, 161]

$$\hat{\mathcal{H}}_I = -J \sum_j \hat{\sigma}_j^x \hat{\sigma}_{j+1}^x - h_z \sum_j \hat{\sigma}_j^z. \quad (5.8)$$

Here we expressed the spin operators in the x and z component in terms of Pauli operators $\hat{\sigma}^x$ and $\hat{\sigma}^y$, respectively. The mapping of the Kitaev chain to the spin model is done by

considering different z -component spin states as empty or occupied lattice sites, and by using the Jordan-Wigner transformation [161]. The mapping is exact and the parameters map as: $J = t$ and $h_z = -\frac{\mu}{2}$ [5, 161].

Equipped with the mapping of the \mathbb{Z}_2 LGT at $h = 0$ to the Kitaev chain, we turn to numerical calculations of the full 1 + 1D \mathbb{Z}_2 LGT, Eq. (5.1), using the DMRG in order to determine the phase diagram. The numerical results obtained in the next section are summarized in Fig. 5.2 for $h = 0$ and $h \neq 0$, respectively.

5.3 Phase diagram in the absence of particle conservation

Numerical calculations are performed by using DMRG [34, 35]. We again make use of the MPS toolkit SYTEN [153, 154]. As all of the numerical simulations of the \mathbb{Z}_2 LGT in this thesis before, we use the mapping to the spin-1/2 model, by making use of the Gauss law, where we constrain our system to the physical sector [5]. We refer the interested reader to Section 1.3.2 for more details on this mapping. The mapping is exact, as due to the Gauss law constraint, the system can be fully determined by the gauge fields, represented by the Pauli matrices [1, 3–5, 7]. We again consider that the system starts and ends with a link (gauge field) and consider OBC. The system size in the calculations is $L = 96$, which results in $L + 1 = 97$ links, and we consider the bond dimension up to $\chi = 1024$ [5].

5.3.1 Entanglement entropy

In order to establish the phase diagram of the \mathbb{Z}_2 LGT Eq. (5.1) we consider the entanglement entropy $S(x)$, extracted from ground state MPS [5]. The entanglement entropy $S(x)$, is calculated by effectively dividing the system into two subsystems A and B , with the cut on lattice site x . We can thus consider that the length of the subsystem A equals to x , and the length of the subsystem B is therefore $L + 1 - x$ [5]. Since we simulate the gauge fields, the cuts are thus exactly on the lattice site x , i.e. between links $\tau_{x-1,x}$ and $\tau_{x,x+1}$ [5]. In the MPS implementation bipartite entanglement entropy can be easily extracted by cutting the bond between two sites that reside on the boundary of system A and B [35].

Entanglement entropy values

We perform the calculations at different values of the electric field term h , for different value of the SC paring λ , and chemical potential μ , which in turn controls the filling n . The results for the entanglement entropy where we divided the system in half, $S(x = L/2)$, are presented in Fig. 5.3 as a function of average filling n , and SC term λ .

When the \mathbb{Z}_2 electric field term is zero, $h = 0$, the system is symmetric around half filling $n = 0.5$; see Fig. 5.3(a). We see a clear change of the entanglement entropy value at low and high fillings, which can be connected to the the topological transition in the Kitaev chain at $\mu = \pm 2t$ [5, 190]. This is made explicit in Fig. 5.4, where we plot the entanglement entropy $S(L/2)$ as a function of chemical potential μ , and we observe sharp drops at $\mu = \pm 2t$ of the entanglement entropy for $h = 0$.

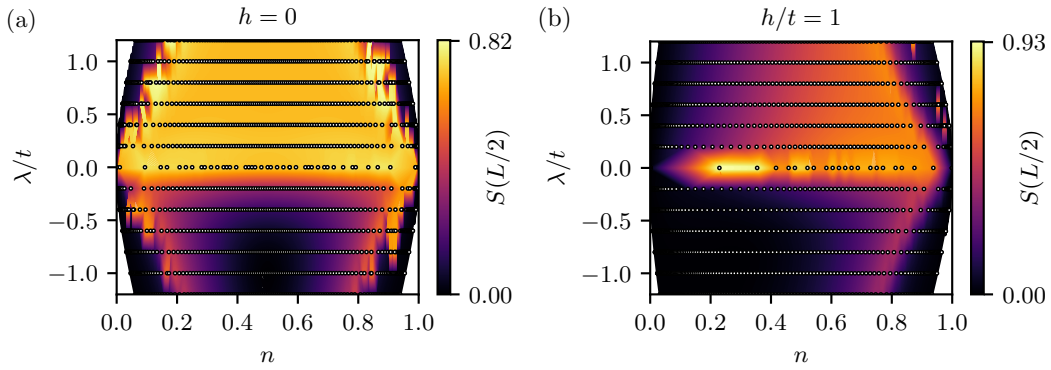


Figure 5.3: Entanglement entropy in the middle of the chain $S(x = L/2)$ for the 1 + 1D \mathbb{Z}_2 LGT, Eq. (5.1), after integrating out the charges by taking into account the Gauss law constraint, as a function of filling n and SC term λ . (a) Entanglement entropy results in the absence of the \mathbb{Z}_2 electric field term $h = 0$, where we observe trapezoid shapes for $|\lambda| > 0$, symmetric around half filling $n = 0.5$, with abrupt change of values for low fillings $n \lesssim 0.15$ and high fillings $n \gtrsim 0.85$. (b) For non-zero electric field, $h/t = 1$, the entanglement entropy gradually increases with filling n . At high fillings $n \gtrsim 0.85$ the value again rapidly decreases. This figure was modified from Fig. 2 in Ref. [5].

For non-zero electric field term, $h/t = 1$, the symmetry around half filling, $n = 1/2$, is not present any more; see Fig. 5.3(a). This is a result of broken particle hole symmetry that is apparent in Eq. (3.9) [1, 2]. Instead, we observe gradual increase of the entanglement entropy with filling, until it rapidly drops for $n \approx 0.85$.

We also observe interesting behaviour for different sign of the SC term λ . We generally obtain substantially higher values of the entanglement entropy for $\lambda > 0$ in comparison to $\lambda < 0$, for zero and non-zero value of the electric field term h . At zero electric field term, $h = 0$, and positive value of the SC term, $\lambda > 0$, we observe a plateau of substantial entanglement entropy, which narrows with increasing value of λ [5]. An outline of a similar shape can be also seen for $\lambda < 0$, with a difference that in the area close to $n \approx 0.5$, the value of the entanglement entropy is low; see Fig. 5.3(a). However, the value of entanglement entropy does increase at the same low and high fillings n , where the abrupt change happens for $\lambda > 0$. For non-zero electric field term $h/t = 1$, the abrupt drop of the entanglement entropy at high fillings also occurs sooner, that is for lower fillings n , with increasing value of $|\lambda|$.

This symmetric behavior around $\lambda = 0$ lines, although with different absolute values of the entanglement entropy, indicates that a similar transition might be taking place [5]. As we mentioned before, a gauge transformation $\hat{a}_j \rightarrow e^{i\frac{\pi}{2}} \hat{a}_j$, shows that the system is equivalent for $\pm\lambda$ [5]. However, it has non-trivial effects on the entanglement entropy calculations since the spin Hamiltonian, to which we exactly map our system by taking into account the Gauss law constraint, has a slightly different form [5]; see also Chapter 1.3 for details.

The entanglement entropy value on line $\lambda = 0$ is always substantial for zero and non-

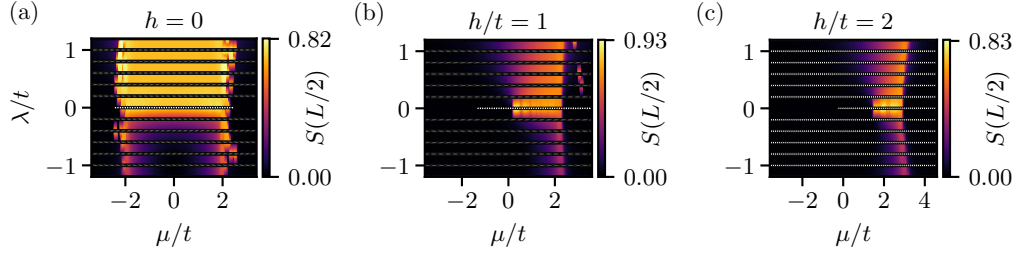


Figure 5.4: Entanglement entropy in the middle of the chain $S(x = L/2)$ for the 1 + 1D \mathbb{Z}_2 LGT, Eq. (5.1) after eliminating matter via Gauss law, as a function of the chemical potential μ and SC term λ . (a) For $h/t = 0$, we observe sharp change of the entanglement entropy at $\mu = \pm 2t$. (b) For finite electric field term, $h/t = 1$, there is a more graduate onset of the entanglement entropy with increasing μ , until it drops again dramatically at $\mu > 2t$. (c) The same affect is even more apparent with increasing electric field term, $h/t = 2$. This figure was modified from Fig. 14 in Ref. [5].

zero value of the electric field h [5]. From previous discussion, we already known that the $\lambda = 0$ line corresponds to the parton or meson LL, for $h = 0$ and $h/t = 1$, respectively, as the parton number is conserved and charges possess a global $U(1)$ symmetry. In the next section, where we extract the central charge, we show that these special $\lambda = 0$ lines are indeed critical and correspond to gapless LL [5]. In addition, we investigate the apparent transitions at $n \lesssim 0.15$ and $n \gtrsim 0.85$.

Central charge from entanglement entropy

In infinite, gapped systems entanglement entropy generally saturates to a constant value with the increase of the subsystem size x [194]. Differently, close to phase transitions and in quantum critical regimes the entanglement entropy diverges [194]. In fact, close to the transition point, the behaviour of the low lying excitations can be described by conformal field theory (CFT) [194–196]. By using CFT, the dependence of the entanglement entropy on the position of the cut x , in a system with OBC, was calculated analytically and can be expressed as [5, 194–196]

$$S(x) = S_0 + \frac{c}{6} \log \left[\left(\frac{2L'}{\pi} \right) \sin \left(\frac{\pi x}{L'} \right) \right]. \quad (5.9)$$

Here, we defined the spin chain length after integrating out the matter as $L' = L + 1$, S_0 is a non-universal constant, and c is the central charge [5]. Due to open boundary conditions, our calculations contain Friedel oscillations, which we mitigate by normalizing the entanglement entropy profiles by the local on-site parton density, $n(x)$, as [5, 197, 198]

$$\tilde{S}(x) = \frac{S(x)}{n(x)} n, \quad (5.10)$$

where n is the total average parton filling [5].

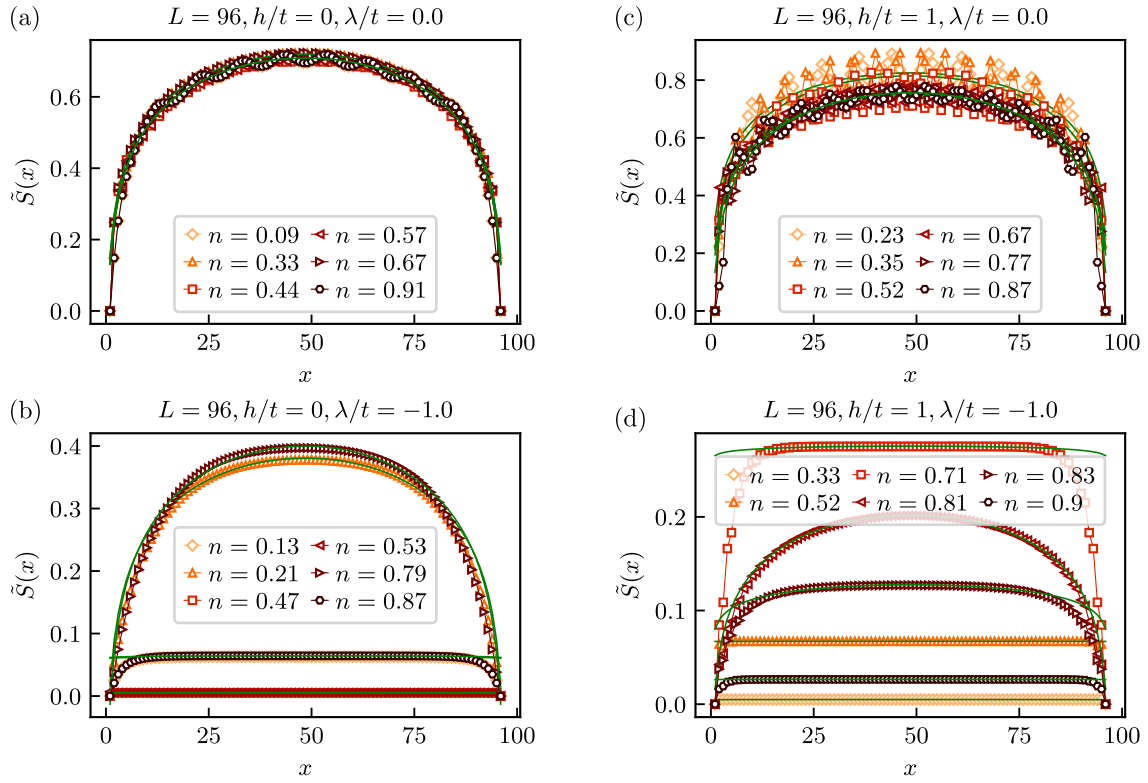


Figure 5.5: Fit of the normalized entanglement entropy $\tilde{S}(x)$ with Eq. (5.10), in the \mathbb{Z}_2 LGT after eliminating the matter via Gauss law. (a) Normalized entanglement entropy curves $\tilde{S}(x)$ for different fillings n almost coincide for $h = \lambda = 0$, and exhibit a nice curvature. (b) For $h/t = 0$ and $\lambda = 0$, similar curvature can be observed, however prominent Friedel oscillations are still observed despite normalization in Eq. (5.10). (c) In the regime when $h = 0$, and $\lambda/t = -1$, the profile of $\tilde{S}(x)$ is flat for most of the fillings n that are away from criticality. Curvature is observed only close to $n \approx 0.2$ and $n \approx 0.8$, which signals a phase transition, consistent with results in Fig. 5.3. (d) When both terms are non zero, $h/t = 1$ and $\lambda/t = -1$, the normalized entanglement entropy profiles are once again flat for most of the fillings, except fillings approaching $n \approx 0.8$. This suggests a transition only at such high fillings, $n \approx 0.8$. The green lines denote the fits. This figure was obtained from Fig. 15 in Ref. [5].

In order to extract the central charge c , we fit Eq. (5.9) to our numerical results for the entanglement entropy normalized by the local density, $\tilde{S}(x)$, as described by Eq. (5.10). We fix the value of the length to L' , so the other fit parameter that remains, besides c , is S_0 [5]. As already mentioned before we do not analyze it as it is non-universal [5]. Some of the typical fits are presented in Fig. 5.5. Normalized data points, $\tilde{S}(x)$, for $\lambda = 0$, exhibit similar curvature across all fillings. For $h = 0$ and $\lambda = 0$, better results were obtained by taking into account the particle-hole symmetry for the free partons and normalize the

entanglement entropy profile for $n > 0.5$ as [5]

$$\tilde{S}(x) = \frac{S(x)}{1 - n(x)}(1 - n). \quad (5.11)$$

For fillings $n < 0.5$, we simply used Eq. (5.10). As a results, the curves for $h = \lambda = 0$ almost coincide; see Fig. 5.5(a). The extracted value of the central charge is close to the analytical value of $c = 1$ for free partons [1, 5, 119, 160]. For finite electric field term $h/t = 1$ but zero SC term $\lambda = 0$, Friedel correlations are still prominent despite the normalization in Eq. (5.10). However, the extracted central charge is also there close to $c = 1$, which signalises gapless meson LL [1, 5, 119, 160].

For finite SC term $\lambda/t = -1$, the entanglement profiles appear to be flat for most of the fillings n . Flat profile of $\tilde{S}(x)$ suggest that the system is gapped and away from criticality. However, for $h = 0$ and $\lambda/t = -1$, the profiles $\tilde{S}(x)$ acquire curvature for low $n \approx 0.2$, and high fillings $n \approx 0.8$ that suggests a phase transition. The extracted values are $c = 0.64 \pm 0.01$ for $n = 0.21$ and $c = 0.72 \pm 0.01$ for $n = 0.79$ [3]. For $h/t = 1$ and $\lambda/t = -1$, similar observation can be made, however in this case only at high filling $n \approx 0.8$.

In all cases we only fit the interval $15 < x < L - 15$, in order to capture correctly also the flat entanglement entropy profiles [5]. However, we note that Eq. (5.9) generally holds only close to quantum criticality and extracted value $c = 0$ simply shows that we are not close to that regime [5, 194]. In addition, we discard the fits with errors bigger than $\Delta c = \pm\sqrt{0.01}$, for $h = 0$, and $\lambda \neq 0$. Furthermore, for $h/t = 1$, we discard fits with errors bigger than $\Delta c = \pm\sqrt{0.05}$ [5]. We estimate the errors from the square root of the covariance matrix element of the fit [5]. In some cases our numerical calculations gave results where some of the data points were missing. We discard that data as well [5].

Extracted values for c for different values of the electric field term h , as a function of filling n and SC term λ are presented in Fig. 5.6. The parameter regime is the same as in Fig. 5.3. For any value of the \mathbb{Z}_2 electric field term, we observe that the central charge results are symmetric in the $\lambda = 0$ axis. Furthermore, we no note that away from quantum criticality or transition, entanglement entropy profiles become flat and there is no associated curvature to $S(x)$. Away from criticality the system is gapped and we thus expect that the extracted central charge values from our fits are zero $c = 0$ [5]. In other words: the region with non-zero central charge value corresponds to a quantum criticality, where the system is gapless [5, 194].

We first analyze the results when the electric field term is zero $h = 0$, which we present in a heat map in Fig. 5.6(a). We observe that the central charge c is non-zero on the line $\lambda = 0$, and on the lines at low and high filling, for non-zero value of the SC term $|\lambda| > 0$ [5]. To be more precise, the lines away from $\lambda = 0$ form the trapezoid shape, which corresponds to the sharp drop/change of the entanglement entropy value in the center of the chain $S(x = L/2)$, already observed in Fig. 5.3(a). The approximate line at low fillings is at around $n \approx 0.15$, and the approximate line at high filling is at $n \approx 0.85$, with slight dependence on λ , making the region inside the lines narrower with increasing value of $|\lambda|$. The central charge value on the line where $\lambda = 0$ is close to $c = 1$, which corresponds to

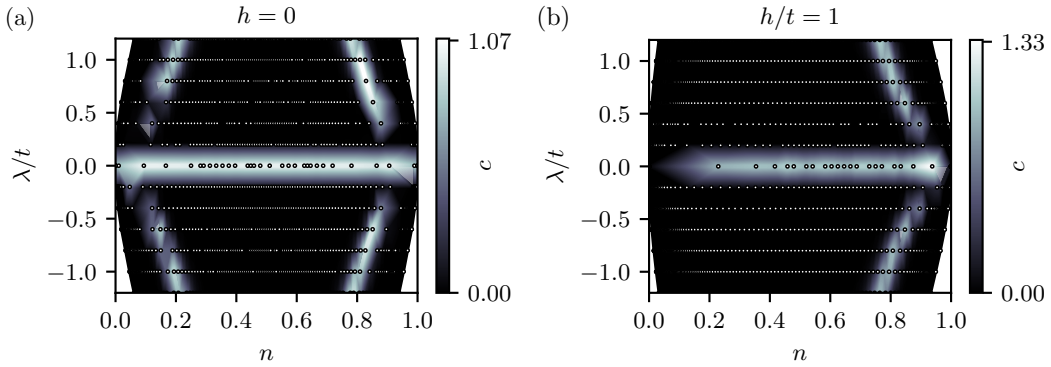


Figure 5.6: Central charge results extracted by fitting Eq. (5.10) to the numerical entanglement entropy results in the \mathbb{Z}_2 LGT Eq. (5.1) after integrating out the matter fields. (a) In the absence of the \mathbb{Z}_2 electric field term $h = 0$, we extract central charge values close to $c = 1$, on the $\lambda = 0$ line, which corresponds to parton LL. For $\lambda \neq 0$ we obtain lines with non-zero value of $c > 0$. These lines correspond to the boundary of the topological regime, which transitions to trivial regimes at low and high fillings. (b) For non-zero value of the electric field term $h/t = 1$, we again obtain central charges close to $c = 1$ on the $\lambda = 0$ line. These, in contrast to the $h = 0$, correspond to the meson LL. For non-zero SC term $\lambda \neq 0$, we obtain non-zero value of c only at high fillings. This is where the confined Higgs phase transitions to a symmetry broken AFM states for $n \gtrsim 0.85$. This figure was modified from Fig. 3 in Ref. [5].

the gapless LL of free partons [1, 5, 119, 160].

The central charge values on the lines away from $\lambda = 0$ are slightly lower. In fact, by relating the \mathbb{Z}_2 LGT back to the Kitaev chain, to which the system maps in the limit when $h = 0$, we can link these lines with the transition to the topological phase at $|\mu| = 2|t|$ observed in the Kitaev chain [5, 190, 191]. The topological non-trivial region is the regime where the values correspond to $|\mu| < 2|t|$ [5, 190, 191]. In the diagram in Fig. 5.6(a) the chemical potential, which corresponds to $|\mu| < 2|t|$, results in finite range of fillings [5]

$$0 < n_{c1} < n < n_{c2} < 1, \text{ for } |\lambda| > 0. \quad (5.12)$$

This means that the non-zero central charge lines at $n_{c1} \approx 0.15$ and $n_{c2} \approx 0.85$ correspond to the boundary of the topological phase [5]. The trivial state lies outside the area bounded by these line, i.e., for lower $n < n_{c1}$ and higher $n > n_{c2}$ fillings. At the transition between the topological and trivial states in the Kitaev chain the value of the central charge equals to $c = \frac{1}{2}$ [5, 199]. Our fit results overshoot this value and thus the value for c is slightly overestimated. However, generally we do get results lower than $c < 1$ [5]. We note that this deviation comes from the fact that the transition point is hard to determine exactly and convergence of the DMRG is more involved the closer we approach it. Since entanglement entropy depends on the bond dimension of the system, the DMRG thus demands larger bond dimensions close to the transition.

Now we turn to the central charge results for non-zero electric field term $h/t = 1$,

presented in Fig. 5.6(b). Similar as for the $h = 0$ case, we also observe non-zero value of the central charge on the line $\lambda = 0$, for $h/t = 1$ at any lattice filling [5]. The value is once again close to $c = 1$, which means that confined partons form a gapless meson LL [1, 5, 160]. Most notably, however, is the absence of a line with non zero central charge at low filling, $n_{c1} \approx 0.15$, away from $\lambda = 0$. We attribute this to the loss of the particle-hole symmetry [5]. The line at high filling remains, with central charge slightly lower, $c < 1$, than on the $\lambda = 0$ line and is thus similar to the case for $h = 0$, where it should approach $c = 0.5$ [5]. Similar feature was observed already in the entanglement entropy value in the center, $S(L/2)$, in Fig. 5.3(b). Due to the presence of only single transition line away from $\lambda = 0$ line for $h \neq 0$, we conclude that we only obtain a trivial state for $|\lambda| > 0$ in the regime when the \mathbb{Z}_2 electric field is non-zero, in agreement with results by Borla et al. [119]. We identify the region for non-zero electric field up to high filling as the confined Higgs state, which transitions to a symmetry broken anti-ferromagnetic (AFM) state at approximately $n_{c2} \approx 0.85$ [5, 119].

We also briefly comment on the nature of the topological trivial states for low $n_{c1} \lesssim 0.15$ and high $n_{c2} \gtrsim 0.85$ fillings. These correspond to ferromagnetic (FM) and AFM states of the \mathbb{Z}_2 electric fields, and are thus SSB state [5]. We once again note, that for non-zero value of the \mathbb{Z}_2 electric field term only transition at high fillings $n_{c2} \gtrsim 0.85$ remains. The SSB states can be understood by considering the Gauss law constraint to the physical sector [5]. Namely, for such low/high fillings the chain is close to being completely empty/full. In the case the chain is nearly empty, the \mathbb{Z}_2 electric fields across almost every lattice sites are aligned, and thus we expect a nearly perfect FM state. In the opposite case at high filling, the chain is almost completely full and across every lattice site the \mathbb{Z}_2 electric fields are anti-aligned. This statement can be made even more explicit by considering the spin-1/2 Hamiltonian after integrating out the charges [5]. For $\lambda = -t$, the spin Hamiltonian reduces to a simple Ising model with transverse and longitudinal fields [5]; see Eq. (1.84) in Chapter 1.3. Hopping and pairing terms take up the role of the transverse field, electric field term corresponds to the longitudinal field, and chemical potential term corresponds to the Ising interaction [5]. The AFM state of the \mathbb{Z}_2 electric field thus corresponds to large positive chemical potential $\mu > 0$, which remains stable for low values of both transverse and longitudinal fields [5, 200]. On the contrarily, the FM state of the \mathbb{Z}_2 electric field is stabilized for large negative values of the chemical potential $\mu < 0$ [200, 201]. For non-zero value of the longitudinal field $h \neq 0$, the chemical potential yielding finite filling n , shifts to larger values of μ [5], away from $\mu = -2|t|$ [200–202]. This explains why there is no transition at low fillings $n_{c1} \lesssim 0.15$, when $h/t = 1$. More details on the transverse field-model is given in Chapter 6, where we reveal that the Mean-field theory of the 1 + 1D \mathbb{Z}_2 LGT coupled to matter is an Ising model with transverse and longitudinal field [5].

The results of the entanglement entropy calculations are in part summarized in a sketch of the phase diagram in Fig. 5.2. However, so far we have not yet discussed the confinement in the regime when $\lambda \neq 0$, which we do in the next section where we consider the gauge invariant Green's function and string-length histograms.

5.3.2 Confinement

In the next section we study the confinement of dynamical charges in the generalized 1 + 1D \mathbb{Z}_2 LGT where gauge fields are coupled to matter Eq. (5.1). We consider the Green's function behaviour [1, 3–5, 160], which can be understood as the generalization of the Wilson loop, and the string length distributions extracted from snapshots, which are experimentally easily accessible [4, 5]; see also Chapter. 2.1.

Green's function

To probe confinement of individual partons into mesons we consider the \mathbb{Z}_2 gauge invariant Green's function, which we already defined in this work multiple times. For convenience we once again define it here [1, 3–5, 160]

$$\mathcal{G}(|x - x_0|) = \left\langle \hat{a}_{x_0}^\dagger \left(\prod_{x_0 \leq \ell < x} \hat{\tau}_{\ell, \ell+1}^z \right) \hat{a}_x \right\rangle. \quad (5.13)$$

We note that the Green's function decays with a power law in the deconfined regime, and exponentially in the confined regime, as was shown for the case when $\lambda = 0$, for $h = 0$ and $h \neq 0$, respectively [1, 160].

Here, we are thus mainly interested in the Green's function behavior for different values of the SC term λ in the regimes with and without the \mathbb{Z}_2 electric field term h . For completeness, we start with the Green's function behavior in the well known regime $\lambda = h = 0$, where partons are deconfined. As can be seen in Fig. 5.7(a), we indeed observe a power law decay for that parameter regime, which is a clear indication that partons are deconfined. In addition, we consider the other well known regime, where the \mathbb{Z}_2 electric field term is finite $h/t = 1$, but the SC term is kept zero $\lambda = 0$, presented in Fig. 5.7(c). Here partons confine into mesons and the Green's function decays exponentially, which we already discussed in Chapter 2. Note that Fig. 2.3 is in fact Fig. 5.7, without sub-figures (b) and (d).

Next, we consider the Green's function for non-zero value of the SC term $\lambda \neq 0$. In Fig. 5.7(b) we show the behaviour in the regime where the \mathbb{Z}_2 electric field term is zero $h = 0$, but the SC term is finite $\lambda/t = -1$, which is much different from the behavior when $\lambda = 0$ [5]. On the one hand, for intermediate chain fillings $0.2 \lesssim n \lesssim 0.8$, Green's function has a nearly constant value as a function of distance x . On the other hand, at low $n \lesssim 0.2$ and high fillings $n \gtrsim 0.8$, Green's function decays exponentially. From the entanglement entropy calculations in the previous section, we know that the system has a transition to SSB states at these low and high fillings. Furthermore, we know that the \mathbb{Z}_2 LGT for $\lambda = -t$ can be mapped to the transverse field Ising model. At such low or high fillings, the \mathbb{Z}_2 electric field is spontaneously ordered, $\langle \hat{\tau}_{(i,j)}^x \rangle \neq 0$ [5]. As discussed, at low filling, $n \lesssim 0.2$, the the \mathbb{Z}_2 electric field ordering is ferromagnetic, and at high fillings $n \gtrsim 0.8$ the ordering is anti-ferromagnetic [5]. This is discussed in greater detail in the next Chapter 6, where we compare the polarization of the electric field in the original and the mean-field theory model. For low filling, the polarization of the electric field becomes substantial, as it is the order parameter of the ferromagnetic state [5]. From such perspective we thus

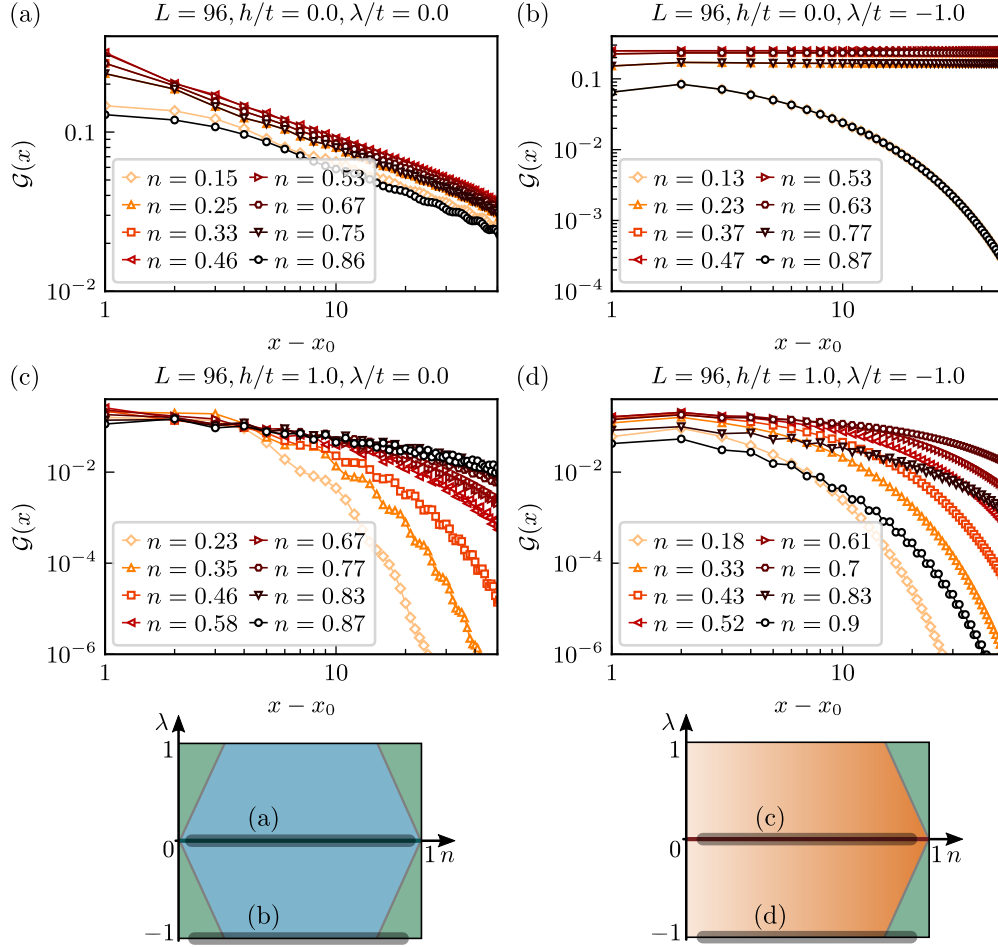


Figure 5.7: Green's function Eq. (5.13) for the generalized 1 + 1D \mathbb{Z}_2 LGT with SC terms Eq. (5.1), after eliminating matter via Gauss law, for different parameter values h, λ and filling n . (a) Green's function decays with a power-law in the free parton regime $h = \lambda = 0$. (b) For non-zero value of the SC term $\lambda/t = -1$, and $h = 0$, Green's function remains nearly constant for fillings $0.2 \lesssim n \lesssim 0.8$. For lower $n \lesssim 0.2$ and higher fillings $n \gtrsim 0.8$, it decays exponentially, signaling a confined state. (c) For non-zero electric field term $h/t = 1$, and zero SC term $\lambda = 0$, we obtain an exponential decay, the rate of which decreases with increasing filling as the mesons become less mobile due to higher filling. (d) When both the \mathbb{Z}_2 electric field term and the SC term are non-zero, $h/t = 1, \lambda/t = -1$, the Green's function decays exponentially across all fillings n . The decay becomes weaker with higher filling up until $n \approx 0.8$, when it starts to become stronger again, indicating transition to the AFM state for the electric field. To avoid boundary effects the initial lattice site as defined in Eq. (5.13) was set to $x_0 = 30$ in a chain of length $L = 96$. Below the results we added the phase diagrams with the highlighted parameter regime for each sub-figure. This figure was modified from Fig. 4 in Ref. [5].

see that spin fluctuations in a nearly FM or AFM state directly correspond to parton pair fluctuations, which makes them effectively confined. We again note that convergence close to the transition was more demanding and it was thus hard to determine at what precise filling the transition occurs [5]. One of the simple checks of convergence was already to verify that the Green's function results are the same for $n \leftrightarrow 1 - n$ due to the particle-hole symmetry for $h = 0$, which can be indeed seen in Fig. 5.7(a) and 5.7(b).

Finally, when we also include non-zero \mathbb{Z}_2 electric field term $h/t = 1$, for finite SC term $\lambda/t = -1$, the Green's function decays exponentially for any lattice filling n , as can be seen in Fig. 5.7(d). There is an interesting effect on how strong is the exponential decay as a function of filling n . The rate of the Green's function exponential decay is decreasing with increasing chain filling n , up to approximately $n \lesssim 0.8$ [5]. For higher fillings, $n \gtrsim 0.8$, the rate of the decay starts to increase. This is different than the behaviour in the regime when $h \neq 0$, $\lambda = 0$, where the rate of the exponential decay decreases with increasing filling up to the fully filled chain [5]. The behaviour for $h, \lambda \neq 0$ can be explained by the transition to the AFM state at high fillings, which occurs at approximately $n_{c2} \approx 0.8$ [5].

Green's function thus shows that partons are confined for any non-zero electric field term $h \neq 0$, also in the presence of the SC term λ . Furthermore, the Green's function indicates that symmetry broken states both for $h = 0$, and $h \neq 0$, in the presence of non-zero SC terms can be understood as confined phases. That is due to the SC term inducing pair fluctuations, meaning that partons always appear in pairs, making them confined [5].

String-length distributions

In addition to the Green's function, we also investigate the behavior of the string and anti-string length distributions, which we sample from our ground state MPS [4, 5, 153, 154, 180]. The motivation to look into string lengths is again to study the microscopic structure of mesons in greater detail. Furthermore, we study whether string length distributions could be used in quantum simulation setups. The definition of strings and anti-strings as well as the procedure to obtain the snapshots is similar to the one described in Section 2.3.3 and Section 4.4. We once note that we define strings as distances between odd-even partons, and anti-string as distances between even-odd sites. The reason for this is again due to the fact that for $h = 0$, there exist a global \mathbb{Z}_2 symmetry in the electric fields and the definition of the strings and anti-strings in terms of the sign is arbitrary. We use the MPS toolkit SYTEN to obtain snapshots [153, 154]. The only difference is that here we sample 400 snapshots for each data set, which is a slightly smaller number than in the finite temperature case in Chapter 4. In the confined regime strings are on average much shorter than anti-strings as partons confine into mesons [4, 5]]. We also note that the string length distributions provide a geometrical picture of confinement, which can be generalized to higher dimensions by considering percolation of the electric strings [5, 174].

We present the results for different parameter regimes in Fig. 5.8. The regimes where the SC term is zero $\lambda = 0$, was already discussed in Chapter 2.3.3 and we show it here again for convenience. In the regime when both SC and electric field terms are zero $\lambda = h = 0$, both distributions are nearly identically indicating that there is no distinction between strings

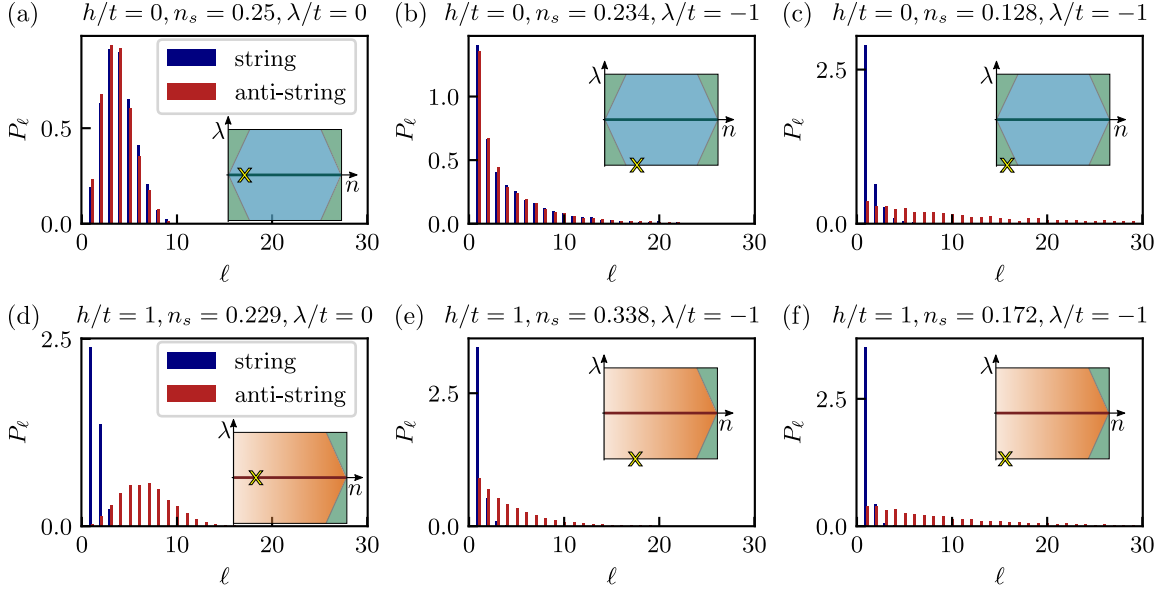


Figure 5.8: String and anti-string length distributions for the 1 + 1D \mathbb{Z}_2 LGT with SC terms Eq. (5.1), after eliminating the matter via Gauss law. The results are obtained from MPS calculations after integrating out the charges. (a) String and anti-string length distribution are identical in the free parton regime $h = \lambda = 0$. The distributions peak at a finite string length $\ell \approx 3$ for filling $n = 0.25$. (b) For non-zero SC term $\lambda/t = -1$ at filling $n \approx 0.234$ the string and anti-string length distributions are again the same when $h = 0$. However, peaks shift to $\ell = 1$, and distributions exhibit long tails. (c) For lower filling $n \approx 0.128$ but the same parameter regime as in (b), the string-length peak at $\ell = 1$ is much higher than the anti-string length peak, which signals confinement of partons. The anti-string length distribution is also much broader. (d) In the regime when $h/t = 1$ but $\lambda = 0$, we observe a clear bimodal distribution with string length peaking at $\ell = 1$, and anti string length peaking at $\ell \approx 5$, which indicates confinement. (e) In the regime when $h/t = 1$ and $\lambda/t = -1$, for filling $n \approx 0.338$, both distributions peak at $\ell = 1$, with string peak significantly higher than the anti-string length distribution, which is significantly broader. This change of distributions again signals confinement. (f) The qualitative features of distributions remains similar as in (e) for lower filling of $n \approx 0.172$, but same parameter values. In the inset of every distribution, we indicate the parameter regime in the conjectured phase diagram with a yellow "X". We also indicate the chain filling, which we obtained from the sampled snapshots with n_s that might slightly deviate from the filling obtained directly from the MPS due to statistical effects. This figure was obtained from Fig. 5 in Ref. [5].

and anti-strings, which means partons are deconfined; see Fig. 5.8(a). However, when the electric field is non-zero $h/t = 1$ without SC terms $\lambda = 0$, string-lengths are much shorter than anti-strings; see Fig. 5.8(d). Such bimodal distribution is a clear indication of confinement [4, 5].

With the presence of the non-zero SC term $\lambda \neq 0$, the shape of distributions are generally quite different. There, in all of the cases regardless of the electric field term value, distributions for string and anti-string lengths peak at $\ell = 1$. When the \mathbb{Z}_2 electric field is absent $h = 0$, and the SC term is finite $\lambda/t = -1$, the string and anti-string length distributions are nearly the same for fillings $n \gtrsim 0.2$, which indicates that partons are deconfined [5]. Furthermore as shown in Fig. 5.8(b), both string and anti-string length distributions have a peak at $\ell = 1$, and have a rather long tail when $h/t = 0$ and $\lambda/t = -1$. However, for lower fillings $n \lesssim 0.2$ and the same parameter regime, the distributions differ [5]. There, string-length distribution has a much higher peak than the anti-string length distribution, which is also much broader; see Fig. 5.8(c) [5]. This results are in agreement with the Green's function behaviour, which exhibits exponential decay for $n \lesssim 0.2$ and $n \gtrsim 0.8$, that brought us to the conclusion that there exists a confined phase for such low and high fillings [5]. Furthermore, these results confirm the microscopical picture where all of the parton fluctuations originate from the SC term and thus always appear in pairs, i.e. in a form of tightly confined meson [5]. When the chains are nearly empty most of the partons come from parton pair fluctuations. These fluctuations can be understood as a parton pair – meson – being created somewhere in the chain, and then soon annihilated, on average much sooner than one of the partons in the meson could hop. As a result, most of the partons detected in the system are confined [5]. At very high fillings the case is similar in a way that parton are barely allowed to move and all of the hole fluctuations again come in pairs. Due to the restrictions on resolving bimodal distributions at high fillings, we only considered low fillings; see the discussion in Section 2.3.3.

We can also consider the behaviour from the perspective of the spin model, which we actually simulate with DMRG, after integrating out the charges by using the Gauss law constraint [5]. As already stated before for $\lambda/t = -1$, this spin model is an Ising model with transverse and longitudinal fields [5]; see Section 1.3.2. In the regime when $\lambda/t = -1$ and $h = 0$, we are left only with an Ising model with a transverse field [5]

$$H_s = -t \sum_{\langle i,j \rangle} \hat{\tau}_{i,j}^z + 2\mu \sum_j \hat{\tau}_{i,j}^x \hat{\tau}_{j,k}^x. \quad (5.14)$$

For chemical potential $\mu < -2t$, which corresponds to fillings $n \lesssim 0.2$, the \mathbb{Z}_2 electric fields form a FM state [5, 200, 201]. In such a state, all spins are aligned and mesons appear as short lived excitation in a form of a flipped spin [5]

When both the SC term and the \mathbb{Z}_2 electric field term are non-zero, string-length distribution peaks at $\ell = 1$ are always much higher than the anti-string length distributions, which are in turn much broader and exhibit long tails; see Fig. 5.8(e) and 5.8(f). Such behaviour is a clear indication of confinement and thus in agreement with the previous numerical results [5].

With these results we have shown that string and anti-string length distributions are a reliable probe of confinement also when $\lambda \neq 0$, and can be readily used in cold atom experiments. Furthermore, these results also give us a better insight into the microscopical picture of confinement. The drawback of the string length distributions is that they are limited to fillings lower than $n \leq 2/3$. In addition, there might be some further analysis needed for obtaining snapshots in the regime when $\lambda \neq 0$ and $h = 0$. As stated in the beginning of this section, we defined strings as distances between odd-even partons. We believe that this is still a good definition to probe mesons, which arise from SC fluctuations. However at higher filling, an already existing parton in the beginning of the chain might complicate such picture and change the orientation of string and anti-string. We believe this complication was not a major problem in the analysis presented so far.

5.4 Summary and conclusion

In this chapter we studied the generalized version of the 1 + 1D \mathbb{Z}_2 LGT, Eq. (5.4), with additional superconducting terms, which break the $U(1)$ symmetry of the charges. This Hamiltonian could also be considered as the gauged Kitaev chain [119], to which there exist a direct mapping in the limit of static charges when the electric field term is zero $h = 0$ [5, 119]. We considered numerical calculations in order to obtain entanglement entropy results, from which we extract the central charge and thus determine the regions with possible quantum criticality or quantum transition. To probe confinement we also considered the Green's function and the string and anti-string length distributions.

Our results are summarized in the sketch of the phase diagram in Fig. 5.2. As already mentioned, in the regime when the \mathbb{Z}_2 electric field is zero $h = 0$, the gauge fields are static and can be eliminated [5]. There we obtain a deconfined, free parton LL in the absence of the SC term $\lambda = 0$. On the other hand when the SC term is non zero $\lambda \neq 0$, the system can be directly mapped to the superconducting model [119, 190]. The system thus exhibits transition from a SPT to trivial SSB states [119]. This transition occurs for a chemical potential $2|\mu| = |t|$ [190, 191]. In terms of lattice filling this translates to an approximate fillings value of $n \approx 0.2$ and $n \approx 0.8$ [5]. For intermediate fillings, $0.2 \lesssim n \lesssim 0.8$, the system is thus in a deconfined, SPT phase. For low $n \lesssim 0.2$ and high filling $n \gtrsim 0.8$, where the system is in the SSB phase, we show that the system exhibits confined features by considering the Green's function and the string and anti-string length distributions [5]. Confinement in this regime can be related to strong pair fluctuations, which come from the SC terms. Thus, mesons appear directly from the SC term as short lived fluctuations. By including the \mathbb{Z}_2 electric field term, the particle-hole symmetry is broken. On the special line where $\lambda = 0$ the system forms a meson LL, since partons are confined into mesons. For non-zero value of the SC term $\lambda \neq 0$, the system is in a confined Higgs phase for fillings up until $n \lesssim 0.8$, where it transitions to an AFM SSB [5, 119], both of which are confined as shown by the Green's function and the string length distributions [5].

To conclude this chapter we discuss our results in a slightly different setting and reformulate our results in a phase diagram as a function of the \mathbb{Z}_2 electric field term h and

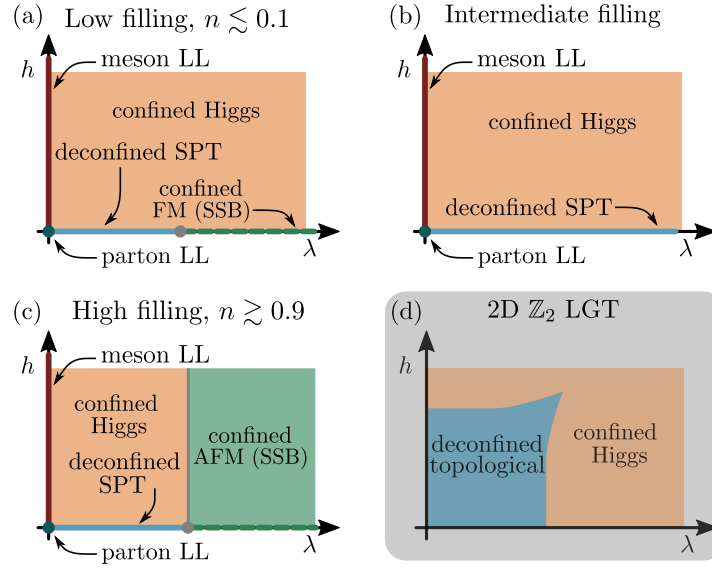


Figure 5.9: Sketches of phase diagrams of the 1 + 1D \mathbb{Z}_2 LGT coupled to dynamical matter as a function of the SC term λ and the electric field term h at different fillings n . (a) Phase diagram at low fillings $n \lesssim 0.1$ exhibits a SPT state for $h = 0$ and low SC term λ , which transitions to a confined symmetry broken ferromagnetic state (of the \mathbb{Z}_2 electric fields) for higher values of λ . For non-zero values of the $h, \lambda \neq 0$, the system is in a confined Higgs state. For $\lambda = 0$, the system has an additional $U(1)$ symmetry in the charges, and the partons form a deconfined parton LL when $h = 0$. When $h \neq 0, \lambda = 0$, the partons confine into mesons, which form a meson LL. (b) The phase diagrams for intermediate fillings $0.1 \lesssim n \lesssim 0.9$ is similar to (a), with a difference that there are no SSB states for larger values of λ , and the system remains an SPT for any value of λ when $h = 0$. (c) For higher fillings $n \gtrsim 0.9$, the phase diagram is similar to (a) with a difference that the symmetry broken state is an anti-ferromagnetic ordering of the electric fields, which in turn remains stable also at finite values of the electric field term $h \neq 0$. (d) A sketch of the phase diagram of a 2 + 1D \mathbb{Z}_2 LGT proposed by Fradkin and Shenker [32] to contrast our results for the 1 + 1D \mathbb{Z}_2 LGT. This figure was modified from Fig. 6 in Ref. [5].

SC term λ ; see Fig. 5.9. We compare the phase diagram derived from our one-dimensional results to the well known phase diagram of Fradkin and Shenker [32], i.e., the perturbed toric code, which we sketch in Fig. 5.9(d). The phase diagram of the Fradkin-Shenker model exhibits a deconfined topological phase, which is surrounded by the confined Higgs phase [17, 32, 193].

For low filling $n \lesssim 0.1$ and $h = 0$, our phase diagram exhibits a deconfined symmetry protected topological state at low SC term λ , which transitions to a confined, symmetry broken FM state for larger λ ; see Fig. 5.9(a). This is similar to the 2D Fradkin-Shenker phase diagram, however in our one-dimensional case the system is deconfined only for $h = 0$, whereas in the 2D case this phase is stable also for low values of h . In our case the system enters a confined case for any non-zero value of the \mathbb{Z}_2 electric field term $h \neq 0$ [5]. As already mentioned, the confined phase in our system for $h = 0$ at low filling, has

a spontaneously broken symmetry, where the \mathbb{Z}_2 electric field, $\hat{\tau}^x$, has a Ferromagnetic ordering. This state undergoes a transition to a paramagnetic state for $h \neq 0$ and remains confined [5]. In addition to all of the above, the 1 + 1D model also forms a Luttinger liquid in the limit when $\lambda = 0$ as already discussed in the previous chapters. For $h \neq 0$, the partons are confined into mesons, which form a meson LL, and in the special point when $\lambda = h = 0$, the partons are deconfined and form a simple free parton LL [1, 5].

For high fillings, $n \gtrsim 0.9$, the phase diagram is similar to the one at the low filling; see Fig. 5.9(c). The only difference is that the SSB state for high fillings is related to the anti-ferromagnetic ordering of the \mathbb{Z}_2 electric fields, $\langle \hat{\tau}_{(j,j+1)}^x \rangle = (-1)^j$ [5]. This in contrast to the FM state remains robust for finite values of $h \neq 0$, and thus extends above the $\lambda = 0$ line [5].

At intermediate fillings, $0.1 \lesssim n \lesssim 0.9$, there are no symmetry broken states at any value of λ ; see Fig. 5.9(b). The line $h = 0$ thus remains a SPT state for any $\lambda \neq 0$, which transitions to a confined Higgs state for $h, \lambda \neq 0$.

With this conclusion we finish the discussion on the phase diagram of the extended 1 + 1D \mathbb{Z}_2 LGT coupled to dynamical matter. This phase diagram will be directly compared to the mean-field theory for the \mathbb{Z}_2 LGT, which we discuss in the next chapter. With these results we also paves the way for future cold atom experiments, where such rich phase diagrams could be explored.

Chapter 6

Mean-field theory of the \mathbb{Z}_2 lattice gauge theory

In this chapter we develop a mean-field (MF) theory for a generalized 1 + 1D \mathbb{Z}_2 LGT where dynamical particles are coupled to gauge fields, studied in Chapter 5. In the introductory Chapter 2.1, we discussed how LGT formulation of physical problems results in additional degrees of freedom. On the one hand, LGT formulation allows for numerical treatment, which could sometimes not be effectively formulated otherwise or makes analytical approach easier. On the other hand, the additional gauge structure effectively enlarges the Hilbert space, making numerical calculations complicated. In addition, there is a vast amount of local constraints related to the gauge structure, e.g., the Gauss law. Although we can tackle the 1 + 1D \mathbb{Z}_2 LGTs numerically quite well, which we demonstrate in this thesis, numerical calculations in higher dimension become way more complicated. This holds in particular for the LGTs with dynamical matter, where the quantum Monte Carlo methods encounter the infamous sign problem at finite doping [133, 203, 204].

This motivated us to come up with a simpler mean-field theory that captures the main features of the exact \mathbb{Z}_2 LGT. For that we employ the slave-particle approach, which is a powerful method in strongly correlated systems. It can be used to reformulate difficult problems and thus offer significant new insights, often in a more intuitive way [33, 205–207]. As an example we can note that it has been applied to problems related to frustrated quantum magnets [207] and the Kondo problem [173]. The basic idea of the slave-particle mean-field theories is to expand the Hilbert space to reformulate the problem and make it easier to solve [5]. Such Hilbert space expansion means that one has to impose some constraints in order to obtain the correct physics. These constraints are, enforced only on the mean-field level, i.e., on average [5]. This approach is perfectly suited for the \mathbb{Z}_2 LGT, where we can decouple matter from the gauge field and enforce the Gauss law (set of constraints) on the mean-field level only [5]. In order to study the mean-field theory and how well it captures the exact \mathbb{Z}_2 LGT, we frequently relate to the results on the exact 1 + 1D \mathbb{Z}_2 LGT from Chapter 5.

This Chapter is based on Ref. [5], from which the content, including figures, has been adapted and extended. We also note that a much more simple version of the \mathbb{Z}_2 LGT

mean-field theory without the SC terms was already studied in the author's master thesis in Ref. [2]. However, the discussion here is a significant expansion on the initial problem tackled in [2].

6.1 Introduction

As already stated above the main idea of the \mathbb{Z}_2 LGT mean field theory is to decouple matter from the gauge field while still enforcing the gauge constraints, i.e., the Gauss law, on the mean field level [5]. In our derivation we obtain two separate mean-field theories, one for the charges (partons) and the other for the gauge fields. The former resembles the one-dimensional superconducting model [190] encountered in Chapter 5, and perfectly captures the regime when the \mathbb{Z}_2 electric field term is zero. However, it fails to capture the confined phase when the \mathbb{Z}_2 electric field term is non-zero. This is in part due to the fact that the exact \mathbb{Z}_2 LGT reduces to the one-dimensional superconducting model in the limit of static gauge fields.

The mean-field theory for the gauge fields is an Ising model with transverse and longitudinal fields. We solve it by performing DMRG calculations, where we have to find the correct chemical potential, which gives us the right filling [5]. This has to be done self consistently. It captures the main qualitative features of the exact \mathbb{Z}_2 LGT, in particular the phenomena related to confinement and spontaneous symmetry breaking for any value of the \mathbb{Z}_2 electric field. The only drawback is that it always breaks the $U(1)$ symmetry in the charges and thus it does not capture the parton and meson LL [5].

In order to compare the mean-field model to the exact \mathbb{Z}_2 LGT, we calculate the entanglement entropy and again consider the central charge. To study confinement in the mean-field theory we consider the Green's function and the string-length distributions obtained from snapshots. In addition, we directly compare the ground state energies and the \mathbb{Z}_2 electric field polarization obtained for the mean-field theory for the gauge fields to the ground state energies of the exact \mathbb{Z}_2 LGT [5].

6.2 Derivation of the mean-field theory

We start the derivation of the mean-field theory for the extended 1 + 1D \mathbb{Z}_2 LGT theory with dynamical matter, Eq (5.1), defined in Chapter 5, by making the product ansatz [5]

$$|\psi\rangle = |\psi_\tau\rangle \otimes |\psi_a\rangle. \quad (6.1)$$

With such ansatz we effectively decouple charge (\hat{a}) and gauge ($\hat{\tau}$) degrees of freedom. The Gauss law will be enforced on the mean field level, and thus comes in a form of extra terms (Lagrange multipliers) [5]. As a result, we obtain two different models: one which corresponds to the mean-field theory for the gauge fields, and the other that correspond to the mean-field theory for the partons (matter field).

We first derive the mean-field Hamiltonian for the matter by considering the gauge and

electric fields (link variables) on the mean field level. The mean-field theory for the charges can thus be expressed as [5]

$$\hat{\mathcal{H}}_{\text{MF}}^a = -t \langle \hat{\tau}_{(i,j)}^z \rangle \sum_j \left(\hat{a}_{j+1}^\dagger \hat{a}_j + \hat{a}_j^\dagger \hat{a}_{j+1} \right) + \lambda \langle \hat{\tau}_{(i,j)}^z \rangle \sum_j \left(\hat{a}_{j+1}^\dagger \hat{a}_j^\dagger + \hat{a}_j \hat{a}_{j+1} \right) - h \langle \hat{\tau}_{(i,j)}^x \rangle (L+1) + \mu_a \sum_j \left(\hat{a}_j^\dagger \hat{a}_j - n \right). \quad (6.2)$$

Here we define the average value of the \mathbb{Z}_2 gauge and electric field as [5]

$$\langle \hat{\tau}_{(i,j)}^z \rangle = \langle \psi_\tau | \hat{\tau}_{(i,j)}^z | \psi_\tau \rangle, \quad \langle \hat{\tau}_{(i,j)}^x \rangle = \langle \psi_\tau | \hat{\tau}_{(i,j)}^x | \psi_\tau \rangle, \quad (6.3)$$

respectively. In order to enforce the correct chain filling we also add the Lagrange multiplier μ_a , which takes the role of the chemical potential. In addition, we reiterate that the chain length (number of matter lattice sites) is defined by L , and the chain filling is defined as $n = N/L = \frac{1}{L} \sum_{j=1}^L \langle \hat{n}_j \rangle$, where N is the total number of partons in the chain, and $\hat{n}_j = \hat{a}_j^\dagger \hat{a}_j$ is the on-site parton number.

The model in Eq. (6.2) is the one-dimensional superconducting quantum wire model [190], which we already encountered in Chapter 5. We note that the hopping term t and the SC term λ are simply normalized by $\langle \hat{\tau}_{(i,j)}^z \rangle$, and that the \mathbb{Z}_2 electric field term becomes a constant energy offset, which can thus be discarded [5]. Such model can be solved by performing the Jordan-Wigner and Bogoliubov transformation [192]. In the limit when $\lambda = 0$ the system is simply a free parton model and in the limit when $\lambda = -t$, the model is the well known Kitaev model [5, 161, 190]. In Chapter 5 we demonstrated that the extended 1 + 1D \mathbb{Z}_2 LGT with SC terms, without the electric field term $h = 0$, reduces to the one-dimensional quantum wire model. Thus we showed that for static gauge field in the limit when $h = 0$, the mean-field theory for the charges coincides with the exact \mathbb{Z}_2 LGT. However, when the \mathbb{Z}_2 electric field term is finite $h \neq 0$, the mean-field theory for the charges will remain a simple one-dimensional SC model, as the electric field term is just a constant energy offset. Hence, no confined Higgs state or meson LL can be realized.

Next, we derive the mean-field theory for the gauge field. We perform similar calculations as before, however this time we consider the charge operators on the mean-field level instead of the \mathbb{Z}_2 fields, which can be expressed as [5]

$$\hat{\mathcal{H}}_{\text{MF}}^\tau = -t \sum_j \left(\langle \hat{a}_{j+1}^\dagger \hat{a}_j \rangle + \langle \hat{a}_j^\dagger \hat{a}_{j+1} \rangle \right) \hat{\tau}_{(j,j+1)}^z + \lambda \sum_j \left(\langle \hat{a}_{j+1}^\dagger \hat{a}_j^\dagger \rangle + \langle \hat{a}_j \hat{a}_{j+1} \rangle \right) \hat{\tau}_{(j,j+1)}^z - h \sum_{\langle i,j \rangle} \hat{\tau}_{(i,j)}^x + \mu_\tau \sum_{\langle i,j,k \rangle} \left(\hat{\tau}_{(i,j)}^x \hat{\tau}_{(j,k)}^x - 1 - 2n \right). \quad (6.4)$$

Here we defined the average value of the charge operators as $\langle \hat{a}_{j+1}^\dagger \hat{a}_j \rangle = \langle \psi_a | \hat{a}_{j+1}^\dagger \hat{a}_j | \psi_a \rangle$. We also added the Lagrange multiplier μ_τ , which ensures the correct filling. This term is derived directly by considering the Gauss law constraint Eq. (5.2) for the physical sector,

without background charges, on the mean-field level [5]. It can be expressed as [5]

$$\left\langle \sum_{\langle i,j,k \rangle} \hat{\tau}_{\langle i,j \rangle}^x \hat{\tau}_{\langle j,k \rangle}^x \right\rangle = L(1 - 2n), \quad (6.5)$$

where $\langle i,j,k \rangle$ denotes the sum over two neighboring links [5].

The obtained Hamiltonian Eq. (6.4) is an Ising model with transverse and longitudinal fields. The chemical potential term μ_τ is the Ising interaction, electric field term h is a longitudinal field and the hopping term t and SC term λ , normalized by the average or mean-field values of the charge operators, correspond to the transverse field [5].

The full mean-field theory is thus given by the two equations Eq. (6.2) and Eq. (6.4). We have already commented on the mean-field theory for the charges, Eq. (6.2), which corresponds to the exact \mathbb{Z}_2 LGT in the limit of static charges, for any value of h . It thus does not capture the effects related to the electric field term, in particular confinement at any filling n , when $h \neq 0$. The mean-field theory, Eq. (6.4), is therefore different in a sense that all terms of the exact \mathbb{Z}_2 LGT remain, albeit some slightly modified, i.e., normalized by the average values of the parton operators. We will thus focus mainly on the mean-field theory for the gauge fields, Eq. (6.4), which we write for convenience as [5]

$$\hat{\mathcal{H}}_{\text{MF}} = -g \sum_{\langle i,j \rangle} \hat{\tau}_{\langle i,j \rangle}^z - h \sum_{\langle i,j \rangle} \hat{\tau}_{\langle i,j \rangle}^x + \mu_\tau \sum_j \hat{\tau}_{\langle i,j \rangle}^x \hat{\tau}_{\langle j,k \rangle}^x. \quad (6.6)$$

Above we omitted constant terms and defined the prefactor in front of the transverse field as [5]

$$g = t \left(\langle \hat{a}_{j+1}^\dagger \hat{a}_j \rangle + \langle \hat{a}_j^\dagger \hat{a}_{j+1} \rangle \right) - \lambda \left(\langle \hat{a}_{j+1}^\dagger \hat{a}_j^\dagger \rangle + \langle \hat{a}_j \hat{a}_{j+1} \rangle \right). \quad (6.7)$$

We note that the Ising model with transverse and longitudinal fields cannot be simply solved. Hence, we resort again to numerical simulations, more precisely we again employ DMRG calculations [5]. In order to run the calculations, we first have to determine the value of g , which depends on the average values of the charge operators Eq. (6.7) coming from the mean-field theory for the charges Eq. (6.2) [5]. This can be done by calculating the average ground state energy of the superconducting model per lattice site, for given parameter values t, λ and filling n [5]. We make use of the Jordan-Wigner transformation and the Bogoliubov transformation to diagonalize the Hamiltonian Eq. (6.2), and express the parameter g as [5]

$$g = \frac{1}{2\pi} \int_0^\pi dk \sqrt{(\tilde{\mu}_a - 2t \cos(k))^2 + (2\lambda \sin(k))^2} + \tilde{\mu}_a \left(n - \frac{1}{2} \right). \quad (6.8)$$

More details on the above derivation can be found in Appendix C. We note that in order to obtain the above expression, Hamiltonian in Eq. (6.7) was normalized by $\langle \hat{\tau}_{\langle i,j \rangle}^z \rangle$ [5]. Hence, the chemical potential becomes $\tilde{\mu}_a = \mu_a / \langle \hat{\tau}_{\langle i,j \rangle}^z \rangle$. This makes the solution of Eq. (6.8) simpler as at a given filling n , we simply need to find the correct $\tilde{\mu}_a$ for given hopping term t and SC term λ [5]. This means that the solution at a given filling n is independent of the

average values of the gauge fields [5]. The solution to Eq. (6.8) can be found by minimizing the ground state energy of the mean-field model for the charges Eq. (6.2), which yields a self-consistency equation [5]

$$n = \frac{1}{2} \left(1 - \frac{1}{\pi} \int_0^\pi dk \frac{\tilde{\mu}_a - 2t \cos(k)}{\sqrt{(\tilde{\mu}_a - 2t \cos(k))^2 + \lambda^2(k)}} \right). \quad (6.9)$$

By solving the above equation for $\tilde{\mu}_a$ at a given filling n , we can perform the integral in Eq. (6.8) numerically [5]. We note that when $\lambda = 0$, the calculations can be simplified as we can use free fermion results, and perform the calculations analytically [2, 5].

After we calculate the value of g for given filling n , hopping term t , and SC term λ , we can perform DMRG calculations. We have to search for the correct value of the Ising interaction, i.e, the chemical potential term μ_τ , which yields the correct filling as defined by Eq. (6.5). Details on this procedure can be found in Section 6.3.2.

With this we conclude the derivation of the mean-field theory for the 1 + 1D \mathbb{Z}_2 LGT. In the next section we establish the phase diagram of the mean-field theory for the gauge fields, by discussing the Ising model with the transverse and longitudinal fields, and by performing DMRG calculations and calculating the entanglement entropy.

6.3 Phase diagram of the mean-field theory

6.3.1 Ising model with transverse and longitudinal fields

We first consider the phase diagram of a generic Ising model with transverse and longitudinal fields, which is well known as it has been extensively studied in the past [200, 201, 208, 209]. It has been even studied experimentally in a cold atom setup [210].

The Ising model without any fields will exhibit ordered, symmetry broken phases [200, 208, 209]. The sign of the Ising interaction, μ_τ in the case of our formulation in Eq. (6.6), determines whether the ordered state will be ferromagnetic (FM) or anti-ferromagnetic (AFM) [208]. For negative values $\mu_\tau < 0$, the ordering will be FM with all spins aligned, and for positive values $\mu_\tau > 0$, the ordering will be AFM. In the absence of the longitudinal field, $h = 0$, both states are equivalent as the sign in front of the Ising interaction can be changed if one performs the transformation on two of the three components of the spin: $\hat{S}_j^x \rightarrow (-1)^j \hat{S}_j^x$, $\hat{S}_j^y \rightarrow (-1)^j \hat{S}_j^y$, while $\hat{S}_j^z \rightarrow \hat{S}_j^z$ [182, 201, 208]. This transformation is in fact a particle-hole mapping in the gauge sector of our \mathbb{Z}_2 LGT system as demonstrated in Chapter 3, where the \mathbb{Z}_2 fields are represented by the Pauli matrices [1, 5]. The particle-hole mapping can also be explicitly seen in the mapping between the XXZ chain and the hard-core boson model [182], which we present in Appendix A. For non-zero values of the electric field term, $h \neq 0$, the sign of μ_τ is important, as the simple constant field $\propto h$ will become a staggered field $\propto (-1)^j h$.

Next we consider the behaviour of the Ising model upon introducing finite transverse field $|g| > 0$, while $h = 0$. There the system exhibits the aforementioned ordered states

only for low field value $g/|\mu_\tau| < 1$ (FM for $\mu_\tau < 0$ and AFM for $\mu_\tau > 0$) [200–202, 208]. For higher values of the transverse field $g/|\mu_\tau| > 1$ the system is disordered [200].

For $\mu_\tau < 0$ and non-zero value of the longitudinal field $h \neq 0$, the spin orientation remains ferromagnetic for $g < |\mu_\tau|$, as the system chooses one of the FM states according to the sign of the h [202]. The $h = 0$ line can be understood as the first order phase transition line [202].

The behaviour is more interesting on the AFM side $\mu_\tau > 0$. There the AFM state transitions to disordered/paramagnetic states at finite value of the longitudinal field $h \neq 0$ [200, 208]. There is in fact an AFM lobe, where the AFM state remains stable with boundaries at $h/\mu_\tau < 2$ and $g/\mu_\tau < 1$ [200, 208].

As we have seen from this short review of the Ising model with transverse and longitudinal fields, the transitions between ordered, symmetry broken states (AFM or FM) to disordered states occur as a function of the chemical potential μ_τ . This in turn controls the effective filling in the \mathbb{Z}_2 LGT picture, where spin domain walls represent partons [5]. We saw similar transitions in the previous Chapter 5, where we discussed the exact \mathbb{Z}_2 LGT. In the next section we solve the mean-field model for the gauge fields self-consistently using DMRG and show that these transitions in the mean-field theory indeed describe the transitions in the exact \mathbb{Z}_2 LGT.

6.3.2 Numerical simulation of the mean-field theory

We employ DMRG calculations [34, 35] to find the ground state solution of the spin system, representing the mean-field theory for the gauge fields Eq. (6.6). We again use the MPS toolkit SYTEN [153, 154]. As already mentioned in the section on the derivation of the mean-field theory, we first have to find the value of g , for given parameter values t, λ , and filling n . For that we have to self-consistently solve the equations Eq. (6.8) and Eq. (6.9), which is done by means of numerical integration [5].

After the value of the transverse field g is established for chosen parameter values t, λ , and filling n , we start using DMRG calculations. We set the desired transverse field (electric field term) h , and search for the correct chemical potential μ_τ , that gives us the correct filling n . This filling already had to be choose when we were calculating the value for g . The procedure to find the correct chemical potential is as follows [5]:

1. We define a minimal and maximal chemical potentials μ_{\min} and μ_{\max} . In addition, we define the starting chemical potential $\mu_{p=1}$, $\mu_{\min} < \mu_{p=1} < \mu_{\max}$, for which we calculate the ground state and the corresponding filling $n(p = 1)$. Typically this is $\mu_{p=1} = 0.1t$. The filling is calculated via the Gauss law, Eq. (6.5).
2. Depending on the filling $n(p)$, which we obtain from the grounds state calculations where the chemical potential was μ_p , in step p , we redefine either the minimal or maximal value of the chemical potential. If the calculated filling $n(p)$ is greater than the "correct" filling n , then $\mu_{\max} = \mu_p$. Contrarily, if the calculated filling $n(p)$ is smaller than the "correct" filling n , then $\mu_{\min} = \mu_p$.

3. Next we redefine the chemical potential for the next step $l = p + 1$, as

$$\mu_l = \frac{1}{2} (\mu_{\min} + \mu_{\max}). \quad (6.10)$$

We then run the DMRG again with the new chemical potential μ_l , and calculate the corresponding filling $n(l)$.

4. In order to get high accuracy for μ_τ , and thus the filling that is close to the target filling n , we repeat procedures 2. and 3. for 15 times [5]. The chemical potential in the final step, $\mu_\tau = \mu_{p=p_{\max}}$, is then declared as the correct chemical potential, which solves the mean field equations. The ground state from the final DMRG calculation is the solution to our problem and is used in further calculations. We typically exclude results where the filling in the last step differs from the target filling by more than one percent $\frac{n-n(p_f)}{n} > 0.01$ [5].

The above algorithm works very well for generic parameter values. The only problems where it could get slightly stuck is close to the transitions, which are known to exist in the Ising model with transverse and longitudinal field, discussed in the previous Section 6.3.1. However, since we fix some finite filling n we are usually never completely at this transition point and thus we do not encounter this problem that often [5]. We again simulate $L = 96$ lattice sites, which result in $L + 1 = 97$ spins (links).

The obtained ground state MPS is then used to calculate all the desired physical observable. To make the direct comparison with the exact \mathbb{Z}_2 LGT, which we studied in Chapter 5, we consider the entanglement entropy to study the general phase diagram. In order to study confinement we consider the Green's function and the string-length histograms [5].

6.3.3 Entanglement entropy calculations in the mean-field theory

For a direct comparison to the exact \mathbb{Z}_2 LGT we first study the entanglement entropy in the mean-field theory for the gauge field Eq. (6.6). We calculate it in the same way as in Chapter 5, where we cut the system at link site x , and thus obtain entanglement entropy profiles $S(x)$ [5]. In addition, we reiterate that away from quantum criticality the entanglement entropy will saturate to finite value at long distance, and close to quantum criticality it will diverge [5, 194].

Entanglement entropy value

We calculate the central entanglement entropy $S(L/2)$, i.e., entanglement entropy when the system is cut in half, $x = L/2$. The results for different parameter values λ, h and filling n , are shown in Fig. 6.1. When the \mathbb{Z}_2 electric field is zero $h = 0$, we can observe two vertical lines with substantial entanglement entropy as a function of the SC term λ at low $n \approx 0.2$ and high $n \approx 0.8$ chain fillings [5]. For finite \mathbb{Z}_2 electric field, only the vertical line at high filling $n \approx 0.8$ remains.

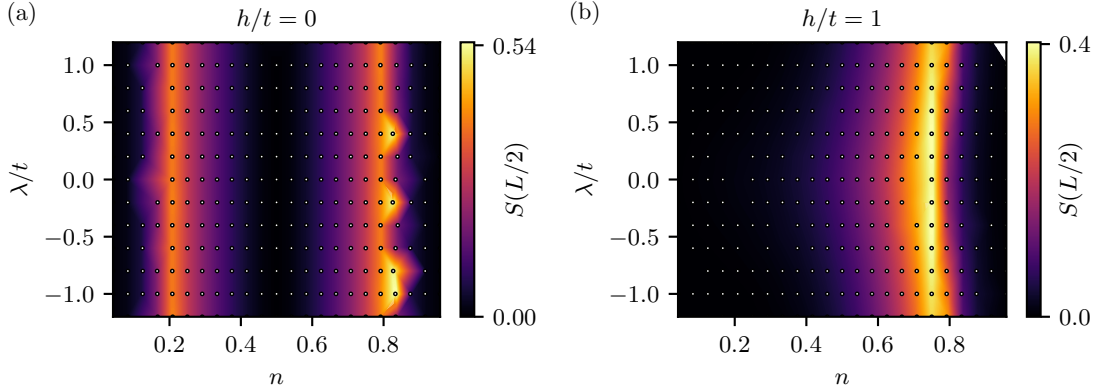


Figure 6.1: Entanglement entropy $S(L/2)$ for the mean-field theory of the gauge sector Eq. (6.6) as a function of filling n and the SC term λ . (a) For $h = 0$, we obtain two vertical lines with substantial entanglement entropy as a function of λ at fillings $n \approx 0.2$ and $n \approx 0.8$. (b) For non-zero electric field term $h/t = 1$, only one such line remains at high filling $n \approx 0.8$. No features can be seen on the line $\lambda = 0$ in both cases. This figure was adapted from Fig. 7 in Ref. [5].

These lines are similar to what we observed for the exact \mathbb{Z}_2 LGT model in Fig 5.3. To be more precise, at $\lambda/t = -1$ we observe similar feature at similar fillings, both for zero and non-zero electric field term. This could be expected from the fact that the full 1 + 1D \mathbb{Z}_2 LGT, Eq. (5.1), for $\lambda/t = -1$ reduces to an Ising model with transverse and longitudinal fields after integrating out the charges [5]. For more details on this limit we refer the reader to Section 1.3.2. We can thus already assume that the mean-field theory for the \mathbb{Z}_2 fields correctly captures the transitions to the symmetry broken phases. For non-zero value of the electric field term $h \neq 0$ this is the transition between the confined Higgs and the confined symmetry broken phase [5]. However, we note that there is no observed dependence on the filling and that these lines appear to be almost vertical.

In contrast to the exact \mathbb{Z}_2 LGT, we do not observe any features on the $\lambda = 0$ lines for the entanglement entropy results of the mean-field theory for the gauge fields. That is because these lines, in the exact \mathbb{Z}_2 LGT, are related to the $U(1)$ symmetry of the charges, where the system forms a parton LL or a meson LL in the deconfined and confined regimes, respectively. The partons are directly related to the domain wall number in the \mathbb{Z}_2 electric fields as dictated by the Gauss law. In the mean-field theory for the gauge field, parton number is thus directly related to the number of domain walls of the spins in the x -basis. Looking at the mean-field theory model for the spins Eq. (6.6), we see that the transverse field $\propto \hat{\tau}^z$, explicitly breaks the domain wall number conservation. In other words: the mean-field theory does not possess the $U(1)$ symmetry for the charges when $\lambda = 0$, and the filling is imposed only on average, i.e., on the mean-field level via the Lagrange multiplier μ_τ [5]. The quantum criticality on $\lambda = 0$ line can thus not be obtained with the mean-field theory for the fields, at least not without projecting to states with correct parton number. However, we note that the mean-field theory for the charges, Eq (6.2), does possess the $U(1)$ symmetry for the charges on the $\lambda = 0$ line as it simply reduces to a free parton model [5].

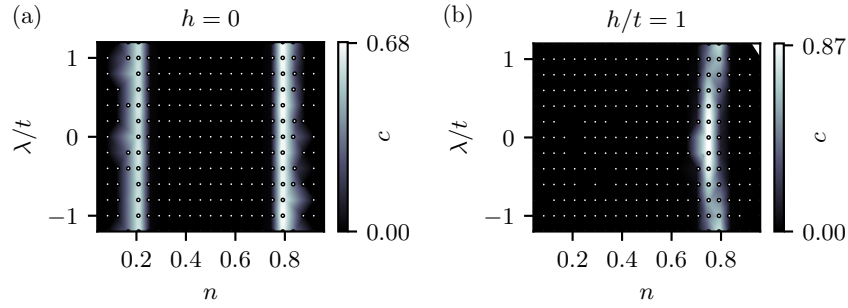


Figure 6.2: Central charge c in the mean-field theory for the gauge field Eq. (6.6) for different electric field values as a function of filling n and the SC term λ . (a) In the absence of the \mathbb{Z}_2 electric field term $h = 0$, we obtain two vertical lines with non-zero central charge values as a function of the SC term $\lambda = 0$. These two lines are at approximately $n \approx 0.2$ and $n \approx 0.8$, coincide with similar lines observed in the $S(L/2)$ diagram in Fig. 6.1(a). (b) For finite electric field term $h/t = 1$, only a single vertical line at high filling remains, again in agreement with the results for $S(L/2)$ in Fig. 6.1(b). No finite value of c is extracted on the $\lambda = 0$ lines, as the $U(1)$ symmetry in the charges is always broken in the mean-field theory for the gauge field. This figure was adapted from Fig. 8 in Ref. [5].

The combined mean-field ansatz thus correctly captures the deconfined free parton regime for $h = 0$, however it still fails to capture the meson LL liquid at $h \neq 0, \lambda = 0$, as the electric field term is irrelevant in the mean-field theory of the charges [5].

Central charge in the mean-field theory

We analyze the entanglement entropy in greater detail by also extracting the central charge c from the entanglement entropy profiles $S(x)$. The procedure to obtain c , is the same as in Chapter 5. We first normalize the entanglement entropy by local densities to obtain $\tilde{S}(x) = nS(x)/n(x)$ [5, 7, 197], and then fit $\tilde{S}(x)$, with the CFT formula Eq. (5.9) [5, 194–196]. The fit results for the mean-field theory for the gauge field qualitatively resemble (to the naked eye) the curves obtained for the exact \mathbb{Z}_2 LGT when $\lambda \neq 0$ [5]. We typically exclude fits where the fit error for the central charge exceeds $\Delta c = \pm\sqrt{0.02}$, which we again estimate from the square root of the covariance matrix element of the fit [5].

The extracted central charge c , for the mean-field theory of the gauge fields for different electric field value h , as a function of filling n and SC term λ , are presented in Fig. 6.2. We extract non-zero value of c on the lines as function of λ at fillings $n \approx 0.2$, and $n \approx 0.8$, which correspond to the lines with substantial entanglement entropy in Fig. 6.1. For zero electric field $h = 0$, we again obtain two lines: one at low filling $n \approx 0.2$, and one at high filling $n \approx 0.8$. For non-zero electric field term $h/t = 1$, however, we only observe such line at high filling $n \approx 0.8$.

The results for the central charge thus agree with the results in Fig. 6.1, and support the claim that we observe a transition to symmetry broken states [5]. Furthermore, the extracted central charge value is close to $c = \frac{1}{2}$, which is the expected value in the transition line between disordered and symmetry broken phase in a transverse-field Ising model [199].

We once again note that the transverse-field Ising model can be mapped to the Kitaev chain [161]. This shows that the transition observed in the mean-field model for the gauge fields are the same as in the exact \mathbb{Z}_2 LGT model, Eq. (5.1), at finite values of the SC term $\lambda \neq 0$. However, we do not extract finite central charge results at $\lambda = 0$ lines for any value of h . This is in agreement with the entanglement entropy results in Fig. 6.1, as the mean-field theory for the gauge field does not conserve the global parton number.

For $h = 0$ and for intermediate fillings $0.2 \lesssim n \lesssim 0.8$, we thus obtain disordered system in terms of the \mathbb{Z}_2 electric fields. For lower $n \lesssim 0.2$ and higher fillings $n \gtrsim 0.8$ we obtain ordered systems, where in the former case the \mathbb{Z}_2 electric fields align in a ferromagnetic order, and in the latter case, $n \gtrsim 0.8$, electric field aligns in an AFM fashion [5]. For finite electric field term $h \neq 0$, only the transition from disordered to ordered AFM system is present. This can also be understood in terms of the Ising model with transverse and longitudinal fields: when $h \neq 0$, the solutions for μ_τ at finite values of n shift to higher values away from $|g|/\mu_\tau = -1$ [5]. Thus only the transition at the positive $|g|/\mu_\tau = 1$ remains, which is indeed the transition from disordered to AFM state in terms of the spins in the x -direction, which correspond to the \mathbb{Z}_2 electric field in the \mathbb{Z}_2 LGT language [5].

6.4 Confinement in the mean-field theory

Next we study the confinement in the mean-field theory for the gauge fields. We again consider the Green's function and the string-length distributions obtained from snapshots [5]. In the previous section we have seen that the mean-field theory ansatz qualitatively correctly captures all relevant transitions and phases, with the only exception being the meson LL, on the special $\lambda = 0$ line for $h \neq 0$ [5]. Here we study whether confinement properties are also captured correctly.

6.4.1 Green's function in the mean-field theory

In order to study confinement we consider the same gauge invariant Green's function, which we discuss throughout this thesis, and is defined as [1, 3–5, 160]

$$\mathcal{G}(|x - x_0|) = \left\langle \hat{a}_{x_0}^\dagger \left(\prod_{x_0 \leq \ell < x} \hat{\tau}_{(\ell, \ell+1)}^z \right) \hat{a}_x \right\rangle. \quad (6.11)$$

We are considering the mean-field theory for the gauge fields, Eq. (6.6). Here we thus state the Green's function with \mathbb{Z}_2 fields, i.e., in spin language, which is expressed as [5]

$$\mathcal{G}(x) = \left\langle \frac{1}{4} \left(\prod_{x_0 \leq \ell < x} \hat{\tau}_{(\ell, \ell+1)}^z \right) \left(1 - \hat{\tau}_{(x-1, x)}^x \hat{\tau}_{(x, x+1)}^x \right) \left(1 + \hat{\tau}_{(x_0-1, x_0)}^x \hat{\tau}_{(x_0, x_0+1)}^x \right) \right\rangle. \quad (6.12)$$

We note that this is in fact how the Green's function is calculated for all Green's function results presented in this thesis, since we always integrate out the matter by considering the Gauss law restricted to the physical sector. More details can be found in Chapter 1.3.

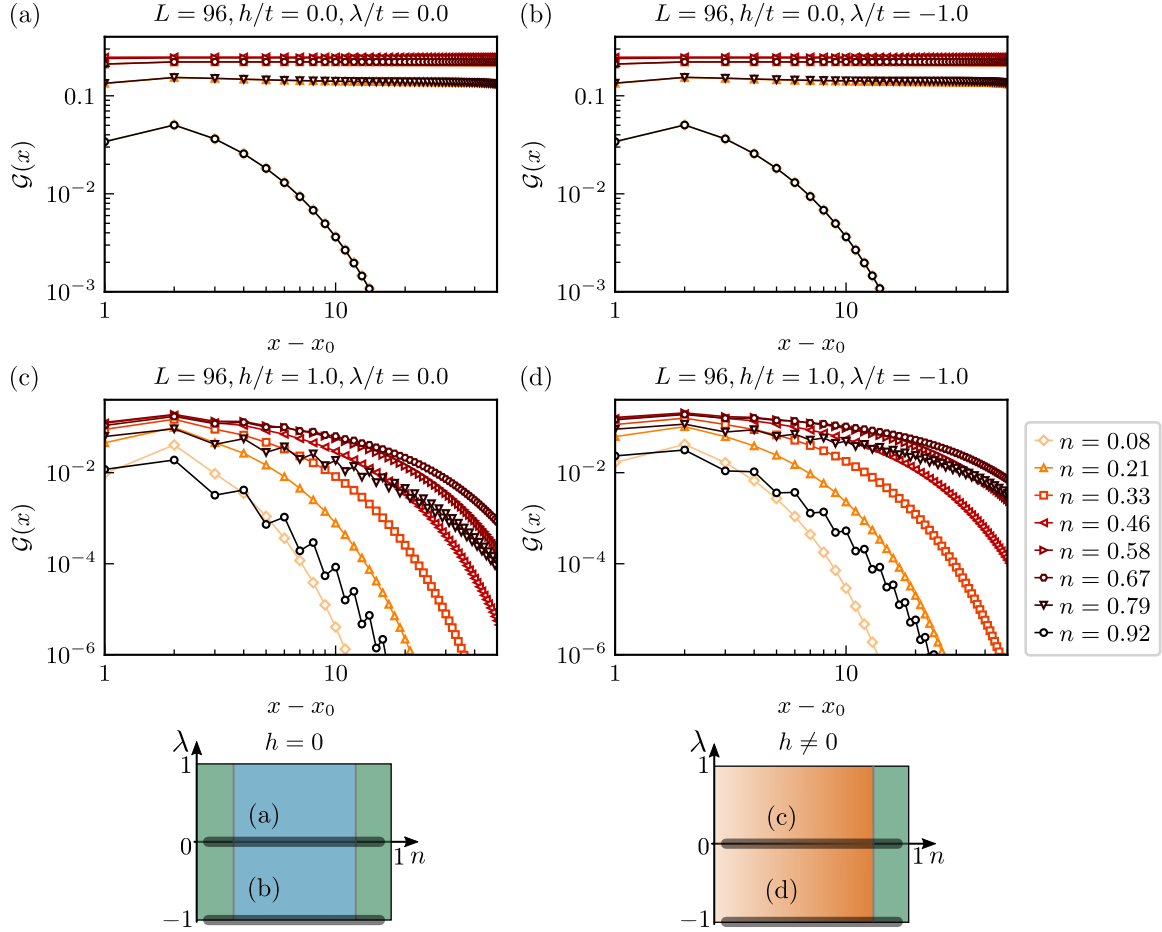


Figure 6.3: Green's function results Eq. (6.12) for the mean-field theory of the gauge field Eq. (6.6) for different electric field h , SC term λ and filling n . (a) For $h = \lambda = 0$ the Green's function has nearly constant values for intermediate fillings $0.2 \lesssim n \lesssim 0.8$, indicating deconfined regime. For low $n \lesssim 0.2$ and high fillings $n \gtrsim 0.8$, the Green's function decays exponentially indicating deconfined regime as the system transitions into a symmetry broken FM regime for $n \lesssim 0.2$, and AFM regime for $n \gtrsim 0.8$. (b) The same qualitative behaviour as in (a) can be seen when the SC term is non-zero $\lambda/t = -1$. (c) For non-zero \mathbb{Z}_2 electric field term and $\lambda = 0$, the Green's function decays exponentially for any chain filling n . (d) The same qualitative behaviour of the Green's function can be seen as in (c) when the SC term is non-zero $\lambda/t = -1$. Below the plots we sketch the parameter regime in a sketch of the phase diagram of the MF theory for the gauge field, where we consider the Green's function. In order to reduce the finite size effects we again consider $x_0 = 30$, and $x > x_0$ in a chain with length $L = 96$. This figure was modified from Fig. 9 in Ref. [5].

The Green's function results are presented in Fig. 6.3 for different values of the electric field term h , SC term λ , and for different values of the filling n . The parameters were chosen in a way that a direct comparison with the Green's function results in the exact \mathbb{Z}_2 LGT can be made in Fig. 5.7.

In the absence of the \mathbb{Z}_2 electric field term $h = 0$, the Green's function is almost constant for intermediate fillings $0.2 \lesssim n \lesssim 0.8$, see Fig. 6.3(a) and 6.3(b), and thus signals a deconfined partons in that parameter regime. This can also be understood in terms of the mean-field theory Hamiltonian for the gauge field Eq. (6.6). In such parameter regime, the transverse field $\propto g\hat{t}^z$ dominates the system and we can imagine that all spins governed by Eq. (6.6) align with the field in the z -direction [5]. In other words, spins align as a paramagnet with the transverse field [5]. Contrarily, for lower $n \lesssim 0.2$ and higher fillings $n \gtrsim 0.8$, the Green's function decays exponentially, which indicates confinement. These result coincide with the transition to FM and AFM symmetry broken states discussed in the previous Section 6.3 and agree with the results for the exact \mathbb{Z}_2 LGT when $\lambda \neq 0$ in Chapter 5 [5]. However, same qualitative behaviour for $h = 0$ can be seen for any value of the SC term λ ; see Fig. 6.3(a) and 6.3(b). This agrees with the entanglement entropy results from the previous section, where no dependence of the transition on λ could be observed. This is a result of the broken $U(1)$ symmetry for any value of λ in the mean-field theory for the gauge field. Hence, confined signatures at low and high fillings could also be seen for $\lambda = 0$, which is not the case for the exact \mathbb{Z}_2 LGT.

For non-zero value of the \mathbb{Z}_2 electric field term $h \neq 0$, the Green's function decays exponentially for any filling n [5]; see Fig. 6.3(c) and 6.3(d). The confined phase for non-zero electric field term, $h \neq 0$, is thus correctly captured by the mean-field theory for the gauge field [5]. Also here, the same qualitative behavior of the Green's function can be seen for any value of the SC term λ , which is again in agreement with the entanglement entropy calculations for the mean-field theory in the previous Section 6.3. Furthermore, we observe decrease of the decay rate of the Green's function with increasing filling up to $n \approx 0.8$, when the rate of decay again increases with increasing filling. This feature can be also observed in the exact model when $\lambda/t = -1$. However, we observe this for any λ in the mean-field theory, which is again the consequence of the $U(1)$ symmetry breaking for any λ in the mean-field theory. Namely, for $\lambda = 0$ in the exact \mathbb{Z}_2 LGT the rate of decay decreases monotonically with increasing filling n , as the mesons form a LL [1, 5].

We have thus shown that the mean-field theory for the gauge field correctly captures the behaviour of the Green's function for $\lambda \neq 0$ for any value of the \mathbb{Z}_2 electric field term h [5]. For the non-zero electric field term $h \neq 0$, the Green's function decays exponentially for any value of λ and filling n . In the absence of the \mathbb{Z}_2 electric field term it also correctly captures the transition between deconfined and confined symmetry broken states at low, $n \lesssim 0.2$, and high, $n \gtrsim 0.8$, fillings. The only drawback is that the mean-field theory for the gauge field Eq. (6.6) breaks the $U(1)$ symmetry also for $\lambda = 0$ while the exact \mathbb{Z}_2 LGT does not. Accordingly, the mean-field theory for the gauge field exhibits a transition to the confined regime for $\lambda = 0$, which is not the case for the exact \mathbb{Z}_2 LGT.

In conclusion, the behaviour is fully captured for $\lambda \neq 0$, whereas for $\lambda = 0$, it is captured

qualitatively only for $h \neq 0$. However, even there we see features around $n \approx 0.8$, which are not seen in the exact \mathbb{Z}_2 LGT [5].

6.4.2 String-length histograms in the mean field theory

In addition to the Green's function, we also study the string and anti-string length distributions, which we again obtain from snapshots, sampled from our ground state MPS [5]. For details we thus refer the reader again to Section 2.3.3 and Section 5.3.2. The procedure is again exactly the same as in the exact \mathbb{Z}_2 LGT, where we also sample in the x -basis of the link variables, i.e., in the \mathbb{Z}_2 electric field basis [4, 5].

In order to directly compare the mean-field results with the exact \mathbb{Z}_2 LGT results in Fig. 5.8, we sample snapshots and compute the string and anti-string length distributions for different values of the \mathbb{Z}_2 electric field term h , SC term λ and average filling n . The results are presented in Fig. 6.4.

For any parameter value and filling, the string and anti-string length distributions have a peak at $\ell = 1$. For non-zero electric field term $h/t = 1$, peaks at $\ell = 1$ in the string length distributions are much higher than peaks in the anti-string length distributions, which signals confinement of partons [5]. Furthermore, the anti-string length distributions are significantly wider, with longer tails than the string length distributions; see Figs. 6.4(d)-6.4(f).

When the \mathbb{Z}_2 electric field term is zero $h = 0$, the string and anti-string length distributions almost completely coincide for intermediate fillings $0.2 \lesssim n \lesssim 0.8$; see Fig. 6.4(a) and 6.4(b). This is a clear signature of the deconfined phase and is in agreement with the Green's function results. Additionally, for low fillings $n \lesssim 0.2$, the peak of the string-length distribution at $\ell = 1$ is significantly higher than the peak of the anti-string length distribution, which is also much broader [5]; see Fig. 6.4(c). This indicates that also the string and anti-string length distributions capture the transition to the confined regime when the system orders in a symmetry broken FM state [5].

String and anti-string length distributions are in full agreement with the Green's function results and are thus once again a reliable and robust measure of confinement also for the mean-field theory for the gauge field [5].

6.4.3 Summary of the Mean-field theory phase diagram

We summarize our results in a sketch of the phase diagram of the mean-field theory in Fig. 6.5. The mean-field theory for the gauge sector, in the absence of the \mathbb{Z}_2 electric field term exhibits a deconfined SPT phase for intermediate fillings $0.15 \lesssim n \lesssim 0.85$, which is confirmed by the Green's function results and the string and anti-string length histograms [5]. For lower, $n \lesssim 0.15$, and higher, $n \gtrsim 0.85$, fillings, the system transitions to a symmetry broken FM and AFM states, respectively. These two states exhibit confined features, with exponential decay of the Green's function and differences in the distributions of string and anti-string lengths [5]. When the \mathbb{Z}_2 electric field term is non-zero, $n \neq 0$, the system is in a confined regime up to approximate filling $n \lesssim 0.85$, which corresponds to the confined

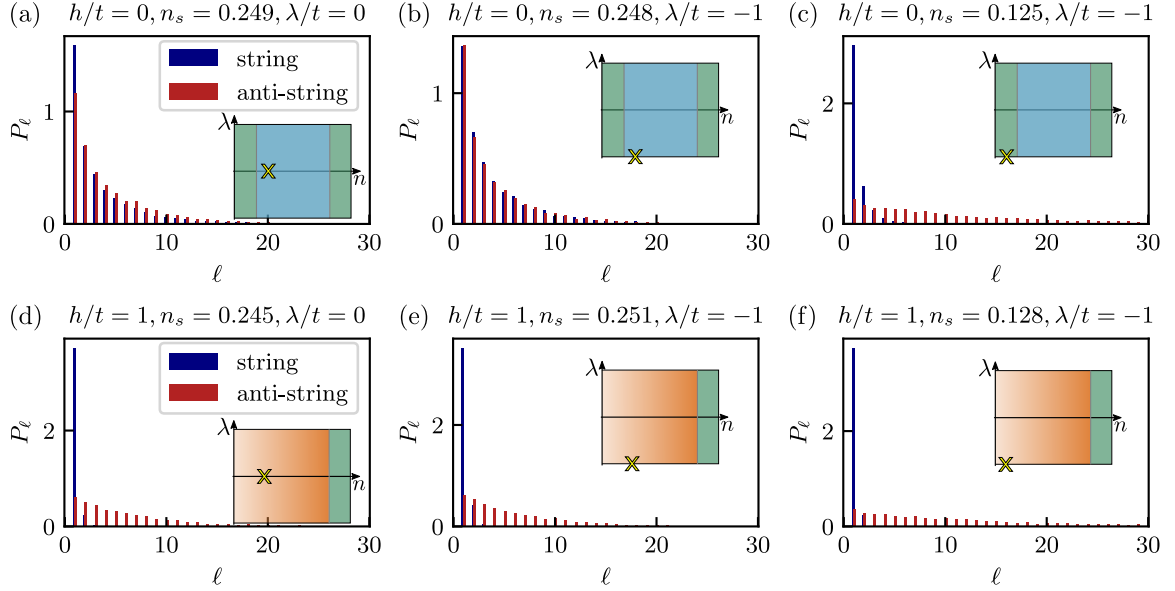


Figure 6.4: String and anti-string length histograms in the mean-field theory for the gauge field, Eq. (6.6), for different parameter values h, λ and filling n . (a) When $\lambda = h = 0$, the string and anti-string length distributions are nearly identical for the filling $n_s \approx 0.249$. (b) For non-zero SC term $\lambda/t = -1$ and zero electric field term $h = 0$, the string and anti-string length distributions are again nearly identical at similar filling $n_s \approx 0.248$ as in (a). (c) For lower filling $n_s \approx 0.125$, but the same parameter values as in (b), string-length distribution peak at $\ell = 1$ is much higher than the anti-string length distribution peak at $\ell = 1$. In addition, the anti-string length distribution is also much broader. Both features signal confinement. (d) For finite \mathbb{Z}_2 electric field value $h/t = 1$, but zero SC term $\lambda = 0$, for filling $n_s \approx 0.245$, string length distribution has a higher peak at $\ell = 1$ than the anti-string length distribution, which is also broader. Both of these features are a clear signature of confinement. (e) When both terms are finite, $h/t = 1$ and $\lambda/t = -1$, same confining features can be seen as in (e) for similar filling $n \approx 0.251$. (f) The qualitative features remain the same for lower filling $n_s \approx 0.128$, but same parameter values as in (e), showing that the system is confined for any non-zero electric field $h \neq 0$. With yellow "x" we show the parameter values in the inset with a sketch of the mean-field phase diagram. This figure was obtained from Fig. 10 in Ref. [5].

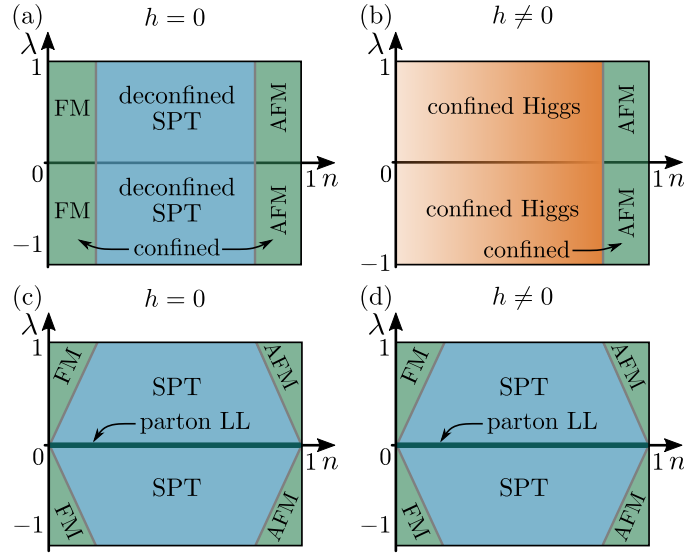


Figure 6.5: Qualitative sketch of the phase diagram of the mean-field theory for the paradigmatic 1 + 1D \mathbb{Z}_2 LGT with matter, which summarizes our results. (a) Gauge sector mean-field theory, Eq. (6.6), in the regime when $h = 0$, exhibits a deconfined SPT state for intermediate fillings $0.15 \lesssim n \lesssim 0.85$. This is a simple disordered state in the spin language of the mean-field Hamiltonian Eq. (6.6). For lower and higher fillings, the spin system forms a FM and an AFM state that corresponds to confined states in the \mathbb{Z}_2 LGT picture. (b) The gauge sector mean-field theory for finite \mathbb{Z}_2 electric field $h \neq 0$, exhibits a disordered state up to high fillings $n \lesssim 0.85$, which corresponds to the confined Higgs state in the \mathbb{Z}_2 language. For higher filling the spins align in the AFM order state, and the partons remain confined. (c) Mean-field theory in the charge sector, Eq. (6.2), directly maps to the exact 1 + 1D \mathbb{Z}_2 LGT in the limit of static charges at $h = 0$. It thus shares the same phase diagram as the exact \mathbb{Z}_2 LGT for $h = 0$ in Fig. 5.2(a). (d) The non-zero electric field term $h \neq 0$, does not change the phase diagram of the mean-field theory model for the charges as it is simply a constant energy offset. The phase diagram thus remains the same as the phase diagram of the exact \mathbb{Z}_2 LGT for $h = 0$. This figure was obtained from Fig. 11 in Ref. [5].

Higgs phase in the \mathbb{Z}_2 LGT picture. For higher filling $n \gtrsim 0.85$ the system transitions to a confined symmetry broken AFM regime [5].

Hence, the mean-field theory in the gauge sector exhibits a phase diagram that qualitatively captures almost all of the features of the exact \mathbb{Z}_2 LGT. There are only two exceptions where the mean-field theory in the gauge sector fails. As it does not conserve the number of spin domain walls, which translates to the $U(1)$ symmetry in the partons in the \mathbb{Z}_2 LGT picture via the Gauss law Eq. (6.5), it fails to capture any of the two possible LL on $\lambda = 0$ lines [5]. It thus does not exhibit the free parton LL for $h = \lambda = 0$, or the meson LL when $h \neq 1, \lambda = 0$. The second qualitative difference is that there is no dependence on the SC term λ when the system transitions from the SPT or the Higgs phase to the symmetry broken states [5].

The phase diagram of the mean-field theory in the charge sector is identical to the phase

diagram of the exact \mathbb{Z}_2 LGT when the electric field term is zero $h = 0$ [5]. This is because the mean-field theory in the charge sector reduces to the one-dimensional superconducting wire model [5, 190]. The exact \mathbb{Z}_2 LGT reduces to the same model in the limit when $h = 0$ [5, 160]. Hence, the phase diagrams coincide. It thus captures the parton LL on the $\lambda = 0$ line. However, nothing changes to the mean-field theory in the charge sector, Eq. (6.2), when the \mathbb{Z}_2 electric field term becomes finite $h \neq 0$, as the electric field term becomes a simple energy offset in that case [5]. Hence, the charge sector mean-field theory does not exhibit confinement across all fillings n in the regime when $h \neq 0$, as it does not capture the confined Higgs phase observed in the exact \mathbb{Z}_2 LGT up to high filling $n \lesssim 0.85$ [5]. It also does not capture the meson LL [5].

6.5 Comparison between the mean-field theory and the exact LGT

From our calculations so far we have shown that the mean-field ansatz captures the main features of the exact \mathbb{Z}_2 LGT. In order to compare the mean-field theory in the gauge sector even more closely to the exact \mathbb{Z}_2 LGT, we directly compare the ground state energies and the polarization of the \mathbb{Z}_2 electric field.

6.5.1 Ground state energy comparison

We calculate the ground state energy in the exact \mathbb{Z}_2 LGT, Eq. (5.1), and the mean-field Hamiltonian in the gauge sector, Eq. (6.6), for different parameter values h, λ and filling n , and plot them together in Fig. 6.6. We again use DMRG in order to obtain the ground state energy, which we normalize by the system length L . In addition, we subtract the chemical potential contribution to the ground state energy.

In the absence of the \mathbb{Z}_2 electric field term, the ground state energy of the exact \mathbb{Z}_2 LGT has a parabolic-like dependency as a function of filling n , symmetric in half filling $n = 0.5$, for any value of the SC term λ [5]. This is expected as for $h = \lambda = 0$, the system is formed by free partons. More precisely, the shape of the curve for $h = \lambda = 0$ is proportional to $\propto -t \sin(\pi n)$, a result obtained by considering a simple tight binding model. The mean-field ground state energy in the gauge sector, has a similar dependency as a function of filling. Furthermore the exact values match very well close to half filling $n = 0.5$. The mean-field theory in the gauge sector thus qualitatively matches the ground state energy of the exact \mathbb{Z}_2 LGT.

For finite \mathbb{Z}_2 electric field term $h/t = 1$, the ground state energy in the exact \mathbb{Z}_2 LGT, rises monotonically as a function of n for $\lambda = 0$. For finite values of $\lambda \neq 0$, the curve again obtains a minimum, and with higher values of λ the shape slowly starts transforming to deformed concave curve observed for $h = 0$ [5]. The shape of the curves thus depend on the interplay of h and λ . The mean-field theory for the gauge sector for finite electric field term, $h \neq 0$, also qualitatively captures the exact \mathbb{Z}_2 LGT ground state results. The concrete values become closer to the exact values for higher fillings. In conclusion, we have demonstrated that the mean-field theory Hamiltonian for the gauge sector qualitatively

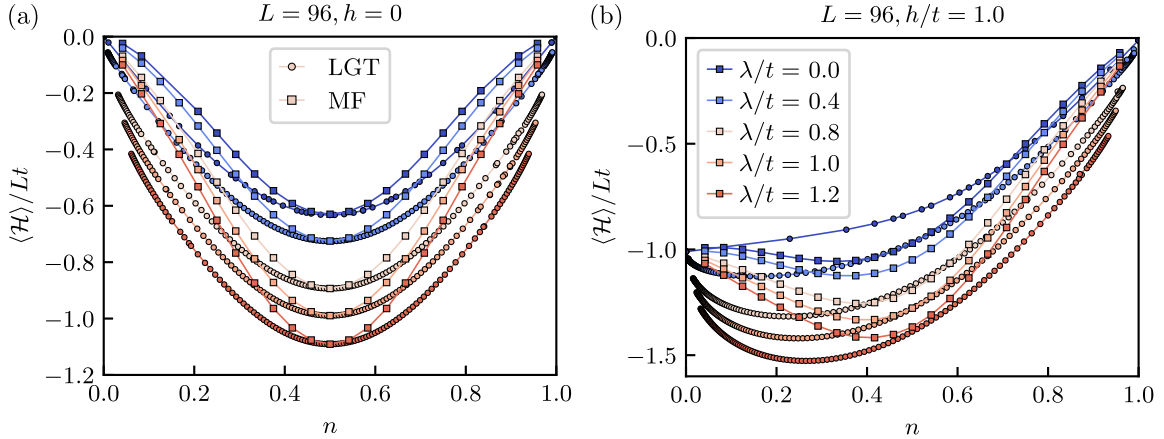


Figure 6.6: Ground state energy comparison between the exact 1 + 1D \mathbb{Z}_2 LGT, Eq. (5.1), after eliminating matter (smaller circles) and the mean-field theory in the gauge sector, Eq. (6.6), (squares) as a function of filling n , for different electric field term value h , and SC term λ . (a) In the absence of the \mathbb{Z}_2 electric field term, $h = 0$, the ground state energy is symmetric in $n = 0.5$ in both models for any SC term value λ , where it also has a minimum. The mean-field theory qualitatively captures the overall ground state energy behaviour of the exact \mathbb{Z}_2 LGT, with the same filling dependency and values, which are not far off from the exact values. (b) For finite value of the \mathbb{Z}_2 electric field, $h/t = 1$, the exact \mathbb{Z}_2 LGT ground state rises monotonically with filling n , when $\lambda = 0$. By including non-zero value of the SC term $\lambda \neq 0$, the curve obtains a minimum and its shape resembles as skewed/deformed parabola, more similar to the $h = 0$ results. The mean-field energy again qualitatively resembles the ground state results. The energy is captured more precisely at higher filling n and for $|\lambda| > 0$. We note that the ground state results are identical for $\lambda \rightarrow -\lambda$, and thus we only present $\lambda > 0$ results. This figure was obtained from Fig. 12 in Ref. [5].

captures the main features of the ground state energy behaviour in the exact \mathbb{Z}_2 LGT [5].

6.5.2 Electric field polarization comparison

Finally, we also directly compare the \mathbb{Z}_2 electric field polarization. It plays an important role in understanding the transitions to ordered FM state as it is its order parameter [5]. To be more precise, all of the symmetry broken FM and AFM states are ordered in the x -direction or component of the spin. Hence, the total \mathbb{Z}_2 electric field polarization can give us a better insight into the transition to the FM state [5]. Contrarily, staggered polarization would indicate a transitions to the AFM state. In addition to the FM and AFM states, finite \mathbb{Z}_2 electric field polarization also indicates confinement of partons, because strings connecting mesons are on average much shorter than anti-strings [5]. Hence, for any finite filling, confinement should be reflected in finite polarization, which becomes higher for lower filling.

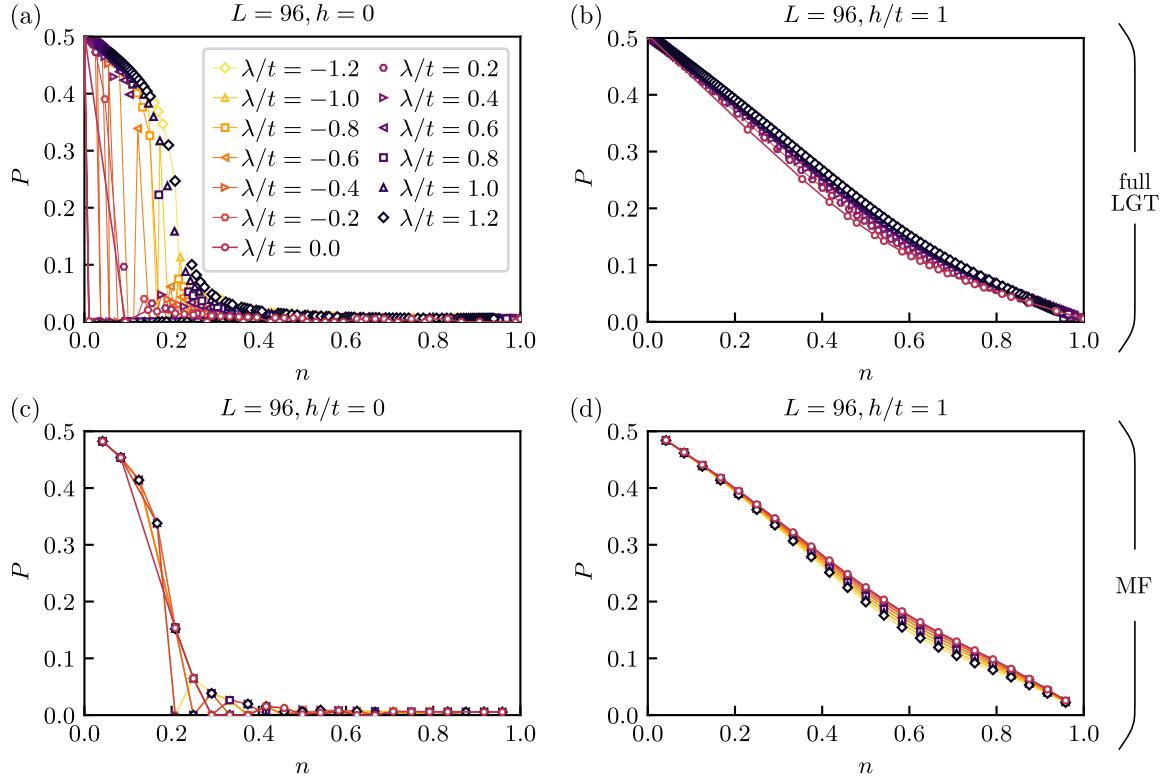


Figure 6.7: Polarization of the \mathbb{Z}_2 electric field, Eq. (6.13), in the exact 1 + 1D \mathbb{Z}_2 LGT, Eq. (5.1), after eliminating the matter, and its mean-field theory in the gauge sector, Eq. (6.6), for different parameter values h and λ as a function of filling n . (a) The polarization in the absence of the electric field term, $h = 0$, is finite for low filling and finite SC term, $\lambda \neq 0$, for the exact \mathbb{Z}_2 LGT. (b) For finite electric field term $h/t = 1$, the polarization is finite for any finite filling n , in the exact \mathbb{Z}_2 LGT, with an almost linear decay as a function of filling n . (c) The polarization in the regime with zero electric field term, $h = 0$, is finite for any value of the SC term λ , at low filling in the mean-field theory in the gauge sector. These results qualitatively match the exact \mathbb{Z}_2 LGT for $\lambda \neq 0$. (d) Excellent agreement in polarization in the mean-field theory with the exact \mathbb{Z}_2 LGT can be seen for finite electric field value $h/t = 1$. This figure was obtained from Fig. 13 in Ref. [5].

We define the \mathbb{Z}_2 electric field polarization as [5]

$$P = \frac{1}{L+1} \sum_j \langle \hat{\tau}_{(j,j+1)}^x \rangle. \quad (6.13)$$

The results for different parameter values h , λ and filling n are presented in Fig. 6.7, for both the exact \mathbb{Z}_2 LGT and the mean-field theory for the gauge sector.

For the exact \mathbb{Z}_2 LGT in the absence of the \mathbb{Z}_2 electric field term $h = 0$, and finite SC term $\lambda \neq 0$, we observe finite polarization for low filling $n \lesssim 0.2$. The onset of finite polarization as a function of filling depends on the value of the SC term λ , see Fig. 6.7(a). It shifts to higher value of n , with increasing value of $|\lambda|$. This is in agreement with the previous

numerical results where we observed dependence on the SC term λ for the transition to the FM state. When $h = \lambda = 0$, the polarization remains close to zero for any finite filling $n > 0$, which indicates no transition to the FM state. This is also in agreement with the previous results, as at $\lambda = 0$ free partons form a LL [5].

Comparing these results to the mean-field theory for the gauge sector in Fig. 6.7(c), reveals excellent agreement when SC term is finite $\lambda \neq 0$. However, we do not see any dependence on λ , and the transition always occurs at approximately same filling $n \approx 0.2$. In addition, we also observe finite polarization for low filling when $\lambda = 0$. These results are thus in agreement with previous numerical results for the mean-field theory in the gauge sector, which captures the main features of the exact \mathbb{Z}_2 LGT, except on the $\lambda = 0$ line [5].

For finite \mathbb{Z}_2 electric field term $h/t = 1$, the polarization in the exact \mathbb{Z}_2 LGT is finite for any finite filling n ; see Fig. 6.7(b). It has an almost linear dependence on filling as it decreases with increasing filling n . There is no significant change in this behaviour for different values of λ . Mean-field theory for $h/t = 1$, shows excellent agreement with the polarization in the exact model; see Fig. 6.7(d). The results match very well, and almost coincide [5].

In conclusion, we see that the mean-field theory in the gauge sector exhibits excellent agreement in the \mathbb{Z}_2 electric field polarization, and thus the agreement in confining features and transitions come as no surprise [5]

6.6 Summary and conclusion of the mean-field theory for the LGT

In this chapter we have developed a mean-field theory for the extended 1 + 1D \mathbb{Z}_2 LGT with SC term, where matter is coupled to a gauge field. We first derived the mean-field theory by considering a product ansatz and thus effectively factorized matter and gauge degrees of freedom. We enforced the Gauss law on the mean field level by imposing Lagrange multipliers, which act as constraints that enforce correct filling. The mean-field model in the gauge sector, Eq. (6.2), reduces to a simple one-dimensional superconducting wire model [190]. Such class of models can be solved via Jordan-Wigner and Bogoliubov transformations [192]. The gauge field simply renormalizes the interaction parameters, and the confining \mathbb{Z}_2 electric field becomes a constant energy offset [5]. On the one hand, the mean-field theory for the charge sector exactly captures the regime when the \mathbb{Z}_2 electric field term is zero, $h = 0$, as the exact model also maps to the same SC model in the limit of static charges, i.e., when $h = 0$ [5, 119]. On the other hand, it completely misses the confined Higgs phase or the confined meson LL, when $h \neq 0$, as the electric field term is simply a constant energy offset and thus does not modify the physics and the phase diagram.

In the gauge sector the mean-field theory, Eq. (6.6), is identified as an Ising model with transverse and longitudinal fields [5]. The Ising interaction comes from the Lagrange multiplier and controls the domain-wall number, i.e., enforces the Gauss law and controls the parton number in the chain [5]. The transverse field term comes from the combined contribution of the hopping t , and SC term λ , and is renormalized by the matter field

[5]. Finally, the longitudinal field is simply the \mathbb{Z}_2 electric field term h . We solved the mean-field theory self-consistently for given parameter values and filling [5]. We started by first determining the value of the longitudinal field g , by solving the mean-field theory in the matter sector via the Bogoliubov transformation. We then used DMRG calculations to search for the correct chemical potential μ_τ , which yields the desired filling.

Next, we determined the phase diagram of the mean-field theory for the gauge sector by studying the entanglement entropy, from which we extracted the central charge. In order to study confinement we also calculate the gauge invariant Green's function and the string-length histograms. We found excellent agreement of the mean-field theory with the exact \mathbb{Z}_2 LGT. It correctly captures the transition between the deconfined SPT phase to the confined symmetry broken FM and AFM when $h = 0$. For finite electric field term, $h \neq 0$, it also correctly captures the transition from confined Higgs to the confined AFM state at high filling. A minor limitation of the mean-field theory is that transitions at finite fillings do not exhibit any dependence on the SC term λ , whereas a weak dependence is seen in the exact \mathbb{Z}_2 LGT [5]. A slightly bigger limitation is the fact that the mean-field theory breaks the $U(1)$ symmetry related to the parton number conservation. Consequently, on the special line $\lambda = 0$ no parton LL is obtained when $h = 0$, and no meson LL is seen for $h \neq 0$ [5]. Nevertheless, the deconfined regime for $h = \lambda = 0$ at intermediate fillings, and confinement at $h \neq 0, \lambda = 0$, for any filling, is still captured qualitatively [5].

We have demonstrated that a simple mean-field theory can be derived for a paradigmatic 1 + 1D \mathbb{Z}_2 LGT with dynamical matter, which captures the main features of the exact LGT. The most important among these are confined and deconfined phases, which are fully captured by the mean-field theory for the gauge fields [5]. In addition, we gained new physical insights into the \mathbb{Z}_2 LGT. The mean-field developed for the one-dimensional \mathbb{Z}_2 LGT can be also extended to higher or mixed dimensional \mathbb{Z}_2 LGTs, where a simplified theory is even more desirable as the treatment of the exact LGT is even more complicated.

Chapter 7

Beyond one-dimension: mixed dimensional XXZ model

In this chapter, we study a mixed-dimensional spin system where we consider a two-dimensional square lattice with full XXZ interactions in one of the dimensions, and a simple Ising interaction in the other dimension. The motivation to study such system is twofold. On the one hand, this model can be simulated in state-of-the-art quantum simulation setups with atoms that possess dipolar interactions, or with ultracold molecules [31, 211]. On the other hand, such mixed dimensional models can be mapped to an effective $1 + 1\text{D } \mathbb{Z}_2$ LGT, which we extensively studied in this thesis. Hence, this model can exhibit a confinement-deconfinement transition, where spin domain walls are formulated in terms of partons that bind into mesons.

We first study the ground state phase diagram by performing DMRG calculations, where we wind the MPS chain on a cylinder with limited circumference in order to implement a two-dimensional system. We uncover an interesting phase diagram, which contains a stripe order of spins for sufficient Ising coupling, and a disordered state otherwise. In addition to the ground state results, we also simulate the system at finite temperature and study the meson gas state at low magnetization and temperature. In such state partons bind into mesons in a similar fashion as in the pure \mathbb{Z}_2 LGT system. The mapping to the \mathbb{Z}_2 LGT system thus offers a nice reformulation of the problem and explanation of the underlying physical mechanism.

This chapter is based on a manuscript, which at the time of writing this thesis was in preparation and had a preliminary title *Mixed-dimensional XXZ model*, [6]. We note that the author list and its order were also preliminary at that stage.

7.1 Introduction

The main motivation to study such system is its potential to be experimentally realized in quantum simulation setups where the constituents possess dipolar interactions. Possible candidates are thus atoms with dipolar interactions, or polar molecules. One of the possible

platforms are cold atom optical lattices with Erbium [31]. There, an extended Bose-Hubbard model has already been experimentally realized, which can be expressed as [31]

$$\hat{\mathcal{H}}_{\text{BH}} = -t \sum_{\langle i,j \rangle} \left(\hat{a}_i^\dagger \hat{a}_j + \text{H.c.} \right) - \sum_j \mu_j \hat{n}_j + \sum_{i < j} V_{i,j} \hat{n}_i \hat{n}_j. \quad (7.1)$$

Such system has long distance interactions $V_{i,j}$, arising from dipole-dipole forces between Erbium atoms, which can be expressed as [31]

$$V_{i,j} = V_0 \frac{1 - 3((x/r) \sin \theta \cos \phi + (y/r) \sin \theta \sin \phi)^2}{r^3} \quad (7.2)$$

The interactions thus decay as $\propto 1/r^3$, where $r = |\mathbf{i} - \mathbf{j}|$ is the distance between the atoms [31]. In addition, we define the x and y component distance between the atoms, and (θ, ϕ) are the dipole polar and azimuthal angles, respectively [31].

We will consider the hard-core boson limit, and truncate the long distance interactions only to nearest-neighbour (NN). Such model then maps to a two-dimensional XXZ chain with interactions that are tunable in the x and y direction.

The model that we study in this chapter contains another restriction, namely, we only allow for atom hopping in the x -direction of the optical lattice, which is also experimentally feasible [31]. As we will soon see in the next section where we formally define the model, this results in spin raising and lowering operators acting only in one of the spatial directions. In such sense, our model is an analog to mixed-dimensional $t - J$ models, where hopping is also restricted only to a single dimension, whereas the interactions are two-dimensional [132, 169]. The above restriction to one-dimensional hopping brings our model closer to the mixed-dimensional $t - J_z$ model, which in turn can directly be mapped to a 1 + 1D \mathbb{Z}_2 LGT [132]. We will show that already in the absence of holes, i.e., when the system reduces purely to spins, similar mapping can be performed, where the \mathbb{Z}_2 electric field value emerges on the mean-field level [6].

Detail studies of such models is thus interesting from the perspective of the study of confinement in the context of \mathbb{Z}_2 LGTs and their experimental realization with cold atoms. The seemingly simple spin system thus has a far reaching influence in different fields of physics.

7.2 Model

We consider a two-dimensional spin-1/2 lattice, with spin raising/lowering operators acting only in one spatial direction, whereas the Ising interactions act in both, which we express as [6]

$$\hat{\mathcal{H}} = \sum_{\langle i,j \rangle_x} \left[\frac{J_x^\perp}{2} \left(\hat{S}_i^+ \hat{S}_j^- + \hat{S}_j^+ \hat{S}_i^- \right) + J_x^z \hat{S}_i^z \hat{S}_j^z \right] - J_y \sum_{\langle i,j \rangle_y} \hat{S}_i^z \hat{S}_j^z. \quad (7.3)$$

Here, the sum $\langle i,j \rangle_x$ is to be understood over NN in the x -direction, and $\langle i,j \rangle_y$ as a NN sum in the y -direction; see Fig. 7.1(a). The spin raising/lowering operators are defined

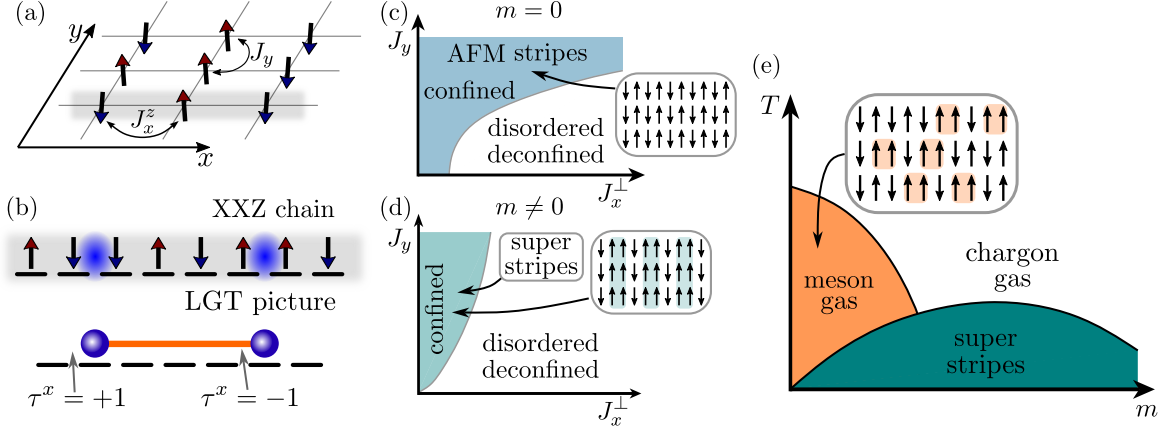


Figure 7.1: Mixed-dimensional XXZ model, Eq. (7.3). (a) A sketch of the two-dimensional spin-1/2 lattice, where in the x -direction, the system has full XXZ interactions (highlighted in grey), and a simple FM Ising coupling in the y -direction. (b) Mapping between the XXZ chain basis and the \mathbb{Z}_2 LGT picture. The orange line denotes the \mathbb{Z}_2 string, which denotes negative orientation of the \mathbb{Z}_2 electric field $\tau_{j,j+1}^x = \langle \hat{\tau}_{j,j+1}^x \rangle = -1$. No string denotes positive orientation. (c) Ground state phase diagram of the mixed-dimensional XXZ model, Eq. (7.3), for zero total magnetization $m = 0$, which exhibits an AFM stripe order (sketch of a possible spin configuration in the bracket), stabilized by the inter-chain coupling J_y . (d) Ground state phase diagram for finite filling, $m \neq 0$, which exhibits a super stripe order in the y -direction (sketch of the spin configuration in the inset) stabilized by the FM inter-chain coupling J_y . (e) A phase diagram of the mixed-dimensional XXZ model as a function of magnetization m and temperature T , with a sketch of the meson gas residing at low magnetization and temperature. This figure will be presented in Ref. [6].

as \hat{S}^\pm , and the z -component spin operator as \hat{S}^z . If not stated otherwise, we will always consider AFM interactions in the x -direction $J_x^z > 0$, and FM interactions, $J_y > 0$, in the y -direction. In addition, the size of our system in the x -direction is L_x , and in the y -direction L_y , with a total number of spin sites equal to $A_s = L_x L_y$. We typically consider open boundary conditions (OBC) in the longer x -direction and periodic boundary conditions (PBC) in the shorter y -direction. We can thus consider our system also as consisting of L_y one-dimensional XXZ chains, which are coupled in the y -direction by a simple NN Ising interaction, as sketched in Fig. 7.1(a). Related to the above, we define the magnetization of the y -th chain as [5]

$$m_c^y = \frac{1}{L_y} \sum_{\langle i,j \rangle_y} \langle \hat{S}_j^z \rangle. \quad (7.4)$$

When the Ising interaction in the y -direction is zero, $J_y = 0$, the XXZ chains are decoupled, meaning that the system reduces to L_y isolated, identical XXZ chains [6]. The physics of such system is well known, and can be solved using the Bethe ansatz [182, 184–186]. The one-dimensional XXZ chains form a Luttinger liquid for generic magnetization m_c , and parameter value J_x^\perp / J_x^z [6, 182]. Such regime can be parameterized by the Luttinger liquid parameter K , which determines the strength of the interactions in the system [182]. The

Luttinger liquid parameter can be extracted from the long distance behaviour of the spin-spin correlations, which typically decay with a power law [182]. For zero magnetization, $m_c^y = 0$, the spins form an ordered anti-ferromagnetic (AFM) phase for dominant Ising interaction $J_x^\perp / J_x^z < 1$. This is a BKT transition, where the system becomes gapped [182].

When the coupling between chains is finite $J_y > 0$, such order can be stabilized also for higher values of the J_x^\perp term [6]. It also induces coherence between chains, and we can thus obtain various stripe ordering in the y -direction. When the coupling J_y is weak, we can still consider the system to be one-dimensional, and the coupling J_y can be considered as an interaction, which renormalizes the interactions in the one-dimensional chain [6, 182].

We treat the mixed-dimensional XXZ model, Eq. (7.3), by employing DMRG calculations, where the MPS are winded on a cylinder with circumference L_y .

7.2.1 Mapping to the \mathbb{Z}_2 lattice gauge theory

The mixed-dimensional XXZ model, Eq. (7.3), can be effectively mapped to a paradigmatic one-dimensional \mathbb{Z}_2 LGT with dynamical matter. As was discussed in great detail in this work, such LGT exhibits confinement of individual particles (partons) into dimers (mesons), at finite \mathbb{Z}_2 electric field value [1, 3–5, 160]. Such formulation will also help us interpret the numerical results in the next section.

The starting point of this mapping is to consider the spin domain walls in an AFM spin background as hard-core bosons, which we define as [6]

$$\hat{n}_{\langle j,j+1 \rangle} = \hat{a}_{\langle j,j+1 \rangle}^\dagger \hat{a}_{\langle j,j+1 \rangle} = \frac{1}{2} \left(1 + 4\hat{S}_j^z \hat{S}_{j+1}^z \right), \quad (7.5)$$

where $\hat{a}^\dagger(\hat{a})$ are again hard-core boson creation (annihilation) operators. The idea behind such definition comes directly from the Gauss law, and will become apparent below. We note that contrary to the usual \mathbb{Z}_2 electric field representation with the $\hat{\tau}^x$, this time we are in the z -component spin basis. The hard-core parton definition is sketched in Fig. 7.1(b), where we also sketch the \mathbb{Z}_2 strings. These again indicate the orientation of the \mathbb{Z}_2 electric field, which we define as [1, 2, 6]

$$\hat{\tau}_j^x = 2(-1)^j \hat{S}_j^z. \quad (7.6)$$

Such definition fulfills the Gauss law, which is defined in the usual way as [1, 6, 121]

$$\hat{G}_j = \hat{\tau}_{\langle j-1,j \rangle}^x \hat{\tau}_{\langle j,j+1 \rangle}^x (-1)^{\hat{n}_j}. \quad (7.7)$$

More precisely, it satisfies the Gauss law constraint in the physical sector where the states take positive eigenvalues, $\hat{G}_j |\psi\rangle = + |\psi\rangle, \forall j$ [1, 3–5, 121, 160].

By using the definitions in Eq. (7.5) and Eq. (7.6), we can map each term in the mixed-dimensional XXZ model into the \mathbb{Z}_2 LGT basis. We can first consider the spin raising/lowering term proportional to J_x^\perp , which in the LGT basis has two effects, as sketched in Fig. 7.2. In the first case, Fig. 7.2(a), it can move an existing domain wall over two lattice sites, which in the \mathbb{Z}_2 LGT basis results in hopping of the parton over two lattice sites. In the second case, Fig. 7.2(b), it can add a pair of domain walls in an AFM configuration,

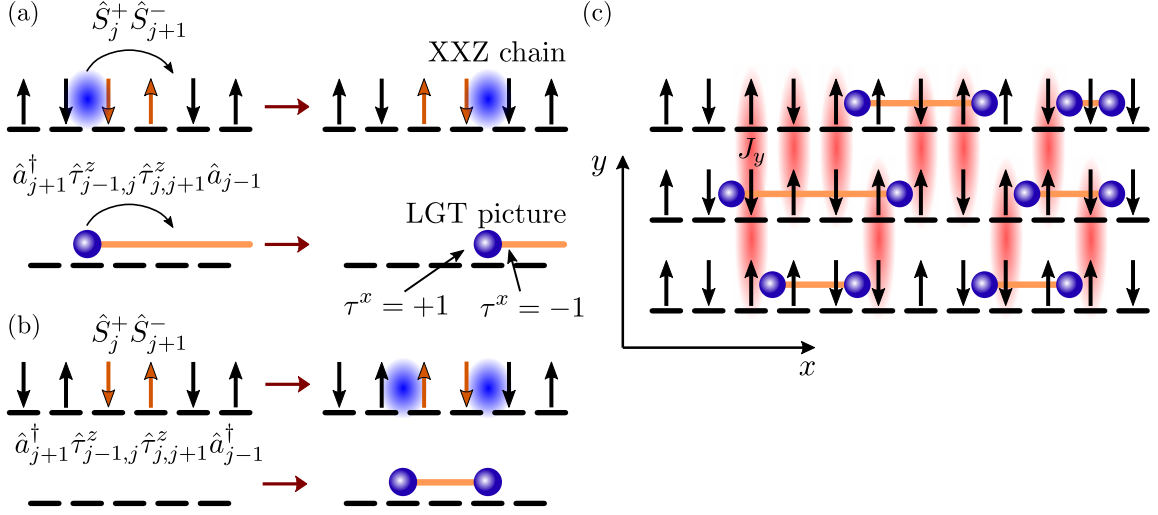


Figure 7.2: Mapping between the mixed-dimensional XXZ spin basis and the \mathbb{Z}_2 LGT basis. (a) Hopping term across two lattice sites in the \mathbb{Z}_2 LGT basis originates from the spin raising/lowering operator acting on a spin configuration, which already contains a spin domain wall. (b) Pair-creation in the \mathbb{Z}_2 LGT basis originates from the same process as in (a) applied to an AFM spin configuration. (c) A sketch of the XXZ model and its \mathbb{Z}_2 LGT picture indicating the inter-chain spin coupling. This interaction induces stripe and super-stripe phases in the XXZ chain, and is the origin of the \mathbb{Z}_2 confining electric field on the mean-field level in the \mathbb{Z}_2 LGT basis. This figure will be presented in Ref. [6].

which results in pair creation at links $\langle j-1, j \rangle$ and $\langle j+1, j+2 \rangle$ in the \mathbb{Z}_2 LGT picture. Both cases and their reverse processes are thus mapped to the \mathbb{Z}_2 picture as [6]

$$\left(\hat{S}_{j+1}^+ \hat{S}_j^- + \hat{S}_j^+ \hat{S}_{j+1}^- \right) \rightarrow \left(\hat{a}_{\langle j-1, j \rangle}^\dagger \hat{\tau}_j^z \hat{\tau}_{j+1}^z \hat{a}_{\langle j+1, j+2 \rangle} + \hat{a}_{\langle j-1, j \rangle}^\dagger \hat{\tau}_j^z \hat{\tau}_{j+1}^z \hat{a}_{\langle j+1, j+2 \rangle}^\dagger + \text{H.c.} \right) \left(1 - \hat{a}_{\langle j, j+1 \rangle}^\dagger \hat{a}_{\langle j, j+1 \rangle} \right). \quad (7.8)$$

Here we also take into account the necessary condition that only configurations with anti-aligned spins will result in states that do not vanish after applying such terms. This results in the condition where, if we consider that partons hop from site $j-1$ to site $j+1$, the central lattice site j has to be vacant [6]. The same condition also applies when a pair is created on sites $j-1$ and $j+1$.

Next we consider the AFM Ising interaction term in the x -direction, which directly maps to the chemical potential term via Eq. (7.5), and can be expressed as [6]

$$\hat{S}_{x,y}^z \hat{S}_{x+1,y}^z \rightarrow \frac{1}{4} \left(1 - 2\hat{n}_{\langle x, x+1 \rangle, y} \right). \quad (7.9)$$

We note that we switched to a more explicit coordinate labeling, (x, y) , of the position of the spin operators on the two-dimensional lattice.

The FM Ising interaction in the y -direction has a slightly more complicated mapping.

By considering Eq. (7.6), it can be expressed as [6]

$$\hat{S}_{x,y}^z \hat{S}_{x,y+1}^z \rightarrow \frac{1}{2} (-1)^x \hat{\tau}_{x,y}^x \frac{1}{2} (-1)^x \hat{\tau}_{x,y+1}^x = \frac{1}{4} \hat{\tau}_{x,y}^x \hat{\tau}_{x,y+1}^x. \quad (7.10)$$

By combining all of the terms we can express the mixed-dimensional model in the \mathbb{Z}_2 LGT picture [6]

$$\begin{aligned} \hat{\mathcal{H}}_{LGT} = t \sum_{x,y} & \left[\left(\hat{a}_{x-1,y}^\dagger \hat{\tau}_{\langle x-1,x \rangle,y}^z \hat{\tau}_{\langle x,x+1 \rangle,y}^z \hat{a}_{x+1,y} + \text{H.c.} \right) (1 - \hat{n}_{x,y}) \right. \\ & \left. + \left(\hat{a}_{x-1,y}^\dagger \hat{\tau}_{\langle x-1,x \rangle,y}^z \hat{\tau}_{\langle x,x+1 \rangle,y}^z \hat{a}_{x+1,y}^\dagger + \text{H.c.} \right) (1 - \hat{n}_{x,y}) \right] \\ & + \frac{J_y}{8} \sum_{x,y} \hat{\tau}_{\langle x,x+1 \rangle,y+1}^x \hat{\tau}_{\langle x,x+1 \rangle,y}^x - \mu \sum_{x,y} \hat{n}_{x,y}, \quad (7.11) \end{aligned}$$

where we defined $t = J_x^\perp/2$ and $\mu = J_x^z/2$. In addition, $\hat{\tau}^z$ again represents the \mathbb{Z}_2 gauge field, and represents the minimal coupling of the gauge field to matter [6]. We also relabeled spin links to matter sites and vice versa, $\langle j-1, j \rangle \rightarrow j$, in order to arrive at the standard formulation of the LGTs used throughout this thesis [6].

The \mathbb{Z}_2 LGT we derived above is slightly different in comparison to what we studied in the previous chapters in this thesis. The most obvious difference is that hopping of partons takes place over two lattice sites, e.g. $j-1$ to $j+1$. Similarly, the SC term, which breaks the overall $U(1)$ symmetry of the partons, also creates or annihilates a parton pair over two lattice site, e.g., at sites $j-1$ and $j+1$. This comes with the condition that the central site j in both cases has to be empty. Despite of these differences we expect that the overall physical behaviour should not change, and thus similar properties are assumed for this model to the ones encountered for the $1+1\text{D}$ \mathbb{Z}_2 LGT with SC terms in Chapter 5.

However, a bigger difference in terms of physical properties comes from the inter-chain coupling J_y . By considering this term on the mean-field level we can rewrite it in a linear form as [6]

$$\frac{J_y}{4} \sum_{x,y} \hat{\tau}_{\langle x,x+1 \rangle,y}^x \hat{\tau}_{\langle x,x+1 \rangle,y+1}^x \rightarrow h \sum_{x,y} \hat{\tau}_{\langle x,x+1 \rangle,y}^x. \quad (7.12)$$

Here we defined the \mathbb{Z}_2 electric field term h as [6]

$$h = \frac{J_y}{8} \left(\langle \hat{\tau}_{\langle x,x+1 \rangle,y+1}^x \rangle + \langle \hat{\tau}_{\langle x,x+1 \rangle,y-1}^x \rangle \right), \quad (7.13)$$

where we furthermore defined the average value of the \mathbb{Z}_2 electric field in chains neighbouring the chain y , on the mean-field level as [6]

$$\langle \hat{\tau}_{\langle x,x+1 \rangle,y\pm 1}^x \rangle = 2m_s^{y\pm 1} = \frac{2}{L_x} \sum_x (-1)^j \langle \psi | \hat{S}_{x,y\pm 1}^z | \psi \rangle. \quad (7.14)$$

As can be seen from the expression above, this is simply the staggered magnetization of the neighbouring chains. As a result we can see that on the mean-field level the system

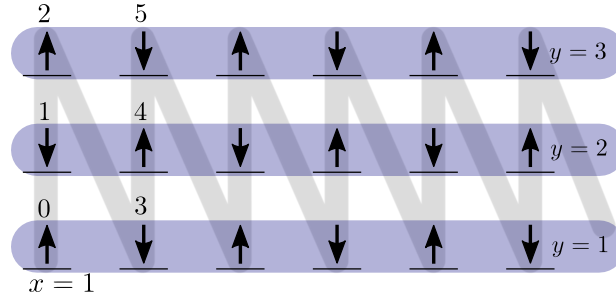


Figure 7.3: A sketch of the MPS chain meandering on a two-dimensional lattice, and thus implementing a two-dimensional system, where one of the dimensions is significantly shorter from the other one. This example shows $L_y = 3$, which results in NN interactions in the x -direction effectively being third neighbour interactions in the MPS chain. This figure will be presented in Ref. [6].

will be confining for non-zero value of the inter-chain coupling J_y and when the chains have a non-zero staggered magnetization. The system thus has to possess an underlying AFM order to exhibit confinement in a sense studied so far in this thesis [6].

By tuning the parameter values of the mixed-dimensional XXZ model we can change the level of AFM ordering in the system and thus change the value of the effective h , which can result in a confinement-deconfinement transition [6]. Uncoupled chains $J_y = 0$ are always deconfined. However, coupled chains $J_y > 0$, will become confining only when there is an underlying AFM order, and should deconfine once the spins are completely disordered, i.e., when $J_x^\perp \gg J_x^z, J_y$.

7.3 Ground state phase diagram

7.3.1 Numerical simulation of the mixed-dimensional XXZ model with MPS

To study the mixed-dimensional XXZ model we turn to DMRG simulations of the system. For that we again use SYTEN [153, 154]. Since we are in fact simulating a system on a two-dimensional lattice, we have to wind the MPS chain as sketched in Fig. 7.3. As a result, the NN interactions in the x -direction become L_y -th neighbour interactions in the MPS implementation. This makes the calculations more challenging as DMRG thrives when the interactions are local, and begins to struggle when the interactions span over more lattice sites [35]. This greatly limits the L_y of the system, and great care needs to be taken in order to converge the results. In order to reduce the boundary effects in the y -direction we thus employ PBC in that dimension while keeping the OBC in the x -direction [6]. Due to the limitations listed above, this is thus a two-dimensional system with a significant limitation since $L_x \gg L_y$.

We typically consider bond dimension up to $\chi = 2048$, and where possible use the $U(1)$ symmetry where we limit the system to a sector with a set total magnetization m . The system size considered for the ground state calculations are $L_x = 40$ and $L_y = 3$.

We also perform finite temperature calculations in a similar manner as described in Section 1.3.3. Since we consider a mixed-dimensional system the doubling of the MPS chain results in $2L_y$ -th neighbour interactions. As a result, we have to use a global $U(1)$ symmetry for the whole system (physical sites and ancilla sites), when performing the calculations. We have to choose the sector where the combined magnetization is zero, $m_{\text{physical}} + m_{\text{ancilla}} = 0$, as the maximally entangled state is formed by singlets between physical and the corresponding ancilla sites [167]. In order to induce finite magnetization in the physical chain we add a finite field $\propto h_z \sum_{x,y} \hat{S}_{x,y}^z$. The full Hamiltonian in the numerical calculations is thus equal to [6]

$$\hat{\mathcal{H}} = \sum_{\langle i,j \rangle_x} \left[\frac{J_x^\perp}{2} (\hat{S}_i^+ \hat{S}_j^- + \hat{S}_j^+ \hat{S}_i^-) + J_x^z \hat{S}_i^z \hat{S}_j^z \right] - J_y \sum_{\langle i,j \rangle_y} \hat{S}_i^z \hat{S}_j^z + h_z \sum_j \hat{S}_j^z. \quad (7.15)$$

This is allowed since in this method the magnetization is not conserved in the physical and ancilla sites separately, however it is conserved for the combined system [167]. The typical system size for finite temperature calculations are $L_x = 20$ and $L_y = 3$. We again note that in the quantum purification method, the Hamiltonian $\hat{\mathcal{H}}$ in the imaginary time evolution [6, 164, 167]

$$|\psi(\beta)\rangle = e^{-\beta \hat{\mathcal{H}}/2} |\psi(\beta = 0)\rangle, \quad (7.16)$$

acts only on the physical states. These are in our case again even sites, and ancilla sites thus correspond to odd sites, of the doubled MPS chains. The sums in Eq. (7.15) are thus to be understood accordingly.

7.3.2 Spin-spin correlations

In order to study the ground state phase diagram of the mixed-dimensional XXZ model we first consider spin-spin correlations in the longer x -direction. In the limit when there is no Ising coupling in the y -direction, $J_y = 0$, our system reduces to L_y identical XXZ chains [6]. As already discussed, a simple one-dimensional XXZ chain forms a Luttinger liquid where the spin-spin correlations decay with a power law [182]

$$\langle \hat{S}_j^z \hat{S}_{j+x}^z \rangle = m_c^2 - \frac{K}{2\pi^2} \frac{1}{x^2} + C_1 \cos(\pi[1 + 2m_c]x) \frac{1}{x^{2K}}, \quad (7.17)$$

where m_c is the magnetization of the chain, and K is the LL parameter [6, 182]. Furthermore, C_1 is a model dependent constant [182].

Although the above expression, Eq. (7.17), strictly holds only in one-dimension, i.e., when $J_y = 0$, we can still use it in the full mixed-dimensional setting in order to determine the strength of the spin-spin correlations, and thus study whether the system is ordering. For example, in order to probe the AFM stripe regime, where all of the spins have coherent AFM correlations, see Fig. 7.1(c), we can also consider the behaviour of [6]

$$C_{AFM_x}^z(x) = (-1)^x \langle \hat{S}_{x_0, y_0}^z \hat{S}_{x_0+x, y_0}^z \rangle. \quad (7.18)$$

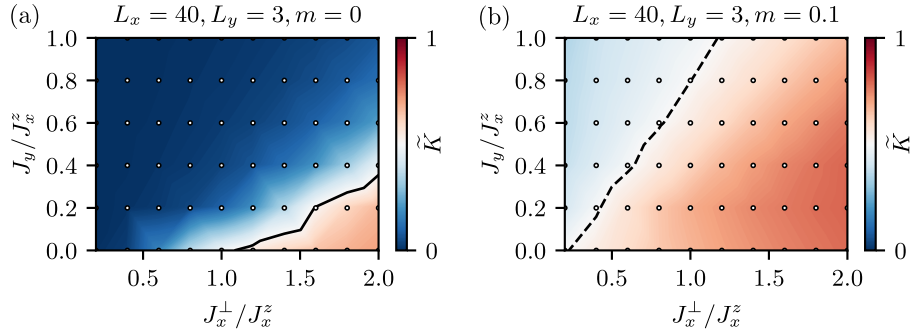


Figure 7.4: LL-like parameter \tilde{K} extracted from the spin-spin correlations, Eq. (7.17), in the longer, x -dimension. (a) For zero magnetization $m = 0$, we obtain low value $\tilde{K} < 1/2$ when $J_x^\perp < J_x^z$ and $J_y = 0$, which signals ordered AFM regime. These value are also obtained for $J_y > 0$, for higher values $J_x^\perp < J_x^z$, which shows that inter-chain coupling stabilizes the AFM stripe order. (b) For finite magnetization $m = 0.1$, the LL-like parameter \tilde{K} , decreases below $\tilde{K} < 1/2$, when $J_x^\perp \ll J_x^z$ and $J_y > 0$, indicating increased spin coherence in that regime. The black lines in both cases signals the regime where the extrapolated values of the LL parameter equal to $\tilde{K} = 1/2$. This figure will be presented in Ref. [6].

In the regime where the system exhibits long-range AFM correlations the above correlator saturates to a finite value $\lim_{x \rightarrow \infty} (-1)^x \langle \hat{S}_{x_0, y_0}^z \hat{S}_{x_0+x, y_0}^z \rangle \neq 0$. The super-stripe regime as sketched in Fig. 7.1(d), is slightly more complicated as the AFM stripe regime, however similar reasoning can be used.

As a first probe of the spin-spin correlations we fit the LL expression, Eq. (7.17), to the data obtained from one of the chains in our mixed-dimensional XXZ model, for different parameter values J_x^\perp/J_x^z , and J_y/J_x^z . In Fig. 7.4 we present the obtained value of the power law exponent in Eq. (7.17), which we denote with \tilde{K} and name the Luttinger liquid-like parameter. That it is to stress the fact that this is a conventional LL parameter only in the regime when $J_y = 0$ [6]. However, as already stated before, we expect that the expression holds also for weak coupling J_y and can be used to determine the strength of the spin-spin correlation for general J_y . Generally, low values of the LL parameter K , signal strong interactions in the chain, which results in weak decays of the correlation functions [182].

For zero magnetization $m = 0$, we uncover excellent agreement on the line $J_y = 0$ with the expected values for the XXZ chains, as the value of \tilde{K} approaches the value of $\tilde{K} = 1/2$ close to $J_x^\perp/J_x^z = 1$ [182]. This is the transition point to the gapped AFM state at zero magnetization, $m = 0$, in a pure one-dimensional XXZ chain. We define the region close to $\tilde{K} \approx 1/2$ as the boundary where the system orders in an AFM state, which for finite chain coupling $J_y > 0$, results in the AFM stripe ordered state. As can be seen in Fig. 7.4(a) the inter-chain coupling extends the area where $\tilde{K} < 1/2$ also for $J_x^\perp > J_x^z$ when $J_y > J_x^z$. We relate this area to the stripe AFM ordered regime, sketched in the inset of Fig. 7.1(c).

For finite magnetization, $m \neq 0$, the one-dimensional XXZ chain can not exhibit an AFM ordered state, and the system remains a Luttinger liquid, with the Luttinger liquid parameter approaching the value $K \rightarrow 1/4$, as $m \rightarrow 0$, for $J_x^\perp < J_x^z$ [6, 182]. At finite inter-chain coupling $J_y > 0$, we thus don't expect AFM ordering in the x -direction, however we can

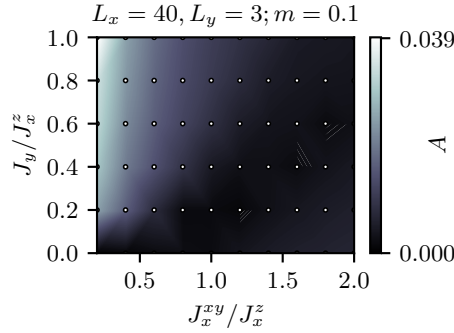


Figure 7.5: Heat diagram of the parameter A , extracted by fitting Eq. (7.19) to the absolute value of the spin-spin correlations. This figure will be presented in Ref. [6].

expect that finite J_y increases the coherence between the chains in the y -direction, which can thus form a stripe like pattern sketched in the inset of Fig. 7.1(d). The results obtained for \tilde{K} from the fits, show that at finite magnetization $m = 0.1$, the LL-like parameter decreases significantly for high inter-chain coupling $J_y > 0$ and low spin raising/lowering term $J_x^\perp \ll J_x^z$; see Fig. 7.4(b). This shows that the inter-chain coupling enhances the spin correlations, which already hints at super-stripe formation [6]. We probe whether the super stripes are really formed more directly in the next section.

7.3.3 Super-stripe order at finite magnetization

Stripe spin-spin correlation patterns

First we consider the spin-spin correlations at finite magnetization only in the x -direction. The AFM strip order is relatively clear already in terms of the correlation function discussed in the previous section. The super-stripe regime on the other hand is not that clear, as there is no ordered regime in the one-dimensional XXZ chain, to which we could relate the super-stripe order. For that we consider to probe the stripe order a bit more directly, by considering the absolute value of the spin-spin correlations and probe whether the correlations saturate to a finite value. We fit the absolute value of the spin-spin correlations with the following function, where the spin modulation is explicit [6]

$$f(x) = \cos(\pi\varphi x + \theta) \left(A + \frac{B}{x^{2K}} \right) + C. \quad (7.19)$$

In the stripe regime, we would expect the parameter A to saturate to a finite value as the stripes become coherent at longer distance x [6]. Other parameters are simply fit parameters, which we do not consider in our analysis. The results for A are presented in Fig. 7.5 and show that there is a finite value of A extracted in the region consistent with low LL-like parameter \tilde{K} in Fig. 7.4(b). This shows that there indeed exists a periodic spin modulation, which suggests a super stripe structure [6].

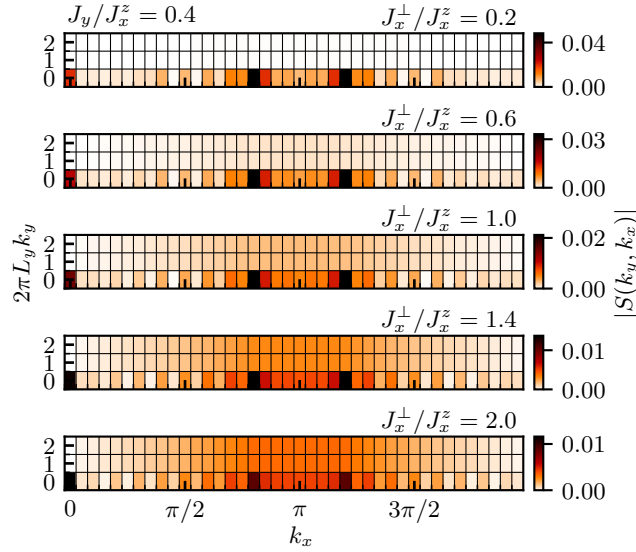


Figure 7.6: Fourier transformation, Eq. (7.21), of the spin-spin correlations for different values of J_x^\perp , at fixed value of $J_y = 0.4J_x^z$. We observe pronounced peaks at $k_x = \pi(1 \pm 2m)$ and $k_y = 0$ for low values of the spin raising/lowering term, J_x^\perp . With increasing value of J_x^\perp the peaks become less pronounced, and finite signal can be observed for $k_y > 0$, which indicates lower coherence of the stripe order. This figure will be presented in Ref. [6].

Static structure factor for the super stripes

Next we study the spin-spin correlations in both spatial dimensions. We calculate the correlations between a reference spin in the middle of the chain at $x_0 = 20$, $y_0 = 2$, with other spins in the lattice [6]

$$C^z(x, y) = \langle \hat{S}_{x_0, y_0}^z \hat{S}_{x, y}^z \rangle. \quad (7.20)$$

After we compute the above correlations we perform a Fourier transformation, which is defined as [6]

$$S(k_x, k_y) = \frac{1}{L_x L_y} \sum_{x=0}^{L_x-1} \sum_{y=0}^{L_y-1} e^{-i(x-x_0)k_x} e^{-i(y-y_0)k_y} C^z(x, y), \quad (7.21)$$

where the Fourier modes were discretized as $\Delta k_x = \frac{2\pi}{L_x}$ and $\Delta k_y = \frac{2\pi}{L_y}$, respectively. The expression in Eq. (7.21) can be thus understood as a version of a static structure factor, which probes translational symmetry breaking [3, 6, 187]. The super-stripe structure will thus exhibit well defined peaks related to the periodicity of the stripes [6]. Furthermore, since the stripes are coherent in the y -direction, the peaks have to be limited to a single $k_y = 0$ mode [6].

The results presented in Fig. 7.6 show well defined peaks at $k_x = \pi(1 \pm 2m)$, limited to $k_y = 0$, for inter-chain coupling $J_y = 0.4J_x^z$ and low spin raising/lowering term $J_x^\perp \gg J_x^z$, as expected in the super-stripe regime [6]. These peaks become less pronounced as J_x^\perp becomes stronger, signaling melting of the stripe order. In addition, weak signal in $k_y > 0$ can be seen, which means that the spin coherence in the y -direction decreases. The formation of

stripes could also be understood in terms of confinement, as the spin domain walls become locked into stripes.

7.3.4 Summary of the ground state results

The ground state results are summarized in Fig. 7.1(c) and 7.1(d), for different magnetization regimes, respectively. We obtain AFM stripe order with spins aligned in the y -direction and AFM ordering of the spins in the x -direction for zero magnetization regime $m = 0$. This is stabilized by non-zero inter-chain coupling $J_y > 0$, and destabilized by high $J_x^\perp \gg J_y, J_x^z$ terms.

For finite magnetization, $m \neq 0$, spin-spin correlations reveal super-stripe formation for strong inter-chain coupling J_y and weak spin raising/lowering term, $J_x^\perp \ll J_y, J_x^z$. There, spins align in the y -direction, and form a standing wave pattern in the x -direction; see the inset in Fig. 7.1(d). This becomes apparent by considering the Fourier transformation of the spin-spin correlations.

7.4 Meson gas at finite temperature

Now we turn our focus to finite temperature properties of the mixed-dimensional XXZ model. In order to obtain the finite temperature results we again employ the quantum purification scheme where we enlarge our system by adding an ancilla lattice site to every physical lattice site [164, 165, 167, 168]. The procedure is thus similar to the one described in Chapter 1.3.3, and Chapter 4; see also Section 7.3.1. We note that we again use the MPS toolkit SYTEN [153, 154]. As a result of the doubling of the MPS lattice site, the physical lattice that we consider in our finite temperature calculations are lower and we consider a system with the physical dimension of $L_x = 20$, and $L_y = 3$; see also Section 7.3.1.

Our results for the ground state showed that the system forms a stripe order in the strong coupling regime $J_y, J_x^z \gg J_x^\perp$. The exact nature of the stripe pattern depends on the magnetization m . By developing the \mathbb{Z}_2 LGT picture, where we mapped our mixed-dimensional XXZ model to a one-dimensional \mathbb{Z}_2 LGT, we saw that the domain walls in the LGT picture become partons, which can bind and form a confined phase. In order for that to happen, the inter-chain coupling has to be finite in addition to the finite staggered magnetization in the chains; see Section 7.2.1.

The formation of stripes in the ground state can be understood as domain walls being bound or locked to the stripes [6]. The partons can be therefore seen as being spatially bound to stripes and not necessarily confined to each other, i.e., the partons can be considered to be confined to the stripes that they form. Here, we are therefore interested how finite temperature can melt the super-stripe order and if confinement, where partons confine into mesons, can be observed for low enough temperature.

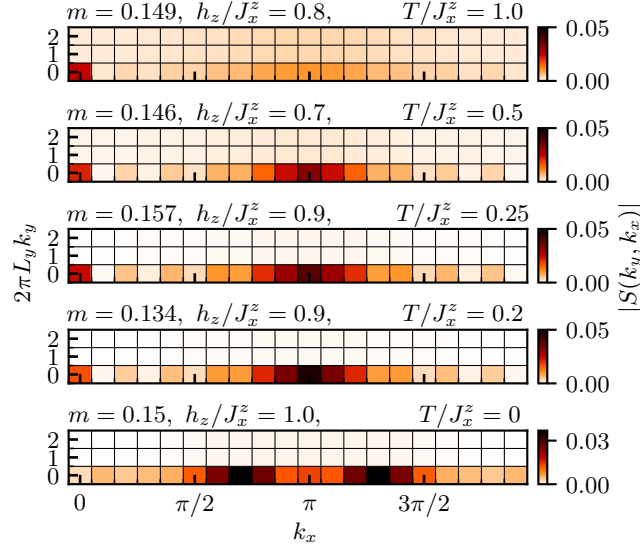


Figure 7.7: Fourier transformation of the spin-spin correlations, Eq. (7.21) for different temperature T and finite magnetization $|m| \approx 0.15$. The chosen parameters are $J_x^\perp/J_x^z = 0.4$, $J_y/J_x^z = 0.8$, where we added a field in the z -direction in order to induce finite magnetization at approximate $|m| \approx 0.15$. In the ground state two peaks are seen at $k_x = \pi(1 \pm 2m)$, $k_y = 0$, indicating a super stripe order. At low temperature, $T \lesssim 0.3J_x^z$, we observe a single peak at $k_x = \pi$, which indicates the meson gas regime as the magnetization is finite. For higher temperature, $T \gtrsim 0.5J_x^z$, the peak at $k_x = \pi$ broadens and becomes less pronounced, which signals that the AFM correlations become weaker, and the system forms a free chargin gas. This figure will be presented in Ref. [6].

7.4.1 Melting the stripe order

In order for the partons to be confined in the \mathbb{Z}_2 LGT picture, the spins in the mixed-dimensional XXZ model have to possess a finite staggered magnetization, $(-1)^j \langle \hat{S}_j^z \rangle \neq 0$, and the coupling between the chains has to be finite $J_y > 0$. At finite temperature $T > 0$, we expect to destroy the super-stripe order. We study whether spinons (partons) confine in the presence of underlying AFM order and form a gas of mesons [6]. We are thus interested whether the local AFM order is present at low temperatures that can mediate the confinement on the mean-field level as explained in Section 7.2.1. For higher temperatures such order is ultimately destroyed and the spinons form a free parton (chargin) gas [6, 132].

To study such behaviour we consider the Fourier transformation of the spin-spin correlations, Eq. (7.21), which directly probes any ordered, symmetry broken state. To uncover the meson gas, where partons are confined, we thus need to observe a well defined peak at $k_x = \pi$, localized to $k_y = 0$, which would indicate AFM correlations that are the necessary ingredient for confinement [6]. To see a clear change from the stripe order to the meson gas regime, we consider a system with finite magnetization $m \neq 0$. There, the super-stripe order, indicated by peaks at $k_x = \pi(1 \pm m)$, for $T = 0$ is melted into a meson gas regime at

low but finite temperature $T > 0$, provided the Fourier transformation, Eq. (7.21), exhibits a well defined peak at $k_x = \pi$ [6]. Such change of behaviour would be a clear indication that the super-stripe order is destroyed, but local AFM correlations arise that mediate confinement of partons, resulting in the meson gas. The benefit of weak magnetization, $m \neq 0$, is also that the system always contains a finite number of partons, which are therefore not just present because of the spin fluctuations [6].

In order to probe the meson gas we consider the Fourier transformation of the spin-spin correlations at different temperatures T and finite magnetization $m = 0.15$. Furthermore, we choose the parameter regime where the ground state calculations indicate well defined super-stripes: $J_x^\perp / J_x^z = 0.4$, and $J_y / J_x^z = 0.8$ [6]; see Fig. 7.4 for the ground state results with similar magnetization. The results presented in Fig. 7.7, show well defined peaks at $k_x = \pi(1 \pm 2m)$, $k_y = 0$, in the ground state $T = 0$, which indicate the super-stripe order. For low temperature, $T \lesssim 0.5J_x^z$, we observe a single, well defined peak at $k_x = \pi$, $k_y = 0$. This is the key signature of the confined meson gas as the system has finite magnetization, $|m| \approx 0.15$. The partons confine into mesons in the spin AFM ordered background, as described in the \mathbb{Z}_2 LGT picture [6]. For higher temperature, $T \gtrsim 0.5J_x^z$, the height of the peak at $k_x = \pi$ lowers and significantly broadens. This indicates that the AFM correlations become weaker and the partons form a free chargin gas, i.e., the spinon excitations become deconfined [6].

Similar features are also observed for higher magnetization. However, there the peaks at $k_x = \pi$ are much broader already for lower temperatures, and we thus assume that the super-stripes melt directly into the spinon gas. With these data we conjecture the phase diagram in Fig 7.1(e), where we assume that the meson gas forms only for low magnetization m . This reasoning comes from the fact that at higher magnetization, more spins will have to be orientated in the same direction. This results in more spinons or partons in the \mathbb{Z}_2 LGT language, which also results in the AFM correlations becoming weaker. For the meson gas to form, the system needs to have enough energy to melt the stripes at low temperature T_{stripes} , but still retain some level of AFM correlations, which completely disappear at T_{AFM} . Thus we see that at low magnetization the following condition has to be met: $0 < T_{\text{stripes}} < T_{\text{AFM}}$, in order to stabilize a meson gas regime [6].

7.4.2 Confinement in the context of LGT

Finally, we also consider the string and anti-string length distributions for the mixed-dimensional XXZ model, as defined in the \mathbb{Z}_2 LGT mapping in Section 7.2.1. This allows us to understand the microscopic picture of the meson gas better, and provides an experimental probe of confinement.

The procedure to obtain snapshots is again similar as already discussed in the previous chapters of this thesis. We note that this time we sample in the z -component spin basis, as per definition in Eq. (7.7). We again record the lengths between odd-even and even-odd partons, which are defined via Eq. (7.5). However, since the confining \mathbb{Z}_2 electric field emerges on the mean-field level, it is not straight forward which orientation of the \mathbb{Z}_2 electric field in the snapshots represents the string and which the anti-string. As a

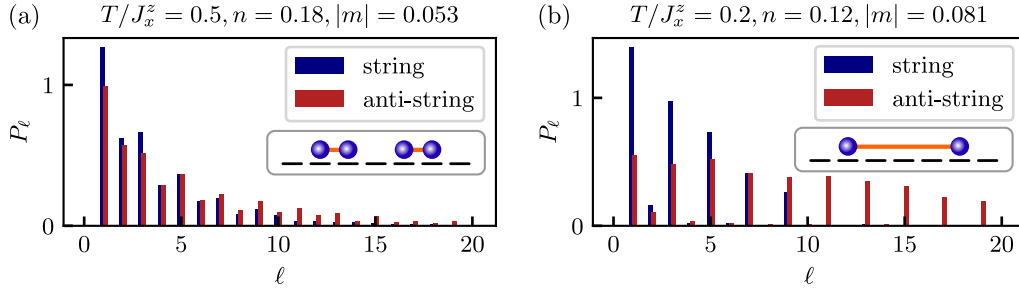


Figure 7.8: String and anti-string length distributions as defined from the effective mapping of the mixed-dimensional XXZ model, Eq. (7.3), to the \mathbb{Z}_2 LGT Eq. (7.11) for different temperature T . In both cases the parameter values are $J_x^\perp/J_x^z = 0.4$, $J_y/J_x^z = 0.8$ and the physical system size is $L_x = 20$ and $L_y = 3$. (a) For higher temperature, $T = 0.5J_x^z$, the string and anti-string distributions are similar. Both have peaks at $\ell = 1$, with approximate same heights and both distributions are relatively broad. (b) For lower temperature $T = 0.25J_x^z$, the string length distribution has a much higher peak at $\ell = 1$, than the anti-string length distribution, which is also much broader. This indicates confinement of partons and thus a meson gas. In both cases we used finite field values in the z-component of the field. For case (a) the value was $h_z = 0.3J_x^z$ and for (b) $h_z = 0.8J_x^z$. The number of snapshots is 400. This figure will be presented in Ref. [6].

result, we compute the staggered magnetization of the chains m_s^y . In the confined regime, partons consisting of the same meson are on average much closer to each other than to other partons, which belong to the neighboring mesons. This is another way of stating that the \mathbb{Z}_2 electric strings are on average much shorter than anti-strings in the confined regime. In this setting we can thus use the prefactor of the staggered magnetization in order to determine whether our system started with a string or an anti-string [6]. In the case when the staggered magnetization in a particular snapshot was positive, we exchange the identity of strings and anti-string for that snapshot [6]. We note that the same technique could have been applied already in Chapter 6 for the regime when $h = 0$ in the extended \mathbb{Z}_2 LGT with SC terms. However in that case, most partons came in pairs from the SC term and we assumed that there is no significant amount of partons in the beginning of the chain that do not have their origin in the SC term. That case is thus slightly different from the mixed-dimensional XXZ model. The above method could have artificially discriminated some snapshots in the pure \mathbb{Z}_2 LGT with SC terms, and as a result we did not use it there.

To analyze the string and anti-string length distributions we again chose the parameter regime, $J_x^\perp/J_x^z = 0.4$, $J_y/J_x^z = 0.8$, which results in super-stripes in the ground state. We choose the results with low magnetization $|m|$ and parton (spinon) density, n . We note that magnetization is tuned by the field h_z in the z-direction, and the parton density depends on parameter values, magnetization, and temperature. Hence, tuning the exact value is complicated [6]. Generally, the parton number is rather low at low magnetization and it is important to have at least two partons in the system in order to see any confining signatures [6]. In our case this means $n \geq 2/20 = 0.1$.

For temperature $T/J_x^z = 0.5$, which is where the peak at $k_x = \pi$ in Fig. 7.7 starts to be-

come broader, we see that the string and anti-string distributions are similar; see Fig. 7.8(a). They both peak at $\ell = 1$ with approximate same peak heights and both distributions are relatively broad. This behaviour thus corresponds to the deconfined regime, in agreement with the Fourier transformation of the spin-spin correlations at higher magnetization in Fig. 7.7. For lower temperature, $T/J_x^z = 0.2$, approximately similar magnetization m , and parton density n , the string and anti-string length distributions differ significantly; see Fig. 7.8(b). Strings have a much higher peak at $\ell = 1$ than the anti-string length peak, and the anti-string length distribution is much broader. We attribute this bimodal distribution to confinement and the meson gas phase [6]. We have thus showed that string and anti-string length histograms are once again a good measure of confinement, which could be obtained in cold atom experiments.

We note that in both cases the shape of distributions are similar to what we obtained for the extended $1 + 1$ \mathbb{Z}_2 LGT with the SC term in Chapter 5.3.2 [5, 6]. This is in agreement with the mapping of the mixed-dimensional XXZ model to the \mathbb{Z}_2 LGT model Eq. (7.11) that contains the SC term, which breaks the $U(1)$ symmetry of the partons. Hence such similarity comes as no surprise.

7.5 Conclusion and outlook

In this chapter we studied a mixed-dimensional XXZ model, where we consider full XXZ interactions in the longer x -dimension of the system that have an AFM nature, and a simple FM Ising interaction in the shorter y -dimension. The main motivation to study such system is advancement of quantum simulation experiments, where such system can be experimentally simulated in platforms utilizing cold atoms with tunable dipole interaction, e.g., atoms with magnetic dipoles like Erbium [31]. We employ MPS calculations in order to obtain numerical results for the ground state as well as at finite temperature. We consider PBC in the shorter dimension and OBC in the longer one. Our system can be thus considered as a cylinder with circumference L_y .

In the ground state the system forms ordered stripe phases. At zero magnetization, the spins order in an AFM fashion in the longer direction, and align in a FM order in the y -direction. For finite magnetization, the spins form super-stripes, where the spins are again aligned ferromagnetically in the y -direction. In the x -direction they form coherent spin waves with periods proportional to magnetization m . These regimes are probed by considering the Fourier transformation of the spin-spin correlations, where in the stripe regime we obtain peaks at $k_x = \pi(1 \pm 2m)$, which reflect the periodicity of the stripes. In addition, the peaks are restricted to $k_y = 0$, which signals coherence in the y -direction, i.e., FM alignment of spins in that dimension.

We map the mixed-dimensional model to the \mathbb{Z}_2 LGT basis, where the \mathbb{Z}_2 electric field term, responsible for confinement of partons into mesons, emerges on the mean-field level, at finite FM coupling in the y -direction, and for finite staggered magnetization in the x -direction.

This mapping motivated us to consider the finite temperature properties of the sys-

tem, where the stripe order is destroyed by finite temperature, however the AFM interactions in the x -directions still induce local AFM ordering, which results in finite staggered magnetization. In such regime spinons (partons in the \mathbb{Z}_2 LGT picture), bind into pairs (mesons), and form a meson gas. We uncover this regime by calculating the spin-spin correlations at finite temperature T , and magnetization. We show that the super stripes peaks at $k_x = \pi(1 \pm 2m)$ and $T = 0$, are replaced by a single peak at $k_x = \pi$ at low but finite temperature. This is the key signature of the meson gas, as the underlying AFM correlations at finite magnetization signal that partons confine into mesons in an AFM background [6]. For high temperatures, the peaks at $k_x = \pi$ become less pronounced, and gradually disappear with higher temperature, which indicates that the AFM correlations vanish and partons (spinons) become free. This picture is valid for low magnetization. At higher magnetization it becomes more difficult for the AFM interactions to induce local AFM order. As a result we expect a transition from stripes directly to a free spinon (chargon) gas at high enough temperature. We summarize our results for the ground state and for finite temperature in Fig. 7.1(c)–(e). We note that stripes can be considered as a confined phase, where spinons (partons) are locked into the stripes.

Finally, we also calculate string and anti-string length distribution according to the mapping to the \mathbb{Z}_2 LGT basis, and are thus completely analogous to the distributions studied in the previous chapters for the pure \mathbb{Z}_2 LGTs. Here we show that string and anti-string length distributions are an excellent probe of confinement and thus the meson gas regime, which can be readily obtained from the cold atom experiments involving dipolar atoms like Erbium [6, 31].

Conclusion and Outlook

In this thesis we studied a one-dimensional \mathbb{Z}_2 lattice gauge theory, where dynamical matter is coupled to a \mathbb{Z}_2 gauge field. The main motivation to study such class of models comes from the recent advancement of quantum simulations with cold atoms where such models could be simulated [21–23, 80]. In addition, \mathbb{Z}_2 LGTs often emerge as low lying effective theories in condensed matter systems [17, 29, 30]. Furthermore, this \mathbb{Z}_2 LGT is interesting as it is one of the simplest platforms to study confinement of individual particles into bound pairs, which we name as mesons.

Confinement itself is a difficult problem, which still has many open questions as the study of it becomes complicated when the matter density is finite [9]. It also spans across different branches of physics, as it is an important concept to better understand binding in high-energy superconductors in condensed matter setting [16], on the one hand, and the binding of quarks into baryons in high-energy physics (HEP), on the other hand [9]. Although the model studied here is a vast simplification of non-Abelian models studied in HEP, it can serve as a simple toy model. Better understanding in such simple \mathbb{Z}_2 LGT might guide us to tackle more complicated problems in the future. More importantly it can also be used as first benchmarks of quantum simulations of lattice gauge theories with cold atoms, which are becoming more powerful, and might help us to gain better insights into more complicated systems.

In Chapter 1, we provide a brief theoretical introduction into the topics of this thesis. We briefly outline quantum simulation experiments, and the recent progress on simulating LGTs. We then introduce \mathbb{Z}_2 LGT by starting from a more general $U(1)$ LGT. Finally, in the last section we describe how the \mathbb{Z}_2 LGT can be numerically simulated using MPS.

The major part of this thesis is devoted to understanding confinement. In Chapter 2, we provide a solution to the confinement problem of the \mathbb{Z}_2 LGT with $U(1)$ matter in the ground state. We start by first defining the problem and by introducing simple limits, e.g., a limit where the parton dynamics is frozen. There, confinement emerges from the \mathbb{Z}_2 electric field term, which induces linear confining potential in the so called strings that connect parton pairs. The string picture comes directly from a set of local constraints, which resemble the Gauss law on a lattice [1, 3–5, 121]. As a result of the linear confining potential, parton pairs bind into tight dimers, which we dub as mesons. Next, we explain how confinement becomes more complicated when matter and gauge field become dynamical. We resort to numerical simulations using DMRG, where we consider the \mathbb{Z}_2 gauge invariant Green's function at long distances. It decays exponentially in the confined regime, and with

a power law in the deconfined regime [1, 160]. We provide a formal solution of the confinement problem by mapping the original Hamiltonian to a string-length basis where Green's function can be related to the operator of translations in the new basis [1]. In addition, we introduce the Friedel oscillations, the period of which doubles in the confined regime, as a measure of confinement in systems with open boundary conditions [1, 3, 160]. In order to detect confinement in quantum simulation experiments using cold atoms, we also consider string and anti-string lengths in the system obtained from numerical snapshots. Similar snapshots can be obtained in cold atom experiments, with site resolved microscopic resolution. We show that string and anti-string length histograms feature a distinctive bimodal distribution in the confined regime, making it a good and simple geometric probe of confinement.

Motivated by the exciting opportunity of simulating the \mathbb{Z}_2 LGT with cold atoms we set to explore the phase diagram of the \mathbb{Z}_2 LGT with $U(1)$ matter in the next Chapter 3. For generic fillings, the \mathbb{Z}_2 LGT with matter that is globally conserved exhibits a simple parton Luttinger liquid (LL) in the deconfined regime and a slightly more complicated meson LL in the confined regime. By including the nearest-neighbor (NN) repulsion between partons, which can be implemented in cold atom experiments, we uncover rich phase diagrams at two-thirds and at half-filling. We use a combination of MPS calculations, and analytical considerations in tractable limits. At two-thirds filling, both interactions work together to stabilize a Mott state of mesons, where every tightly confined meson is followed by a single vacant lattice site [1]. At half-filling, the case is opposite as the NN repulsion stabilizes a simple parton Mott state, where lattice sites alternate between being occupied and vacant, but the \mathbb{Z}_2 electric field term tries to confine the partons into tight mesons [3]. This results in interesting behavior on the interface between the Mott state and the meson LL regime, where due to quantum frustration, partons effectively behave deconfined on short length scales, although they are in fact confined on longer length scales. This is once again verified by considering the Green's function, which has a delayed onset of the exponential decay in that regime. Mott states are uncovered by considering the meson charge gap and the static structure factor, which is also experimentally easily obtainable.

In Chapter 4 we study confinement in the \mathbb{Z}_2 LGT with matter at finite temperature. We study how confinement is affected at finite temperature, in particular if partons remain confined at low temperature. This is again partially motivated by cold atom experiments, which naturally operate at finite temperature. We uncover a smooth confinement-deconfinement crossover at finite temperature, by studying the correlation length of the Green's function [4]. We employ quantum purification scheme via MPS to obtain the thermal states of the \mathbb{Z}_2 LGT. In addition to the Green's function, we also analyze Friedel oscillations and string length distributions, which show that mesons are in fact pre-formed already above the crossover temperature, where thermal fluctuations destroy the coherence.

In the next Chapter 5, we study phase diagrams of the extended \mathbb{Z}_2 LGT with matter, where we include pair creation and annihilation terms that break the $U(1)$ symmetry of the matter. We map out full phase diagrams at zero and non-zero electric field term, and uncover that the system exhibits symmetry broken phases at low and high filling, where the

superconducting (SC) terms induce meson fluctuations, which makes the partons appear confined. For finite \mathbb{Z}_2 electric field term, only such transition at high filling remains, whereas the rest of the system for finite SC terms is in a confined Higgs state.

In order to understand the physics of the \mathbb{Z}_2 LGT with matter better, we develop a mean-field theory description in Chapter 6. We do this by decoupling matter and gauge degrees of freedom while enforcing the Gauss law constraint on the mean-field level via Lagrange multipliers. We thus obtain two decoupled mean-field theories for the two degrees of freedom [5]. We uncover excellent qualitative agreement between the exact \mathbb{Z}_2 LGT and the gauge field theory for the gauge fields. While the mean-field theory for the gauge field fails to capture the LL regimes when the SC term is absent, it does capture all of the main confining features for generic parameter values. In addition, the mean-field theory for the charges captures the limit where the gauge field is static. However, it fails to capture the regime where the \mathbb{Z}_2 electric field term is finite. The mean-field theory for the gauge field is thus the better choice for a general description of the \mathbb{Z}_2 LGT. We believe our approach could be extended to higher dimensions, and offers better insights into understanding the \mathbb{Z}_2 LGT.

Finally, in Chapter 7 we study a mixed dimensional XXZ model, which can be mapped to a version of a \mathbb{Z}_2 LGT. We show how \mathbb{Z}_2 LGT formalism can be used to explain the behaviour of the system at finite temperature, and uncover the so called meson gas at low spin magnetization and temperatures [6]. This state constitutes to confined state of spinons in an antiferromagnetic background, which we interpret in terms of partons in the \mathbb{Z}_2 LGT formulation. The study of such system was motivated by the quantum simulation of ultra-cold atoms with magnetic dipoles, which can realize such systems. We thus demonstrate that we can study the confinement-deconfinement transition in such system, which makes this platform extremely interesting.

In conclusion, we have extensively studied the confinement in a one-dimensional \mathbb{Z}_2 LGT coupled with matter both in the ground state and at finite temperature, and showed that confinement of mesons can be detected at low temperatures. In addition, we studied rich phase diagrams when the matter has a global $U(1)$ symmetry, and in a general case when this symmetry is lost. We have developed simple probes of confinement and various phases in this system, which could be probed in cold atom experiments. Finally, we found interesting physics in a mixed-dimensional XXZ model, which can be explained with the \mathbb{Z}_2 LGT formalism. We provided a deep understanding of a paradigmatic \mathbb{Z}_2 LGT with matter in one dimension. We hope this could be used when studying more complicated gauge structure or higher dimensional systems, and that it provides a road map for what could already be simulated in quantum simulators with cold atoms.

There are many more aspects that could be explored in the future. A natural extension of our work would be to consider confinement and phase diagrams of more complicated gauge structure like the \mathbb{Z}_3 or \mathbb{Z}_4 . For example a possible future direction could also be to couple gauge field to spinful matter, which would exhibit similar confinement features, but the phase diagrams could become even richer. This could once again be tackled by employing DMRG. Another possible direction would be to consider a two-dimensional

\mathbb{Z}_2 LGT coupled to matter. In particular the case, where the total number of hard-core bosons is conserved has not been studied extensively so far, but is an important aspect to be explored especially from the perspective of cold atom experiments. There the problem of confinement is in fact not so well defined as different probes of confinement used in pure \mathbb{Z}_2 LGTs can not be used when including matter [174]. Such systems could be also explored with MPS on cylinders with low circumference or by using, for example projected entangled pair states (PEPS) [212, 213].

One could also probe dynamical properties of the \mathbb{Z}_2 LGT, which can be implemented with MPS and are also extremely relevant from quantum simulation point of view. For example, it was already shown that \mathbb{Z}_2 LGTs exhibit quantum scar behaviour [214, 215]. Another exciting direction is also to consider dynamics in such systems, where a recent proposal by Su et al. [216] developed a scheme to study particle collisions in cold atom setups, analogous to particle colliders. In addition, one could also study transport properties in \mathbb{Z}_2 LGTs. We in fact already started exploring the effect of confinement on the transport properties in a one-dimensional chain, however the results were rather preliminary and we thus did not include it in this work.

There are thus many possible directions on this topics, and we believe quantum simulations in combination with new numerical techniques will result in interesting developments in the near future.

Appendix A

Mapping between the hard core bosons and the XXZ model

The mapping between the hard-core bosons with nearest-neighbor (NN) interactions to a spin-1/2 XXZ chain is achieved by considering the occupied and empty lattice site as a spin up and down states, respectively [182]

$$\hat{b}_j^\dagger \hat{b}_j - \frac{1}{2} \rightarrow \hat{S}_j^z. \quad (\text{A.1})$$

In addition, the hard-core boson creation and annihilation operators are replaced with spin raising and lowering operators accordingly [182]

$$\begin{aligned} \hat{b}_j^\dagger &\rightarrow \hat{S}_j^+, \\ \hat{b}_j &\rightarrow \hat{S}_j^-. \end{aligned} \quad (\text{A.2})$$

We can now define the Hamiltonian with hard-core bosons hopping in a one-dimensional lattice, with some hopping amplitude t , which experience NN interaction with strength V as [182]

$$\hat{\mathcal{H}}^b = -t \sum_j \left(\hat{b}_j^\dagger \hat{b}_{j+1} + \text{H.c.} \right) + V \sum_j \left(\hat{n}_j^b - \frac{1}{2} \right) \left(\hat{n}_{j+1}^b - \frac{1}{2} \right). \quad (\text{A.3})$$

Above we defined the onsite number operator $\hat{n}_j^b = \hat{b}_j^\dagger \hat{b}_j$. With the mapping defined in Eq. (A.1) and Eq. (A.2) the bosonic Hamiltonian can be mapped to a XXZ model [3, 182]

$$\hat{\mathcal{H}}_{\text{XXZ}} = \sum_j \left[J_{xy} \left(\hat{S}_{j+1}^x \hat{S}_j^x + \hat{S}_{j+1}^y \hat{S}_j^y \right) + J_z \hat{S}_{j+1}^z \hat{S}_j^z \right], \quad (\text{A.4})$$

where we took into account the standard spin relations $\hat{S}^\pm = \hat{S}^x \pm i\hat{S}^y$ [122, 173]. Since the mapping is one-to-one the parameters are directly related as $J_{xy} = 2t$ and $J_z = V$ [3, 182]. Furthermore, we note that magnetization is related to the filling of the bosonic chain via

Eq. (A.1), which we can thus define as [182]

$$m = \frac{1}{L} \sum_{j=1}^L \langle \hat{S}_j^z \rangle = \frac{1}{L} \sum_{j=1}^L \left(\langle \hat{b}_j^\dagger \hat{b}_j \rangle - \frac{1}{2} \right) = n^b - \frac{1}{2}, \quad (\text{A.5})$$

where $n^b = N^b/L$ is the average filling of the bosonic chain, containing N^b hard-core bosons and L is the chain length.

We can also add a chemical potential term to the hard-core boson model in order to control the filling [182]

$$\hat{\mathcal{H}}_\mu^b = -\mu \sum_j \left(\hat{n}_j^b - \frac{1}{2} \right). \quad (\text{A.6})$$

In the spin language this is simply a field term [182]

$$\hat{\mathcal{H}}_{h_z} = -\mu \sum_j \hat{S}_j^z. \quad (\text{A.7})$$

For generic filling n^b and parameter ratio V/t , the system forms a Luttinger liquid, which can be parameterized by the Luttinger liquid parameter, K [182]. The only exception is at half-filling $n^b = 0.5$, where the system undergoes a BKT transition to a Mott state [182]. The Mott state is a doubly degenerate, gapped, state where every occupied lattice site is followed by an empty lattice site. In the spin-1/2 picture this corresponds to a gapped AFM phase where the ground state resembles a Néel state [182].

Appendix B

Details on the structure factor calculations

In this section we provide further details on the calculations of the static structure factor at half-filling discussed in Section 3.4. This discussion is based on the Appendix of Ref. [3]. As already stated in the main text the ground state calculations for half-filling, $n = 1/2$, were performed using the MPS toolkit SYTEN [153, 154]. The chain lengths of the results presented in Section 3.4 were equal to $L = 120$, which thus results in $L + 1 = 121$ link variables as we always begin and end the system with a link; see Section 1.3.2 for the mapping of the \mathbb{Z}_2 LGT to the spin model via Gauss law.

Here we once again define the static structure factor for convenience [3, 187]

$$S(k) = \frac{1}{\mathcal{N}} \sum_{j,l} e^{-i(j-l)k} \langle \hat{n}_j \hat{n}_l \rangle. \quad (\text{B.1})$$

Despite the long chain lengths, there are sizable finite size effects, which we avoid by considering only the central $30 < j, l < 90$ sites. As a result the momentum k , is discretized as $k = \frac{s}{\tilde{L}}\pi$, where $s \in \mathbb{Z}$ and \tilde{L} is the number of considered data points. Since the system size is equal to $L = 120$, and we consider the sites $30 < j, l < 90$, this means that $\tilde{L} = 61$ [3]. As a result of considering only the central 61 sites the normalization factor is defined as $\mathcal{N} = \tilde{L}^2$ [3].

B.1 Peaks at the origin

The results in the main text also contain peaks at the origin with period 2π , which are hard to see since they are substantially higher than the peaks of interest at half-integer and integer multiples of π , see Fig. B.1(a). The peaks at the origin with period 2π arise from considering the non-connected density-density correlations and are thus simply related to the chain filling squared $n^2 = 0.25$ [3].

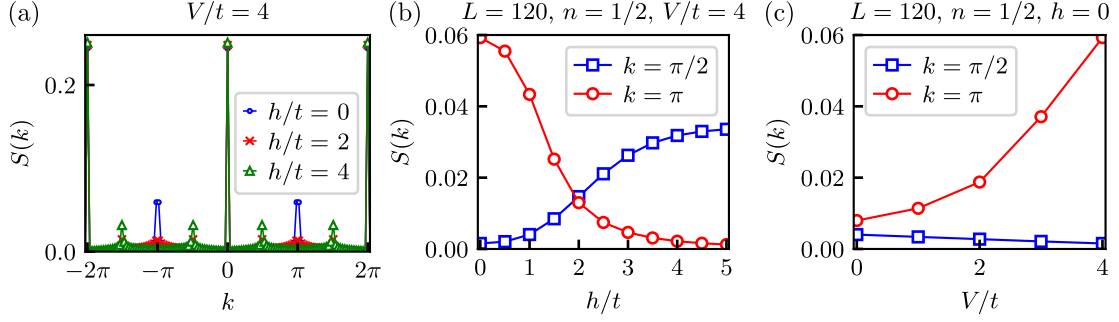


Figure B.1: Numerical details on the structure factor in the \mathbb{Z}_2 LGT after eliminating matter via Gauss law. (a) Structure factor Eq. (B.1) over a larger domain k showing also the peaks at $k = 0, \pm 2\pi$ associated with the total chain filling $n = 1/2$. (a) Structure factor peaks for different value of the electric field term h at $k = \pi/2$ and $k = \pi$ at constant NN repulsion $V = 4t$. (c) Structure factor peaks as a function of V in the absence of the electric field term $h = 0$. This figure was modified from Fig. 11 and Fig. 13 in the Appendix of Ref. [3].

B.2 Details on peak heights

In Fig. B.1(b) we show the behaviour of the peak heights for $V = 4t$ as a function of h [3]. The peak, $k = \pi$, associated with the parton Mott phase drops with increasing value of h . Contrarily, the peak at $k = \pi/2$ associated with the confined meson LL, increases with increasing value of h , the amplitude of which is however much lower than the peak at $k = \pi$, suggesting that this peak is indeed associated with only local correlations and no long-range order. This becomes more clear when considering the system size dependence of the width of these peaks in the next section.

In Fig. B.1(c), we reveal the peak height in the absence of the \mathbb{Z}_2 electric field term $h = 0$, where the system undergoes a transition to a parton Mott state at $V \geq 2t$ [3]. This is reflected in the rising peak $k = \pi$ height for $V \geq 2t$. The peak at $k = \pi/2$ remains low for any value of the NN repulsion V .

B.3 Finite size effects in the static structure factor

We also considered the static structure for smaller system sizes, more precisely at $L = 60$ and $L = 80$, in addition to the longest chain length $L = 120$ [3]. The goal was to study the system size dependence of our numerical results. The results for static structure factor Eq. (B.1) for different system size L and parameter values are presented in Fig. B.2.

We note that peaks generally decrease with increasing system size. However, the peaks are also highly sensitive to the discretization of the momenta k [3]. Thus, at different system sizes we approach closer to the exact values of $k = \pi/2, \pi$, and thus the peak height varies according to how close the discretized value approaches the exact integer and half-integer values of π [3]. As can be seen in Fig. B.2(b) and B.2(c), it appears that this effect might be even more important than the system size as the peaks for the system size $L = 120$ appear higher than the peaks for $L = 80$.

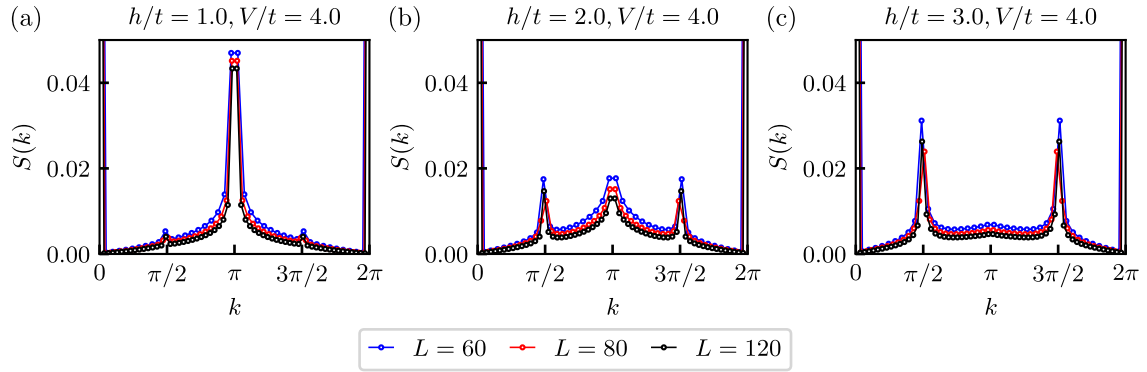


Figure B.2: The static structure factor, Eq. (B.1), for different parameter values and systems sizes $L = 60, 80, 120$. (a) The structure factor for $V = 4t$ and $h = t$ in the parton Mott state. (b) The structure factor for $V = 4t$ and $h = 2t$ in the parton plasma regime showing peaks at half-integer and integer momentum values. (c) The structure factor for $V = 4t$ and $h = 3t$ in the meson LL regime. This figure was modified from Fig. 14 in the Appendix of Ref. [3].

In addition to the change of the height of the peaks with system size, we also observe that the width of the peak changes with the system size. The effect of discretization has a smaller effect on the width of the peaks [3]. The width of peaks at integer π momentum generally decreases with increasing system size, which means that these peaks really signal a true long-range order - the parton Mott state [3]. The width of peaks at half-integer π momentum do not appear to have strong system size dependence, which hints that these peaks really indicate only locally correlated states, and no real long-range order.

Appendix C

Solution of the mean-field theory for the matter sector

The superconducting model, Eq. (6.2) can be diagonalized by using the Bogoliubov transformation [161, 190–192]. The ground state energy of this model is important for the solution of the mean-field theory for the gauge sector, as it directly relates to the value of the parameter g . This short appendix section is based on the Appendix C of Ref. [5].

We start by first rewriting the Eq. (6.2) in terms of spinless fermions by using the Jordan-Wigner transformation [5, 172, 173, 188]

$$\hat{\mathcal{H}}_c = -t_c \sum_{j=1}^{L-1} (\hat{c}_{j+1}^\dagger \hat{c}_j + \text{H.c.}) + \lambda_c \sum_{j=1}^{L-1} (\hat{c}_{j+1}^\dagger \hat{c}_j^\dagger + \text{H.c.}) + \mu_c \sum_{j=1}^L (\hat{n}_j^\ell - n). \quad (\text{C.1})$$

Similar mapping was performed in Section 5.2.1, where we have shown that the original \mathbb{Z}_2 LGT in the limit when $h = 0$, maps to the one-dimensional superconducting model [161]. Above, we also defined $t_c = t \langle \hat{\tau}_{(j,j+1)}^z \rangle$ and $\lambda_c = \lambda \langle \hat{\tau}_{(j,j+1)}^z \rangle$ [5]. Next, we perform a Fourier transformation $\hat{c}_j^\dagger = \frac{1}{\sqrt{L}} \sum_k e^{-ikj} \hat{c}_k^\dagger$, which allows us to express the above equation as [5]

$$\hat{\mathcal{H}}_c = \sum_{k>0} (\mu_c - 2t_c \cos(k)) (\hat{c}_k^\dagger \hat{c}_k + \hat{c}_{-k}^\dagger \hat{c}_{-k}) + \sum_{k>0} 2i\lambda_c \sin(k) (-\hat{c}_k^\dagger \hat{c}_{-k}^\dagger + \hat{c}_{-k} \hat{c}_k) - \mu_c nL. \quad (\text{C.2})$$

Note that we expressed the equation only in terms of positive k modes [5]. We can rewrite the above expression in a slightly different form as [5, 192]

$$\hat{\mathcal{H}}_c = \sum_{k>0} \begin{pmatrix} \hat{c}_k^\dagger & \hat{c}_{-k} \end{pmatrix} \begin{pmatrix} \epsilon(k) & -2i\lambda_c \sin(k) \\ 2i\lambda_c \sin(k) & -\epsilon(k) \end{pmatrix} \begin{pmatrix} \hat{c}_k \\ \hat{c}_{-k}^\dagger \end{pmatrix} + \sum_{k>0} \epsilon(k) - \mu_c nL, \quad (\text{C.3})$$

where we defined $\epsilon(k) = \mu_c - 2t_c \cos(k)$ for convenience [5]. By using the Bogoliubov transformation we can diagonalize this expression as [5, 192]

$$\hat{\mathcal{H}}_c - \sum_{k>0} \epsilon(k) + \mu_c nL = \sum_{k>0} \begin{pmatrix} \hat{c}_k^\dagger & \hat{c}_{-k} \end{pmatrix} \mathbf{H}(k) \begin{pmatrix} \hat{c}_k \\ \hat{c}_{-k}^\dagger \end{pmatrix} = \sum_{k>0} \begin{pmatrix} \hat{b}_k^\dagger & \hat{b}_{-k} \end{pmatrix} \mathbf{\Lambda}(k) \begin{pmatrix} \hat{b}_k \\ \hat{b}_{-k}^\dagger \end{pmatrix}. \quad (\text{C.4})$$

Here we defined the Bogoliubov modes as $\hat{b}^{(\pm)}$, which is simply a linear combination of operators \hat{c}^\dagger and \hat{c} [5, 192]. Furthermore, we defined a diagonal matrix Λ with the following two entries [5]

$$\Lambda_{\pm}(k) = \pm \sqrt{(\mu_c - 2t_c \cos(k))^2 + (2\lambda_c \sin(k))^2}. \quad (\text{C.5})$$

The equation Eq. (C.1) in the diagonal form can be thus expressed as [5]

$$\hat{\mathcal{H}}_c = \sum_k \Lambda_+ \hat{b}_k^\dagger \hat{b}_k - \sum_{k>0} \Lambda_+ + \sum_{k>0} \epsilon(k) - \mu_c n L. \quad (\text{C.6})$$

From this expression the ground estate energy equals to [5]

$$E_0 = \langle \hat{\mathcal{H}}_c \rangle / L = -\frac{1}{L} \sum_{k>0} \Lambda_+ + \frac{1}{L} \sum_{k>0} \epsilon(k) - \mu_c n, \quad (\text{C.7})$$

where we normalized the energy per lattice site. To compute this value we consider the thermodynamic limit, where the above sums can be expressed with integrals [5]

$$E_0 = -\frac{1}{2\pi} \int_0^\pi dk \sqrt{(\mu_c - 2t_c \cos(k))^2 + (2\lambda_c \sin(k))^2} + \frac{1}{2\pi} \int_0^\pi dk (\mu_c - 2t_c \cos(k)) - \mu_c n. \quad (\text{C.8})$$

The above integral can be performed numerically for the set of parameter values t_c and λ_c , for a chemical potential μ_c . However, we are interested in the solution for a given filling n . Hence, we first have to find the chemical potential μ_c that yields the correct filling n , which can be done by solving the self-consistency equation [5]

$$0 \stackrel{!}{=} \frac{dE_0}{d\mu_c} = -\frac{1}{2\pi} \int_0^\pi dk \frac{\epsilon(k)}{\sqrt{\epsilon^2(k) + (2\lambda_c \sin(k))^2}} + \frac{1}{2} - n, \quad (\text{C.9})$$

which gives us an expression for the average filling in terms of μ_c as [5]

$$n = \frac{1}{2} \left(1 - \frac{1}{\pi} \int_0^\pi dk \frac{\epsilon(k)}{\sqrt{\epsilon^2(k) + (2\lambda_c \sin(k))^2}} \right). \quad (\text{C.10})$$

To find the solution for E_0 , we thus need to solve Eq. (C.8) and Eq. (C.10) self-consistently. This can be done by employing simple numerical integration.

However, we are interested in the value of E_0 for a given set of t , λ and filling n , as this directly gives us the parameter g , since [5]

$$E_0 = -t_c \left(\langle \hat{c}_{j+1}^\dagger \hat{c}_j \rangle + \langle \hat{c}_j^\dagger \hat{c}_{j+1} \rangle \right) + \lambda_c \left(\langle \hat{c}_{j+1}^\dagger \hat{c}_j^\dagger \rangle + \langle \hat{c}_j \hat{c}_{j+1} \rangle \right) = -\langle \hat{\tau}_{(j,j+1)}^z \rangle g. \quad (\text{C.11})$$

The parameter g can thus be expressed as $g = -E_0 / \langle \hat{\tau}_{(j,j+1)}^z \rangle$ and we can normalize Eq. (C.8), by the average value $\langle \hat{\tau}_{(j,j+1)}^z \rangle$. This simplifies our calculations as $\langle \hat{\tau}_{(j,j+1)}^z \rangle$ is generally not known, and by normalizing all of the equations by this quantity we simply need to find the solution of our equations in terms of $\tilde{\mu}_c = \mu_c / \langle \hat{\tau}_{(j,j+1)}^z \rangle$, for known parameter values t and

λ , for a given filling n [5]. The two relevant equations thus simplify to [5]

$$g = \frac{1}{2\pi} \int_0^\pi dk \sqrt{(\tilde{\mu}_c - 2t \cos(k))^2 + (2\lambda \sin(k))^2} + \tilde{\mu}_c \left(n - \frac{1}{2} \right), \quad (\text{C.12})$$

and the expression for filling becomes [5]

$$n = \frac{1}{2} \left(1 - \frac{1}{\pi} \int_0^\pi dk \frac{\tilde{\mu}_c - 2t \cos(k)}{\sqrt{(\tilde{\mu}_c - 2t \cos(k))^2 + \lambda^2(k)}} \right). \quad (\text{C.13})$$

These are also the relevant equations presented in the main text.

List of Figures

1.1	Filling of the chain, n , as a function of the chemical potential μ in the $1 + 1\text{D}$ \mathbb{Z}_2 LGT after integrating out the charges, Eq. (1.77). This figure was obtained from Fig. S1 in the Supplemental material of Ref. [4].	28
1.2	A sketch of physical and auxiliary (ancilla) lattice sites, implemented with an extended MPS lattice. This figure was obtained from Fig. S2 in the Supplemental material of Ref. [4].	31
2.1	A sketch of a one-dimensional \mathbb{Z}_2 LGT, where a \mathbb{Z}_2 gauge field is coupled to $U(1)$ matter. Figure was modified from Fig. 1 in Ref. [1].	37
2.2	Second order hopping of mesons in the limit when $h \gg t$	40
2.3	Gauge invariant \mathbb{Z}_2 Green's function Eq. (2.12) in a $1 + 1\text{D}$ \mathbb{Z}_2 LGT coupled to matter. Figure was modified from Fig. 2 in Ref. [5].	41
2.4	Friedel oscillations in a $1 + 1\text{D}$ \mathbb{Z}_2 lattice gauge theory Eq. (2.1). The results presented in this figure come from Ref. [4].	43
2.5	String and anti-string length distributions in a $1 + 1\text{D}$ \mathbb{Z}_2 lattice gauge theory Eq. (2.1). This figure was modified from Fig. 3 in Ref. [5].	44
2.6	Mapping between the original and the string-length basis of the one-dimensional \mathbb{Z}_2 LGT. This figure was modified from Fig. 1 in Ref. [1].	49
3.1	Steps in obtaining the $V \rightarrow \infty$ limit of the \mathbb{Z}_2 LGT coupled to matter at two-thirds filling. This figure was modified from Fig. S8 in the Supplementary material of Ref. [1].	60
3.2	The charge gap, Eq. (3.16), extrapolated in the thermodynamic limit for the $1 + 1\text{D}$ \mathbb{Z}_2 LGT with NN interactions, Eq. (3.7). The figure is modified from Fig. 2 in Ref. [1].	62
3.3	Details on the numerical calculations of the charge gap, Δ_c . The figure is modified from Fig. S7 in the supplementary material of Ref. [1].	63
3.4	Sketch of a phase diagram of the $1 + 1\text{D}$ \mathbb{Z}_2 LGT, Eq. (3.7), coupled to dynamical $U(1)$ charges at half-filling $n = 1/2$. This figure is modified from Fig. 1 in Ref. [3].	65
3.5	Different configurations of dimers in the limit of $t = 0$ and $h, V > 0$. This figure is modified from Fig. 2 in Ref. [3].	67

3.6	The pseudospin picture of squeezed mesons. This figure is modified from Fig. 3 in Ref. [3].	68
3.7	Second-order perturbation NN repulsion terms between pseudospin configurations. This figure is modified from Fig. 9 in the Appendix of Ref. [3].	70
3.8	Details on the extrapolation of the charge gap in the thermodynamic limit for half-filling $n = 1/2$. This figure is modified from Fig. 10(a) in the Appendix of Ref. [3].	72
3.9	The charge gap, Eq. (3.25), extrapolated in the thermodynamic limit for $n = 1/2$. This figure is modified from Fig. 4(a) in Ref. [3]; and Figs. 10(b) and (c) in the Appendix of Ref. [3].	73
3.10	Structure factor Eq. (3.28) at half-filling in the \mathbb{Z}_2 LGT after eliminating matter via Gauss law. This figure was modified from Fig. 5 in Ref. [3].	74
3.11	Height of the structure factor peaks at $k = \pi/2$ and $k = \pi$ in the \mathbb{Z}_2 LGT at half-filling. This figure was modified from Fig. 4 in Ref. [3].	75
3.12	Green's function, Eq. (3.29) results for different value of h and high value of the NN repulsion $V/t = 8$. This figure was modified from Fig. 6 in Ref. [3].	77
3.13	Green's function fitted with Eq.(3.31) for parameter values $2h = V = 4t$ in the \mathbb{Z}_2 LGT after eliminating matter via Gauss law. The length of the chain is $L = 120$. This figure was modified from Fig. 15 in Ref. [3].	78
3.14	Green's function fit results at different parameter values h and V . This figure was modified from Fig. 7 in Ref. [3].	79
3.15	Green's function fits with a power-law and an exponential function in the frustrated regime $2h = V = 4t$ in the \mathbb{Z}_2 LGT. This figure was modified from Fig. 16 in Ref. [3].	80
4.1	1 + 1D \mathbb{Z}_2 LGT coupled to dynamical matter. This figure was obtained from Fig. 1 in Ref. [4].	85
4.2	Finite temperature expectation values of observable in the 1 + 1D \mathbb{Z}_2 Hamiltonian as a function of inverse temperature. This figure was obtained from Fig. S3 in the Supplementary material of Ref. [4].	87
4.3	Green's function, Eq. (4.5), results shown on a log-log scale at a target filling of $n_t = 0.3889$, for different temperatures T in the regime with and without the \mathbb{Z}_2 electric field term. This figure was modified from Fig. S4 in the Supplementary material of Ref. [4].	88
4.4	Density profile $\langle \hat{n}_j \rangle$ in the 1 + 1D \mathbb{Z}_2 LGT at different temperatures and electric field values. This figure was obtained from Fig. S5 in the Supplementary material of Ref. [4].	90
4.5	Fourier transformation Eq. (4.10), of the density profiles in 1 + 1D \mathbb{Z}_2 LGT. This figure was obtained from Fig. 2 in Ref. [4].	91
4.6	Chain filling n in the \mathbb{Z}_2 LGT as a function of the chemical potential μ , at different temperatures T , obtained via snapshots and directly from MPS. This figure was obtained from Fig. S6 in the Supplementary material of Ref. [4].	93

4.7	String and anti-string length distributions obtained from snapshots. This figure was obtained from Fig. 3 in Ref. [4].	94
5.1	A sketch of a $1 + 1\text{D } \mathbb{Z}_2$ LGT with SC terms Eq. (5.1), where dynamical charges are coupled to a \mathbb{Z}_2 gauge field. This figure was modified from Fig. 1 in Ref. [5].	99
5.2	Qualitative sketch of the phase diagram of a $1 + 1\text{D } \mathbb{Z}_2$ LGT with SC terms Eq. (5.1). This figure was modified from Fig. 1 in Ref. [5].	101
5.3	Entanglement entropy in the middle of the chain $S(x = L/2)$ for the $1 + 1\text{D } \mathbb{Z}_2$ LGT, Eq. (5.1), after integrating out the charges by taking into account the Gauss law constraint, as a function of filling n and SC term λ . This figure was modified from Fig. 2 in Ref. [5].	103
5.4	Entanglement entropy in the middle of the chain $S(x = L/2)$ for the $1 + 1\text{D } \mathbb{Z}_2$ LGT, Eq. (5.1) after eliminating matter via Gauss law, as a function of the chemical potential μ and SC term λ . This figure was modified from Fig. 14 in Ref. [5].	104
5.5	Fit of the normalized entanglement entropy $\tilde{S}(x)$ with Eq. (5.10) in the \mathbb{Z}_2 LGT after eliminating the matter via Gauss law. This figure was obtained from Fig. 15 in Ref. [5].	105
5.6	Central charge results extracted by fitting Eq. (5.10) to the numerical entanglement entropy results in the \mathbb{Z}_2 LGT Eq. (5.1) after integrating out the matter fields. This figure was modified from Fig. 3 in Ref. [5].	107
5.7	Green's function Eq. (5.13) for the generalized $1 + 1\text{D } \mathbb{Z}_2$ LGT with SC terms Eq. (5.1) for different parameter values and filling n . This figure was modified from Fig. 4 in Ref. [5].	110
5.8	String and anti-string length distributions for the $1 + 1\text{D } \mathbb{Z}_2$ LGT with SC terms Eq. (5.1). This figure was obtained from Fig. 5 in Ref. [5].	112
5.9	Sketches of phase diagrams of the $1 + 1\text{D } \mathbb{Z}_2$ LGT coupled to dynamical matter as a function of the SC term λ and the electric field term h at different fillings n . This figure was modified from Fig. 6 in Ref. [5].	115
6.1	Entanglement entropy $S(L/2)$ for the mean-field theory of the gauge sector Eq. (6.6) as a function of filling n and the SC term λ . This figure was adapted from Fig. 7 in Ref. [5].	124
6.2	Central charge in the mean-field theory for the gauge field Eq. (6.6) for different electric field values, as a function of filling n and the SC term λ . This figure was adapted from Fig. 8 in Ref. [5].	125
6.3	Green's function results Eq. (6.12), for the mean-field theory of the gauge field Eq. (6.6) for different electric field h , SC term λ and filling n . This figure was modified from Fig. 9 in Ref. [5].	127
6.4	String and anti-string length histograms in the mean-field theory for the gauge field, Eq. (6.6), for different parameter values h, λ and filling n . This figure was obtained from Fig. 10 in Ref. [5].	130

6.5	Qualitative sketch of the phase diagram of the mean-field theory for the 1 + 1D \mathbb{Z}_2 LGT with matter. This figure was obtained from Fig. 11 in Ref. [5].	131
6.6	Ground state energy comparison between the exact 1 + 1D \mathbb{Z}_2 LGT Eq. (5.1) and the mean-field theory in the gauge sector Eq. (6.6) as a function of filling n , for different electric field term value h , and SC term λ . This figure was obtained from Fig. 12 in Ref. [5].	133
6.7	Polarization of the \mathbb{Z}_2 electric field, Eq. (6.13), in the exact 1 + 1D \mathbb{Z}_2 LGT, Eq. (5.1), and its mean-field theory in the gauge sector, Eq. (6.6), for different parameter values h and λ and as a function of filling n . This figure was obtained from Fig. 13 in Ref. [5].	134
7.1	Mixed-dimensional XXZ model, Eq. (7.3). This figure will be presented in Ref. [6].	139
7.2	Mapping between the mixed-dimensional XXZ spin basis and the \mathbb{Z}_2 LGT basis. This figure will be presented in Ref. [6].	141
7.3	A sketch of the MPS chain meandering on a two-dimensional lattice, and thus implementing a two-dimensional system. This figure will be presented in Ref. [6].	143
7.4	LL-like parameter \tilde{K} extracted from the spin-spin correlations, Eq. (7.17), in the longer, x -dimension. This figure will be presented in Ref. [6].	145
7.5	Heat diagram of the parameter A , extracted by fitting Eq. (7.19) to the absolute value of the spin-spin correlations. This figure will be presented in Ref. [6].	146
7.6	Fourier transformation, Eq. (7.21), of the spin-spin correlations for different values of J_x^\perp , at fixed value of $J_y = 0.4J_x^z$. This figure will be presented in Ref. [6].	147
7.7	Fourier transformation of the spin-spin correlations, Eq. (7.21) for different temperature T and finite magnetization $ m \approx 0.15$. This figure will be presented in Ref. [6].	149
7.8	String and anti-string length distributions as defined from the effective mapping of the mixed-dimensional XXZ model, Eq. (7.3), to the \mathbb{Z}_2 LGT Eq. (7.11) for different temperature T . This figure will be presented in Ref. [6].	151
B.1	Numerical details on the structure factor in the \mathbb{Z}_2 LGT. This figure was modified from Fig. 11 and Fig. 13 in the Appendix of Ref. [3].	162
B.2	The static structure factor, Eq. (B.1), for different parameter values and systems sizes $L = 60, 80, 120$. This figure was modified from Fig. 14 in the Appendix of Ref. [3].	163

Bibliography

- [1] M. Kebrič, L. Barbiero, C. Reinmoser, U. Schollwöck, and F. Grusdt, “Confinement and Mott transitions of dynamical charges in one-dimensional lattice gauge theories,” *Physical Review Letters* **127**, 167203, ISSN: 1079-7114 (2021).
- [2] M. Kebrič, “Doped antiferromagnets and \mathbb{Z}_2 lattice gauge theories in one-dimension,” MA thesis (LMU München, Faculty of Physics, 2020).
- [3] M. Kebrič, U. Borla, U. Schollwöck, S. Moroz, L. Barbiero, and F. Grusdt, “Confinement induced frustration in a one-dimensional \mathbb{Z}_2 lattice gauge theory,” *New Journal of Physics* **25**, 013035, ISSN: 1367-2630 (2023).
- [4] M. Kebrič, J. C. Halimeh, U. Schollwöck, and F. Grusdt, “Confinement in $(1 + 1)$ -dimensional \mathbb{Z}_2 lattice gauge theories at finite temperature,” *Phys. Rev. B* **109**, 245110 (2024).
- [5] M. Kebrič, U. Schollwöck, and F. Grusdt, *Mean-field theory of 1+1D \mathbb{Z}_2 lattice gauge theory with matter*, Apr. 2024, arXiv:2404.02890 [cond-mat.quant-gas].
- [6] M. Kebrič, L. Su, A. Douglas, M. Szurek, O. Marković, U. Schollwöck, A. Bohrdt, M. Greiner, and F. Grusdt, *Mixed-dimensional XXZ chains*, In preparation.
- [7] H. Lange, M. Kebrič, M. Buser, U. Schollwöck, F. Grusdt, and A. Bohrdt, “Adaptive quantum state tomography with active learning,” *Quantum* **7**, 1129, ISSN: 2521-327X (2023).
- [8] P. W. Anderson, “More is different: broken symmetry and the nature of the hierarchical structure of science.,” *Science* **177**, 393–396, ISSN: 1095-9203 (1972).
- [9] J. Greensite, *An introduction to the confinement problem* (Springer International Publishing, 2020), ISBN: 9783030515638.
- [10] J. G. Bednorz and K. A. Müller, “Possible high T_c superconductivity in the Ba-La-Cu-O system,” *Zeitschrift für Physik B Condensed Matter* **64**, 189–193, ISSN: 1434-6036 (1986).
- [11] D. Griffiths, *Introduction to elementary particles* (Wiley, Dec. 1987), ISBN: 9783527618460.
- [12] L. N. Cooper, “Bound electron pairs in a degenerate Fermi gas,” *Physical Review* **104**, 1189–1190, ISSN: 0031-899X (1956).

- [13] J. Bardeen, L. N. Cooper, and J. R. Schrieffer, "Theory of superconductivity," *Physical Review* **108**, 1175–1204, ISSN: 0031-899X (1957).
- [14] J. Bardeen, L. N. Cooper, and J. R. Schrieffer, "Microscopic theory of superconductivity," *Physical Review* **106**, 162–164, ISSN: 0031-899X (1957).
- [15] B. Keimer, S. A. Kivelson, M. R. Norman, S. Uchida, and J. Zaanen, "From quantum matter to high-temperature superconductivity in copper oxides," *Nature* **518**, 179–186, ISSN: 1476-4687 (2015).
- [16] S. Sachdev and D. Chowdhury, "The novel metallic states of the cuprates: topological Fermi liquids and strange metals," *Progress of Theoretical and Experimental Physics* **2016**, 12C102, ISSN: 2050-3911 (2016).
- [17] S. Sachdev, "Topological order, emergent gauge fields, and Fermi surface reconstruction," *Reports on Progress in Physics* **82**, 014001, ISSN: 1361-6633 (2018).
- [18] E. Fradkin and L. Susskind, "Order and disorder in gauge systems and magnets," *Physical Review D* **17**, 2637–2658, ISSN: 0556-2821 (1978).
- [19] C. Gross and I. Bloch, "Quantum simulations with ultracold atoms in optical lattices," *Science* **357**, 995–1001, ISSN: 1095-9203 (2017).
- [20] M. Lewenstein, A. Sanpera, and V. Ahufinger, *Ultracold atoms in optical lattices: simulating quantum many-body systems* (OUP Oxford, 2012), ISBN: 9780191627439.
- [21] C. Schweizer, F. Grusdt, M. Berngruber, L. Barbiero, E. Demler, N. Goldman, I. Bloch, and M. Aidelsburger, "Floquet approach to \mathbb{Z}_2 lattice gauge theories with ultracold atoms in optical lattices," *Nature Physics* **15**, 1168–1173, ISSN: 1745-2481 (2019).
- [22] F. Görg, K. Sandholzer, J. Minguzzi, R. Desbuquois, M. Messer, and T. Esslinger, "Realization of density-dependent peierls phases to engineer quantized gauge fields coupled to ultracold matter," *Nature Physics* **15**, 1161–1167, ISSN: 1745-2481 (2019).
- [23] L. Barbiero, C. Schweizer, M. Aidelsburger, E. Demler, N. Goldman, and F. Grusdt, "Coupling ultracold matter to dynamical gauge fields in optical lattices: from flux attachment to \mathbb{Z}_2 lattice gauge theories," *Science Advances* **5**, 10.1126/sciadv.aav7444, ISSN: 2375-2548 (2019).
- [24] J. B. Kogut, "An introduction to lattice gauge theory and spin systems," *Reviews of Modern Physics* **51**, 659–713, ISSN: 0034-6861 (1979).
- [25] K. G. Wilson, "Confinement of quarks," *Physical Review D* **10**, 2445–2459, ISSN: 0556-2821 (1974).
- [26] E. Zohar, J. I. Cirac, and B. Reznik, "Quantum simulations of lattice gauge theories using ultracold atoms in optical lattices," *Reports on Progress in Physics* **79**, 014401, ISSN: 1361-6633 (2015).

- [27] M. C. Bañuls, K. Cichy, J. Ignacio Cirac, K. Jansen, S. Kühn, and H. Saito, "Towards overcoming the Monte Carlo sign problem with tensor networks," *EPJ Web of Conferences* **137**, edited by Y. Foka, N. Brambilla, and V. Kovalenko, 04001, ISSN: 2100-014X (2017).
- [28] M. Troyer and U.-J. Wiese, "Computational complexity and fundamental limitations to fermionic quantum Monte Carlo simulations," *Physical Review Letters* **94**, 170201, ISSN: 1079-7114 (2005).
- [29] T. Senthil and M. P. A. Fisher, " Z_2 Gauge theory of electron fractionalization in strongly correlated systems," *Phys. Rev. B* **62**, 7850–7881 (2000).
- [30] E. Demler, C. Nayak, H.-Y. Kee, Y. B. Kim, and T. Senthil, "Fractionalization patterns in strongly correlated electron systems: spin-charge separation and beyond," *Physical Review B* **65**, 155103, ISSN: 1095-3795 (2002).
- [31] L. Su, A. Douglas, M. Szurek, R. Groth, S. F. Ozturk, A. Krahn, A. H. Hébert, G. A. Phelps, S. Ebadi, S. Dickerson, F. Ferlaino, O. Marković, and M. Greiner, "Dipolar quantum solids emerging in a Hubbard quantum simulator," *Nature* **622**, 724–729, ISSN: 1476-4687 (2023).
- [32] E. Fradkin and S. H. Shenker, "Phase diagrams of lattice gauge theories with Higgs fields," *Physical Review D* **19**, 3682–3697, ISSN: 0556-2821 (1979).
- [33] P. A. Lee, N. Nagaosa, and X.-G. Wen, "Doping a Mott insulator: physics of high-temperature superconductivity," *Reviews of Modern Physics* **78**, 17–85, ISSN: 1539-0756 (2006).
- [34] S. R. White, "Density matrix formulation for quantum renormalization groups," *Physical Review Letters* **69**, 2863–2866, ISSN: 0031-9007 (1992).
- [35] U. Schollwöck, "The density-matrix renormalization group in the age of matrix product states," *Annals of Physics* **326**, 96–192, ISSN: 0003-4916 (2011).
- [36] L. Tarruell and L. Sanchez-Palencia, "Quantum simulation of the Hubbard model with ultracold fermions in optical lattices," *Comptes Rendus. Physique* **19**, 365–393, ISSN: 1878-1535 (2018).
- [37] A. Bohrdt, L. Homeier, C. Reinmoser, E. Demler, and F. Grusdt, "Exploration of doped quantum magnets with ultracold atoms," *Annals of Physics* **435**, 168651, ISSN: 0003-4916 (2021).
- [38] A. Browaeys and T. Lahaye, "Many-body physics with individually controlled Rydberg atoms," *Nature Physics* **16**, 132–142, ISSN: 1745-2481 (2020).
- [39] C. Adams and E. Riis, "Laser cooling and trapping of neutral atoms," *Progress in Quantum Electronics* **21**, 1–79, ISSN: 0079-6727 (1997).

- [40] R. Grimm, M. Weidemüller, and Y. B. Ovchinnikov, "Optical dipole traps for neutral atoms," in *Advances in atomic, molecular, and optical physics*, Vol. 42, edited by B. Bederson and H. Walther, *Advances In Atomic, Molecular, and Optical Physics* (Academic Press, 2000), pp. 95–170, <https://www.sciencedirect.com/science/article/pii/S1049250X0860186X>.
- [41] M. Aidelsburger, "Artificial gauge fields with ultracold atoms in optical lattices," en, PhD thesis (LMU München, 2015).
- [42] K. I. Petsas, A. B. Coates, and G. Grynberg, "Crystallography of optical lattices," *Physical Review A* **50**, 5173–5189, ISSN: 1094-1622 (1994).
- [43] D. Greif, M. F. Parsons, A. Mazurenko, C. S. Chiu, S. Blatt, F. Huber, G. Ji, and M. Greiner, "Site-resolved imaging of a fermionic Mott insulator," *Science* **351**, 953–957, ISSN: 1095-9203 (2016).
- [44] A. Mazurenko, C. S. Chiu, G. Ji, M. F. Parsons, M. Kanász-Nagy, R. Schmidt, F. Grusdt, E. Demler, D. Greif, and M. Greiner, "A cold-atom fermi–hubbard antiferromagnet," *Nature* **545**, 462–466, ISSN: 1476-4687 (2017).
- [45] C. Becker, P. Soltan-Panahi, J. Kronjäger, S. Dörscher, K. Bongs, and K. Sengstock, "Ultracold quantum gases in triangular optical lattices," *New Journal of Physics* **12**, 065025, ISSN: 1367-2630 (2010).
- [46] L. Tarruell, D. Greif, T. Uehlinger, G. Jotzu, and T. Esslinger, "Creating, moving and merging Dirac points with a Fermi gas in a tunable honeycomb lattice," *Nature* **483**, 302–305, ISSN: 1476-4687 (2012).
- [47] C. Chin, R. Grimm, P. Julienne, and E. Tiesinga, "Feshbach resonances in ultracold gases," *Reviews of Modern Physics* **82**, 1225–1286, ISSN: 1539-0756 (2010).
- [48] S. L. Cornish, M. R. Tarbutt, and K. R. A. Hazzard, "Quantum computation and quantum simulation with ultracold molecules," *Nature Physics*, 10.1038/s41567-024-02453-9, ISSN: 1745-2481 (2024).
- [49] J. Zeiher, R. van Bijnen, P. Schauß, S. Hild, J.-y. Choi, T. Pohl, I. Bloch, and C. Gross, "Many-body interferometry of a Rydberg-dressed spin lattice," *Nature Physics* **12**, 1095–1099, ISSN: 1745-2481 (2016).
- [50] M. P. A. Fisher, P. B. Weichman, G. Grinstein, and D. S. Fisher, "Boson localization and the superfluid-insulator transition," *Physical Review B* **40**, 546–570, ISSN: 0163-1829 (1989).
- [51] M. Greiner, O. Mandel, T. Esslinger, T. W. Hänsch, and I. Bloch, "Quantum phase transition from a superfluid to a Mott insulator in a gas of ultracold atoms," *Nature* **415**, 39–44, ISSN: 1476-4687 (2002).

- [52] S. Baier, M. J. Mark, D. Petter, K. Aikawa, L. Chomaz, Z. Cai, M. Baranov, P. Zoller, and F. Ferlaino, "Extended Bose-Hubbard models with ultracold magnetic atoms," *Science* **352**, 201–205, ISSN: 1095-9203 (2016).
- [53] T. Fukuhara, S. Hild, J. Zeiher, P. Schauß, I. Bloch, M. Endres, and C. Gross, "Spatially resolved detection of a spin-entanglement wave in a Bose-Hubbard chain," *Physical Review Letters* **115**, 035302, ISSN: 1079-7114 (2015).
- [54] E. G. Dalla Torre, E. Berg, and E. Altman, "Hidden order in 1d Bose insulators," *Physical Review Letters* **97**, 260401, ISSN: 1079-7114 (2006).
- [55] T. Esslinger, "Fermi-Hubbard physics with atoms in an optical lattice," *Annual Review of Condensed Matter Physics* **1**, 129–152, ISSN: 1947-5462 (2010).
- [56] D. P. Arovas, E. Berg, S. A. Kivelson, and S. Raghu, "The Hubbard model," *Annual Review of Condensed Matter Physics* **13**, 239–274, ISSN: 1947-5462 (2022).
- [57] W. Hofstetter, J. I. Cirac, P. Zoller, E. Demler, and M. D. Lukin, "High-temperature superfluidity of Fermionic atoms in optical lattices," *Physical Review Letters* **89**, 220407, ISSN: 1079-7114 (2002).
- [58] P. A. Lee, "From high temperature superconductivity to quantum spin liquid: progress in strong correlation physics," *Reports on Progress in Physics* **71**, 012501, ISSN: 1361-6633 (2007).
- [59] M. Qin, C.-M. Chung, H. Shi, E. Vitali, C. Hubig, U. Schollwöck, S. R. White, and S. Zhang, "Absence of superconductivity in the pure two-dimensional Hubbard model," *Physical Review X* **10**, 031016, ISSN: 2160-3308 (2020).
- [60] H. Xu, C.-M. Chung, M. Qin, U. Schollwöck, S. R. White, and S. Zhang, "Coexistence of superconductivity with partially filled stripes in the hubbard model," *Science* **384**, 10.1126/science.adh7691, ISSN: 1095-9203 (2024).
- [61] A. Altland and B. D. Simons, *Condensed matter field theory* (Cambridge University Press, Mar. 2010), ISBN: 9780511789984.
- [62] M. Köhl, H. Moritz, T. Stöferle, K. Günter, and T. Esslinger, "Fermionic atoms in a three dimensional optical lattice: observing fermi surfaces, dynamics, and interactions," *Physical Review Letters* **94**, 080403, ISSN: 1079-7114 (2005).
- [63] R. Jördens, N. Strohmaier, K. Günter, H. Moritz, and T. Esslinger, "A Mott insulator of fermionic atoms in an optical lattice," *Nature* **455**, 204–207, ISSN: 1476-4687 (2008).
- [64] U. Schneider, L. Hackermüller, S. Will, T. Best, I. Bloch, T. A. Costi, R. W. Helmes, D. Rasch, and A. Rosch, "Metallic and insulating phases of repulsively interacting fermions in a 3D optical lattice," *Science* **322**, 1520–1525, ISSN: 1095-9203 (2008).

- [65] W. S. Bakr, J. I. Gillen, A. Peng, S. Fölling, and M. Greiner, "A quantum gas microscope for detecting single atoms in a Hubbard-regime optical lattice," *Nature* **462**, 74–77, ISSN: 1476-4687 (2009).
- [66] J. F. Sherson, C. Weitenberg, M. Endres, M. Cheneau, I. Bloch, and S. Kuhr, "Single-atom-resolved fluorescence imaging of an atomic Mott insulator," *Nature* **467**, 68–72, ISSN: 1476-4687 (2010).
- [67] J. Liang, J. Rudolph N. Kohn, M. F. Becker, and D. J. Heinzen, "High-precision laser beam shaping using a binary-amplitude spatial light modulator," *Appl. Opt.* **49**, 1323–1330 (2010).
- [68] T.-L. Ho and Q. Zhou, *Universal cooling scheme for quantum simulation*, Nov. 2009, arXiv:0911.5506 [cond-mat.quant-gas].
- [69] T. A. Hilker, G. Salomon, F. Grusdt, A. Omran, M. Boll, E. Demler, I. Bloch, and C. Gross, "Revealing hidden antiferromagnetic correlations in doped Hubbard chains via string correlators," *Science* **357**, 484–487, ISSN: 1095-9203 (2017).
- [70] F. Nogrette, H. Labuhn, S. Ravets, D. Barredo, L. Béguin, A. Vernier, T. Lahaye, and A. Browaeys, "Single-atom trapping in holographic 2d arrays of microtraps with arbitrary geometries," *Physical Review X* **4**, 021034, ISSN: 2160-3308 (2014).
- [71] D. Barredo, H. Labuhn, S. Ravets, T. Lahaye, A. Browaeys, and C. S. Adams, "Coherent excitation transfer in a spin chain of three Rydberg atoms," *Physical Review Letters* **114**, 113002, ISSN: 1079-7114 (2015).
- [72] H. Labuhn, D. Barredo, S. Ravets, S. de Léséleuc, T. Macrì, T. Lahaye, and A. Browaeys, "Tunable two-dimensional arrays of single Rydberg atoms for realizing quantum ising models," *Nature* **534**, 667–670, ISSN: 1476-4687 (2016).
- [73] M. Saffman, T. G. Walker, and K. Mølmer, "Quantum information with Rydberg atoms," *Reviews of Modern Physics* **82**, 2313–2363, ISSN: 1539-0756 (2010).
- [74] S. Ebadi, T. T. Wang, H. Levine, A. Keesling, G. Semeghini, A. Omran, D. Bluvstein, R. Samajdar, H. Pichler, W. W. Ho, S. Choi, S. Sachdev, M. Greiner, V. Vuletić, and M. D. Lukin, "Quantum phases of matter on a 256-atom programmable quantum simulator," *Nature* **595**, 227–232, ISSN: 1476-4687 (2021).
- [75] G. Semeghini, H. Levine, A. Keesling, S. Ebadi, T. T. Wang, D. Bluvstein, R. Verresen, H. Pichler, M. Kalinowski, R. Samajdar, A. Omran, S. Sachdev, A. Vishwanath, M. Greiner, V. Vuletić, and M. D. Lukin, "Probing topological spin liquids on a programmable quantum simulator," *Science* **374**, 1242–1247, ISSN: 1095-9203 (2021).
- [76] M. Schlosser, S. Tichelmann, J. Kruse, and G. Birkel, "Scalable architecture for quantum information processing with atoms in optical micro-structures," *Quantum Information Processing* **10**, 907–924, ISSN: 1573-1332 (2011).

- [77] D. Bluvstein, S. J. Evered, A. A. Geim, S. H. Li, H. Zhou, T. Manovitz, S. Ebadi, M. Cain, M. Kalinowski, D. Hangleiter, J. P. Bonilla Ataides, N. Maskara, I. Cong, X. Gao, P. Sales Rodriguez, T. Karolyshyn, G. Semeghini, M. J. Gullans, M. Greiner, V. Vuletić, and M. D. Lukin, “Logical quantum processor based on reconfigurable atom arrays,” *Nature* **626**, 58–65, ISSN: 1476-4687 (2023).
- [78] M. Greiner, “Ultracold quantum gases in three-dimensional optical lattice potentials,” en, PhD thesis (LMU München, 2003).
- [79] C. Schweizer, “Minimal instances for \mathbb{Z}_2 lattice gauge theories and spin pumps,” en, PhD thesis (LMU Munich, 2019).
- [80] M. Aidelsburger, L. Barbiero, A. Bermudez, T. Chanda, A. Dauphin, D. González-Cuadra, P. R. Grzybowski, S. Hands, F. Jendrzejewski, J. Jünemann, G. Juzeliūnas, V. Kasper, A. Piga, S.-J. Ran, M. Rizzi, G. Sierra, L. Tagliacozzo, E. Tirrito, T. V. Zache, J. Zakrzewski, E. Zohar, and M. Lewenstein, “Cold atoms meet lattice gauge theory,” *Philosophical Transactions of the Royal Society A: Mathematical, Physical and Engineering Sciences* **380**, 10.1098/rsta.2021.0064, ISSN: 1471-2962 (2021).
- [81] J. C. Halimeh, M. Aidelsburger, F. Grusdt, P. Hauke, and B. Yang, *Cold-atom quantum simulators of gauge theories*, Oct. 2023, arXiv:2310.12201 [cond-mat.quant-gas].
- [82] T. Keilmann, S. Lanzmich, I. McCulloch, and M. Roncaglia, “Statistically induced phase transitions and anyons in 1d optical lattices,” *Nature Communications* **2**, 10.1038/ncomms1353, ISSN: 2041-1723 (2011).
- [83] S. Greschner, G. Sun, D. Poletti, and L. Santos, “Density-dependent synthetic gauge fields using periodically modulated interactions,” *Physical Review Letters* **113**, 215303, ISSN: 1079-7114 (2014).
- [84] A. Bermudez and D. Porras, “Interaction-dependent photon-assisted tunneling in optical lattices: a quantum simulator of strongly-correlated electrons and dynamical gauge fields,” *New Journal of Physics* **17**, 103021, ISSN: 1367-2630 (2015).
- [85] L. W. Clark, B. M. Anderson, L. Feng, A. Gaj, K. Levin, and C. Chin, “Observation of density-dependent gauge fields in a Bose-Einstein condensate based on micromotion control in a shaken two-dimensional lattice,” *Physical Review Letters* **121**, 030402, ISSN: 1079-7114 (2018).
- [86] H.-N. Dai, B. Yang, A. Reingruber, H. Sun, X.-F. Xu, Y.-A. Chen, Z.-S. Yuan, and J.-W. Pan, “Four-body ring-exchange interactions and anyonic statistics within a minimal toric-code Hamiltonian,” *Nature Physics* **13**, 1195–1200, ISSN: 1745-2481 (2017).
- [87] A. Kitaev, “Fault-tolerant quantum computation by anyons,” *Annals of Physics* **303**, 2–30, ISSN: 0003-4916 (2003).

- [88] F. J. Wegner, "Duality in generalized Ising models and phase transitions without local order parameters," *Journal of Mathematical Physics* **12**, 2259–2272, ISSN: 1089-7658 (1971).
- [89] R. Verresen, M. D. Lukin, and A. Vishwanath, "Prediction of Toric code topological order from Rydberg blockade," *Physical Review X* **11**, 031005, ISSN: 2160-3308 (2021).
- [90] L. Homeier, C. Schweizer, M. Aidelsburger, A. Fedorov, and F. Grusdt, " \mathbb{Z}_2 Lattice gauge theories and Kitaev's toric code: a scheme for analog quantum simulation," *Physical Review B* **104**, 085138, ISSN: 2469-9969 (2021).
- [91] L. Homeier, A. Bohrdt, S. Linsel, E. Demler, J. C. Halimeh, and F. Grusdt, "Realistic scheme for quantum simulation of \mathbb{Z}_2 lattice gauge theories with dynamical matter in (2+1)D," *Communications Physics* **6**, 10.1038/s42005-023-01237-6, ISSN: 2399-3650 (2023).
- [92] S. Chandrasekharan and U.-J. Wiese, "Quantum link models: a discrete approach to gauge theories," *Nuclear Physics B* **492**, 455–471, ISSN: 0550-3213 (1997).
- [93] U.-J. Wiese, "Ultracold quantum gases and lattice systems: quantum simulation of lattice gauge theories," *Annalen der Physik* **525**, 777–796, ISSN: 1521-3889 (2013).
- [94] V. Kasper, F. Hebenstreit, F. Jendrzejewski, M. K. Oberthaler, and J. Berges, "Implementing quantum electrodynamics with ultracold atomic systems," *New Journal of Physics* **19**, 023030, ISSN: 1367-2630 (2017).
- [95] A. Mil, T. V. Zache, A. Hegde, A. Xia, R. P. Bhatt, M. K. Oberthaler, P. Hauke, J. Berges, and F. Jendrzejewski, "A scalable realization of local $u(1)$ gauge invariance in cold atomic mixtures," *Science* **367**, 1128–1130, ISSN: 1095-9203 (2020).
- [96] H. Bernien, S. Schwartz, A. Keesling, H. Levine, A. Omran, H. Pichler, S. Choi, A. S. Zibrov, M. Endres, M. Greiner, V. Vuletić, and M. D. Lukin, "Probing many-body dynamics on a 51-atom quantum simulator," *Nature* **551**, 579–584, ISSN: 1476-4687 (2017).
- [97] F. M. Surace, P. P. Mazza, G. Giudici, A. Lerose, A. Gambassi, and M. Dalmonte, "Lattice gauge theories and string dynamics in Rydberg atom quantum simulators," *Physical Review X* **10**, 021041, ISSN: 2160-3308 (2020).
- [98] B. Yang, H. Sun, R. Ott, H.-Y. Wang, T. V. Zache, J. C. Halimeh, Z.-S. Yuan, P. Hauke, and J.-W. Pan, "Observation of gauge invariance in a 71-site bose–hubbard quantum simulator," *Nature* **587**, 392–396, ISSN: 1476-4687 (2020).
- [99] E. A. Martinez, C. A. Muschik, P. Schindler, D. Nigg, A. Erhard, M. Heyl, P. Hauke, M. Dalmonte, T. Monz, P. Zoller, and R. Blatt, "Real-time dynamics of lattice gauge theories with a few-qubit quantum computer," *Nature* **534**, 516–519, ISSN: 1476-4687 (2016).

- [100] J. C. Halimeh and P. Hauke, “Reliability of lattice gauge theories,” *Physical Review Letters* **125**, 030503, ISSN: 1079-7114 (2020).
- [101] J. C. Halimeh and P. Hauke, *Stabilizing gauge theories in quantum simulators: a brief review*, Apr. 2022, arXiv:2204.13709 [cond-mat.quant-gas].
- [102] J. C. Halimeh, H. Lang, J. Mildenerger, Z. Jiang, and P. Hauke, “Gauge-symmetry protection using single-body terms,” *PRX Quantum* **2**, 040311, ISSN: 2691-3399 (2021).
- [103] J. C. Halimeh, L. Homeier, C. Schweizer, M. Aidelsburger, P. Hauke, and F. Grusdt, “Stabilizing lattice gauge theories through simplified local pseudogenerators,” *Physical Review Research* **4**, 033120, ISSN: 2643-1564 (2022).
- [104] J. C. Halimeh, L. Homeier, A. Bohrdt, and F. Grusdt, *Spin exchange-enabled quantum simulator for large-scale non-Abelian gauge theories*, May 2023, arXiv:2305.06373 [cond-mat.quant-gas].
- [105] D. González-Cuadra, T. V. Zache, J. Carrasco, B. Kraus, and P. Zoller, “Hardware efficient quantum simulation of non-Abelian gauge theories with qudits on Rydberg platforms,” *Physical Review Letters* **129**, 160501, ISSN: 1079-7114 (2022).
- [106] D. Banerjee, M. Bögli, M. Dalmonte, E. Rico, P. Stebler, U.-J. Wiese, and P. Zoller, “Atomic quantum simulation of $U(N)$ and $SU(N)$ non-Abelian lattice gauge theories,” *Phys. Rev. Lett.* **110**, 125303 (2013).
- [107] C. W. Bauer, Z. Davoudi, A. B. Balantekin, T. Bhattacharya, M. Carena, W. A. de Jong, P. Draper, A. El-Khadra, N. Gemelke, M. Hanada, D. Kharzeev, H. Lamm, Y.-Y. Li, J. Liu, M. Lukin, Y. Meurice, C. Monroe, B. Nachman, G. Pagano, J. Preskill, E. Rinaldi, A. Roggero, D. I. Santiago, M. J. Savage, I. Siddiqi, G. Siopsis, D. Van Zanten, N. Wiebe, Y. Yamauchi, K. Yeter-Aydeniz, and S. Zorzetti, “Quantum simulation for high-energy physics,” *PRX Quantum* **4**, 027001, ISSN: 2691-3399 (2023).
- [108] E. Zohar, “Quantum simulation of lattice gauge theories in more than one space dimension—requirements, challenges and methods,” *Philosophical Transactions of the Royal Society A: Mathematical, Physical and Engineering Sciences* **380**, 10.1098/rsta.2021.0069, ISSN: 1471-2962 (2021).
- [109] J. Bender, E. Zohar, A. Farace, and J. I. Cirac, “Digital quantum simulation of lattice gauge theories in three spatial dimensions,” *New Journal of Physics* **20**, 093001, ISSN: 1367-2630 (2018).
- [110] N. H. Nguyen, M. C. Tran, Y. Zhu, A. M. Green, C. H. Alderete, Z. Davoudi, and N. M. Linke, “Digital quantum simulation of the Schwinger model and symmetry protection with trapped ions,” *PRX Quantum* **3**, 020324, ISSN: 2691-3399 (2022).
- [111] Z. Wang, Z.-Y. Ge, Z. Xiang, X. Song, R.-Z. Huang, P. Song, X.-Y. Guo, L. Su, K. Xu, D. Zheng, and H. Fan, “Observation of emergent Z_2 gauge invariance in a superconducting circuit,” *Phys. Rev. Res.* **4**, L022060 (2022).

- [112] E. R. Bennewitz, B. Ware, A. Schuckert, A. Lerose, F. M. Surace, R. Belyansky, W. Morong, D. Luo, A. De, K. S. Collins, O. Katz, C. Monroe, Z. Davoudi, and A. V. Gorshkov, *Simulating meson scattering on spin quantum simulators*, Mar. 2024, arXiv:2403.07061 [quant-ph].
- [113] J. Mildenerger, W. Mruczkiewicz, J. C. Halimeh, Z. Jiang, and P. Hauke, *Probing confinement in a \mathbb{Z}_2 lattice gauge theory on a quantum computer*, Mar. 2022, arXiv:2203.08905 [quant-ph].
- [114] Z. Davoudi, N. Mueller, and C. Powers, "Towards quantum computing phase diagrams of gauge theories with thermal pure quantum states," *Physical Review Letters* **131**, 081901, ISSN: 1079-7114 (2023).
- [115] X.-G. Wen, *Quantum field theory of many-body systems* (Oxford University Press, New York, Sept. 2007), ISBN: 9780199227259.
- [116] K. Wilson, "The origins of lattice gauge theory," *Nuclear Physics B - Proceedings Supplements* **140**, 3–19, ISSN: 0920-5632 (2005).
- [117] J. Kogut and L. Susskind, "Hamiltonian formulation of Wilson's lattice gauge theories," *Physical Review D* **11**, 395–408, ISSN: 0556-2821 (1975).
- [118] H. A. Kramers and G. H. Wannier, "Statistics of the two-dimensional Ferromagnet. part i," *Physical Review* **60**, 252–262, ISSN: 0031-899X (1941).
- [119] U. Borla, R. Verresen, J. Shah, and S. Moroz, "Gauging the Kitaev chain," *SciPost Physics* **10**, 10.21468/scipostphys.10.6.148, ISSN: 2542-4653 (2021).
- [120] U. Borla, "Quantum phases of low-dimensional \mathbb{Z}_2 lattice gauge theories," en, PhD thesis (Technische Universität München, 2022), p. 179, <https://mediatum.ub.tum.de/1688950>.
- [121] C. Prosko, S.-P. Lee, and J. Maciejko, "Simple \mathbb{Z}_2 lattice gauge theories at finite fermion density," *Physical Review B* **96**, 205104, ISSN: 2469-9969 (2017).
- [122] F. Schwabl, *Quantum mechanics* (Springer, 2007), ISBN: 9783540719328.
- [123] E. Zohar, J. I. Cirac, and B. Reznik, "Quantum simulations of gauge theories with ultracold atoms: local gauge invariance from angular-momentum conservation," *Physical Review A* **88**, 023617, ISSN: 1094-1622 (2013).
- [124] L. D. Landau and E. M. Lifshitz, *Quantum mechanics: non-relativistic theory*, 3rd ed., Course of theoretical physics (Butterworth Heinemann, Amsterdam, 2005), ISBN: 9780750635394.
- [125] L. D. Landau and E. M. Lifshitz, *The classical theory of fields*, 4th ed. (Butterworth-Heinemann, 1980).

- [126] S. Notarnicola, E. Ercolessi, P. Facchi, G. Marmo, S. Pascazio, and F. V. Pepe, “Discrete Abelian gauge theories for quantum simulations of QED,” *Journal of Physics A: Mathematical and Theoretical* **48**, 30FT01, ISSN: 1751-8121 (2015).
- [127] T. Banks, L. Susskind, and J. Kogut, “Strong-coupling calculations of lattice gauge theories: (1 + 1)-dimensional exercises,” *Physical Review D* **13**, 1043–1053, ISSN: 0556-2821 (1976).
- [128] T. Banks, R. Myerson, and J. Kogut, “Phase transitions in Abelian lattice gauge theories,” *Nuclear Physics B* **129**, 493–510, ISSN: 0550-3213 (1977).
- [129] S. D. Drell, H. R. Quinn, B. Svetitsky, and M. Weinstein, “Quantum electrodynamics on a lattice: a Hamiltonian variational approach to the physics of the weak-coupling region,” *Physical Review D* **19**, 619–638, ISSN: 0556-2821 (1979).
- [130] A. Polyakov, “Quark confinement and topology of gauge theories,” *Nuclear Physics B* **120**, 429–458, ISSN: 0550-3213 (1977).
- [131] J. Schwinger, “Gauge invariance and mass. II,” *Physical Review* **128**, 2425–2429, ISSN: 0031-899X (1962).
- [132] F. Grusdt and L. Pollet, “ \mathbb{Z}_2 Parton phases in the mixed-dimensional $t - J_z$ model,” *Physical Review Letters* **125**, 256401, ISSN: 1079-7114 (2020).
- [133] C. Gatttringer and K. Langfeld, “Approaches to the sign problem in lattice field theory,” *International Journal of Modern Physics A* **31**, 1643007, ISSN: 1793-656X (2016).
- [134] S. Gazit, M. Randeria, and A. Vishwanath, “Emergent Dirac fermions and broken symmetries in confined and deconfined phases of \mathbb{Z}_2 gauge theories,” *Nature Physics* **13**, 484–490, ISSN: 1745-2481 (2017).
- [135] S. Paeckel, T. Köhler, A. Swoboda, S. R. Manmana, U. Schollwöck, and C. Hubig, “Time-evolution methods for matrix-product states,” *Annals of Physics* **411**, 167998, ISSN: 0003-4916 (2019).
- [136] E. Zohar, J. I. Cirac, and B. Reznik, “Simulating compact quantum electrodynamics with ultracold atoms: probing confinement and nonperturbative effects,” *Physical Review Letters* **109**, 125302, ISSN: 1079-7114 (2012).
- [137] E. Zohar, J. I. Cirac, and B. Reznik, “Simulating (2 + 1)-dimensional lattice QED with dynamical matter using ultracold atoms,” *Physical Review Letters* **110**, 055302, ISSN: 1079-7114 (2013).
- [138] J. Osborne, I. P. McCulloch, B. Yang, P. Hauke, and J. C. Halimeh, *Large-scale 2 + 1D U(1) gauge theory with dynamical matter in a cold-atom quantum simulator*, Nov. 2022, arXiv:2211.01380 [cond-mat.quant-gas].

- [139] J. Osborne, B. Yang, I. P. McCulloch, P. Hauke, and J. C. Halimeh, *Spin-S U(1) quantum link models with dynamical matter on a quantum simulator*, May 2023, arXiv:2305.06368 [cond-mat.quant-gas].
- [140] T. V. Zache, M. Van Damme, J. C. Halimeh, P. Hauke, and D. Banerjee, “Toward the continuum limit of a (1 + 1)D quantum link Schwinger model,” *Physical Review D* **106**, 1091502, ISSN: 2470-0029 (2022).
- [141] T. Felser, P. Silvi, M. Collura, and S. Montangero, “Two-dimensional quantum-link lattice quantum electrodynamics at finite density,” *Physical Review X* **10**, 041040, ISSN: 2160-3308 (2020).
- [142] E. Ercolessi, P. Facchi, G. Magnifico, S. Pascazio, and F. V. Pepe, “Phase transitions in Z_n gauge models: towards quantum simulations of the Schwinger-Weyl QED,” *Physical Review D* **98**, 074503, ISSN: 2470-0029 (2018).
- [143] D. Horn, M. Weinstein, and S. Yankielowicz, “Hamiltonian approach to $Z(N)$ lattice gauge theories,” *Physical Review D* **19**, 3715–3731, ISSN: 0556-2821 (1979).
- [144] G. Arakawa and I. Ichinose, “ Z_N gauge theories on a lattice and quantum memory,” *Annals of Physics* **311**, 152–169, ISSN: 0003-4916 (2004).
- [145] U. Borla, B. Jeevanesan, F. Pollmann, and S. Moroz, “Quantum phases of two-dimensional Z_2 gauge theory coupled to single-component fermion matter,” *Phys. Rev. B* **105**, 075132 (2022).
- [146] G. 't Hooft, “On the phase transition towards permanent quark confinement,” *Nuclear Physics B* **138**, 1–25, ISSN: 0550-3213 (1978).
- [147] T. Senthil and M. P. A. Fisher, “Fractionalization, topological order, and cuprate superconductivity,” *Physical Review B* **63**, 134521, ISSN: 1095-3795 (2001).
- [148] T. Senthil and M. P. A. Fisher, “Fractionalization in the cuprates: detecting the topological order,” *Physical Review Letters* **86**, 292–295, ISSN: 1079-7114 (2001).
- [149] R. D. Sedgewick, D. J. Scalapino, and R. L. Sugar, “Fractionalized phase in an XY – Z_2 gauge model,” *Phys. Rev. B* **65**, 054508 (2002).
- [150] F. F. Assaad and T. Grover, “Simple Fermionic model of deconfined phases and phase transitions,” *Physical Review X* **6**, 041049, ISSN: 2160-3308 (2016).
- [151] S. Sachdev, E. Berg, S. Chatterjee, and Y. Schattner, “Spin density wave order, topological order, and Fermi surface reconstruction,” *Physical Review B* **94**, 115147, ISSN: 2469-9969 (2016).
- [152] R. K. Kaul, Y. B. Kim, S. Sachdev, and T. Senthil, “Algebraic charge liquids,” *Nature Physics* **4**, 28–31, ISSN: 1745-2481 (2007).

- [153] C. Hubig, “Symmetry-protected tensor networks,” PhD thesis (LMU München, 2017), <https://edoc.ub.uni-muenchen.de/21348/>.
- [154] C. Hubig, F. Lachenmaier, N.-O. Linden, T. Reinhard, L. Stenzel, A. Swoboda, M. Grundner, and S. Mardazad, *The SYTEN toolkit*, 2024, <https://syten.eu>.
- [155] U. Schollwöck, “The density-matrix renormalization group: a short introduction,” *Philosophical Transactions of the Royal Society A: Mathematical, Physical and Engineering Sciences* **369**, 2643–2661, ISSN: 1471-2962 (2011).
- [156] S. R. White, “Density-matrix algorithms for quantum renormalization groups,” *Physical Review B* **48**, 10345–10356, ISSN: 1095-3795 (1993).
- [157] J. Eisert, M. Cramer, and M. B. Plenio, “Colloquium: area laws for the entanglement entropy,” *Reviews of Modern Physics* **82**, 277–306, ISSN: 1539-0756 (2010).
- [158] G. Golub and C. Van Loan, *Matrix computations*, Johns Hopkins Studies in the Mathematical Sciences (Johns Hopkins University Press, 1996), ISBN: 9780801854149.
- [159] C. Lanczos, “An iteration method for the solution of the eigenvalue problem of linear differential and integral operators,” *Journal of Research of the National Bureau of Standards* **45**, 255, ISSN: 0091-0635 (1950).
- [160] U. Borla, R. Verresen, F. Grusdt, and S. Moroz, “Confined phases of one-dimensional spinless fermions coupled to Z_2 gauge theory,” *Physical Review Letters* **124**, 120503, ISSN: 1079-7114 (2020).
- [161] A. Kitaev and C. Laumann, *Topological phases and quantum computation*, Apr. 2009, arXiv:0904.2771 [cond-mat.mes-hall].
- [162] T. Iadecola and M. Schecter, “Quantum many-body scar states with emergent kinetic constraints and finite-entanglement revivals,” *Physical Review B* **101**, 024306, ISSN: 2469-9969 (2020).
- [163] U. Busch and K. A. Penson, “Tight-binding electrons on open chains: density distribution and correlations,” *Physical Review B* **36**, 9271–9274, ISSN: 0163-1829 (1987).
- [164] A. E. Feiguin and S. R. White, “Finite-temperature density matrix renormalization using an enlarged Hilbert space,” *Phys. Rev. B* **72**, 220401 (2005).
- [165] M. Zwolak and G. Vidal, “Mixed-state dynamics in one-dimensional quantum lattice systems: a time-dependent superoperator renormalization algorithm,” *Phys. Rev. Lett.* **93**, 207205 (2004).
- [166] A. J. Daley, C. Kollath, U. Schollwöck, and G. Vidal, “Time-dependent density-matrix renormalization-group using adaptive effective Hilbert spaces,” *Journal of Statistical Mechanics: Theory and Experiment* **2004**, P04005, ISSN: 1742-5468 (2004).

- [167] A. Nocera and G. Alvarez, "Symmetry-conserving purification of quantum states within the density matrix renormalization group," *Phys. Rev. B* **93**, 045137 (2016).
- [168] A. E. Feiguin and I. Klich, *Hermitian and non-Hermitian thermal Hamiltonians*, Aug. 2013, arXiv:1308.0756 [cond-mat.stat-mech].
- [169] H. Schlömer, A. Bohrdt, L. Pollet, U. Schollwöck, and F. Grusdt, "Robust stripes in the mixed-dimensional $t - J$ model," *Phys. Rev. Res.* **5**, L022027 (2023).
- [170] J. Haegeman, J. I. Cirac, T. J. Osborne, I. Pižorn, H. Verschelde, and F. Verstraete, "Time-dependent variational principle for quantum lattices," *Physical Review Letters* **107**, 070601, ISSN: 1079-7114 (2011).
- [171] J. Haegeman, C. Lubich, I. Oseledets, B. Vandereycken, and F. Verstraete, "Unifying time evolution and optimization with matrix product states," *Physical Review B* **94**, 165116, ISSN: 2469-9969 (2016).
- [172] P. Jordan and E. Wigner, "Über das Paulische Äquivalenzverbot," *Zeitschrift für Physik* **47**, 631–651, ISSN: 1434-601X (1928).
- [173] P. Coleman, *Introduction to many-body physics* (Cambridge University Press, Nov. 2015), ISBN: 9781139020916.
- [174] S. M. Linsel, A. Bohrdt, L. Homeier, L. Pollet, and F. Grusdt, *Percolation as a confinement order parameter in \mathbb{Z}_2 lattice gauge theories*, Jan. 2024, arXiv:2401.08770 [quant-ph].
- [175] J. Friedel, "Metallic alloys," *Il Nuovo Cimento* **7**, 287–311, ISSN: 1827-6121 (1958).
- [176] G. Bedürftig, B. Brendel, H. Frahm, and R. M. Noack, "Friedel oscillations in the open hubbard chain," *Physical Review B* **58**, 10225–10235, ISSN: 1095-3795 (1998).
- [177] P. Schmitteckert and U. Eckern, "Phase coherence in a random one-dimensional system of interacting fermions: a density-matrix renormalization-group study," *Physical Review B* **53**, 15397–15400, ISSN: 1095-3795 (1996).
- [178] R. Egger and H. Grabert, "Friedel oscillations for interacting fermions in one dimension," *Physical Review Letters* **75**, 3505–3508, ISSN: 1079-7114 (1995).
- [179] C. Kittel, *Quantum theory of solids*, 2nd ed. (John Wiley and sons, New York, 1987), ISBN: 0-471-62412-8.
- [180] M. Buser, U. Schollwöck, and F. Grusdt, "Snapshot-based characterization of particle currents and the Hall response in synthetic flux lattices," *Physical Review A* **105**, 033303, ISSN: 2469-9934 (2022).
- [181] A. J. Ferris and G. Vidal, "Perfect sampling with unitary tensor networks," *Physical Review B* **85**, 165146, ISSN: 1550-235X (2012).

- [182] T. Giamarchi, *Quantum physics in one dimension* (Oxford University Press, Dec. 2003), ISBN: 9780198525004.
- [183] L. Barbiero, L. Dell'Anna, A. Trombettoni, and V. E. Korepin, "Haldane topological orders in motzkin spin chains," *Physical Review B* **96**, 180404, ISSN: 2469-9969 (2017).
- [184] B. Sutherland, *Beautiful models* (WORLD SCIENTIFIC, June 2004).
- [185] A. Luther and I. Peschel, "Calculation of critical exponents in two dimensions from quantum field theory in one dimension," *Physical Review B* **12**, 3908–3917, ISSN: 0556-2805 (1975).
- [186] F. D. M. Haldane, "General relation of correlation exponents and spectral properties of one-dimensional Fermi systems: application to the anisotropic $S = \frac{1}{2}$ Heisenberg chain," *Phys. Rev. Lett.* **45**, 1358–1362 (1980).
- [187] T. Chanda, D. Gonzalez-Cuadra, M. Lewenstein, L. Tagliacozzo, and J. Zakrzewski, "Devil's staircase of topological Peierls insulators and Peierls supersolids," *SciPost Physics* **12**, 10.21468/scipostphys.12.2.076, ISSN: 2542-4653 (2022).
- [188] E. Lieb, T. Schultz, and D. Mattis, "Two soluble models of an antiferromagnetic chain," *Annals of Physics* **16**, 407–466, ISSN: 0003-4916 (1961).
- [189] J. I. Kapusta and C. Gale, *Finite-temperature field theory: principles and applications* (Cambridge University Press, Cambridge, United Kingdom, Aug. 2006), ISBN: 9780521173223.
- [190] A. Y. Kitaev, "Unpaired Majorana fermions in quantum wires," *Physics-Uspekhi* **44**, 131–136, ISSN: 1468-4780 (2001).
- [191] M. Greiter, V. Schnells, and R. Thomale, "The 1D Ising model and the topological phase of the Kitaev chain," *Annals of Physics* **351**, 1026–1033, ISSN: 0003-4916 (2014).
- [192] S. Suzuki, J.-i. Inoue, and B. K. Chakrabarti, *Quantum ising phases and transitions in transverse ising models* (Springer Berlin Heidelberg, 2013), ISBN: 9783642330391.
- [193] F. Wu, Y. Deng, and N. Prokof'ev, "Phase diagram of the toric code model in a parallel magnetic field," *Physical Review B* **85**, 195104, ISSN: 1550-235X (2012).
- [194] P. Calabrese and J. Cardy, "Entanglement entropy and quantum field theory," *Journal of Statistical Mechanics: Theory and Experiment* **2004**, P06002, ISSN: 1742-5468 (2004).
- [195] J. Spalding, S.-W. Tsai, and D. K. Campbell, "Critical entanglement for the half-filled extended Hubbard model," *Physical Review B* **99**, 195445, ISSN: 2469-9969 (2019).
- [196] C. Holzhey, F. Larsen, and F. Wilczek, "Geometric and renormalized entropy in conformal field theory," *Nuclear Physics B* **424**, 443–467, ISSN: 0550-3213 (1994).

- [197] F. A. Palm, S. Mardazad, A. Bohrdt, U. Schollwöck, and F. Grusdt, “Snapshot-based detection of $\nu = \frac{1}{2}$ Laughlin states: coupled chains and central charge,” *Phys. Rev. B* **106**, L081108 (2022).
- [198] H. Lange, L. Homeier, E. Demler, U. Schollwöck, F. Grusdt, and A. Bohrdt, “Feshbach resonance in a strongly repulsive ladder of mixed dimensionality: a possible scenario for bilayer nickelate superconductors,” *Physical Review B* **109**, 045127, ISSN: 2469-9969 (2024).
- [199] R. Verresen, R. Moessner, and F. Pollmann, “One-dimensional symmetry protected topological phases and their transitions,” *Physical Review B* **96**, 165124, ISSN: 2469-9969 (2017).
- [200] O. F. d. A. Bonfim, B. Boechat, and J. Florencio, “Ground-state properties of the one-dimensional transverse Ising model in a longitudinal magnetic field,” *Physical Review E* **99**, 012122, ISSN: 2470-0053 (2019).
- [201] C. J. Turner, K. Meichanetzidis, Z. Papić, and J. K. Pachos, “Optimal free descriptions of many-body theories,” *Nature Communications* **8**, 10.1038/ncomms14926, ISSN: 2041-1723 (2017).
- [202] A. Yuste, C. Cartwright, G. D. Chiara, and A. Sanpera, “Entanglement scaling at first order quantum phase transitions,” *New Journal of Physics* **20**, 043006, ISSN: 1367-2630 (2018).
- [203] C. Gatteringer, T. Kloiber, and V. Sazonov, “Solving the sign problems of the massless lattice Schwinger model with a dual formulation,” *Nuclear Physics B* **897**, 732–748, ISSN: 0550-3213 (2015).
- [204] C. Gatteringer, T. Kloiber, and M. Müller-Preussker, “Dual simulation of the two-dimensional lattice U(1) gauge-Higgs model with a topological term,” *Physical Review D* **92**, 114508, ISSN: 1550-2368 (2015).
- [205] P. Coleman, “New approach to the mixed-valence problem,” *Physical Review B* **29**, 3035–3044, ISSN: 0163-1829 (1984).
- [206] S. E. Barnes, “New method for the Anderson model. II. the U=0 limit,” *Journal of Physics F: Metal Physics* **7**, 2637–2647, ISSN: 0305-4608 (1977).
- [207] A. Auerbach, *Interacting electrons and quantum magnetism*, Corr., 2.print. (Springer-Verlag, New York, 1998), ISBN: 0-387-94286-6.
- [208] A. A. Ovchinnikov, D. V. Dmitriev, V. Y. Krivnov, and V. O. Cheranovskii, “Anti-ferromagnetic Ising chain in a mixed transverse and longitudinal magnetic field,” *Physical Review B* **68**, 214406, ISSN: 1095-3795 (2003).
- [209] H. C. Fogedby, “The Ising chain in a skew magnetic field,” *Journal of Physics C: Solid State Physics* **11**, 2801–2813, ISSN: 0022-3719 (1978).

- [210] J. Simon, W. S. Bakr, R. Ma, M. E. Tai, P. M. Preiss, and M. Greiner, “Quantum simulation of antiferromagnetic spin chains in an optical lattice,” *Nature* **472**, 307–312, ISSN: 1476-4687 (2011).
- [211] T. Lahaye, C. Menotti, L. Santos, M. Lewenstein, and T. Pfau, “The physics of dipolar bosonic quantum gases,” *Reports on Progress in Physics* **72**, 126401, ISSN: 1361-6633 (2009).
- [212] P. Emonts, A. Kelman, U. Borla, S. Moroz, S. Gazit, and E. Zohar, “Finding the ground state of a lattice gauge theory with fermionic tensor networks: a $2 + 1D$ \mathbb{Z}_2 demonstration,” *Physical Review D* **107**, 014505, ISSN: 2470-0029 (2023).
- [213] A. Kelman, U. Borla, I. Gomelski, J. Elyovich, G. Roose, P. Emonts, and E. Zohar, *Gauged Gaussian PEPS – a high dimensional tensor network formulation for lattice gauge theories*, Apr. 2024, arXiv:2404.13123 [hep-lat].
- [214] J. C. Halimeh, L. Barbiero, P. Hauke, F. Grusdt, and A. Bohrdt, “Robust quantum many-body scars in lattice gauge theories,” *Quantum* **7**, 1004, ISSN: 2521-327X (2023).
- [215] J.-Y. Desaulles, T. Iadecola, and J. C. Halimeh, *Mass-assisted local deconfinement in a confined \mathbb{Z}_2 lattice gauge theory*, Apr. 2024, arXiv:2404.11645 [cond-mat.quant-gas].
- [216] G.-X. Su, J. Osborne, and J. C. Halimeh, *A cold-atom particle collider*, Jan. 2024, arXiv:2401.05489 [cond-mat.quant-gas].

Acknowledgements

First of all I would like to thank my supervisor Prof. Dr. Fabian Grusdt, for his immense knowledge and endless enthusiasm. He was an excellent supervisor that guided me through all of the nice, and also some tough moments in the projects during my thesis. I really learned a lot from him and I am feeling very happy to have been one of his first students when he started building his group back in the fall of 2019. I would especially like to thank Fabian for allowing me to travel to many conferences during my studies.

I would like to thank Prof. Dr. Luca Barbiero for being a great collaborator on our projects together and agreeing to be my second referee for this thesis. We had many great discussions in the start of my thesis and I wish we collaborated on more projects together. I hope more opportunities will arise in the future.

Furthermore, I would like to thank the other members on my doctoral committee for their time: Prof. Dr. Tilman Birnstiel, Prof. Dr. Alexander Högele, and Prof. Dr. Steffen Rulands.

I would also like to thank Prof. Dr. Ulrich Schollwöck for all of his work as the head of the department and his collaboration on the projects.

In addition, I would like to thank many other collaborators with who I worked on different projects: Annabelle Bohrdt, Umberto Borla, Jad C. Halimeh, Christian Reinmoser, and Sergej Moroz. I would also like to thank the Erbium lab team in Harvard, especially Lin Su, Alexander Douglas, Ognjen Marković, Michal Szurek, and Markus Greiner.

I would also like to thank IMPRS-QST, and MCQST for organizing many interesting events. I would like to thank Prof. Dr. Michael Knap for being my second IMPRS advisor. For all the administrative help I would like to thank Cordula Weber and Kathrin Higgen.

I had many many opportunities to travel abroad. For that I would like to thank Zohreh Davoudi for inviting me multiple times to visit the University of Maryland. For a warm welcome there I thank Christopher White, Connor Powers, Navya Gupta, Saurabh Kadam, and Alexander Schuckert. In addition, I would also like to thank Prof. Annabelle Bohrdt for inviting me to ITAMP in Boston, and Prof. Markus Greiner for inviting me to visit the Harvard University. Finally, I would also like to thank Prof. Ana Maria Rey for inviting me to visit University of Colorado Boulder.

A special thanks goes to all of my colleagues at the chair for making my time as a PhD extremely enjoyable. For many nice discussions about physics, in addition to many relaxing coffee and lunch breaks I thank (in alphabetical order): Héloïse Albot, Damiano Aliverti, Pit Bermes, Tizian Blatz, Annika Böhler, Pietro Borchia, Giovanni Canossa, Gaia De Paciano,

Lexin Ding, Rajah Nutakki, Martin Grundner, Jad C. Halimeh, Tim Harris, Lukas Homeier, Friederike Horn, Lukas Kienesberger, Hannah Lange, Ke Liao, Julia Liebert, Simon Linsel, Sam Mardazad, Conall McCabe, Mattia Moroder, Nader Mostaan, Sebastian Paeckel, Felix Palm, Prof. Lode Pollet, Fabian Pauw, Nihal Rao, Nicolas Sadoune, Henning Schlömer, Dr. Zhenjiu Wang, and Reja Wilke. I would like to apologize in case I forgot to mention anyone else by name. For reading the manuscript and pointing out typos as well as giving helpful feedback on this thesis I would like to especially thank Pit Bermes, Tim Harris, Lukas Homeier, Hannah Lange, Mattia Moroder, Felix Palm, and Henning Scholömer. For the help with translating the abstract from english to german I thank Fabian Pauw and Lukas Homeier.

I want to thank my family for the support and understanding throughout my studies. I would like to thank my parents, Marija and Marijan, for being always there for me despite me being pretty far away for most of the time. I apologize for all the time I was too busy to come home and visit. I would also like to thank my brother Matej, and my sister-in-law Vesna for the emotional support. In addition, I would like to thank Zoja and Adam, for reminding me not to take myself too seriously.

I want to thank Yu-chan for being on my side in the last part of the PhD. Your support and deep understanding during many stressful moments made everything easier.

In addition, I would like to thank all of my friends for their support, in particular Jernej, my roommate in München.

Finally, I would like to note that I started with my studies confined in home-office due to the pandemics. This made everything more difficult, and has definitely left some scars, which we have already started to forget. Especially in this time I would like to thank all of my friends and colleagues for all the extra effort to stay in touch online.